Identification of Aeroelastic Parameters using Sweep Excitation

by
Catharine Chauvin Marsden

Department of Mechanical Engineering
McGill University
Montreal

May 2000

A thesis submitted to the Faculty of Graduate Studies and Research in partial fulfilment of the requirements of the degree of Master of Engineering.

0-612-70645-1

Abstract

The method of sweep excitation is employed in the resonance testing of aircraft and other structures. The method allows resonant frequencies and corresponding modal damping parameters to be calculated from a limited amount of real time test data. The amount of test time required to obtain the system's frequency response characteristics is reduced by subjecting the structure to an entire range of frequencies within one test pattern, or "sweep", instead of repeating individual tests at a number of different frequencies. The "sweep-rate" is defined as the rate at which the frequency increases or decreases during the frequency sweep. This thesis studies the effect of sweep-rate and sweep-direction on the accuracy of estimated system parameters, as well as assessing two different methods used to reduce discrete time histories to frequency transfer data. The impact of introducing a structural nonlinearity into the aeroelastic system is also investigated.

Numerical simulations of a two-degree-of-freedom airfoil with a flap subject to two-dimensional, incompressible, inviscid flow were performed. The airfoil was subjected to a sweep excitation by applying a flap input at a known frequency and sweep-rate. Data points obtained through numerical integration of the equations-of-motion were used to calculate modal frequency and damping parameters using two techniques, identified as the "time-domain" and Fourier transform methods, and the two methods were compared. Results obtained at different sweep-rates, as well as for increasing and decreasing frequency sweeps were compared for a number of different flow velocities up to the linear flutter speed.

The effect of introducing a structural nonlinearity was investigated by modifiying the linear system with a bilinear spring containing a freeplay region in the pitch degree-of-freedom. The resulting system was subjected to sweep excitations at one of the sweep-rates used on the linear system, and the nonlinear behaviour of the resulting frequency response curves were investigated for a number of different spring configurations. Nonlinear modal frequency and damping values are also compared to the corresponding linear values, and the effect of the system nonlinear response on the Fourier transform method of obtaining the frequency transfer function is investigated.

Sommaire

L'excitation sinusoïdale à fréquence variable est une méthode couramment employée dans le contexte des mises à l'essai et analyses de résonance des aéronefs et autres structures. C'est une méthode qui permet le calcul des paramètres du système à partir d'un minimum de données obtenues en vol. La quantité de donnés requises est réduite en faisant un seul essai de vol comprenant plusieurs fréquences d'excitation au lieu d'effectuer de nombreuses manœvres, chacune ayant une fréquence fixe. L'objectif de ce travail est d'étudier des conséquences de l'emploi de la méthode de la fréquence variable sur la précision de l'identification des paramètres du système. L'étude du système linéaire comprend trois parties; l'effet de la vitesse à laquelle la fréquence de l'excitation est variée, l'effet d'une variation croissante ou décroissante des fréquences ainsi qu'une évaluation de deux méthodes appliquées pour obtenir les fréquences résonantes et les valeurs d'amortissement des modes d'oscillation à partir des données obtenues en vol. Le travail conclu avec une investigation sur l'impact de l'introduction d'une non-linéarité structurelle sur la réponse dynamique du système aéroélastique.

Des simulations numériques ont été effectués dans le cas d'un profil à deux degrés de liberté muni d'un volet et soumis à un écoulement non-visqueux, incompressible et bi-dimensionel. Le profil a été soumis à une excitation périodique par le moyen d'oscillations prédéterminées des volets et les équations de mouvement ont été résolues avec une méthode numérique. Ces données numériques, simulations des données "réelles" d'un essai de vol, ont été utilisées afin de calculer les fréquences naturelles et les valeurs d'amortissement des modes aéroélastiques du profil. Une comparaison des résultats a été effectuée pour plusieurs vitesses d'écoulement différentes.

L'effet de la présence d'une non-linéarité structurelle a été étudié en introduisant un jeu dans le moment de rotation au profil linéaire. Le profil non-linéaire a été soumis a une excitation à fréquence variable et les comportements résultants ont été comparés pour plusieurs paramètres de la non-linéarité. De plus, les valeurs obtenues pour les fréquences naturelles et l'amortissement des modes ont été comparés aux valeurs obtenues pour le système linéaire.

Acknowledgements

I acknowledge a debt of gratitude to Professor S.J. Price for undertaking to supervise my efforts, and, in so doing, affording me a unique and privileged opportunity to continue to study and learn new things. Many thanks for the guidance, the patience, the advice and encouragement, for the time spent reviewing my work, and for always being available.

The financial assistance provided by McGill University and Professor Price, as well as the Max Stern Recruitment Award, is deeply appreciated.

Contents

Nomenclature

A	one half the sweep-rate in radians/(non-dimensional second)^2
B	sine sweep starting frequency
a_h	non-dimensional distance measured from the airfoil mid-chord to the elastic axis
b	airfoil semi-chord
C	Theodorsen's function
C_h	translational viscous damping coefficient in plunge
C_α	torsional viscous damping coefficient in pitch
C_β	torsional viscous damping coefficient in flap hinge
c_β	non-dimensional distance of the flap hinge from the airfoil mid-chord
F	$\overline{F}/K_h h$
$\overline{F}$	nonlinear structural restoring force
h	plunge displacement of the airfoil
I_α	mass moment of inertia of the combined airfoil/flap about the elastic axis
I_β	mass moment of inertia of the flap about the flap hinge
k	reduced frequency or Strouhal number, $\omega b/V$
K_h, K_α	linear structural stiffness in plunge and pitch
K_β	linear structuralstiffness in flap rotation
K_c	bilinear spring central stiffness term, see Figure 2
$L_{c/4}$	aerodynamic lift force acting at the ¼ chord
$L_{e.a.}$	aerodynamic lift force acting at the elastic axis
P_h, P_α, P_β, M_h, M_α, M_β	Theodorsen's coefficients
$L_\xi(\tau)$	aerodynamic lifting force due to plunge displacement
$L_\alpha(\tau)$	aerodynamic lifting force due to pitch displacement

$L_\beta(\tau)$	aerodynamic lifting force due to flap displacement
m	the combined aileron/flap mass per unit span
m_β	the flap mass per unit span
M	$\overline{M}/(K_\alpha \alpha)$
$\overline{M}$	nonlinear structural restoring moment
m_0	restoring moment preload for bilinear spring
$M_{c/4}$	aerodynamic pitching moment about the ¼ chord
$M_{e.a.}$	aerodynamic pitching moment about the elstic axis
r_α	non-dimensional radius of gyration of the airfoil/flap combination about the elastic axis
r_β	non-dimensional radius of gyration of the flap about the flap hinge
S_α	combined airfoil/flap static moment about the elastic axis
S_β	flap static moment about the flap hinge
U	non-dimensional free stream velocity, $V/b\omega_\alpha$
U^*	non-dimensional linear flutter velocity
V	free stream velocity
x_α	non-dimensional distance from the combined airfoil/flap centre of mass to the elastic axis
x_β	non-dimensional distance from the flap centre of mass to the flap hinge
α	pitch rotation of the airfoil, measured about the elastic axis
α_f	α at the start of the freeplay region, see Figure 2
β	angular rotation of flap about flap hinge
δ	length of the bilinear stiffness freeplay region, see Figure 2
ζ_α	non-dimensional structural damping moment, $C_\alpha/2\sqrt{mK_h}$
ζ_ξ	non-dimensional structural damping force, $C_h/2\sqrt{mk_h}$
μ	airfoil-air mass ratio, $m/\pi\rho b^2$

ξ	non-dimenional plunge displacement, h/b
τ	non-dimensional time, tV/b
ρ	air density
ϕ	Wagner's function
ω	frequency of oscillation
ω_h, ω_α	uncoupled frequencies in plunge and pitch, $(K_h/m)^{\frac{1}{2}}$, $(K_\alpha/I_\alpha)^{\frac{1}{2}}$
$\overline{\omega}$, $\overline{\omega}_\xi$	uncoupled frequency ratio, ω_h/ω_α
Z	system impedance

1 Introduction

1.1 Aeroelasticity

Aeroelasticity is the study of the effect of aerodynamic forces on elastic structures. In the context of aeroelasticity, the external forces and the deformation of the elastic body are interdependent. This differs from classical elasticity where, in general, the deformation of the body does not affect the force being applied to it. Aeroelastic analysis is applicable to many problems in both civil and mechanical engineering: such as the flow of fluids around bridges and tall structures, around the blades of turbomachinery and within flexible pipes. One of the primary fields of application is in the area of aircraft design, particularly lifting surfaces such as wings and tails, and control surfaces such as flaps and ailerons.

The aerodynamic forces and moments acting on an airfoil are functions of the airfoil shape, the angle of the airfoil relative to the airflow, and the velocity with which it moves. These aerodynamic forces in turn influence the subsequent motion of the airfoil. When the airfoil deforms elastically in response to an applied force, the external aerodynamic forces acting on it change in response to the deformation. In this way, a sort of feedback mechanism is created where a small deflection of the airfoil may cause a change in the aerodynamic force that leads to a larger deflection of the airfoil. This larger deflection may result in an increased aerodynamic force, until the initial disturbance becomes very large. When this happens, the result is termed aeroelastic instability.

Not all the forces acting within an aeroelastic system are aerodynamic. Collar's aeroelastic triangle (Collar 1946), shown in the following, illustrates the three sets of forces that may be present and their possible interactions.

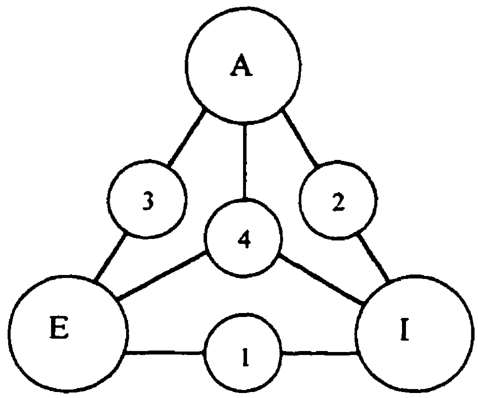

In the above diagram, the vertices A, E and I represent the aerodynamic, elastic and inertial forces, respectively, and the various combinations may be described as follows:

1. Interactions between the elastic and inertial forces that give rise to mechanical vibrations.
2. Interactions between the aerodynamic and elastic forces, and where the inertial forces do not play a role, are a special case of aeroelastic problems termed "static aeroelasticity". Some examples of static aeroelastic phenomena are wing divergence and control reversal.
3. The interactions between the aerodynamics and the inertial forces of the solid body form the class of problems known as aircraft stability and control.
4. Dynamic aeroelasticity deals with the interactions of all three aerodynamic, elastic and inertial forces. Flutter and buffeting are both examples of dynamic aeroelastic problems.

Dynamic aeroelastic response problems are those in which the oscillatory response of an aeroelastic system to an externally applied load is to be found. The external load may be caused by the forced deformation of the elastic body, such as is the case with the displacement of an aircraft wing or tail control surface, or by a disturbance such as a gust load or a turbulent airflow. In some cases the oscillations can become unstable and the vibrations may obtain very large amplitudes. This is the case with the instability known as "flutter".

1.2 Flutter

Classical flutter is a dynamic aeroelastic instability in which small disturbances in the airflow around an elastic body may induce oscillations of large amplitude. It is a phenomenon involving the oscillation of aircraft wings and control surfaces that has been observed since the very early days of flight.

If an aircraft wing at rest, and thus subject to no aerodynamic forces, were to be disturbed from its equilibrium position, it would oscillate, or move in harmonic motion about its equilibrium position. The oscillations would be damped by the structural damping in such a way that the amplitude of the motion would become progressively smaller with each oscillation, until the vibration would eventually die out. Thus the steady state condition of the wing would have no motion, and the only solution would be the transitory one. This is a mechanical vibration problem and involves the interaction between the system elastic and inertial forces. If the same wing is subject to aerodynamic forces due to its movement through an airflow, and is again disturbed from its equilibrium position, the interaction between the aerodynamic, inertial and elastic forces will typically cause the damping of the induced oscillation to increase with increasing airspeed. This increase in damping reaches a maximum at a specific airspeed and then decreases rapidly. When the airspeed reaches the "critical flutter speed", the aeroelastic system damping has decreased to the point where the induced oscillation will be self-sustaining, or the total damping is zero. At airspeeds beyond this critical speed, the induced oscillation will grow rapidly and may initiate violent oscillations, called flutter.

An oscillating body may be termed aerodynamically unstable if it gains energy from the airstream during a cycle of oscillation. The energy exchange may be the result of an external excitation or internal friction, both of which can affect the energy balance and resulting motion. When there is no external exciting force or internal friction and the airfoil extracts energy from the airstream, the resulting aerodynamic instability may be defined uniquely as flutter. A fluttering wing usually has oscillatory motion components in both the bending and the pitching degrees of freedom. The oscillation is harmonic, and the bending motion is out of phase with the torsional motion. The phase shift and amplitude ratios of the bending and torsional motions depend on the airspeed. Flutter occurs when the fluid flow past the airfoil reaches a critical speed where the phase difference between the motions allows the airfoil to gain energy from the surrounding airstream.

An aircraft wing may have an infinite number of degrees-of-freedom, but, for large aspect ratio wings, its deformation may generally be described by two quantities: the deflection at a point of reference, and the angular rotation about that point. The deformation of a control surface such as a flap or an aileron is generally described in terms of the angular rotation about its hinge line. Classical flutter requires the coupling of more than one degree-of-freedom. A flutter mode involving oscillations in all three of the above degrees-of-freedom is termed ternary flutter, while motion in two of the three degrees-of-freedom is termed binary flutter.

The many degrees-of-freedom of aircraft wings and tail surfaces, as well as the freedom of the aircraft to move as a rigid body, result in many potential flutter modes. Each of these modes will have a corresponding critical speed, and it is essential to the design of safe aircraft that the lowest of these critical speeds be identified during the design process. Both theoretical and experimental methods exist for the determination of critical flutter speeds.

1.3 Historical Remarks

The earliest studies of flutter were made in 1916 (Lanchester, Bairstow and Fage) in connection with the Handley Page bomber. Blasius (1925) attempted some calculations in 1919 after an Albatross D3 biplane suffered a wing failure. Detailed theoretical investigations of the flutter phenomenon required the use of nonstationary airfoil theory developed by Kutta and Joukowsky between 1902 and 1906. In 1919, Ackerman applied Prandtl's theory of bound vortices to a stationary airfoil, and Birnbaum extended it to nonstationary airfoils. At the same time, Wagner developed a theory for airfoils that change suddenly from a stationary configuration to a constant velocity or a sudden change in angle of attack. In 1929 Glauert calculated the forces and moments on a cylindrical object undergoing arbitrary motion. In 1934 Theodorsen's exact solution for a two-dimensional wing with a flap performing harmonic oscillations in incompressible flow was published.

Once the aerodynamic theory for oscillatory and unsteady airfoil motion had been developed, the potential for theoretical flutter analysis was greatly increased. From 1934 to 1937 much research was conducted on flutter. The two-dimensional problem of airfoil flutter with two degrees-of-freedom was solved, as was the two-dimensional problem with three degrees-of-freedom (airfoil-flap combinations). Three-dimensional wings were also treated using strip-theory aerodynamics and much of the theory was confirmed with wind tunnel testing.

There has recently been a resurgence of interest in aeroelasticity as exemplified by the January 1999 issue of the A.I.A.A. Journal of Aircraft which was devoted entirely to aeroelasticity (Friedman 1999, Livne 1999, Karpel 1999, Vari and Baker 1999).

1.4 The Aerodynamics of Flutter Analysis

Developing the equations of motion for an aeroelastic system requires the use of an adequate aerodynamic model to describe the lift force and moment as functions of the airfoil motion. One such model is based on linearized, incompressible thin airfoil theory (Glauert, 1924). The theory of thin airfoils is based on the assumptions of two-dimensional steady flow, small thickness to chord ratio, and small camber and gives quite accurate results for thin, slightly cambered airfoils.

The linearized theory is based on the assumption that the motion is of small amplitude and flow separation does not occur. When the expression for the aerodynamics is linear, the solution may be the superposition of several individual solutions. In the study of oscillating airfoils, the solution for an airfoil of finite thickness and having finite camber may be expressed as the superposition of the solution for an airfoil of zero thickness and zero camber performing unsteady oscillatory motion, and an airfoil with finite thickness and camber at a finite but steady angle of attack. Because we are interested quite specifically in the properties (such as frequency and damping) of the oscillatory motion, the steady portion of the solution is not considered in the analysis. The assumption of small angles is thus applicable to the amplitude of the oscillatory motion rather than the actual airfoil angle of attack. It is important to note, however, that the equations formulated without considering finite thickness and camber do not yield representative results for the true amplitudes of motion. In addition, the behaviour near the flutter speed can result in large displacements that violate the small disturbance assumption of the linearized theory.

The solution for the aerodynamic forces acting on a thin airfoil performing harmonic motion in an incompressible flow is based on thin airfoil theory and was developed by Theodorsen (Theodorsen, 1935). The aerodynamic response of an airfoil undergoing unsteady motion may be derived from Theodorsen's equations by means of a Fourier analysis and the Laplace transformation (Fung, 1955). The resulting equations are used to represent the aerodynamic forces and moments in this study.

1.5 Model Experiments

In many cases, theoretical analysis is inadequate in determining critical flutter modes for aircraft design due to the large number of degrees-of-freedom and the resulting potential for an equally large number of flutter modes. For this reason it is often necessary to determine critical speeds experimentally. Model wind tunnel testing has been used successfully to determine the critical speeds for a number of flutter modes, and many of the theoretical developments in flutter analysis have been validated by such tests.

The difficulties involved in creating scale models with dimensional similarity in all the required degrees-of-freedom often makes even wind tunnel testing inadequate in determining all the possible modes of an aircraft. In most cases, flight testing of full sized aircraft is a necessary step in aircraft design in order to ensure that the critical conditions for aeroelastic instability cannot be encountered within the design flight envelope.

1.6 Aircraft Flight Flutter Testing

The main objective of flight flutter testing is to demonstrate that an aircraft will not encounter flutter instabilities within its design envelope. During flight testing, a safety margin from the critical speed must be maintained to ensure the aircraft does not enter a potentially dangerous flight regime. In a typical flight test sequence, the aircraft is flown at a given airspeed, is subjected to a disturbance in one degree-of-freedom and the frequency and damping of the resulting free oscillation of the structure is measured. Alternatively, the aircraft may be subjected to a forced excitation, and the amplitude of the resulting oscillation measured for a number of different excitation frequencies. The process is repeated at increasing airspeeds until the critical combination of airspeed and frequency can be identified from a very large amplitude response. At each increment of airspeed, potentially dangerous flight conditions are avoided by evaluating the stability of the aircraft at the next increment.

The assessment of whether or not a mode will go unstable at the next increment of airspeed is normally based on the "trend" of the measured modal damping. For a given mode, the damping will increase with increasing airspeed, and then begin to decrease as the airspeed approaches the flutter speed. The prediction of the critical airspeed can be difficult due to a number of factors. Depending on the specific combination of aeroelastic parameters, the decrease in damping can be quite sudden and at low values of damping such as those associated with the onset of flutter, there is considerable uncertainty in the experimental measurement and determination of the damping values. In addition, it is not known in advance which mode will go unstable and damping estimates must be made for a number of potentially unstable configurations.

The use of the "flutter-margin" (Zimmerman and Weissenburger, 1964) is an alternative to relying on the modal damping trend to predict the onset of flutter. The flutter margin is a quantity that may be calculated from the experimental values of frequency and damping. The flutter margin decreases in an approximate linear manner with increasing airspeed until it reaches zero at the flutter speed. The advantage of the flutter margin over the modal damping lies in its almost linear variation with airspeed, making it possible to predict the onset of flutter from velocities as low as 50% of the flutter speed.

1.7 Sine Sweep Testing

One method of obtaining the flight test data necessary to calculate modal frequency and damping parameters involves applying a forced excitation of a specified frequency, and measuring the subsequent system response. The resonant or unstable frequency is found by increasing the frequency of the excitation in small increments and repeating the measurements at each increment. The method referred to as "sine sweep testing" reduces the amount of time required to obtain the required data by including a range of frequencies in one test. This is accomplished by increasing or decreasing the frequency in such a way that the peak response of the system is captured within the frequency range of the sweep. The rate at which the frequency is increased or decreased, the so-called "sweep-rate", must be as fast as possible in order to limit the time involved in high speed, low altitude flight testing. The sweep-rate should also be slow enough that the transient effects due to the changing frequency have died out and the steady state parameters may be measured with sufficient accuracy. It has been shown, for purely mechanical systems, that the sweep-rate, as well as the choice of increasing or decreasing sweep can have an effect on the measured modal frequency and damping values (Haslinger, 1986). Ewins (1984) recommends a maximum sweep rate of $216 f^2 \zeta^2$ Hz/min, where f is the modal natural frequency in Hz and ζ is the modal viscous damping factor. Analytical investigations, or "simulations" of sine sweep response have been limited to linear, one degree-of-freedom mechanical systems (Sanderson and Bartsch, 1958, Ewins, 1984, Haslinger, 1986) and one- and two-degree-of-freedom, linear and nonlinear mechanical (non aeroelastic) systems (Price, 1997).

1.8 Nonlinear Effects

Nonlinearities in aeroelastic systems can affect system frequency and damping parameters and may result in limit cycle oscillations or in some cases, chaotic response. Nonlinearities can initiate aeroelastic instabilities well below the flutter speed predicted using linear theory (Brietbach, 1977). Nonlinearities in aircraft aeroelastic systems can arise from both structural and aerodynamic sources. Aerodynamic nonlinearities are generally associated with transonic flow regimes, dynamic stall and shock induced effects, while structural nonlinearities may have a number of origins, including worn control surface hinges, loose control linkages, and nonlinear material properties.

Structural nonlinearities may be classified as either distributed or concentrated. Distributed nonlinearities are governed by elastodynamic deformations that affect the entire structure, whereas concentrated nonlinearities act locally. Most concentrated structural nonlinearities may be approximated as one of three main types: cubic, freeplay and hysteresis (Lee et al., 1999).

Theoretical investigations into the effect of structural nonlinearities on airfoil behaviour have, for the most part, been concentrated in the area of self-excited oscillatory motion where the system is not subject to a forced input (Lee and Tron, 1989, Price et al., 1995, Alighanbari and Price, 1996). Lee et al. (1997) and Gong et al. (1998) have studied the forced oscillation of a two-dimensional airfoil for incompressible aerodynamics with cubic nonlinear restoring forces in both degrees-of-freedom. Although complex and chaotic behaviours have been observed in the case of free oscillations, the systems subject to a forced oscillations appear to always respond harmonically.

1.9 Objectives of this Study

The objective of the current work is to study the effect of a sine sweep excitation on an aeroelastic, two degree-of-freedom system. The system is represented by a two-dimensional airfoil free to move in both bending and torsion and possessing a rigid flap. The aerodynamic forces are represented as those due to unsteady, oscillatory motion in incompressible flow, and the sine sweep excitation is applied to the system through a forced oscillation of the flap. The time history solutions to the equations of motion are obtained for a number of airspeeds up to the flutter boundary in order to simulate an actual flight test. At each airspeed, the time histories are obtained for a variety of sweep-rates, and for both increasing and decreasing sweeps. The results are used to calculate the modal frequency and damping using methods similar to those used to evaluate flight test time histories. The modal frequency and damping parameters thus obtained are compared with each other and with the known "exact" values for different combinations of sweep-rates and airspeeds.

The effect of introducing a simple structural nonlinearity in the pitch degree-of-freedom is also investigated. A freeplay type nonlinearity is introduced in the restoring moment, and the sine sweep simulations described above for the linear system are repeated.

1.10 Thesis Oultine

In Chapter 2, the general equations of motion are derived for the two-dimensional thin airfoil with a rigid flap performing unsteady motion in an incompressible flow. Some methods commonly used to solve the resulting equations are discussed.

In Chapter 3, the method used to simulate the flight test practice of sine sweep resonance testing is explained. The complete system of equations used to represent both the linear and nonlinear system subject to a sine sweep is presented. The techniques used to obtain frequency and damping parameters from the system response is explained.

The frequency and damping values obtained for the linear aeroelastic system at a variety of sweep-rates are presented in Chapter 4. The true values of modal frequency and damping at a series of airspeeds are compared to results obtained for increasing and decreasing frequency sweeps at four different sweep-rates.

In Chapter 5, a freeplay nonlinearity is introduced in the pitch degree-of-freedom. Frequency and damping values obtained from sine sweep simulations are presented for four different increasing and decreasing sweep-rates. Comparisons are made between values obtained for the linear and nonlinear systems. The parameters, or geometry, of the freeplay nonlinearity are varied, and the effects on the modal frequencies and damping investigated.

2 The Equations of Motion

The *typical section* is a two-dimensional airfoil model commonly used in the study of aeroelastic problems. It is particularly applicable to the study of binary flutter involving coupling between the bending and torsional motions of an aircraft wing or tail surface. When the aspect ratio of the lifting surface is large, the sweep is small, and the sectional characteristics vary smoothly along the span, a two-dimensional section with the properties of a typical section at 70-75% of the semi-span has been shown to yield accurate aerodynamic equations. The two-dimensional model cannot, however, account for three-dimensional flow effects or the rigid body degree-of-freedom in the aeroelastic system.

Figure 1 reproduces the typical section that is used as the basis for the equations of motion to be developed in this chapter. The airfoil is rigid and is mounted by a torsional and translational spring attached at the elastic axis, or shear centre of the section. The airfoil is free to move in both the bending and pitching directions, while the flap is constrained to move only as a forced input (it has infinite stiffness). The flap moves through an angle β about the flap hinge and relative to the airfoil chord, where β is positive for the flap trailing edge down. The bending deflection, h is measured positive downward and the pitch angle about the elastic axis, α, is positive for the airfoil leading edge up.

This chapter is divided into four sections. In Section 2.1 the equations of motion for the two-dimensional airfoil model are derived from Lagrange's equations. In Section 2.2, the right hand side of the equations from Section 2.1 are given in terms of unsteady, thin airfoil aerodynamic theory. Some methods commonly employed to solve the resulting system of equations are discussed in Section 2.3. In Section 2.4, a description is given of the particular nonlinearity that is considered within the scope of this study.

2.1 Obtaining the Equations of Motion

The equations of motion about the elastic axis for the aeroelastic, two-dimensional airfoil with a flap may be obtained from Figure 1 and Lagrange's equations. The kinetic energy of the system is

$$T=\frac{1}{2}\int_{-b(1+a_h)}^{b(c_\beta-a_h)}\left(\dot{h}+\dot{\alpha}x\right)^2\rho_{a/f}dx+\frac{1}{2}\int_{b(c_\beta-a_h)}^{b(1-a_h)}\left\{\dot{h}+\dot{\alpha}x+\dot{\beta}\left[x-\left(c_\beta-a_h\right)b\right]\right\}^2\rho_{a/f}dx\,. \quad (2.1)$$

In Equation 2.1, the origin of the x-dimension is at the elastic axis, located at a distance a_hb aft of the mid-chord, with x negative from the elastic axis to the airfoil leading edge and positive from the elastic axis to the airfoil/flap trailing edge. The airfoil leading edge is a distance $b+a_hb$ forward of the elastic axis, and the trailing edge a distance $b-a_hb$ aft of the elastic axis. The flap hinge is located at a distance $c_\beta b$ aft of the mid-chord, or a distance $bc_\beta-ba_h$ aft of the elastic axis. The density per unit span of the airfoil/flap combination is given by $\rho_{a/f}$, and the dot represents differentiation with respect to time. Expanding the integrals in equation (2.1) yields

$$T=\frac{1}{2}\int_{-b(1+a_h)}^{b(c_\beta-a_h)}\left(\dot{h}^2+2\dot{\alpha}\dot{h}x+\dot{\alpha}^2x^2\right)\rho_{a/f}dx$$

$$+\int_{b(c_\beta-a_h)}^{b(1-a_h)}\left\{\dot{h}^2+\dot{\alpha}^2x^2+\dot{\beta}^2\left[x-b\left(c_\beta-a_h\right)\right]^2+2\dot{\alpha}\dot{h}x+2\dot{h}\dot{\beta}\left[x-b\left(c_\beta-a_h\right)\right]+2\dot{\alpha}\dot{\beta}x\left[x-b\left(c_\beta-a_h\right)\right]\right\}\rho_{a/f}d$$

Combining the first two terms of the second integral with the first integral, and changing the variable in the second integral to $y=x-b\left(c_\beta-a_h\right)$ yields

$$T=\int_{b}^{b}\left(\dot{h}^2+2\dot{\alpha}\dot{h}x+\dot{\alpha}^2x^2\right)\rho_{a/f}dx$$

$$+\int_0^{b(1-c_\beta)}\left[\dot{\beta}^2y^2+2\dot{h}\dot{\beta}y+2\dot{\alpha}\dot{\beta}\left(y^2+b\left(c_\beta-a_h\right)y\right)\right]\rho_{a/f}dy$$

$$=\frac{1}{2}m\dot{h}^2+S_\alpha\dot{\alpha}\dot{h}+\frac{1}{2}I_\alpha\dot{\alpha}^2+\frac{1}{2}I_\beta\dot{\beta}^2+S_\beta\dot{h}\dot{\beta}+I_\beta\dot{\alpha}\dot{\beta}+b\left(c_\beta-a_h\right)S_\beta\dot{\alpha}\dot{\beta} \quad (2.2)$$

where

$S_\alpha=\int_{b}^{b}\rho_{a/f}x\,dx=mbx_\alpha$ the combined aileron/flap static moment about the elastic axis

$S_\beta=\int_0^{b-bc_\beta}\rho_{a/f}y\,dy=m_bbx_\beta$ the flap static moment about the flap hinge

$I_\alpha = \int_{-b}^{b} \rho_{a/f} x^2 dx$ the mass moment of inertia of the combined aileron/flap about the elastic axis

$I_\beta = \int_0^{b-bc_\beta} \rho_{a/f} y^2 dy$ the mass moment of inertia of the flap about the flap hinge.

$m = \int_{-b}^{b} \rho_{a/f} dx$ the mass per unit span of the airfoil/flap.

$m_\beta = \int_0^{b-bc_\beta} \rho_{a/f} dy$ the mass per unit span of the flap.

Lagrange's equations for the combined airfoil/flap system of Figure 1 are

$$\begin{aligned}
\frac{d}{dt}\left(\frac{\partial T}{\partial \dot{h}}\right) - \frac{\partial T}{\partial h} + \frac{\partial V}{\partial h} &= Q_{hnc}, \\
\frac{d}{dt}\left(\frac{\partial T}{\partial \dot{\alpha}}\right) - \frac{\partial T}{\partial \alpha} + \frac{\partial V}{\partial \alpha} &= Q_{\alpha nc} \\
\frac{d}{dt}\left(\frac{\partial T}{\partial \dot{\beta}}\right) - \frac{\partial T}{\partial \beta} + \frac{\partial V}{\partial \beta} &= Q_{\beta nc}
\end{aligned} \tag{2.3}$$

The elastic potential energy due to deformation of the structure, V, is a result of the restoring force and moments, $\overline{F}(h,)$, $\overline{M}(\alpha)$, and $\overline{M}_\beta(\beta)$, which are possibly nonlinear function of h, α, or β. Because the potential energies are not necessarily linear functions of the system variables, the potential energy terms in equation (2.3) are set to zero and the non-conservative generalized forces Q_{hnc}, $Q_{\alpha nc}$ and $Q_{\beta nc}$ are defined as

$$Q_{hnc} = P(t) - C_h \dot{h}(t) - \overline{F}(h) \tag{2.4}$$

$$Q_{\alpha nc} = R(t) - C_\alpha \dot{\alpha}(t) - \overline{M}(\alpha) \tag{2.5}$$

$$Q_{\beta nc} = S(t) - C_\beta \dot{\beta}(t) - \overline{M}_\beta(\beta) \tag{2.6}$$

where C_h, C_α and C_β are the translational and torsional damping coefficients, respectively. $\overline{F}(h)$, $\overline{M}(\alpha)$ and $\overline{M}_\beta(\beta)$ represent the structural restoring force and moments in the pitch, plunge and flap angular displacement directions, respectively. If the structure is linear then $\overline{F}(h)$, $\overline{M}(\alpha)$ and $\overline{M}(\beta)$ are replaced by $K_h h$, $K_\alpha \alpha$ and $K_\beta \beta$. Other externally applied forces and moments are represented by $P(t)$, $R(t)$ and $S(t)$ respectively, including the aerodynamic forces and other mechanical excitations.

Combining equation (2.2) with (2.3) and using the expressions for the generalized forces from equations (2.4), (2.5) and (2.6), the following equations of motion are obtained:

$$m\ddot{h}(t) + S_\alpha \ddot{\alpha}(t) + S_\beta \ddot{\beta}(t) + C_h \dot{h}(t) + \bar{F}(h) = P(t) \tag{2.7}$$

$$S_\alpha \ddot{h}(t) + I_\alpha \ddot{\alpha}(t) + \left[I_\beta + b(c_\beta - a_h)S_\beta\right]\ddot{\beta}(t) + C_\alpha \dot{\alpha}(t) + \bar{M}(\alpha) = R(t) \tag{2.8}$$

$$S_\beta \ddot{h}(t) + \left[I_\beta + b(c_\beta - a_h)S_\beta\right]\ddot{\alpha}(t) + I_\beta \ddot{\beta}(t) + C_\beta \dot{\beta}(t) + \bar{M}_\beta(\beta) = S(t) \tag{2.9}$$

Equation (2.9) is the equation of motion for the flap, and may be omitted from the solution because the flap is subject to a forced oscillation at a forced amplitude about its hinge, rather than being free to respond to the aerodynamic and structural forces and moments.

The natural frequencies for the linear, uncoupled system described by equations (2.7) and (2.8) are

$$\omega_\xi = \sqrt{\frac{K_h}{m}}$$

$$\omega_\alpha = \sqrt{\frac{K_\alpha}{I_\alpha}}$$

The nonlinear structural restoring force and moment, $\bar{F}(h)$ and $\bar{M}(\alpha)$, may be normalized with respect to their linear terms $K_h h$ and $K_\alpha \alpha$ to give $F(h)$ and $M(\alpha)$,

$$F(h) = \frac{\bar{F}(h)}{K_h h} = \frac{\bar{F}(h)}{m\omega_h^2 h} \quad \text{and} \quad M(\alpha) = \frac{\bar{M}(\alpha)}{K_\alpha \alpha} = \frac{\bar{M}(\alpha)}{I_\alpha \omega_\alpha^2 \alpha}. \tag{2.10}$$

When the structural restoring force and moment are linear, $M(\alpha(\tau)) = \alpha(\tau)$ and $F(h(t)) = h(t)$.

Equations (2.7) and (2.8) may be expressed in terms of equations (2.10) and the non-dimensional quantities

$U = \dfrac{V}{b\omega_\alpha}$, the non-dimensional airspeed,

$\tau = \dfrac{tV}{b} = tU\omega_\alpha$, dimensionless time,

$\xi = \dfrac{h}{b}$, the non-dimensional plunge displacement

$r_\alpha = \sqrt{\dfrac{I_\alpha}{mb^2}}$ the non-dimensional radius of gyration of the airfoil/flap,

$r_\beta = \sqrt{\dfrac{I_\beta}{m_\beta b^2}}$ the non-dimensional radius of gyration for the flap about the flap hinge,

$\zeta_\xi = \dfrac{C_h}{2\sqrt{mK_h}}$ the non-dimensional structural damping force and

$\zeta_\alpha = \dfrac{C_\alpha}{2\sqrt{I_\alpha K_\alpha}}$ the non-dimensional structural damping moment

to obtain

$$\begin{aligned}&\xi''(\tau) + x_\alpha \alpha''(\tau) + \frac{m_\beta}{m} x_\beta \beta''(\tau) + 2\zeta_\xi \frac{\overline{\omega}_\xi}{U} \xi'(\tau)\\ &+\left(\frac{\overline{\omega}_\xi}{U}\right)^2 F(\xi(\tau)) = p(\tau, \xi, \alpha)\end{aligned} \tag{2.11}$$

$$\begin{aligned}&\frac{x_\alpha}{r_\alpha^2}\xi''(\tau) + \alpha''(\tau) + +\left[\frac{r_\beta^2}{r_\alpha^2} + \frac{m_\beta}{m}\frac{x_\beta}{r_\alpha^2}\left(c_\beta - a_h\right)\right]\beta''(\tau)\\ &+2\zeta_\alpha \frac{1}{U}\alpha'(\tau) + \frac{1}{U^2} M(\alpha(\tau)) = r(\tau, \xi, \alpha)\end{aligned} \tag{2.12}$$

where the prime symbol denotes differentiation with respect to non-dimensional time τ. The uncoupled frequency ratio, $\overline{\omega}_\xi$, is defined as

$$\overline{\omega}_\xi = \frac{\omega_\xi}{\omega_\alpha} \tag{2.13}$$

and the non-dimensional aerodynamic forces and moments are defined as

$$p(\tau,\xi,\alpha,\beta)=\frac{-L(\tau,\xi,\alpha,\beta)}{mbU^2\omega_\alpha^2} \text{ and} \tag{2.14}$$

$$r(\tau,\xi,\alpha,\beta)=\frac{M_\alpha(\tau,\xi,\alpha,\beta)}{mb^2r_\alpha^2U^2\omega_\alpha^2}. \tag{2.15}$$

2.2 The Aerodynamic Forces

The lifting characteristics of an airfoil below the stall speed are negligibly influenced by viscosity. In addition, when the ratio of maximum thickness to chord length is small, the camber is small and the airfoil is operating at small angles of attack, the overall lifting characteristics may be closely approximated by "thin airfoil" theory. The airfoil is replaced by the curved line that is the mean of the upper and the lower surfaces, and this curve is regarded as a small deviation from a straight line. The fluid flow pattern is established by placing a bound vortex sheet on the curve and adjusting its strength to accommodate the boundary condition of no-flow across the curve. The circulation about the body is established by the Kutta-Joukowsky condition that the velocity must remain finite and tangent to the airfoil at the trailing edge, and the overall airfoil lifting characteristics are determined from the integral of the pressure forces. Glauert's proposed vortex distribution (Glauert, 1924) may be used to obtain expressions for lift and moment about the ¼ chord position where:

1. the lift coefficient for the two-dimensional section is directly proportional to the angle of attack and is zero when the angle of attack is zero,
2. the slope of the lift curve is equal to 2π,
3. the centre of pressure is at the ¼ chord for all values of the lift coefficient.

A similar approach may be used to obtain expressions for lift and moment due to the motion of a flap.

2.2.1 Oscillatory Aerodynamic Forces

The expressions used for the aerodynamic forces and moments due to the combined motion of the airfoil and the flap in the h, α and β directions are obtained from the theory of oscillating airfoils (Fung, 1955). The theory is based on thin airfoils oscillating at small amplitudes and may be applied to a fluttering airfoil. For an inviscid fluid the boundary condition at the fluid-solid interface requires that the fluid velocity component normal to the surface be equal to the normal velocity of the surface on the instantaneous position of the surface. This requirement, when applied to an airfoil undergoing vertical translation, such as the oscillating aeroelastic airfoil, leads to an aerodynamic lift force due to what is termed the "downwash velocity".

At the flutter condition, it is assumed that

$$\frac{h}{b} = \frac{h_0}{b} e^{i\omega t}, \quad \alpha = \alpha_0 e^{i(\omega t + \theta_1)}, \quad \beta = \beta_0 e^{i(\omega t + \theta_2)} \tag{2.16}$$

where h_0, α_0, and β_0 are real numbers, θ_1 and θ_2 are the phase angles by which α and β lead the wing bending displacement, and ω is the flutter frequency in radians per second. For a two-dimensional airfoil having these three degrees-of-freedom, in an incompressible flow of airspeed V, the aerodynamic forces are a function of the reduced frequency, or Strouhal number,

$$k = \frac{\omega b}{V}. \tag{2.17}$$

For subsonic flow the aerodynamic centre is located at the ¼ chord point aft of the leading edge, and the equations are developed with respect to the following displacements:

$$\frac{(h)_{c/4}}{b} = \frac{h - b\left(\tfrac{1}{2} + a_h\right)\alpha}{b} = \text{bending displacement of the ¼ chord point,} \tag{2.18}$$

α = pitching displacement about the ¼ chord point and

β = flap rotation about the flap hinge, located at the flap leading edge

The bending displacement is measured positive downward, the pitch displacement is positive for the airfoil leading edge nose up, and the flap rotation is positive for the trailing edge down. When the flap hinge is at the flap leading edge, a combination of the above three displacements completely describes any motion of the airfoil.

When h, α, and β all vary as given in equation (2.16), the aerodynamic lift per unit span is a linear combination of the lift forces due to the bending, pitching and flap displacements. The lift force acts at the ¼ chord, is positive upward and may be written as:

$$L_{c/4} = -\pi\rho b^3\omega^2\left[\left(\frac{h}{b}\right)_{c/4} P_h + \alpha P_\alpha + \beta P_\beta\right] \tag{2.19}$$

where P_h, P_α and P_β are dimensionless coefficients.

Similarly, the aerodynamic moment per unit span about the ¼ chord, positive in the clockwise direction, or the nose-up sense, can be written as

$$M_{c/4} = \pi\rho b^4\omega^2\left[\left(\frac{h}{b}\right)_{c/4} M_h + \alpha M_\alpha + \beta M_\beta\right] \tag{2.20}$$

The above equations are valid when the aerodynamics are linear and the principle of superposition is applicable. In the theoretical derivation of the coefficients, the fluid is assumed to be inviscid, and for incompressible flow the coefficients are functions of the Strouhal number, k. For compressible flow, the same equations may be used, but the coefficients are functions of the Mach number, c, as well as the Strouhal number, k. For a real, viscous fluid, the coefficients are functions of the Strouhal number, the Mach number and the Reynolds number.

The aerodynamic coefficients may be obtained from several different source references, such as Theodorsen (1934), Küssner and Schwarz (1941), Jones (1942), Scanlan and Rosenbaum (1951), or Smilg and Wasserman (1942). For this project, the coefficients used are from Theodorsen and are given in Appendix A.

The *elastic axis* of the wing is located at a distance $\left(\frac{1}{2}+a_h\right)b$ aft of the ¼ chord point.

The expression for the aerodynamic force may be expressed in terms of *h*, the bending displacement at the elastic axis.

$$L_{c/4} = L_{e.a.} = -\pi\rho b^3\omega^2\left\{\frac{h}{b}P_h + \alpha\left[P_\alpha - \left(\tfrac{1}{2}+a_h\right)P_h\right] + \beta P_\beta\right\} \tag{2.21}$$

Similarly, the aerodynamic moment about the elastic axis can be written as

$$M_{e.a.} = \pi\rho b^4\omega^2\left\{\begin{array}{l}\frac{h}{b}\left[M_h - \left(\tfrac{1}{2}+a_h\right)P_h\right] + \\ \alpha\left[M_\alpha - \left(\tfrac{1}{2}+a_h\right)\left(P_\alpha + M_h\right) + \left(\tfrac{1}{2}+a_h\right)^2 P_h\right] \\ +\beta\left[M_\beta - \left(\tfrac{1}{2}+a_h\right)P_\beta\right]\end{array}\right\} \tag{2.22}$$

2.2.2 Unsteady Aerodynamic Forces

The equations for the aerodynamic forces and moments developed in Section 2.2.1 are for airfoils performing harmonic, oscillatory motion. If the aerodynamics are linear, the equations for an airfoil undergoing arbitrary, unsteady motion may be obtained from the above expressions by means of a Fourier analysis.

The airfoil displacements are considered as the forcing function, or input to the system and the induced lifting forces and moments the response. The system admittance $1/Z(i\omega)$ is obtained from the theory of harmonically oscillating airfoils outlined above. From the previous section and the theory of oscillating airfoils, the total lift force acting on the airfoil is given by equation (2.21) and may be expressed in terms of Theodorsen's coefficients (Appendix A), the Strouhal number and the non-dimensional time, τ as

$$L_{e.a.} = L_\xi + L_\alpha + L_\beta$$

where

$$L_\xi = -\pi\rho b V^2 k^2 \xi_0\left(1 - \frac{2i}{k}C(k)\right)e^{ik\tau} \tag{2.23}$$

$$L_\alpha = -\pi\rho b V^2 k^2 \alpha_0 \left[\left(\tfrac{1}{2} - \frac{i}{k}\left[1+2C(k)\right] - \frac{2}{k^2}C(k)\right) - \left(\tfrac{1}{2}+a_h\right)\left(1-\frac{2i}{k}C(k)\right)\right]e^{ik\tau} \quad (2.24)$$

$$L_\beta = -\pi\rho b V^2 k^2 \beta_0 \left[-\frac{T_1}{\pi} + \frac{i}{k}\frac{T_4}{\pi} - \frac{i}{k}\frac{T_{11}}{\pi}C(k) - \frac{2}{k^2}\frac{T_{10}}{\pi}C(k)\right]e^{ik\tau} \quad (2.25)$$

The function $C(k)$ is called Theodorsen's function, and is a complex function of reduced frquency, $k = \omega b/V$. The exact expression for $C(k)$ is

$$C(k) = \frac{H_1^{(2)}(k)}{H_1^{(2)}(k) + iH_0^{(2)}(k)} = \frac{K_1(ik)}{K_0(ik)+K_1(ik)}$$

where H and K are Hankel and modified Bessel functions, respectively. In equations (2.23), (2.24) and (2.25), the following substitutions have been made:

$$\frac{h}{b} = \xi = \xi_0 e^{i\omega t} = \xi_0 e^{ik\tau},$$

$$\alpha = \alpha_0 e^{i\omega t} = \alpha_0 e^{ik\tau} \text{ and}$$

$$\beta = \beta_0 e^{i\omega t} = \beta_0 e^{ik\tau}.$$

Replacing ik by s, remembering that $\xi_0 e^{ik\tau}$, $\alpha_0 e^{ik\tau}$ and $\beta_0 e^{ik\tau}$ represent the forcing functions and L_ξ, L_α and L_β the responses in the above equations, the admittances may be obtained as

$$\frac{1}{Z_\xi(s)} = \pi\rho b V^2 s^2\left(1+\frac{2}{s}C(-is)\right) \quad (2.26)$$

$$\frac{1}{Z_\alpha(s)} = \pi\rho b V^2 s^2\left[\left(\tfrac{1}{2}+\frac{1}{s}\left[1+2C(-is)\right]+\frac{2}{s^2}C(-is)\right)-\left(\tfrac{1}{2}+a_h\right)\left(1+\frac{2}{s}C(-is)\right)\right] \quad (2.27)$$

$$\frac{1}{Z_\beta(s)} = \pi\rho b V^2 s^2\left[-\frac{T_1}{\pi} - \frac{1}{s}\frac{T_4}{\pi} + \frac{1}{s}\frac{T_{11}}{\pi}C(-is) + \frac{2}{s^2}\frac{T_{10}}{\pi}C(-is)\right]. \quad (2.28)$$

Because the Laplace transform of the response is equal to the Laplace transform of the forcing function multiplied by the admittance, equations (2.26), (2.27) and (2.28) may be used to find the aerodynamic lift force due to a non-harmonic function $\xi(\tau)$ through the expression

$$\mathcal{L}\{L_\xi(\tau)\} = \frac{\mathcal{L}\{\xi(\tau)\}}{Z_\xi(s)} = \pi\rho b V^2 s^2 \mathcal{L}\{\xi(\tau)\}\left(1+\frac{2}{s}C(-is)\right). \tag{2.29}$$

Using the convolution theory and the following results from Laplace transform theory (Le Page, 1961) where $\delta(\tau)$ is the Dirac delta function;

$$\mathcal{L}^{-1}\{1\} = \delta(\tau)$$

$$\mathcal{L}^{-1}\{s\} = \delta'(\tau)$$

$$\int_0^\tau \delta(\sigma)y(\sigma)d\sigma = y(0)$$

$$\int_0^\tau \delta'(\sigma)y(\sigma)d\sigma = -y'(0)$$

$$\mathcal{L}^{-1}\left\{s^2\mathcal{L}\{y(\tau)\}\right\} = y''(t) + y(0)\delta'(\tau) + y'(0)\delta(\tau),$$

and defining Wagner's function as

$$\phi(\tau) = \mathcal{L}^{-1}\left\{\frac{C(-is)}{s}\right\},$$

the expression for the lifting force due to the bending displacement, equation (2.23) may be rewritten as

$$L_\xi(\tau) = \pi\rho b V^2 \mathcal{L}^{-1}\left[s^2\mathcal{L}\{\xi(\tau)\}\left(1+\frac{2}{s}C(-is)\right)\right]$$

$$= \pi\rho b V^2\begin{bmatrix}\xi''(\tau) + 2\int_0^\tau \xi''(\sigma)\phi(\tau-\sigma)d\sigma - \xi(0)\delta'(\tau) - 2\xi(0)\phi'(\tau) \\ +\xi'(0)\delta(\tau) + 2\xi'(0)\phi(\tau)\end{bmatrix} \tag{2.30}$$

The third and fifth terms of equation (2.30) do not form part of the long-term solution because they involve the impulse function and hence are transient. In addition, the term involving $\phi'(\tau)$ may be excluded from the steady state solution because the time derivatives of Wagner's function approaches zero asymptotically for large τ.

The steady-state solution for the lift force due to the general motion $\xi = \xi(\tau)$, from equation (2.30), becomes,

$$L_\xi = \pi\rho b V^2\left(\xi''(\tau) + 2\xi'(0)\phi(\tau) + 2\int_0^\tau \xi''(\sigma)\phi(\tau-\sigma)d\sigma\right) \tag{2.31}$$

The aerodynamic force due to the pitch and flap deflections may be obtained in a similar fashion and the results are

$$L_\alpha = \mathcal{L}^{-1}\left\{\frac{\mathcal{L}\{\alpha(\tau)\}}{Z_\alpha(s)}\right\}$$

$$= \pi\rho b V^2\begin{bmatrix}\alpha'(\tau) - a_h\alpha''(\tau) + 2\alpha(0)\phi(\tau) + (1-2a_h)\alpha'(0)\phi(\tau) \\ +2\int_0^\tau\left[\alpha'(\sigma) + \left(\tfrac{1}{2} - a_h\right)\alpha''(\sigma)\right]\phi(\tau-\sigma)d\sigma\end{bmatrix} \tag{2.32}$$

$$L_\beta = \mathcal{L}^{-1}\left\{\frac{\mathcal{L}\{\beta(\tau)\}}{Z_\beta(s)}\right\}$$

$$= \pi\rho b V^2\begin{bmatrix}-\frac{T_1}{\pi}\beta''(\tau) - \frac{T_4}{\pi}\beta'(\tau) + \int_0^\tau\left[\frac{T_{11}}{\pi}\beta''(\sigma) + \frac{2T_{10}}{\pi}\beta'(\sigma)\right]\phi(\tau-\sigma)d\sigma \\ +\left(\frac{T_{11}}{\pi}\beta'(0) + \frac{2T_{10}}{\pi}\beta(0)\right)\phi(\tau)\end{bmatrix} \tag{2.33}$$

Equations (2.31), (2.32) and (2.33) may be combined to yield an expression for the aerodynamic lift force due to the combined wing bending, pitching and aileron motions,

$$L(\tau) = \pi\rho b U^2\left[\xi''(\tau) - a_h\alpha''(\tau) - \frac{T_1}{\pi}\beta''(\tau) + \alpha'(\tau) - \frac{T_4}{\pi}\beta'(\tau) + 2XTM\right] \tag{2.34}$$

where

$$XTM = C_1\phi(\tau) + \int_0^\tau \lambda(\sigma)\phi(\tau-\sigma)d\sigma, \tag{2.35}$$

with

$$C_1 = \xi'(0) + \left(\tfrac{1}{2} - a_h\right)\alpha'(0) + \alpha(0) + \frac{T_{11}}{2\pi}\beta'(0) + \frac{T_{10}}{\pi}\beta(0)$$

and

$$\lambda(\sigma) = \xi''(\sigma) + \left(\tfrac{1}{2} - a_h\right)\alpha''(\sigma) + \alpha'(\sigma) + \frac{T_{11}}{2\pi}\beta''(\sigma) + \frac{T_{10}}{\pi}\beta'(\sigma).$$

The same method was employed to derive the equations for the aerodynamic moment about the elastic axis,

$$M_\alpha(\tau) = \pi\rho b^2 V^2 \begin{bmatrix} a_h \xi''(\tau) - \left(1/8 + a_h^2\right)\alpha''(\tau) + \frac{1}{\pi}\left[T_7 + \left(c_\beta - a_h\right)T_1\right]\beta''(\tau) \\ -\left(1/2 - a_h\right)\alpha'(\tau) - \frac{1}{\pi}\left[T_1 - T_8 - \left(c_\beta - a_h\right)T_4 + \frac{T_{11}}{2}\right]\beta'(\tau) \\ -\frac{1}{\pi}\left(T_4 + T_{10}\right)\beta(\tau) + 2\left(1/2 + a_h\right)XTM \end{bmatrix} \tag{2.36}$$

Finally, the complete equations of motion for the two degree-of-freedom system are obtained by combining equations (2.11), (2.12), (2.14), (2.15), (2.34) and (2.36) to give

$$\begin{aligned} &\xi''(\tau) + x_\alpha \alpha''(\tau) + \frac{m_\beta}{m} x_\beta \beta''(\tau) + 2\zeta_\xi \frac{\overline{\omega}_\xi}{U}\xi'(\tau) + \left(\frac{\overline{\omega}_\xi}{U}\right)^2 F(\xi(\tau)) \\ &= -\frac{1}{\mu}\left[\xi''(\tau) - a_h \alpha''(\tau) - \frac{T_1}{\pi}\beta''(\tau) + \alpha'(\tau) - \frac{T_4}{\pi}\beta'(\tau) + 2XTM\right] \end{aligned} \tag{2.37}$$

and

$$\begin{aligned} &\frac{x_\alpha}{r_\alpha^2}\xi''(\tau) + \alpha''(\tau) + \left[\frac{r_\alpha^2}{r_\beta^2} + \frac{m_\beta}{m}\frac{x_\beta}{r_\alpha^2}\left(c_\beta - a_h\right)\right]\beta''(\tau) + 2\zeta_\alpha \frac{1}{U}\alpha'(\tau) + \frac{1}{U^2}M(\alpha(\tau)) \\ &= \frac{1}{\mu r_\alpha^2}\begin{bmatrix} a_h \xi''(\tau) - \left(1/8 + a_h^2\right)\alpha''(\tau) + \frac{1}{\pi}\left[T_7 + \left(c_\beta - a_h\right)T_1\right]\beta''(\tau) \\ -\left(1/2 - a_h\right)\alpha'(\tau) - \frac{1}{\pi}\left[T_1 - T_8 - \left(c_\beta - a_h\right)T_4 + \frac{T_{11}}{2}\right]\beta'(\tau) \\ -\frac{1}{\pi}\left(T_4 + T_{10}\right)\beta(\tau) + 2\left(1/2 + a_h\right)XTM \end{bmatrix} \end{aligned} \tag{2.38}$$

2.3 Solving the Equations of Motion

When the equations are linear, aeroelastic techniques such as the *p-k* method and the *u-g* method may used to evaluate the flutter speed for the system. These methods may also be applied to an equivalent linearized system, obtained from the nonlinear system via a describing function technique. These methods, however, do not seek time histories of the steady state motion of a forced system, but are methods for finding the flutter speed of an unforced system.

Equations (2.37) and (2.38) contain integral terms on the right hand side, introduced by the unsteady aerodynamic theory, and may not be solved using existing numerical methods for ordinary differential equations. Time history solutions to the nonlinear, integro-differential equations may be obtained using a finite difference method developed by Houbolt (1950). The method has been used to obtain solutions for unforced oscillations by Lee and Desrocher (1987) and by Price et al.(1994, 1995).

Equations (2.37) and (2.38) may also be reformulated to allow them to be integrated numerically. A simpler set of equations than the above has been obtained by Lee et al. (1997) and solved numerically to obtain time histories of the unsteady airfoil motion. In this study, the equations are reformulated as ordinary differential equations using a method developed by Alighanbari and Price (1996). This method is described, and the resulting system of ordinary differential equations is given in Chapter 3.

2.4 The Freeplay Nonlinearity

The structural nonlinearity known as the *bilinear nonlinearity* is sometimes employed in aeroelastic analysis to represent a worn or loose control surface hinge. Two such nonlinearities exist on the CF-18 aircraft, one at the wing fold hinge, and another at the outboard flap leading edge. A schematic of a typical bilinearity in the pitch direction is shown in Figure 2. The restoring moment in the pitch direction, $M(\alpha)$, is given by

$$M(\alpha)=\begin{cases} m_0+\alpha-\alpha_f, & \text{for } \alpha<\alpha_f \\ m_0+K_c(\alpha-\alpha_f) & \text{for } \alpha_f\le\alpha\le\alpha_f+\delta \\ m_0+\alpha-\alpha_f+\delta(K_c-1) & \text{for } \alpha_f+\delta<\alpha \end{cases} \tag{2.39}$$

In this study, the particular case of a bilinear nonlinearity with zero central stiffness, or $K_c=0$ is investigated. This type of nonlinearity is often called freeplay or backlash, and the freeplay region may have preload ($m_0\neq 0$) or no preload ($m_0=0$).

3 The Simulation of Sine Sweep Data

The simulation of a sine sweep test is achieved by subjecting the system to an input force due to a flap displacement, where the motion of the flap is given by the equation

$$\beta = \beta_0 \sin\left(A\tau^2 + B\tau\right). \tag{3.1}$$

The input forcing frequency is given by

$$\omega_\beta = \frac{d}{d\tau}\left(A\tau^2 + B\tau\right) = 2A\tau + B, \tag{3.2}$$

where the starting frequency for the sweep is B and the sweep-rate is $2A$. Time histories of the airfoil motion are obtained by substituting equation (3.1) into the equations of motion and then integrating numerically. The numerical integration is repeated at each increment of non-dimensional airspeed, U. Time histories are calculated for motion in both the bending and pitch directions, as well as for the flap input. The time histories are "simulations" of data acquired during a flight test frequency sweep, and are used to calculate the system transfer functions, modal frequencies and damping values.

In this Chapter, the equations of motion developed in Chapter 2 are transformed from a set of two coupled integro-differential equations into a set of eight ordinary differential equations that may be solved using standard numerical techniques. The method used to accomplish this reformulation was introduced by Alighanbari and Price (1996) and is outlined in Section 3.1. Two different methods are used to obtain the transfer function from the time history of the system response, and these methods are described in Section 3.2. The calculation of the system frequency and damping parameters is outlined in Section 3.3. In Section 3.4, the choice of input function used to calculate the transfer functions is presented, and Sections 3.4 and 3.5 describe the method used to introduce a structural nonlinearity into the aeroelastic system. The calculation of the linear flutter speed, U^*, which is used as a basis for comparing the linear and nonlinear results, is presented in Section 3.5.

3.1 Reformulating the Equations of Motion

In order to solve the equations of motion using standard numerical techniques, they must be reformulated to eliminate the integrals contributed by the aerodynamic terms. The equations of motion given in equations (2.37) and (2.38) may be rewritten as, in the bending degree-of-freedom,

$$\left(1+\frac{1}{\mu}\right)\xi''(\tau)+\left(x_\alpha-\frac{a_h}{\mu}\right)\alpha''(\tau)+\left(\frac{m_\beta}{m}x_\beta-\frac{T_1}{\mu\pi}\right)\beta''(\tau)+\frac{1}{\mu}\alpha'(\tau)+2\zeta_\xi\frac{\overline{\omega}_\xi}{U}\xi'(\tau)$$
$$-\frac{T_4}{\mu\pi}\beta'(\tau)+\left(\frac{\overline{\omega}_\xi}{U}\right)^2\xi(\tau)=-\frac{2}{\mu}\left\{C_1\phi(\tau)+\int_0^\tau\phi(\tau-\sigma)\lambda(\sigma)d\sigma\right\} \tag{3.2}$$

and in the pitch direction,

$$\left(\frac{x_\alpha}{r_\alpha^2}-\frac{a_h}{\mu r_\alpha^2}\right)\xi''(\tau)+\left(1+\frac{1}{8\mu r_\alpha^2}+\frac{a_h^2}{\mu r_\alpha^2}\right)\alpha''(\tau)$$
$$+\left(\frac{r_\alpha^2}{r_\beta^2}+\left[\frac{m_\beta}{m}\frac{x_\beta}{r_\alpha^2}\left(c_\beta-a_h\right)\right]-\frac{\left[T_7+\left\{c_\beta-a_h\right\}T_1\right]}{\mu\pi r_\alpha^2}\right)\beta''(\tau)$$
$$+\left(\frac{2\zeta_\alpha}{U}+\frac{(0.5-a_h)}{\mu r_\alpha^2}\right)\alpha'(\tau)+\frac{1}{\mu\pi r_\alpha^2}\left(T_1-T_8-\left[c_\beta-a_h\right]T_4+0.5T_{11}\right)\beta'(\tau)$$
$$+\frac{(T_4+T_{10})}{\mu\pi r_\alpha^2}\beta(\tau)+\frac{M(\alpha)}{U^2}=\frac{2}{\mu r_\alpha^2}(0.5+a_h)\left[C_1\phi(\tau)+\int_0^\tau\phi(\tau-\sigma)\lambda(\sigma)d\sigma\right]. \tag{3.3}$$

The integral terms in equations (3.2) and (3.3) are eliminated as follows: Equations (3.2) and (3.3) are differentiated with respect to non-dimensional time, τ, to obtain equations (3.4) and (3.5), and then differentiated again to obtain equations (3.6) and (3.7). Equations (3.2) and (3.3) are multiplied by *bd* to obtain equations (3.8) and (3.9), and equations (3.4) and (3.5) are multiplied by *(b+d)* to obtain equations (3.10) and (3.11). The full text of equations (3.4) through (3.11) are given in Appendix C, where Wagner's function has been replaced by the approximation given by Jones (1940),

$$\phi(\tau)=1-0.165e^{-0.0455\tau}-0.335e^{-0.3\tau}.$$

Adding equations (3.6), (3.8) and (3.10) for the plunge direction, and equations (3.7), (3.9) and (3.11) for the pitch direction, results in two equations free of integral terms. For the plunge and pitch directions, respectively, the equations of motion become

$$m_1\xi''''(\tau)+m_2\alpha''''(\tau)+m_3\beta''''(\tau)+m_4\xi'''(\tau)+m_5\alpha'''(\tau)+m_6\beta'''(\tau)+m_7\xi''(\tau)$$
$$+m_8\alpha''(\tau)+m_9\beta''(\tau)+m_{10}\xi'(\tau)+m_{11}\alpha'(\tau)+m_{12}\beta'(\tau)+m_{13}\xi(\tau)+m_{14}\alpha(\tau)$$
$$+m_{15}\beta(\tau)=\frac{4}{\mu}bd(0.5-a_h)\alpha'(0) \qquad (3.12)$$

and

$$n_1\xi''''(\tau)+n_2\alpha''''(\tau)+n_3\beta''''(\tau)+n_4\xi'''(\tau)+n_5\alpha'''(\tau)+n_6\beta'''(\tau)+n_7\xi''(\tau)$$
$$+n_8\alpha''(\tau)+n_9\beta''(\tau)+n_{10}\xi'(\tau)+n_{11}\alpha'(\tau)+n_{12}\beta'(\tau)+n_{13}\xi(\tau)+n_{14}\alpha(\tau)$$
$$+n_{15}\beta(\tau)+\frac{bd}{U^2}M(\alpha(\tau))+\frac{(b+d)}{U^2}M'(\alpha(\tau))+\frac{M''(\alpha(\tau))}{U^2}$$
$$=-\frac{4bd}{\mu r_\alpha^2}(0.5+a_h)(0.5-a_h)\alpha'(0) \qquad (3.13)$$

The coefficients in equations (3.12) and (3.13) are independent of time and are functions of the airfoil physical parameters and the airspeed only. Detailed equations for the coefficients are given in Appendix C.

Equations (3.12) and (3.13) may be reduced to a system of first order equations by making the following substitutions

$$x_1(\tau)=\xi(\tau) \qquad x_2(\tau)=\alpha(\tau)$$
$$x_3(\tau)=\xi'(\tau) \qquad x_4(\tau)=\alpha'(\tau)$$
$$x_5(\tau)=\xi''(\tau) \qquad x_6(\tau)=\alpha''(\tau)$$
$$x_7(\tau)=\xi'''(\tau) \qquad x_8(\tau)=\alpha'''(\tau)$$

to yield

$$m_1x_7'(\tau)+m_2x_8'(\tau)+m_4x_7(\tau)+m_5x_8(\tau)+m_7x_5(\tau)+m_8x_6(\tau)$$
$$+m_{10}x_3(\tau)+m_{11}x_4(\tau)+m_{13}x_1(\tau)+m_{14}x_2(\tau)=f_1 \qquad (3.14)$$

where

$$f_1 = -m_3\beta''''(\tau) - m_6\beta'''(\tau) - m_9\beta''(\tau) - m_{12}\beta'(\tau) - m_{15}\beta(\tau) \tag{3.15}$$

and

$$n_1x_7'(\tau) + n_2x_8'(\tau) + n_4x_7(\tau) + n_5x_8(\tau) + n_7x_5(\tau) + n_8x_6(\tau)$$
$$+n_{10}x_3(\tau) + n_{11}x_4(\tau) + n_{13}x_1(\tau) + n_{14}x_2(\tau) = f_2 \tag{3.16}$$

where

$$\begin{aligned} f_2 = &-\frac{bd}{U^2}M(\alpha(\tau)) - \frac{(b+d)}{U^2}M'(\alpha(\tau)) - \frac{M''(\alpha(\tau))}{U^2} \\ &-n_3\beta''''(\tau) - n_6\beta'''(\tau) - n_9\beta''(\tau) - n_{12}\beta'(\tau) - n_{15}\beta(\tau) \end{aligned} \tag{3.17}$$

Equations (3.14) and (3.16) may be written in matrix form as

$$[A]\{X'\} + [B]\{X\} = \{F\} \tag{3.16}$$

where $[A]$ and $[B]$ are given in Appendix C,

$$\{X\} = \{x_1, x_2, x_3, x_4, x_5, x_6, x_7, x_8\}^T, \tag{3.17}$$

and

$$\{F\} = \{0,0,0,0,0,0, f_1(\tau), f_2(\tau)\}^T. \tag{3.18}$$

Equations (3.16) to (3.18) form a system of ordinary differential equations, that may be solved using a number of standard numerical techniques. In this study, they were solved using the *Numerical Recipes* (Press, Flannery, Teukolsky and Vetterling, 1989) subroutine *rkdumb*. This subroutine integrates the equations using a fourth-order Runge-Kutta method with constant stepsize of .005 non-dimensional seconds per step. The size of the timestep was determined by running the program at progressively smaller stepsizes until the time histories produced did not change more than .01% with a .0025 second decrease in stepsize. Each numerical solution provides a time history of the response over a time period determined by the length of time the program is required to run.

The subroutine requires that the initial conditions up to the fourth derivative be input by the user. The required values were obtained by substituting the initial conditions

$\xi(0) = 0$,

$\xi'(0) = 0$,

$\alpha(0) = 0$,

$\alpha'(0) = 0$,

$\beta(0) = 0$

into the equations of motion, (3.2) and (3.3), and solving for $\xi''(0)$ and $\alpha''(0)$. The expressions obtained for $\xi''(0)$ and $\alpha''(0)$ are then substituted into the third order equations (3.4) and (3.5) to obtain $\xi'''(0)$ and $\alpha'''(0)$, respectively. Expressions for $\beta'(0)$, $\beta''(0)$, and $\beta'''(0)$ were obtained from successive differentiations of equation (3.1).

3.2 The Aeroelastic Transfer Function

The aeroelastic transfer function is a measure of the frequency transfer between the force input to the system and the system response. The response that is in phase with the forcing function is represented by the magnitude of the transfer function, while the response that is out of phase with the input is given by the phase difference. The transfer function is calculated from the time histories of the system input and response, and may be used to obtain values for the system natural frequencies and damping ratios.

Figure 3 shows a typical example of a simulated frequency sweep. Figure 3(a) shows the time history of the input to the system, and Figure 3(b) the time history of the system response in the pitch direction. The system responds at the same frequency as the input, but not necessarily in phase with it. Figure 3(c) shows the frequency of both the input and the response as a function of time.

Two different methods may be employed to obtain the transfer function from a response signal consisting of a number of discrete data points. The numerical integration procedure used in this study generates such a signal, as does "real life" test data transmitted by motion transducers. The two techniques may be referred to as the time-domain and spectral, or Fourier-transform methods. Both methods result in a transfer function magnitude and phase-lag that defines the frequency transfer between the force input and the system response for each of the two degrees-of-freedom.

3.2.1 The Time-domain Method

Using this method, the transfer function for the system input and response shown in Figure 4 is obtained by dividing the peak-to-peak magnitudes of the response curve by the peak-to-peak magnitudes of the corresponding peaks from the input force curve. Figure 4(a) illustrates this method for a portion of the curve from Figure 3. The corresponding frequencies for each peak are obtained from equation (3.2). The magnitudes and frequencies plotted against each other produce the transfer function magnitude plot shown in Figure 4(b).

The phase difference between the excitation and the response is calculated by finding the time delay between corresponding peaks of the forcing function and system response, and dividing the result by the period, or time required to complete a cycle of oscillation. The concept of phase lag is illustrated in Figure 4(a) and the results are plotted against their corresponding frequencies in Figure 4(c).

The transfer function magnitude and phase difference may be used together in a Nyquist plot. In the Nyquist plot, each point of the curve corresponds to a point in the transfer function (response divided by input), and is represented as a complex number $R_{tf} - iI_{tf}$. The real and imaginary parts are

$$R_{tf}=X\cos\theta,$$

and

$$I_{tf}=X\sin\theta,$$

respectively, where X is the magnitude of the transfer function and θ is the phase lag between the input and the response. Figure 5 is a typical example of a Nyquist diagram and was obtained from the transfer function magnitudes and phase angles shown in Figures 3(b) and (c).

3.2.2 The Spectral Method

The transfer function may also be obtained via spectral methods using the Fast Fourier Transform, or FFT. The method consists of converting the time histories of the system input and response to their frequency domains via the Fourier transform. The transfer function magnitude as a function of frequency is then obtained by dividing the frequency domain of the response by that of the input. This method is more commonly used to analyze flight test data where the signals are noisy and the time-domain approach is impossible to apply.

The FFT method is strictly applicable to time histories that represent a stationary signal, or a signal for which various statistical averages do not vary with time. Because the frequency of the sine sweep varies with time, the response time history is a non-stationary signal. In order to analyse the non-stationary signal a length of time, or "window" is chosen during which it is assumed that the signal does not change significantly. The FFT is taken, the window is moved along in time and the process repeated. As the window is moved along, subsequent sections are overlapped. Due to the choice of a finite window, the signal may not have zero value and slope at each end of the window. This may cause the FFT method to find frequencies not actually present in the signal. In order to avoid this "frequency leakage", the signal within the window is multiplied by a weighting function having the necessary zero values and slope to eliminate any possible discontinuity. Common weighting functions used for sinusoidal or random data are the Hamming and Hanning windows. Once the entire signal has been analysed, all the FFT's are averaged to obtain the transfer function magnitude and phase angle. The results may be expressed as a transfer function magnitude versus frequency plot or as a Nyquist diagram for the system.

The parameters used to obtain the transfer function via the spectral method were chosen to provide the most accurate values of frequency and damping. *T*, the period of time over which the Fast Fourier Transform was calculated gives the fundamental frequency and frequency resolution for the FFT process, $f = \Delta f = 1/T$. The sampling frequency is given as $f_s = 1/t_s$, where t_s is the time interval between samples. The frequency resolution may be expressed in terms of the block size or window length, *nw* and sampling frequency as $\Delta f = 1/(nw * t_s)$. The maximum frequency, f_{max}, that the FFT can represent is given by $f_{max} = f_s/2$ and is often referred to as the Nyquist frequency. The type of weighting function and the overlap between successive windows can also be important. The results presented in this study were obtained using the Hanning windowing function with a 50% overlap. The window length was chosen between 3500 and 9500 samples and the sampling frequency used was either 4 or 8 samples per non-dimensional time unit.

3.3 Frequency and Damping Calculations

The system natural frequencies and damping values may be obtained from either the transfer function magnitude plot shown in Figure 4(b) or from the Nyquist plot of Figure 5.

The system natural frequency, ω_0, is taken from the absolute peak-value, X_{max}, of the transfer function shown in Figure 4. The half power point frequencies, ω_1 and ω_2, are defined as the frequencies for which the magnitude of the transfer function is $X_{max}/\sqrt{2}$. The damping may then be found from

$$2\zeta = \frac{\omega_2 - \omega_1}{\omega_0}. \tag{3.19}$$

Alternatively, the frequency and damping may be found from the Nyquist plot of Figure 5. The exact location of the natural frequency, ω_0, is given by the point on the circle where the spacing between equal frequency increments is at a maximum. If two points, ω_1 and ω_2, are chosen either side of the natural frequency, it can be shown that

$$2\zeta = \left(\frac{\omega_2 - \omega_1}{\omega_0}\right)\left(\frac{2}{\tan\left[\phi_1/2\right] + \tan\left[\phi_2/2\right]}\right). \tag{3.20}$$

If $\phi_1 = \phi_2 = 90°$, then equation (3.20) reduces to equation (3.19).

3.4 Input Force Calculation

The input or forcing function required to calculate the transfer function is obtained from the original equations of motion.

In the sine sweep excitation, the actual input to the system is a flap motion rather than a direct force. For the purposes of calculating the transfer function, the input force is taken as the aerodynamic forces generated by the motion input. The forced motion of the flap generates both an aerodynamic lift force and a moment acting about the airfoil elastic axis, and the resulting input force has both a lift and a moment component. The equations used to describe this force and moment originate with equations (2.34) and (2.36), or Theodorsen's equations for the linear aerodynamic lift force and moment due to the flap motion. Once the equations are reformulated to eliminate the integral terms, the required expressions may be obtained from equations (3.15) and (3.17) as

$$l(\tau) = m_3\beta''''(\tau) + m_6\beta'''(\tau) + m_9\beta''(\tau) + m_{12}\beta'(\tau) + m_{15}\beta(\tau) \tag{3.21}$$

$$m_\beta(\tau) = n_3\beta''''(\tau) + n_6\beta'''(\tau) + n_9\beta''(\tau) + n_{12}\beta'(\tau) + n_{15}\beta(\tau), \tag{3.22}$$

where the constants are given in Appendix C and the $\beta(\tau)$ terms, obtained by successive differentiation of equation (3.1), are

$$\beta'(\tau) = \beta_0(2A\tau + B)\cos(A\tau^2 + B\tau) \tag{3.23}$$

$$\beta''(\tau) = 2A\beta_0\cos(A\tau^2 + B\tau) - \beta_0(2A\tau + B)^2\sin(A\tau^2 + B\tau)$$

$$\beta'''(\tau) = -6A\beta_0(2A\tau + B)\sin(A\tau^2 + B\tau) - \beta_0(2A\tau + B)^3\cos(A\tau^2 + B\tau)$$

$$\beta'''(\tau) = -12A^2\beta_0 \sin(A\tau^2 + B\tau) - 12A\beta_0(2A\tau + B)^2 \cos(A\tau^2 + B\tau)$$
$$+\beta_0(2A\tau + B)^4 \sin(A\tau^2 + B).$$

Alternatively, the instantaneous angular velocity of the flap, described by equation (3.23) may be used as an approximation for the forcing function common to both degrees-of-freedom. In "real life" flight testing, this is the value that is usually used as the input function because it is relatively easy to measure compared to the aerodynamic forces and moments. One of the objectives of this study is to compare transfer functions obtained using both methods in order to verify the accuracy of the flight test method.

3.5 The Nonlinear Equations

A nonlinear structural element may be added to the system by choosing an appropriate function to represent the restoring forces $F(\xi(\tau))$ or $M(\alpha(\tau))$ in equation (2.11) and (2.12). In this study, the effect of a bilinear structural restoring moment in the pitch direction is investigated.

The typical bilinear curve introduced in Chapter 2 and shown in Figure 2 has discontinuities at each end of the freeplay region. These discontinuities can cause instabilities in numerical solutions, making the expression in equation (2.39) unsuitable for numerical integration. The Runge-Kutta numerical integration scheme requires continuous derivatives up to $M''(\alpha(\tau))$ in order to produce reasonable time histories. In this study, continuous 'radii', or corners replace the discontinuous portions of the curve. A schematic of the resulting curve for the non-linear restoring moment, $M(\alpha(\tau))$ is shown in Figure 6 and may be described mathematically as

$$M(\alpha(\tau)) = M_0 + \alpha(\tau) + \alpha_f. \qquad \text{for } \alpha \le \frac{\sqrt{2}}{2}h - \left(1 + \frac{\sqrt{2}}{2}\right)\delta$$

$$M(\alpha(\tau)) = M_0 - r + \sqrt{r^2 - (\alpha(\tau) - h)^2} \qquad \text{for } \frac{\sqrt{2}}{2}h - \left(1 + \frac{\sqrt{2}}{2}\right)\delta < \alpha(\tau) < -h$$

$$M(\alpha(\tau)) = M_0 \qquad \text{for } -h \le \alpha(\tau) \le h$$

$$M(\alpha(\tau)) = M_0 + r - \sqrt{r^2 - (\alpha(\tau) - h)^2} \qquad \text{for } h < \alpha(\tau) < \left(1 + \frac{\sqrt{2}}{2}\right)\delta - \frac{\sqrt{2}}{2}h$$

$$M(\alpha(\tau)) = \alpha(\tau) - \alpha_f - \delta + M_0 \qquad \text{for } \alpha(\tau) \ge \left(1 + \frac{\sqrt{2}}{2}\right)\delta - \frac{\sqrt{2}}{2}h$$

The size of the radius and the size of the time step used in the numerical integration must be calculated to allow a smooth transition between the linear and freeplay regions of the restoring moment. In this study the combination of a .005 second time step and a radius of .003 radians provided the required transition.

3.6 Finding the Linear Flutter Speed

Nonlinearities can affect the airspeed at which the system becomes unstable, and may also induce limit cycle flutter at airspeeds below the flutter margin. For this reason, when comparing modal frequencies and damping values obtained from the nonlinear equations, the results are often referred to the *linear flutter speed.*

When the equations are linear, $M(\alpha(\tau)) = \alpha(\tau)$ and an eigenvalue analysis of the aeroelastic system under free vibration (without the forced flap oscillation) gives the analytical values of natural frequency and damping. Equation (3.18), without the aileron input and for a linear restoring moment, may be written as

$$\{X'\} + [A]^{-1}[B_2]\{X\} = \{0\} \tag{3.24}$$

where the matrices $[A], \{X'\}$ and $\{X\}$ have already been defined and

$$[B_2] = \begin{bmatrix} 0 & 0 & -1 & 0 & 0 & 0 & 0 & 0 \\ 0 & 0 & 0 & -1 & 0 & 0 & 0 & 0 \\ 0 & 0 & 0 & 0 & -1 & 0 & 0 & 0 \\ 0 & 0 & 0 & 0 & 0 & -1 & 0 & 0 \\ 0 & 0 & 0 & 0 & 0 & 0 & -1 & 0 \\ 0 & 0 & 0 & 0 & 0 & 0 & 0 & -1 \\ m_{13} & m_{14} & m_{10} & m_{11} & m_7 & m_8 & m_4 & m_5 \\ n_{13} & n_{14}^2 & n_{10} & n_{11}^2 & n_7 & n_8^2 & n_4 & n_5 \end{bmatrix} \tag{3.25}$$

with

$$n_8^2 = n_8 + \frac{1}{U^2}$$

$$n_{11}^2 = n_{11} + \frac{1}{U^2}(b + d) \text{ and}$$

$$n_{14}^2 = n_{14} + \frac{bd}{U^2} \tag{3.26}$$

The characteristic equation for this problem gives eight eigenvalues, four with zero imaginary parts and two sets of complex conjugate pairs. The real eigenvalues represent potentially divergent or non-oscillatory modes of the system. These modes are independent of time and will become divergent if the eigenvalue approaches zero. The complex conjugate pairs with positive imaginary parts represent the natural frequency and damping values for each of the aeroelastic system's two modes.

A complex eigenvlaue, λ, has the form

$$\lambda = p + iq .$$

The real part of the eigenvalue, p, is the modal damping factor, ζ. When p is negative, the damping is positive, any oscillatory motions will die out with time, and the system is stable. As the non-dimensional airspeed is increased, the real parts of the eigenvalues become smaller. The flutter speed, or the airspeed at which the system will become unstable, is that for which $p = 0$. If the airspeed is increased beyond this point, the damping becomes negative, the amplitude of any induced oscillatory motion will increase with increasing time, and the aeroelastic system is unstable. The imaginary part of the eigenvalue, q, gives the frequency of the response in radians per non-dimensional second.

For an aeroelastic system, the aerodynamic terms contribute to the system stiffness and the frequency of the dynamic response is not at the same frequency as the structural natural frequency. Because the A and B_2 matrices are functions of the non-dimensional airspeed, U and the airfoil physical parameters, there is a unique set of eigenvalues and hence frequency and damping factor, for each different combination of parameters and airspeed. In this study, the natural frequency and damping values obtained from the eigenvalues are considered the "real" or true values for the system and are compared with the values obtained "experimentally", or from numerically simulated time histories.

The linear flutter speed, U^*, was found by numerically solving for the system eigenvalues at increments of U until the real part of the eigenvalue, p, became zero. The corresponding value of airspeed, U is the linear flutter speed, U^*.

4 Linear Results

In this chapter, the results of simulated sine-sweeps are presented for a two degree-of-freedom airfoil in incompressible flow. The equations of motion were numerically integrated, and the modal frequencies and damping values were obtained using the techniques described in Chapter 2. In all cases the airspeed, U is presented as a percentage of the linear flutter speed, U^*. Results presented are for the following airfoil parameters: $\beta_0 = 2.0°$, $\overline{\omega} = 0.6$, $\mu = 100$, $a_h = -0.5$, $r_\alpha = 0.5$, $r_\beta = 0.002$, $x_\alpha = 0.25$, $x_\beta = 0.002$, $c_\beta = 0.6$, $\zeta_\alpha = 0.001$ and $\zeta_\xi = 0.001$.

The linear flutter speed for the system described above was found using the method described in Section 3.6. The complex eigenvalues were calculated numerically for increasing values of non-dimensional airspeed, U, until the real part of the eigenvalue became zero. For this case, the non-dimensional linear flutter speed, U^*, was found to be $U^* = 4.04$.

The aeroelastic system natural frequencies and damping values vary with non-dimensional airspeed. Well below the instability boundary the mode shapes are determined primarily by the system structural parameters, the two modes are well separated, the natural frequencies are close to the structural natural frequencies, and both modes are well defined by the transfer function. As the airspeed approaches the flutter speed the aeroelastic terms become increasingly important, the two natural frequencies move towards each other, the first mode damping decreases and the second mode damping increases.

Transfer functions, Nyquist diagrams, frequency and damping estimates were obtained for four different increasing and decreasing sweep-rates at values of non-dimensional airspeed ranging from 59% to 98% of the system flutter speed. The four sweep-rates used were .000003, .000006, .000012 and .000024 radians/(non-dimensional second)^2. These rates were chosen to represent a range of values from 1 to 600% of Ewing's recommended sweep-rate, depending on the airspeed at which the sweep was carried out.

Table 1 compares each of the four sweep-rates used with Ewing's recommended sweep-rate for each of the two modes at each of the ten non-dimensional airspeeds.

The system modal frequencies and damping were calculated using various combinations of forcing function, response signal, frequency sweep-rate and sweep direction, and results are presented for several typical combinations. The effect of sweep-rate on the accuracy of the estimated system parameters is investigated by comparing these results to the "exact" values of frequency and damping obtained from the eigenvalue analysis.

The first three sections of this chapter compare some of the different transfer functions that may be obtained at various combinations of airspeed and sweep-rate. The shape of the transfer function can depend on the method used to convert the time history to the frequency domain, the degree-of-freedom from which the time history is obtained, or the definition of the forcing function used as input to the transfer function. In Section 4.1, transfer functions obtained using the time-domain and Fourier transform methods are compared. In Section 4.2, transfer functions calculated using different choices of input function are compared at different sweep-rates, while in Section 4.3, transfer functions calculated using bending, or plunge response are compared to those obtained using pitch response.

Once the transfer function has been calculated, the frequency and damping values may be obtained using the half power point or Nyquist plot methods. The effect of the sweep-rate on the transfer function magnitude, the Nyquist diagram and the frequency and damping values obtained are presented in Section 4.4. In Section 4.5, the impact of using increasing and decreasing sweep-rates are compared. Finally, some conclusions are made based on the results presented.

4.1 Time-domain and Spectral Methods

Transfer functions may be obtained from the simulated time histories by either of two methods previously described – the time-domain and the spectral, or Fourier-transform methods. Figures 7 through 9 compare the transfer functions obtained at four different sweep-rates and two non-dimensional airspeeds.

When using the FFT method, a large window combined with a high sampling frequency results in a frequency resolution similar to that obtained using a shorter window and a lower sampling frequency. The time history responses for slow sweep-rates contained many more data points than those obtained at fast sweep-rates for sine sweep simulations over the same frequency range. For this reason, the data obtained at the slowest sweep-rate was analysed using a large window size and a sampling frequency of 8 points per second. At the higher sweep-rates, a smaller window was used and the sampling frequency was reduced to 4 points per second. In all cases, the frequency resolution was maintained at approximately 0.0063 rad/sec, which was found to be the combination of window size and sampling frequency that gave the most accurate results for frequency and damping. The particular values used for each combination of airspeed and sweep-rate was determined by trial and error to give the best definition for the first mode.

Figure 7(a) compares two transfer functions calculated using the spectral method, from time histories obtained at 68% of the linear flutter speed and at sweep-rates of .000003 rads/s^2 and .000024 rads/s^2. At this airspeed, the two sweep-rates represent 8% and 63% of Ewing's recommended rate, respectively, for the first mode and 2% and 13%, respectively for the second mode. Although the two time histories were analysed using different window lengths and sampling rates, they have the same frequency resolution. The sweep-rate does not have much impact on the transfer function obtained, provided the right combination of window length and sampling frequency is found.

As the airspeed is increased toward the flutter speed, the damping of the first mode decreases, and for the same frequency resolution the curve definition becomes increasingly poor. Figure 7(b) demonstrates the effect of decreased modal damping on the FFT transfer function. The sweep-rate for both curves is the same at 0.000003 radians/sec^2, which, for the first mode, represents 8% and 29% of the recommended rate at 68% and 96% of the linear flutter speed, respectively. For the second mode, this sweep-rate is equivalent to 1% and 2% of the recommended rate at 68% and 96% of U*, respectively. The curve obtained at 96% of the flutter speed has a slightly higher frequency resolution than the curve for $U/_{U^*} = .68$. Even at the slowest sweep-rate the number of points defining the maximum magnitudes of the first mode near the flutter margin are very few.

Transfer functions obtained using the time-domain and spectral methods are compared in Figures 8 and 9. Figure 8 compares curves obtained at the same airspeed and two different increasing sweep-rates, while Figure 9 shows transfer functions obtained at the same sweep-rate, .000003 radians/(non-dimensional second)^2, but for two different airspeeds. In general, the curves obtained using the spectral method do not contain enough points to provide a well-defined peak value for lightly damped modes. In order to calculate damping values for these modes, it was necessary to extrapolate the function in order to locate an approximate maximum magnitude and phase angle, and then use these values as the basis for the damping and natural frequency estimates. The time-domain transfer function, on the other hand, always had enough points to provide a well-defined maximum for both modes, and never required any extrapolation or curve fitting to obtain frequency and damping values. The time-domain curves are shifted to the right with respect to the curves obtained using the spectral method. This is, at least partially, due to the method used to match the peaks in the output with the input peaks when calculating the transfer function in the time domain method. The method used, particularly at the higher sweep rates and higher non-dimensional airspeeds, resulted in an overestimate of the frequency for a given magnitude of the input/output ratio.

Values of natural frequency and damping for the two methods are compared in Tables 2 and 3. In general, both methods give reasonable approximations for the natural frequency. The time-domain method increasingly overestimated the frequency with increasing sweep-rate (this is only true for increasing sweep-rates, and will be discussed in Section 4.5). The spectral method often underestimated the frequency, even at the higher sweep-rates but the error was inconsistent, and did not appear to be as a result of the sweep-rate. When the frequency resolution was poor, the first mode peak in the transfer function was obtained by a linear extrapolation of the two points each side of the peak. It is likely that this method of finding an approximation to the peak value is the cause of the inconsistent results. Damping values obtained using the time-domain method overestimated the correct values and the error increased with increasing sweep rate. Results obtained using the spectral method were again inconsistent, although values obtained for the more highly damped second mode were more accurate than those obtained for the first mode. Sometimes the half-power point and Nyquist damping values were similar, and sometimes they were very different. In some cases the need to extrapolate the curve to find the maximum magnitudes for the lightly damped first mode resulted in very inaccurate values of damping.

When the spectral method was employed, the same time-history could provide a range of possible frequency and damping values depending on which parameters were chosen when the analysis was done. Table 4 lists some of the values obtained from one such time history at three different combinations of frequency and window length. The first mode is lightly damped and the mode shape was, in general, inadequately defined by the transfer function curve and provided the most inconsistent results. The second mode is more heavily damped and the spectral analysis allowed enough points to make a good estimate of the modal damping, even at the higher sweep rates. It was found that a lower sampling frequency combined with a smaller window gave better results for the second mode than when the sampling frequency was doubled and the window contained more points.

4.2 Forcing Function Input

For each degree of freedom response, three separate transfer functions were calculated, each for a different choice of forcing function. In the first case, the set of peak values of angular velocity from each motion cycle of the flap was chosen as the input. In the second case, the peak values of aerodynamic lift attributable to the flap motion, obtained from terms in the linear aerodynamic equations, were used as the forcing function. In the third case the peak values of aerodynamic moment were used. Figures 10 through 13 compare typical transfer functions obtained from the different input signals. The comparison is made for airspeeds corresponding to 68% and 98% of the linear flutter speed, increasing sweep-rates of .000003 and .000024 radians/(non-dimensional second)^2, and both plunge and pitch response signals.

Figures 10 and 11 show the plunge response transfer functions calculated from time historie obtained at 68% and 98% of the flutter speed, respectively. The transfer function was calculated using the time-domain method. The two curves obtained using aerodynamic input and flap velocity are practically indistinguishable when plotted together on scaled axes and yield identical values for modal frequency and damping. At the slowest sweep-rate of .000003 radians/(non-dimensional second)^2, natural frequency and damping calculations obtained from the curve in Figure 10 (a) are:

$\omega_1 = .209$, $\zeta_1 = .0403$, $\omega_2 = .369$ and $\zeta_2 = .0583$ using aerodynamic input, and

$\omega_1 = .209$, $\zeta_1 = .0403$, $\omega_2 = .369$ and $\zeta_2 = .0588$ using flap velocity input.

The discrepancy between the respective values of frequency and damping is greatest for the second mode at 0.14% for frequency and 0.84% for damping, but is never greater than 1%.

At the fastest sweep-rate of .000024 radians/(non-dimensional second)^2, the curve in Figure 10 (b) yields:

$\omega_1 = .214$, $\zeta_1 = .0508$, $\omega_2 = .371$ and $\zeta_2 = .0609$ using aerodynamic input, and

$\omega_1 = .215$, $\zeta_1 = .0509$, $\omega_2 = .372$ and $\zeta_2 = .0607$ using flap velocity input.

At this sweep-rate, the values never differ by more than 0.4%.

The transfer functions plotted in Figure 11 were obtained at 98% of the flutter speed. At this airspeed the second mode had disappeared from the transfer function, and only the first mode parameters could be calculated. At a sweep-rate of .000003 radians/(non-dimensional second)^2, the values of frequency and damping obtained were:

$\omega_1 = .176$ and $\zeta_1 = .0201$ using aerodynamic lift input and

$\omega_1 = .176$ and $\zeta_1 = .0202$ using flap velocity input.

The differences between the results obtained using the two inputs are 0.06 and 0.45 percent, respectively.

At the same non-dimensional airspeed but with a sweep-rate of .000024 radians/(non-dimensional second)^2, the transfer functions yield:

$\omega_1 = .183$ and $\zeta_1 = .0302$ using aerodynamic lift input and

$\omega_1 = .184$ and $\zeta_1 = .0305$ using flap velocity input

A comparison of these results yields discrepancies of 0.49% in the frequency values and 0.93% for damping.

The above examples are typical of the results that were obtained at all combinations of sweep-rate and airspeed. The frequency and damping values calculated from the plunge response did not depend on the choice of input signal to the transfer function.

When the pitch response transfer functions were calculated, the two forcing functions produced noticeably different curves. Figures 12 and 13 show the transfer functions obtained at non-dimensional airspeeds corresponding to 68% and 98% of the flutter speed. At the lower airspeed, the maximum amplitude of the transfer function is less using the aerodynamic input compared to the flap velocity input. However, as the airspeed is increased toward the flutter limit the two curves become increasingly similar.

The natural frequency and damping values obtained from the curve in Figure 12 (a) at 68% of the flutter speed and a sweep-rate of .000003 radians/(non-dimensional second)^2 are:

$\omega_1 = .208$, $\zeta_1 = .0423$, $\omega_2 = .376$, and $\zeta_2 = .0442$ using aerodynamic input and

$\omega_1 = .208$, $\zeta_1 = .0421$, $\omega_2 = .375$, and $\zeta_2 = .0447$ using flap velocity input.

At a sweep-rate of .000024 radians/(non-dimensional second)^2, the values are:

$\omega_1 = .214$, $\zeta_1 = .0538$, $\omega_2 = .377$, and $\zeta_2 = .0488$ using aerodynamic input and

$\omega_1 = .214$, $\zeta_1 = .0522$, $\omega_2 = .379$, and $\zeta_2 = .0482$ using flap velocity input.

The above results for natural frequency are similar to those presented previously for the plunge response in that the choice of input function does not significantly affect the values obtained. The difference between the damping factors was slightly greater than for the first mode, between 1% and 2.5% depending on the airspeed. In the above example, the difference between damping factors calculated for the second mode are 0.9 and 1.2 percent for sweep-rates of .000003 and .000024 radians/(non-dimensional second)^2, respectively. Other combinations of sweep-rate and airspeed produced similar results. In some cases, the results obtained from the aerodynamic input were closer to the true values, and in others the more accurate values were produced from the flap velocity function.

Although the second mode frequency and damping values were more sensitive to the choice of forcing function than the first mode values, the difference between the transfer functions obtained using the two input signals was never more than 2.5%. For this reason, only the results calculated using the aerodynamic terms are presented in the remainder of this report.

4.3 Response Function

The two degree-of-freedom system responds to the simulated sine sweep excitation in both the plunge and pitch directions, and transfer functions may be obtained from either response time history. The impact of the choice of response function on the natural frequency and damping values obtained for each mode was investigated over the entire range of non-dimensional airspeeds, and at all four sweep-rates.

4.3.1 Transfer function

Figures 14 and 15 compare transfer functions obtained from each of the two degrees-of-freedom. These examples were obtained at non-dimensional airspeeds corresponding to 68% and 98% of the linear flutter speed, and at increasing sweep-rates of .000003 and .000024 radians/(non-dimensional second)^2. It is evident from all four curves that the first mode is well defined at all sweep-rates and airspeeds regardless of which degree-of-freedom is represented.

The second mode is more heavily damped than the first mode, and the shape of the transfer function was more sensitive to the choice of response signal. The results presented in Figure 14 demonstrate that even well below the flutter speed, the second mode is difficult to identify in the plunge response curve. The second mode definition becomes increasingly poor as flutter is approached, until it disappears altogether. A comparison of the four transfer functions obtained at 98% of the flutter speed and presented in Figure 15, reveals that the second mode is only present in one case – a combination of pitch response signal and the slowest sweep-rate.

4.3.2 Frequency and Damping Values

Figures 16 through 19 compare first mode frequency and damping estimates obtained using plunge and pitch transfer functions at increasing sweep-rates of .000003, .000006, .000012 and .000024 radians/(non-dimensional second)^2, respectively. The modal frequencies were obtained from the peaks in the transfer function magnitude versus frequency curves, and the damping values are from the Nyquist plot. In all cases, the values of frequency and damping are compared to the values obtained from an eigenvalue analysis of the linear system.

Frequency estimates for the first mode were not sensitive to the response signal used to calculate the transfer function. As an example, at 82% of the flutter speed, the frequency estimates from Figures 16 through 19 (a) are 0.4%, 1.0%, 2.1% and 3.5% higher than the analytical values at .000003, .000006, .000012 and .000024 radians/(non-dimensional second)^2 respectively, while the second mode response values are 0.07%, 0.6%, 1.6% and 3.0% higher. Below 90% of the linear flutter speed the total error does not change significantly with airspeed, while above this value there is a noticeable decrease in precision with increasing airspeed.

The Nyquist damping values for this mode were more sensitive to the choice of response signal than were the frequency estimates. From the examples in Figures 16 through 19, at 82% of the flutter speed the plunge response gives damping estimates that are 4.7%, 7.5%, 15.4% and 35.1% higher at .000003, .000006, .000012 and .000024 radians/(non-dimensional second)^2, respectively, than the analytical values. The error was greater in the values obtained from the pitch response at 8.3%, 15.1%, 19.4% and 37.5% above the eigenvalues. Below 90% of the linear flutter speed, the total error remains reasonably constant with airspeed, and above 90% there was a steady decrease in precision with increasing airspeed.

Figures 20 through 23 compare second mode frequency and damping estimates obtained from plunge and pitch responses to the four increasing sweep-rates. The second mode is more highly damped than the first mode, and for some combinations of sweep-rate, input and response, the transfer function did not contain an identifiable second mode shape. In the examples presented below, the plunge time history did not contain an identifiable second mode response above 77% of the flutter speed, and the pitch time history did not respond in the pitch mode at the fastest sweep-rate of .000024 radians/(non-dimensional second)^2. Where the signal was inadequate, it was impossible to obtain second mode frequency and damping estimates.

When the mode peak was present in the transfer function, the second mode frequency estimates were insensitive to the choice of response signal at all sweep-rates and airspeeds. Even the plunge response gives reasonable values for the second mode natural frequency up to 77% of the flutter speed, when the mode disappears from the signal. All of the frequency estimates obtained were within 2.0% of the eigenvalues.

When the pitch response was used at airspeeds below 80% of the linear flutter speed, all frequency sweeps gave good approximations for modal damping. At the fastest sweep-rate of .000024 radians/(non-dimensional second)^2 (Figure 23) and 82% of flutter speed, the error in the values obtained was only 3.7%. As the airspeed increased toward the flutter speed, the gap between the estimated damping and the eigenvalues increased and above 82% it was difficult to obtain accurate estimates of damping.

In summary, the plunge and the pitch response transfer functions yielded practically identical values of natural frequency for the first mode. For the second mode, it was necessary to use the pitch response in order to obtain natural frequency estimates above 77% of the linear flutter speed, and below this value, the plunge response tended to underestimate the modal frequency. First mode damping values obtained from the plunge response transfer function were more accurate than those obtained from the pitch response at the lowest sweep-rates. At higher sweep-rates, the pitch response transfer function yielded the most precise values of damping above 80% of the flutter speed. For the second mode, the plunge response transfer function was inadequate for calculating the modal damping values, and only the pitch response transfer function could be used.

4.4 The Effect of Sweep-rate.

The impact of sweep-rate was investigated on both the plunge and pitch response signals obtained at non-dimensional airspeeds ranging from 59% to 98% of the flutter speed. The figures discussed below demonstrate the effect on the transfer function, Nyquist plot and estimated system parameters for frequency sweeps carried out at 68% of the system flutter speed, and at increasing sweep-rates of .000003, .000006, .000012 and .000024 radians/(non-dimensional second)^2. The remaining results, from other airspeeds and at decreasing sweep-rates, are presented in Tables 5 through 20.

4.4.1 Transfer function

Figures 24 and 25 compare the first mode transfer functions obtained at the four sweep-rates from the plunge and pitch time histories, respectively. The transfer function obtained by evaluating the response at a series of input frequencies, without sweep, is shown in all the figures for the purpose of comparison. Figures 26 and 27 make the same comparison for the second mode transfer function.

In all cases, the results from the slowest sweep-rate, at .000003 radians/(non-dimensional second)^2, most closely duplicated the curves obtained without sweep. As the sweep-rate was increased, the maximum amplitude of the transfer functions decreased, the frequency at which this amplitude peak occurs increased, and the number of points that could be obtained and used to define the curve decreased. The shapes of the first mode curves obtained from plunge and pitch time histories were similar, while the two second mode transfer functions had distinctly different shapes. For the second mode, the plunge response curves shown in Figure 26 have a much smaller and less well defined peak on the low frequency side than do the pitch response curves of Figure 27. The sweep-rate has a less pronounced effect on this mode, and the curves representing the different sweep-rates are closer together.

4.4.2 Nyquist Diagram

The Nyquist plots for the first mode, obtained from the plunge time history are plotted in Figure 28. The curve obtained by evaluating the response at a series of input frequencies without sweep is also plotted for the purpose of comparison. The Nyquist diagrams for the same mode, but obtained from the pitch response history are plotted in Figure 29. The Nyquist diagram obtained using the slowest sweep-rate, at .000003 radians per non-dimensional time unit, most closely duplicates the results obtained without sweep. As the sweep-rate was increased the number of points that could be obtained and used to define the curve decreased, the curve moved and the circular shape of the plot became distorted in the positive direction along the real axis. The shapes of the curves shown in the two figures are similar – the shape and behaviour of the curve does not appear to depend on which modal response is chosen as input to the transfer function.

The Nyquist diagrams for the second mode, obtained using the plunge response signal are plotted in Figure 30, and those obtained from the pitch time history are shown in Figure 31. The Nyquist diagram obtained by evaluating the response at a series of input frequencies without sweep is plotted for the purpose of comparison.

For the second mode, the Nyquist diagrams obtained at different sweep-rates did not differ much in shape, and only the number of points available to define the curve decreased with increasing sweep-rate. When the pitch response was used to calculate the second mode Nyquist diagram (Figure 31), the magnitude and phase angle of the transfer function obtained was defined over a larger range of frequencies than those obtained using the plunge response signal.

4.4.3 Frequency and Damping Values

Figures 32 through 35 compare the values of natural frequency and damping factor calculated using transfer functions obtained at four different sweep-rates. The modal frequencies were obtained from the peaks in the transfer function magnitude curves, and the damping values are from the Nyquist plot. Results are presented for plunge and pitch response signals at increasing frequency sweeps. In all cases, the values of frequency and damping are compared to the values obtained from an eigenvalue analysis of the linear system.

Figure 32 compares frequency and damping estimates obtained using the plunge response to an increasing sweep-rate, while Figure 33 compares the results obtained using the pitch response. In all cases, the most accurate results were obtained at the slowest sweep-rate, and the calculated values of natural frequency and damping were higher than the analytical values. The spread between the analytical and the calculated values increases as the airspeed approaches the flutter speed. This effect was more pronounced at faster sweep-rates, resulting in the greatest error at a combination of the highest airspeed and the fastest sweep-rate.

Figure 34 compares second mode frequency and damping estimates obtained from the plunge response to an increasing sweep-rate, while Figure 35 compares the results obtained from the pitch response. In Figure 34, there are no results plotted for values of airspeed above 77% of the system flutter speed, because at the higher airspeeds the plunge response did not contain a well-defined second mode, and values of frequency and damping were impossible to obtain. The pitch response signal used to obtain the values shown in Figure 35 contained two well-defined modes, and values of frequency and damping could be calculated over the full range of airspeed.

Although the most precise results were obtained at the slowest sweep-rate, the calculated values of natural frequency for the second mode varied little with sweep-rate or non-dimensional airspeed. At the lower values of airspeed the calculated values of damping did not vary much with sweep-rate. As the airspeed increased, the damping was increasingly underestimated and the sweep-rate became increasingly important. Near the flutter speed, the damping could not be calculated using the half powerpoint method, and the values obtained for the damping factor became dependent on which points of the Nyquist plot were used.

It is evident from the results presented above that the sweep-rate is an important parameter in the accuracy of the frequency and damping estimates, with the error increasing significantly with increasing sweep-rate. This is particularly true for the first, or most lightly damped mode, and the error increases as the modal damping decreases near the flutter speed, for all sweep-rates.

4.5 Increasing and Decreasing Sweep-rates

The effect of increasing and decreasing sweep-rates was investigated for transfer functions calculated from both the plunge and pitch response signals, with the aerodynamic lift and moment used as the input signal. Values of natural frequency and damping factor were obtained at four different sweep-rates, and were compared to the linear system eigenvalues. The modal frequencies were obtained from the peaks in the transfer function magnitude versus frequency curves, and the damping values are from the Nyquist plot.

4.5.1 Transfer function

The first mode transfer functions obtained at a sweep-rate of .000003 radians/(non-dimensional second)^2 are plotted in Figure 36 for both increasing and decreasing frequency sweeps. The transfer function obtained without sweep is shown for comparison. The maximum amplitude of the transfer function was smaller for the increasing sweep, and larger for the decreasing sweep when compared to the curve obtained without sweep. The frequency at which the amplitude peak occurs was higher for the increasing sweep and lower for the decreasing sweep when compared to the frequency at which the amplitude peak occurs without sweep.

The first mode transfer functions obtained at a sweep-rate of .000024 radians/(non-dimensional second)^2 are plotted in Figure 37 for both increasing and decreasing frequency sweeps. The effect of increasing and decreasing sweeps on the frequency at which the amplitude peaks was similar but more pronounced at the higher sweep-rate. The effect on the magnitude of the peak in the transfer function is also amplified. For a decreasing frequency sweep at the higher sweep-rate, the peak magnitude was larger than that obtained using an increasing frequency sweep at the same sweep-rate, but was smaller than the value obtained without sweep.

The second mode transfer functions obtained at a sweep-rate of .000003 radians/(non-dimensional second)^2 are plotted in Figure 38 for both increasing and decreasing frequency sweeps. The transfer function obtained without sweep is shown for comparison. For this mode, and at the slowest sweep-rate, there is little difference between the curves obtained for increasing and decreasing frequency sweeps. The second mode transfer functions obtained at a sweep-rate of .000024 radians/(non-dimensional second)^2 are plotted in Figure 39 for both increasing and decreasing frequency sweeps. The maximum amplitude of the transfer function is smaller for the increasing sweep and larger for the decreasing sweep when compared to the curve obtained without sweep. The frequency at which the amplitude peak occurs is higher for the increasing sweep and lower for the decreasing sweep when compared to the frequency at which the amplitude peak occurs without sweep.

4.5.2 Nyquist Diagram

The first mode Nyquist diagrams obtained at a sweep-rate of .000003 radians/(non-dimensional second)^2 are plotted in Figure 40 for both increasing and decreasing frequency sweeps. The diagram obtained without sweep is shown for comparison. The circular shape of the curves plotted for increasing and decreasing frequency sweeps are shifted to either side of the curve obtained without sweep, but the shape of the curves is not significantly distorted.

The first mode Nyquist diagrams obtained at a sweep-rate of .000024 radians/(non-dimensional second)^2 are plotted in Figure 41 for both increasing and decreasing frequency sweeps. The effect of increasing and decreasing sweep on the shape of the plot is much more apparent at the higher sweep-rate. In the case of the increasing sweep, the upper part of the diagram is shifted, and the lower part of the diagram is distorted when compared to the curve obtained without sweep. In the case of the decreasing sweep the effect is reversed, and the upper part of the diagram is distorted while the lower part of the diagram is shifted when compared to the curve obtained without sweep.

The second mode Nyquist diagrams, obtained at a sweep-rate of .000003 radians/(non-dimensional second)^2, are plotted in Figure 42 for both increasing and decreasing frequency sweeps. In the case of this more highly damped mode, and at this sweep-rate, the difference between increasing sweep, decreasing sweep and no sweep is insignificant.

The second mode Nyquist diagrams obtained at a sweep-rate of .000024 radians/(non-dimensional second)^2 are plotted in Figure 43 for both increasing and decreasing frequency sweeps. The effect of increasing and decreasing sweeps on the shape of the plot is more apparent at the higher sweep-rate. In the case of the increasing sweep, the diagram is shifted upward with respect to the imaginary axis when compared to the curve obtained without sweep. In the case of the decreasing sweep the effect is reversed, and the curve is shifted downward with respect to the imaginary axis when compared to the curve obtained without sweep.

4.5.3 Frequency and Damping Values

Figures 44 through 59 compare the values of natural frequency and damping factor calculated using transfer functions from increasing and decreasing sweeps. Results were obtained at four different sweep-rates, and using transfer functions obtained from both plunge and pitch response signals. The modal frequencies were obtained from the peaks in the transfer function magnitude versus frequency curves, and the damping values are from the Nyquist plot. In all cases, the values of frequency and damping are compared to the values obtained from an eigenvalue analysis of the linear system.

Figures 44, 46, 48 and 50 compare frequency and damping estimates obtained from the plunge response to increasing and decreasing frequency sweeps at .000003, .000006, .000012 and .000024 radians/(non-dimensional second)^2, respectively. Figures 45, 47, 49 and 51 compare frequency and damping estimates obtained from the pitch response to the same frequency sweeps.

First mode frequency estimates were not sensitive to the response signal used to calculate the transfer function. For increasing sweep-rates, the frequency estimates are higher than the analytical values, while for decreasing sweep-rates the frequency is underestimated with respect to the eigenvalues. This effect increases with increasing airspeed and sweep-rate. For example in Figure 44(a), the sweep-rate is .000003 radians/(non-dimensional second)^2, and at 59% of the flutter speed the frequency estimates are 0.4% higher (increasing sweep) and 0.8% lower (decreasing sweep) than the analytical value, while at 98% of the flutter speed the estimates are 1.6% higher and 2.2% lower. Figure 50 (a) presents the values obtained at the fastest sweep-rate of .000024 radians/(non-dimensional second)^2, and at 59% of the flutter speed the estimated frequencies are 2.5% higher and 4.0% lower than the analytical value, while at 98% of the flutter speed the values are 5.9% greater and 7.2% smaller than the eigenvalues.

The effect of increasing versus decreasing frequency sweeps on the estimated damping parameter for the first mode was more complex than the effect on frequency. The closest approximations to the analytical values were always obtained at the slowest sweep, but even at this rate the decreasing sweep gave more precise values than the increasing sweep. The data shown in Figure 44 (b) was obtained using plunge response data at .000003 radians/(non-dimensional second)^2, and the error in the estimated values of damping range from 2.9% at 59% of the flutter speed, to 32.1% at 98% for an increasing sweep. Using a decreasing sweep at 59% and 98% of the flutter speed, the errors in the damping values were 0.5% and 27.9%, respectively. Both increasing and decreasing frequency sweeps overestimated the eigenvalue damping factor, but the decreasing sweep gave more accurate values. The values in Figure 45(b) were obtained using pitch response data at the same sweep-rate as the previous figure. In this case, the trend was the same, with both sweeps overestimating the modal damping and the increasing sweep being the least accurate of the two. At this sweep-rate the decreasing sweep gave quite accurate estimates throughout the range of airspeeds. Figures 46(b) and 47(b) demonstrate a similar reaction to sweep direction for a sweep-rate of .000006 radians/(non-dimensional second)^2.

As the sweep-rate was increased, the overall accuracy of the values for the first mode damping decreased, with a decreasing sweep and plunge response signal giving the best approximations to the analytical values. At a sweep-rate of .000012 radians/(non-dimensional second)^2, (Figure 48(b)), the decreasing frequency sweep yields estimates of damping within 10% of the eigenvalues for airspeeds up to 82% of the flutter speed. Above this value, the most accurate values were obtained from an increasing frequency sweep. For example, at 91% of flutter speed, the decreasing sweep resulted in a damping factor error of 20%, while the value obtained at an increasing sweep was within 6.0% of the analytical value. The same behaviour was observed at a sweep-rate of .000024 radians/(non-dimensional second)^2 (Figures 50 and 51).

Figures 52, 54, 56 and 58 compare second mode frequency and damping estimates obtained using plunge response to increasing and decreasing frequency sweeps of .000003, .000006, 000012 and 000024 radians/(non-dimensional second)^2, respectively. The plunge response signal does not contain a second mode response at values of dynamic pressure above 77% of the flutter speed, and even below this airspeed, the damping values obtained were scattered and gave inconsistent estimates for modal damping. Figures 53, 55, 57 and 59 compare frequency and damping estimates obtained using pitch response time histories to increasing and decreasing frequency sweeps of .000003, .000006, 000012 and 000024 radians/(non-dimensional second)^2, respectively.

Second mode frequency estimates were very accurate for all sweep-rates and all airspeeds. There was no noticeable increase in error between .000003, .000006 and .000012 radians/(non-dimensional second)^2, with all estimates at both increasing and decreasing sweeps within 1.5% of the eigenvalues. At the fastest sweep-rate used (Figure 59), there was no second mode peak in the transfer function for an increasing sweep above 91% of the flutter speed, while the decreasing sweep yielded values for the whole range of airspeeds. At this sweep-rate and airspeed, the calculated natural frequency was within 0.3% of the true value.

For the second mode, only the transfer functions obtained using the pitch response data yielded reasonable values for the modal damping factor. When the pitch response time history was used at airspeeds below 80% of the linear flutter speed, all sweep-rates at both increasing and decreasing sweeps gave reasonable approximations for modal damping. Even at a sweep-rate of .000024 radians/(non-dimensional second)^2 (Figure 57) and 82% of flutter speed, the error in the values obtained were only 3.7% and 3.4% for increasing and decreasing sweeps, respectively. As the airspeed was increased toward the flutter speed, the gap between the estimated damping and the eigenvalues increased, but the error is not significantly greater for faster sweep-rates.

In general, increasing frequency sweeps overestimated both the modal frequency and damping values. Decreasing frequency sweeps underestimated frequency, overestimated first mode damping values, and underestimated second mode damping values. The decreasing sweeps gave significantly more precise estimates of damping than the increasing sweeps. The amount by which the estimated values are in error increases with increasing sweep-rate, and is greater for more lightly damped modes.

4.6 Summary

The three parameters having the greatest effect on the calculation of modal frequency and damping values were found to be the choice of response time history, sweep-rate and sweep direction. The choice of response time-history was very important if the more heavily damped mode is of interest, and was less important for the lightly damped mode. Sweep-rate was found to be the most important overall parameter, and the fastest sweep-rates caused the largest errors in both frequency and damping estimates, particularly for the more lightly damped of the two modes.

Although the slowest sweep-rate was always the most precise, the total error was a result of the combination of all three parameters. For example, the pitch response transfer function overestimated the first mode damping, as did the increasing frequency sweep. For this reason, the combination of pitch response and increasing sweep results in larger errors in damping values than does the combination of plunge response with the same increasing sweep-rate. The best choice of parameters depends on which results are important, in particular which mode is of interest, and at which airspeeds the sine sweep is to be performed.

5 Nonlinear Results

A nonlinear system was obtained by replacing the "linear spring" restoring moment in the pitch direction, $M(\alpha) = \alpha$, by a nonlinear spring with a freeplay region as described in Chapter 3, Section 3.5. The pitch response of the nonlinear system was compared to the pitch response of the equivalent linear system.

In Section 5.1, the general behaviour of a one degree-of-freedom, mechanical system with a nonlinear restoring force is discussed. The general properties of this system provide a basis for comparison with the behaviour of the aeroelastic system and are taken from the basic theory of nonlinear systems (Broch J.T., 1980). In Section 5.2, the pitch response waveforms obtained for the nonlinear system are compared to those of the linear system, and in Section 5.3 the linear and nonlinear frequency response curves are compared. Section 5.4 describes the effect of the "size" or length of the nonlinear region, as well as the amount of preload in the freeplay region. Section 5.6 compares modal damping values obtained for the nonlinear system with the parameters previously calculated for the linear system. The time-domain and frequency-domain methods of obtaining the frequency transfer function are evaluated with respect to their application to the nonlinear system.

5.1 One Degree-of-Freedom Nonlinear Systems

Consider first the example of a one degree-of-freedom mechanical system subject to a nonlinear spring force. If such a system has no excitation force and no damping, then the free oscillations of the disturbed system are not sinusoidal, as is the case for a linear system. In the linear case, the frequency and the shape of the oscillation are independent of the amplitude. In the non-linear case both the frequency and the form of the response vary with the amplitude. The relationship between amplitude and natural frequency for the linear system, and a typical hardening spring with a freeplay nonlinearity are shown in Figure 60. For this type of nonlinear spring, the frequency of the system increases with amplitude and approaches the natural frequency of the equivalent linear system asymptotically at large amplitudes.

When light damping and periodic excitation are added to the system described above, the steady-state response is generally periodic, and at the same frequency as the excitation. For fixed amplitudes of the excitation force and light damping, the response curves have the form shown in Figure 61. The nonlinear curves are similar to the corresponding curve for the linear system, but the "backbone" of the resonant peaks is the nonlinear free vibration amplitude-frequency curve from Figure 60(b).

Figure 62 illustrates the *hysteresis* effect that the nonlinearity may have on the steady state response in the case of a frequency sweep. The segment between points 2 and 3 is unstable, and if the excitation frequency is swept from zero at an increasing sweep-rate, the quasi-steady response amplitude follows the curve from 1 to 2, and then jumps to point 4. Under a decreasing frequency sweep, there will be a sudden jump in steady state response from 3 to 1. This effect results in very different frequency response peaks for increasing and decreasing sweep-rates.

Another property of nonlinear systems is that they distort the wave shape of the response signal. Even if the forcing function is purely sinusoidal, the wave shape of the response will not be sinusoidal. Normally, the response wave shape will contain a number of frequency components harmonically related to the frequency of the driving force. These ordinary, or "superharmonics" are present in almost all non-linear systems, and their amplitude values are normally small compared to the dominant response frequency. Under some circumstances, particularly low damping, the system may respond at a subharmonic of the forcing frequency, although purely subharmonic response is rare.

The phenomenon of superharmonic and subharmonic frequencies can be important in multi-degree-of-freedom systems such as aircraft wings and tail surfaces. If a frequency sweep is being carried out to cover two specific vibration modes in a resonance test, a nonlinearity in one of the degrees-of-freedom may result in an oscillatory response at one or more frequencies other than the forcing frequency. If one of these harmonics by chance coincides with the resonant frequency of some other mode of the system, a large amplitude response may be created at a frequency that is not within the range of the frequency sweep. Although the simulated frequency sweep used in this study cannot duplicate such an incident, it can be used to investigate the existence of superharmonic and subharmonic oscillations in the response of the aeroelastic system to a sine sweep input.

5.2 Frequency Response Curve

The response of the nonlinear aeroelastic system to a sine sweep excitation was investigated for a nonlinear restoring moment in the pitch degree-of-freedom. The waveform of the system response varied considerably across the range of the frequency sweep. For each value of non-dimensional airspeed, the variation of response waveform with input frequency was different. The results presented in this section are for a maximum input flap angle of $\beta_0 = 2.0°$, a nonlinear spring defined by $\alpha_f = 0.25°$, $\delta = 0.25°$, $m_0 = 0.25°$ (see Figure 2), and a decreasing sweep-rate of .000012 radians/second^2. The remainder of the system parameters are the same as those for the linear system described in Chapter 4.

The nonlinear restoring force in the pitch degree-of-freedom has a hysteresis effect on the frequency response curve similar to that discussed in Section 5.1. The first mode is lightly damped, the magnitude of the response is well above the nonlinear pitch range, and the nonlinearity has little effect on the shape of the frequency response. The second mode is the more heavily damped of the two modes, and the nonlinear effect is more pronounced. The second mode responds farther down the "backbone" of the free vibration amplitude-frequency curve of Figure 61. Figure 63 compares the linear and nonlinear frequency responses to increasing and decreasing sweep-rates, for an airspeed equivalent to 55% of the linear flutter speed. At this airspeed, although the second mode is lightly damped, it is much more heavily damped than the first mode, and the nonlinear hysteresis effect is apparent. Figures 64 through 67 make similar comparisons at airspeeds equivalent to 64, 73, 82 and 91% of the linear flutter speed, respectively. For each figure, both the linear and the nonlinear "backbones" have been sketched in, and the "jumps" in frequency response have been indicated. As the airspeed is increased, the second mode damping increases, and the peak in the second mode response curve moves farther down the "backbone". Also, for increasing airspeed, the nonlinear response lies on the more horizontal portion of the backbone curve, and the hysteresis effect becomes increasingly less evident at the high frequency side of the response curve. At the low frequency side of the second mode response peak, with increasing airspeed, the hysteresis effect is influenced by the increasing proximity of the first mode. At 82% of the linear flutter speed, the two mode responses have begun to overlap, and the nonlinear hysteresis effect is no longer evident. The high frequency side of the second mode contains a range of nonlinear, subharmonic frequency response at airspeeds above 73% of the linear flutter speed. On the frequency response plot, these regions are characterized by unstable, or scattered, frequency response amplitudes at ranges of input frequency above the second mode natural frequency. Figures 65, 66 and 67 illustrate this sort of nonlinear response, and a comparison of the three figures shows how the airspeed affects the length of the subharmonic, nonlinear region as well as the amplitude of the response.

5.3 Response Waveforms

For the system parameters described above, and at six different airspeeds between 55 and 91% of the linear flutter speed, several visually different response waveforms were identified. Each waveform occurred over a distinct frequency range. Not all waveforms were present at all airspeeds, and some were evident for more than one range of frequencies within the same frequency sweep. Figures 68 through 78 illustrate some typical examples of the response waveforms that were obtained.

A typical response with superharmonics at two, three and four times the forcing frequency is shown in Figure 68. The corresponding power spectral density plot is shown in Figure 68(b). This response occurred for only one short frequency range, at low frequencies, and at only one of the airspeeds tested (a more complete discussion of the different input frequency ranges over which the different nonlinear responses occurred, is given at the end of this section, and is illustrated in Figures 79 through 83). Figure 69 illustrates a more common response with harmonics at two and three times the forcing frequency. This type of response occurred at the lower values of forcing frequency, typically between 50 and 65% of the first mode resonant frequency, depending on the airspeed. The most common superharmonic in the aeroelastic response was at twice the forcing frequency, and an example of this is shown in Figure 70. This particular response waveform was found at some point in the frequency sweep at all airspeeds, and always occurred at frequencies below the first mode resonant peak. The length of the frequency range over which the second harmonic response was sustained was longer than that for any other type of waveform.

The nonlinear responses at two, three, and four times the input frequency always occurred below the first mode resonant frequency. The nonlinear behaviour was limited to the low amplitude regions of the frequency response curve, and the particular type of waveform appeared to be a function of the magnitude of the response. At the lower end of the frequency range, lower airspeeds produce lower amplitude responses. The amplitude of the response increases with increasing frequency and airspeed until it peaks at the first mode resonant frequency. The fourth harmonic only occurs at the very smallest amplitudes, and so is only found at very low airspeeds. As the amplitude of the response increases, the waveform changes from the fourth to the third and the second harmonics, successively. As the first mode peak in the frequency response curve is approached, the amplitude of the response increases rapidly, and the system response becomes similar to that of the linear system.

At input frequencies between the first and second mode peaks, the pitch response waveform depended on the airspeed at which the frequency sweep was performed. At lower airspeeds, the response amplitude in this region was smaller, and the response waveforms are nonlinear. Typical examples of this sort of motion are shown in Figures 71 and 72, for airspeeds equivalent to 55% and 64% of the linear flutter speed. The response is similar to the superharmonic waveforms described above for frequencies below the first mode natural frequency, except that the response is at one and a half and two times the input frequency, as well as at the input frequency. At airspeeds above 65% of the linear flutter speed, the two modes begin to converge, and the region of small amplitude response between the two disappears. At these airspeeds, and for the frequency range between the two modes, the system responds at the same frequency as the input.

A third type of waveform appeared in the response at frequency ranges beginning just above the second mode natural frequency. An example of this waveform is shown in Figure 73. The harmonic in this case is a subharmonic and the frequency of the oscillation is two thirds of the forcing frequency. At higher values of input frequency, the frequency of the dominant subharmonic response changes from two-thirds of the input to the first mode natural frequency. This second type of subharmonic is illustrated in Figure 74, where the two-thirds harmonic is also present, but is of much smaller magnitude. At the high end of the nonlinear response range, the response is actually dominated by the first mode natural frequency, and not the forcing frequency, as illustrated in Figure 75.

Figures 76, 77 and 78 are examples of the waveform response at an airspeed approaching the linear flutter speed. The response at all frequencies is dominated by the first mode natural frequency, and at higher frequencies (Figure 78), the magnitude of the response at the input frequency becomes very small compared to the magnitude of the harmonic. This type of motion was found at frequencies just above the second mode at all airspeeds above 70% of the flutter speed. As the airspeed was increased, the frequency range of nonlinear response became larger. The upper limit of the range remained reasonably stable, at about 0.40 radians/second, but the lower limit of the nonlinear range decreased with increasing airspeed, and as the second mode damping increased.

Figures 79 through 83 show the regions of the frequency response curves where each of the above types of waveform occurred, for five values of non-dimensional airspeed ranging from 55% to 91% of the linear flutter speed. The first nonlinear region is below the first mode resonant peak, where the harmonics were at twice, three times and four times the forcing frequency. The second nonlinear region occurred between the first and second mode resonant peaks, where the superharmonic response was at one-and-a-half and two times the input frequency. The third nonlinear region was characterized by two separate subharmonic responses at two thirds of the input frequency, and at the first mode natural frequency. This response occurred at frequencies above the second mode resonant peak, and was only found at higher airspeeds.

5.4 Length of Freeplay Region

The nonlinear behaviour of the frequency response curve was closely tied to δ, the length of the freeplay region. Figures 84 through 88 compare the linear frequency response at a decreasing sweep rate of .000012 radians/second^2, to the nonlinear response for freeplay lengths of .25, .5 and .75 degrees. The five figures represent results obtained at 55, 64, 73, 82 and 91% of the linear flutter speed, respectively. In all of the figures, the curve that most closely resembles the linear curve is the smallest freeplay length, or .25 degrees. As the length of the freeplay region is increased, the frequency of the second mode peak decreases, the magnitude of the first mode peak increases, and the nonlinear behaviour becomes more pronounced for input frequencies above the first mode natural frequency.

As the airspeed at which the sweep rate is performed is increased, there is a more dramatic increase in nonlinear subharmonic response with increasing freeplay length. In Figures 84 and 85, at 55 and 64% of the linear flutter speed, the first and second mode have distinct response peaks for all values of δ, the hysteresis effect is evident in the shape of the second mode response, and the regions of nonlinear harmonic response above and below the first mode natural frequency are similar in appearance. In Figure 86, at 73% of the linear flutter speed, regions of nonlinear subharmonic response appear in the response curve at frequencies above the second mode peak for freeplay lengths of .5 and .75 degrees. The subharmonic region for the .75 degree freeplay is quite extensive, and the second mode response for this curve is almost entirely nonlinear. At 82% of the flutter speed, the response in the region of the second mode natural frequency is entirely subharmonic and nonlinear for all values of δ except δ=0.25, and the magnitude of the nonlinear response increases significantly with increasing δ. At 91% of the flutter speed (Figure 88), the response is nonlinear across the entire second mode frequency range, and the magnitude of the nonlinear response is significant for the larger values of δ. The effect of freeplay region length on the first mode response does not change significantly with airspeed. Although the second mode peak in the nonlinear response curves seems to "disappear" at a lower airspeed than does the linear case, the flutter speed does not seem to be affected by the length of the nonlinear region. The disappearance of the second mode peak appears to be a result of subharmonic response rather than frequency coalescence.

5.5 Effect of Preload Magnitude

The preload of the freeplay region of Figure 2, or the magnitude of m_0, also influences the shape of the nonlinear frequency response curve. Frequency response curves were obtained for six different values of m_0 ranging from 0.00 to 1.25 degrees, and at five different airspeeds between 55% and 91% of the linear flutter speed. All the curves are for a freeplay length of .25 degrees and a decreasing sweep rate of .000012 radians/(non-dimensional second)^2.

The value of m_0 has a significant effect on the nonlinear behaviour of the response curve, particularly in the region $0.0° < m_0 < 0.5°$. For example, at 55% of the linear flutter speed, and for a value of $m_0=0.0°$, the second mode response peak disappears entirely, as shown in Figure 89(a). Figure 89(b) shows an increase in m_0 to $m_0=0.125°$, which causes the second mode response peak to reappear, and introduces a significant region of nonlinear, subharmonic behaviour at input frequencies between 0.46 and 0.60 radians/second. Figure 90 shows that a further increase in the preload to $m_0=0.25°$ causes the subharmonic region to disappear, and subsequent increases of the preload up to $m_0=1.25°$, (Figures 90 and 91), do not produce any subharmonic responses for this range of input frequency. The shape of the second mode frequency response peak also changes with m_0, with the "jump" across the nonlinear region occurring at higher frequencies for increasing values of m_0.

The nonlinear region below the first mode natural frequency is affected by the value of m_0. As m_0 is increased from 0° to 0.5° (Figures 89 and 90), the magnitude of the superharmonic, nonlinear response in this region increases, and the input frequency range for the nonlinear response extends closer to the first mode natural frequency (Figure 90(a)). Figure 90(b) shows the response at m_0=0.5°, where the input frequency range over which the response is nonlinear suddenly decreases, and continues to decrease with increasing m_0 up to m_0=1.25°, where it disappears (Figure 91).

The first mode response peak was also affected by variations in freeplay preload. The magnitude of the response was larger than the linear response for all values of m_0 except for m_0=1.25°, as shown in Figure 91(b). The width of the first mode response peak, an indicator of modal damping, is larger at smaller values of m_0, as can be seen in Figures 89 (a) and (b). As m_0 is increased, the amplitude of the response peak remains the same, but the width decreases. In Figure 90, the change in width of the response peak from (a) to (b) is evident, for an increase in m_0 from 0.25 to 0.5 degrees.

The results discussed above are all for 55% of the linear flutter speed. Similar results obtained for airspeeds equivalent to 64, 73, 82 and 91% of the linear flutter are presented in Figures 92 through103. The general behaviour of the system with increasing freeplay preload is the same as described above for U/U*=0.55. As the airspeed is increased, the nonlinear, subharmonic behaviour at the high end of the frequency sweep appears at increasingly lower values of m_0, and disappears again at higher values m_0. The nonlinear, subharmonic region found at frequencies below the first mode natural frequency occupies less of the response peak for higher airspeeds, probably because the magnitude of the pitch response in this area is larger. The width of the response peak is less affected by m_0 at the higher airspeeds, and U/U*=0.55 is the only airspeed where the second mode response peak disappears entirely for m_0=0.0°.

5.6 Effect on Modal Damping

Damping values are less easily obtained for the nonlinear system investigated in this chapter than for the linear system presented earlier. The nonlinear hysteresis results in a second mode frequency response curve that is asymmetrical and has frequency 'jumps' across the points that are required for a reasonable calculation of second mode damping using either the half power point or Nyquist methods discussed in Chapter 3. In addition, the second mode response peak disappears at a much lower airspeed than it does with a linear system, due to the existence of a strong subharmonic response in the range of the second mode natural frequency, especially at higher airspeeds. In this study, no attempt was made to calculate second mode damping values.

The first mode response of the nonlinear system was similar to the linear response, but only over a small frequency range each side of the first mode natural frequency. Damping values for this mode were obtained using both the Fourier transform and the time domain methods. In the first method, the frequency transfer function was obtained using the Fourier transform approach described in Chapter 3. The Nyquist method was then used to calculate the modal damping using the first point on either side of the first mode peak value. A second damping value was then calculated using the second point on either side of the peak. The time domain method was applied by selecting only the range of points from the frequency response curve where no harmonic response was present. A 'segment' of the transfer function was then obtained by applying the time domain method described in Chapter 3 to selected response range. Modal damping was calculated using the Nyquist method, with the points chosen as close as possible to the same input frequency as the points from the Fourier transform method described above. An example of the transfer functions obtained using the two methods, at $U/U^*=0.77$, is presented in Figure 104.

Modal damping values for the first mode are presented in Figure 105 for one case only - a decreasing frequency sweep at 0.000012 radians/(non-dimensional second)^2, with a freeplay preload of $m_0=0.25$ degrees and a freeplay length of $\delta=0.25$ degrees. The Fourier transform results were calculated using the first point each side of the peak magnitude, and the time domain results were calculated using points chosen to be at approximately the same input frequency as the corresponding Fourier transform result. The time domain results overestimate the modal damping by a small amount compared to the linear system, but the Fourier transform results overestimate the damping value by up to one and half times, at all airspeeds except 96% of the linear flutter speed. The Fourier transform results obtained using the second point on either side of the frequency peak are not presented because they are less uniform, appear to be more random, and overestimate the damping by an even greater amount.

The Fourier transform method of obtaining the frequency transfer function for the nonlinear system results in much larger damping values than the time domain method for the same system. This is probably because the nonlinear system responds at harmonics of the input frequency for a significant range of frequencies within the range of the frequency sweep, and this harmonic response affects the Fourier transform results. The Fourier transform method assumes that the system responds at the same frequency as the input, or forcing function, and calculates the transfer function as the relative magnitudes of the input and response at each frequency. The nonlinear system does not always respond at the same frequency as the input, and so this assumption is not always true. The nonlinear, subharmonic response of the nonlinear system is often close to, or at the same, frequency as the first mode natural frequency. This distorts the transfer function curve in the area of the first mode peak, because the Fourier transform method calculates the subharmonic as a response to input at the subharmonic frequency.

5.7 Summary

The introduction of a structural nonlinearity in the form of bilinear spring with a freeplay region, had a significant impact on the response of the aeroelastic system to a frequency sweep input. Unlike the linear system, the nonlinear model did not always respond at the same frequency as the input force, and contained regions of both superharmonic and subharmonic response. The nonlinearity had a hysteresis effect on the second mode response curve, and the resulting peak in the frequency response amplitude was at very different frequencies for the increasing and decreasing frequency sweeps. Changes in nonlinear region length and preload magnitude had significant impact on the system response, particularly in the input frequency range containing the second, or more heavily damped mode natural frequency.

The second mode response curve was distorted by the nonlinearity, and reasonable values of modal natural frequency and damping could not be obtained using the methods employed for the linear system. The first mode was much more lightly damped than the second, and the response curve was less affected by the nonlinearity. Natural frequency and damping values for this mode could be calculated using both the time-domain and the spectral methods, although the time-domain method was limited those portions of the frequency response where the response was at the same frequency as the input. Natural frequencies obtained for the first mode were in close agreement with those obtained for the linear system. Damping values obtained using the time-domain method were slightly greater than the linear values, and damping values obtained using the spectral method were much larger – up to one and a half times the corresponding linear values.

6 Summary and Conclusions

The sine sweep is a method commonly employed to perform resonance tests on aircraft wings and tail surfaces. Finding natural aeroelastic frequencies by repeated testing at increments of forcing frequency is not practicable when the testing must be performed on full-scale aircraft under actual flight conditions. Sine sweep tests, or frequency sweeps, permit the analysis of a range of frequencies within the time span of one test flight. The rate at which the frequency is varied during the sine sweep can affect the test results, and it is of practical interest to perform the test at the fastest sweep-rate that can produce accurate data. In this study, the effect of sweep-rate on the accuracy of analytically generated data describing the aeroelastic motion of a two-dimensional airfoil was studied. Two different methods were employed to convert the data to the frequency domain, as well as to calculate frequency and damping parameters for the aeroelastic system. The methods were compared and the accuracy of the different methods, combined with the different sweep-rates, was investigated. Finally, the effect of introducing a simple nonlinearity into the aeroelastic system was investigated.

6.1 Summary

A numerical model of the equations of motion for a two-dimensional, three-degree-of-freedom airfoil performing unsteady motions of small amplitude in incompressible, inviscid flow was produced. The model was used to apply a frequency sweep by means of constraining the third degree of freedom, the flap motion, to oscillate at a variable frequency and thus provide a defined input to the system. Exact solutions to the equations of motion for the linear system were obtained from an eigenvalue analysis. Numerical solutions to the equations of motion were obtained for a number of different combinations of airspeed, sweep-rate and forcing function input, and a number of different comparisons were made.

The impact of introducing a structural nonlinearity into the aeroelastic system was investigated for the case of a nonlinear restoring force with a freeplay region in the pitch degree of freedom. The behaviour of the frequency response curve and the response waveform were compared to that of the linear system, as well as to the general behaviour of a purely mechanical system subject to a similar nonlinearity. If the nonlinear system response is presented in the form of a transfer function, much of the information about the nonlinear behaviour is lost. For this reason, the nonlinear characteristics of the aeroelastic system were studied in terms of the frequency response curve rather than the transfer function.

6.2 Conclusions

6.2.1 Linear Aeroelastic System

- When resonance testing is carried out using the sine sweep method, the choice of frequency sweep-rate can significantly affect the accuracy of the resulting modal frequency and damping calculations.
- Parameters calculated using the time-domain method are, in general, more precise than those obtained using the spectral, or Fourier transform method.
- The Nyquist plot yields more accurate damping values than the transfer function magnitude plot and the half power point method, but the sweep-rate has an important effect on the shape of the plot, and points must be carefully selected to provide accurate results at higher sweep-rates.
- The ideal sweep-rate is a function of modal natural frequency, modal damping, and airspeed.
- The accuracy of the calculated system parameters is dependent on the modal damping. If the mode is highly damped, a faster sweep-rate is still quite accurate. For lightly damped modes, a slow sweep-rate is essential for accurate results. For the aeroelastic system, modal damping is a function of airspeed, and as the airspeed is increased, the sweep-rate must be decreased to maintain the same accuracy.
- For the same sweep-rate, a decreasing sweep yields more accurate damping values than an increasing sweep.

6.2.2 Nonlinear Aeroelastic System

- The frequency response of the nonlinear aeroelastic system is much more complex than that of the linear system, even for small nonlinearities.

- The type of nonlinearity, as well as the geometric parameters of the specific nonlinearity, can have an important effect on the response behaviour of the nonlinear system.
- The most significant difference between the linear and the nonlinear systems is that the nonlinear system response is not at the same frequency as the forcing function across the entire range of the frequency sweep.
- The Fourier transform method of obtaining the transfer function assumes that the system responds at the same frequency as the input, or forcing function. This assumption is not true for the nonlinear system studied, and the applicability of the FFT method for calculating modal damping values is questionable.
- The introduction of a nonlinear restoring force in one of the two degrees of freedom caused the Fourier transform method to overestimate the first mode damping values by as much as 150%.

6.3 Recommendations for Future Research

In this study, the linear, two-degree-of-freedom aeroelastic system subject to a sine sweep excitation has been studied in some detail, but only one simple case of an equivalent, structurally nonlinear aeroelastic system was studied. The results obtained for the nonlinear system suggest a number of potentially interesting extensions of the current work:

- An investigation into the effect of sweep-rate on the nonlinear system response, as well as a comparison of the nonlinear responses to increasing and decreasing frequency sweeps at a constant sweep-rate.
- An investigation into possible modifications to the time-domain and spectral methods of obtaining the system transfer function that would accommodate the harmonic frequencies present in the nonlinear response.
- A more detailed investigation of the nonlinear harmonic response with the objective of determining the factors (apart from response amplitude) responsible for the appearance and disappearance of the harmonic waveforms in the frequency response curve.

- The addition of a third degree of freedom with a natural frequency outside the range of the frequency sweep, but close to one of the nonlinear harmonic responses, could be used to investigate other possible implications of the nonlinear response.
- The addition of a nonlinearity in the plunge degree of freedom, and a comparison of the resulting system response to the results of this study.
- The combination of structural nonlinearities in both degrees of freedom.
- The introduction of aerodynamic nonlinearities associated with transonic or separated flow.
- A comparison of the response of an aeroelastic system subject to a freeplay nonlinearity to the response of an aeroelastic system subject to other types of structural nonlinearities.

References

- Alighanbari, H., Price, S.J. (1996), 'The Post-Hopf-bifurcation Response of an Airfoil in Incompressible Two-dimensional Flow', *Nonlinear Dyn; 10:381-400.*

- Bairstow, L., Fage, A. (1916), 'Oscillations of the Tailplane and Body of an Aeroplane in Flight', British Aeronautical Research Committee, *Rep. & Memo. 276, part ii.*

- Blasius, H. (1925), 'Über Schwingungserscheinungen an Einholmigen Unterflügeln', *Z. Flugtech. u. Motorluftschif;16:39-42.*

- Brietbach, E.J. (1977), 'Effect of Structural Nonlinearities on Aircraft Vibration and Flutter', AGARD *Report 665.*

- Brietbach, E.J. (1980), 'Flutter Analysis of an Airplane with Multiple Structural Nonlinearities in the Control System', NASA *TP 1620.*

- Collar, A.R. (1946), 'The Expanding Domain of Aeroelasticity', *J of the Royal Aeronautical Society; 1:613-36.*

- Dowell, E.H., Curtiss Jr., H.C.,Scanlan, R.H., Sisto, F. (1989) *A Modern Course in Aeroelasticity,* Kluwer Academic Publishers, Boston.

- Ewins, D. (1984), *Modal Testing: Theory and Practice,* John Wiley, New York.

- Friedman, P.P. (1999), 'Renaissance of Aeroelasticity and its Future', *Journal of Aircraft; 36:106-121.*

- Fung, Y.C. (1955), *An Introduction to the Theory of Aeroelasticity,* John Wiley, New York.

- Glauert, H. (1924), 'A Theory of Thin Airfoils", British Aeronautical Research Committee, *Rep. & Memo. 910.*

- Glauert, H. (1927), 'Theoretical Relationships for an Airfoil with Hinged Flap', British Aeronautical Research Committee, *Rep. & Memo. 1095.*

- Houbolt, J.C. (1950), 'A Recurrence Matrix Solution for the Dynamic Response of Elastic Aircraft', *Journal of Aeronautical Sciences; 17:540-550.*

- Jones R.T. (1940), 'The Unsteady Lift of a Wing of Finite Aspect Ratio', *NACA Report 681.*

- Jones W.P. (1942), 'Summary of Formulae and Notations Used in Two-Dimensional Derivative Theory', British Aeronautical Research Committee, *Rep. & Memo. 1958*

- Karpel M. (1999), 'Reduced-Order Models for Integrated Aeroservoelastic Optimization', *Journal of Aircraft; 36:146-155.*

- Küssner H.G., Schwarz L. (1941), 'The Oscillating Wing with Aerodynamically Balanced Elevator', NACA *Tech. Memo. 991.* Translated from *Luftfahrt-Forsch.; 17:337-354.*

- Lanchester F.W. (1916), 'Torsional Vibration of the Tail of an Airplane', British Aeronautical Research Committee, *Rep. & Memo. 276, part i.*

- Lee B.H.K., Gong L., Wong Y.S. (1997), 'Analysis and Computation of Nonlinear Dynamic Response of a Two-degree-of Freedom System and its Application in Aeroelasticity. *J Fluids Struct; 11:225-46.*

- Lee B.H.K., Desrocher J. (1987), 'Flutter Analysis of a Two-Dimensional Airfoil Containing Structural Nonlinearities', National Research Council of Canada, *Aeronautical Report LR-618.*

- Lee B.H.K., Price S.J., Wong Y.S. (1999), 'Nonlinear Aeroelastic Analysis of Airfoils: Bifurcation and Chaos', *Progress in Aerospace Sciences; 35:205-334.*

- Lee B.H.K., Tron A. (1989), 'Effects of Structural Nonlinearities on Flutter Characteristics of the CF-18 Aircraft', *J Aircraft; 26:781-6.*

- Le Page W.R. (1961), *Complex Variables and the Laplace Transform for Engineers,* McGraw-Hill, NewYork.

- Livne E. (1999), 'Integrated Aeroservoelastic Optimization: Status and Direction', *Journal of Aircraft; 36:122-145.*

- Press W.H., Flannery B.P., Teukolsky S.A., Vetterling W.T. (1989), *Numerical Recipes,* Cambridge University Press, New York.

- Price S.J., Alighanbari H., Lee B.H.K. (1995), 'The Aeroelastic Response of a Two-dimensional Airfoil with Bilinear and Cubic Structural Nonlinearities', *J Fluids Struct; 9:175-193.*

- Price S.J., Lee B.H.K., Alighanbari H. (1994), 'Post Instability Behaviour of a Two-Dimensional Airfoil with a Structural Nonlinearity'. *J Aircraft; 31:1395-401.*

- Sanderson G.E., Bartsch E.A. (1958), 'In-Flight Damping Measurement', *Proceedings of the 1958 Flight Flutter Testing Symposium,* NASA *SP-385.*

- Scanlan R.H., Rosenbaum R. (1951), *Introduction to the Study of Aircraft Vibration and Flutter*, Macmillan Co., New York.

- Smilg B., Wasserman L.S., *'Application of Three-Dimensional Flutter Theory to Aircraft Structures'* U.S. Army Air Force *Tech. Report 4798.*

- Theodorsen T. (1934) 'General Theory of Aerodynamic Instability and the Mechanism of Flutter', NACA *Report 496*, 1934.

- Vari R.D., Baker M. (1999), 'Aeroelastic Loads and Sensitivity Analysis for Structural Loads Optimization', *Journal of Aircraft; 36:156-166.*

- Zimmerman N.H., Weissenburger J.T. (1964), 'Prediction of Flutter Onset Speed Based on Flight Testing at Subcritical Speeds", *Journal of Aircraft, Vol 1, No. 4;190-202.*

Appendix A – Aerodynamic coefficients (from Theodorsen)

$$P_h = 1 - \frac{2i}{k} C(k)$$

$$P_\alpha = \frac{1}{2} - \frac{i}{k}\left[1 + 2C(k)\right] - \frac{2}{k^2} C(k)$$

$$P_\beta = \frac{-T_1}{\pi} + \frac{i}{k}\frac{T_4}{\pi} - \frac{i}{k}\frac{T_{11}}{\pi} C(k) - \frac{2}{k^2}\frac{T_{10}}{\pi} C(k)$$

$$M_h = \frac{1}{2}$$

$$M_\alpha = \frac{3}{8} - \frac{i}{k}$$

$$M_\beta = -\frac{T_7}{\pi} - \left(c_\beta + \tfrac{1}{2}\right)\frac{T_1}{\pi} + \frac{i}{k\pi}\left[T_4 - \frac{2}{3}\left(\sqrt{1 - c_\beta^2}\right)^3\right] - \frac{1}{k^2 \pi}\left(T_4 + T_{10}\right)$$

where

$$T_1 = -\frac{1}{3}\sqrt{1 - c_\beta^2}\left(2 + c_\beta^2\right) + c_\beta \cos^{-1} c_\beta$$

$$T_4 = -\cos^{-1} c_\beta + c_\beta \sqrt{1 - c_\beta^2}$$

$$T_7 = -\left(\frac{1}{8} + c_\beta^2\right)\cos^{-1} c_\beta + \frac{1}{8} c_\beta \sqrt{1 - c_\beta^2}\left(7 + 2c_\beta^2\right)$$

$$T_{10} = \sqrt{1 - c_\beta^2} + \cos^{-1} c_\beta$$

$$T_{11} = \cos^{-1} c_\beta \left(1 - 2c_\beta\right) + \sqrt{1 - c_\beta^2}\left(2 - c_\beta\right)$$

Appendix B - Fourier analysis and the Laplace transform in theory of vibrations

From the theory of vibrations, if the equation of motion of a system is

$$mx''(t) + cx'(t) + Kx(t) = F_0 e^{i\omega t} \tag{B.1}$$

It can be shown that the steady state solution may be written as

$$x(t) = \frac{F_0 e^{i\omega t}}{Z(i\omega)}.$$

Z(iω) is called the impedance of the system where,

$$Z(i\omega) = m(i\omega)^2 + c(i\omega) + K.$$

The admittance of the system is the inverse of the impedance, or

$$\frac{1}{Z(i\omega)}$$

Because the differential equation (B.1) is linear, the principle of superposition is applicable. If the right hand side of equation (B.1) is

$$F_1(t) + F_2(t) = F_{10} e^{i\omega t} + F_{20} e^{i2\omega t}$$

then the solution will be

$$x(t) = \frac{F_1}{Z(i\omega)} + \frac{F_2}{Z(i2\omega)}.$$

More generally, if the right hand side, or forcing function is

$$F(t) = \sum_{n=-\infty}^{\infty} c_n e^{in\omega t}$$

then the solution will be

$$x(t) = \sum_{n=-\infty}^{\infty} \frac{c_n}{Z(in\omega)} e^{in\omega t}.$$

If the forcing function is represented by a Fourier integral

$$F(t)=\frac{1}{\sqrt{2\pi}}\int_{-\infty}^{\infty}G(\omega)e^{i\omega t}d\omega$$

where

$$G(\omega)=\frac{1}{\sqrt{2\pi}}\int_{-\infty}^{\infty}F(t)e^{-i\omega t}dt \tag{B.2}$$

then the solution will be

$$x(t)=\frac{1}{\sqrt{2\pi}}\int_{-\infty}^{\infty}\frac{G(\omega)}{Z(i\omega)}e^{i\omega t}d\omega. \tag{B.3}$$

The above procedure may also be expressed through the Laplace transform. If $i\omega$ is replaced by s in equations (B.2) and (B.3) and it is assumed that $F(t)=0$ for $t<0$; then equation (B.2) becomes

$$\sqrt{2\pi}G(-is)=\int_{0}^{\infty}F(t)e^{-st}dt \tag{B.4}$$

and equation (B.3) becomes

$$x(t)=\frac{1}{2\pi i}\int_{-\infty i}^{\infty i}\frac{\sqrt{2\pi}G(-is)}{Z(s)}e^{st}ds. \tag{B.5}$$

From equation (B.4) it can be seen that $\sqrt{2\pi}G(-is)$ is the Laplace transform of $F(t)$ and from equation (B.5) that $x(t)$ is the inverse Laplace transform of $\mathcal{L}\{F\}/Z(s)$, i.e.,

$$x(t)=\mathcal{L}^{-1}\left\{\frac{\mathcal{L}\{F\}}{Z(s)}\right\}$$

or

$$\mathcal{L}\{x(t)\}=\frac{\mathcal{L}\{F(t)\}}{Z(s)}$$

To summarize, the Laplace transform of the response is equal to the Laplace transform of the forcing function multiplied by $1/Z(s)$.

Appendix C – Full Text Equations for Chapter 3

Equation 3.4

$$
\left(1+\frac{1}{\mu}\right)\xi'''(\tau)+\left(x_\alpha-\frac{a_h}{\mu}\right)\alpha'''(\tau)-\left(\frac{m_\beta}{m}x_\beta-\frac{T_1}{\mu\pi}\right)\beta'''(\tau)+\frac{1}{\mu}\alpha''(\tau)+2\zeta_\xi\frac{\overline{\omega}_\xi}{U}\xi''(\tau)-\frac{T_4}{\mu\pi}\beta''(\tau)
$$

$$
+\left(\frac{\overline{\omega}_\xi}{U}\right)^2\xi'(\tau)=-\frac{2C_1}{\mu}\left(abe^{-b\tau}+cde^{-d\tau}\right)
$$

$$
-\frac{2}{\mu}\int_0^\tau\left(abe^{-b\tau}e^{b\sigma}+cde^{-d\tau}e^{d\sigma}\right)\lambda(\sigma)d\sigma-\frac{2}{\mu}(1-a-c)\lambda(\tau)
$$

Equation 3.5

$$
\left(\frac{x_\alpha}{r_\alpha^2}-\frac{a_h}{\mu r_\alpha^2}\right)\xi'''(\tau)+\left(1+\frac{1}{8\mu r_\alpha^2}+\frac{a_h^2}{\mu r_\alpha^2}\right)\alpha'''(\tau)+\left(\frac{\bar{z}_\beta}{r_\alpha^2}-\frac{1}{\mu\pi r_\alpha^2}\left[T_7+\{c_\beta-a_h\}T_1\right]\right)\beta'''(\tau)
$$

$$
+\left(\frac{2\zeta_\alpha}{U}+\frac{(0.5-a_h)}{\mu r_\alpha^2}\right)\alpha''(\tau)+\frac{1}{\mu\pi r_\alpha^2}\left(T_1-T_8-[c_\beta-a_h]T_4+0.5T_{11}\right)\beta''(\tau)+\frac{(T_4+T_{10})}{\mu\pi r_\alpha^2}\beta'(\tau)
$$

$$
+\frac{M'(\alpha)}{U^2}=\frac{2C_1}{\mu r_\alpha^2}(0.5+a_h)\left(abe^{-b\tau}+cde^{-d\tau}\right)+\frac{2}{\mu r_\alpha^2}(0.5+a_h)\int_0^\tau\left(abe^{-b\tau}e^{b\sigma}+cde^{-d\tau}e^{d\sigma}\right)\lambda(\sigma)d\sigma
$$

$$
+\frac{2}{\mu r_\alpha^2}(0.5+a_h)(1-a-c)\lambda(\tau)
$$

Equation 3.6

$$
\left(1+\frac{1}{\mu}\right)\xi''''(\tau)+\left(x_\alpha-\frac{a_h}{\mu}\right)\alpha''''(\tau)+\left(\frac{m_\beta}{m}x_\beta-\frac{T_1}{\mu\pi}\right)\beta''''(\tau)+\frac{1}{\mu}\alpha'''(\tau)+2\zeta_\xi\frac{\overline{\omega}_\xi}{U}\xi'''(\tau)-\frac{T_4}{\mu\pi}\beta'''(\tau)
$$

$$
+\left(\frac{\overline{\omega}_\xi}{U}\right)^2\xi''(\tau)=\frac{2C_1}{\mu}\left(ab^2e^{-b\tau}+cd^2e^{-d\tau}\right)
$$

$$
+\frac{2}{\mu}\int_0^\tau\left(ab^2e^{-b\tau}e^{b\sigma}+cd^2e^{-d\tau}e^{d\sigma}\right)\lambda(\sigma)d\sigma-\frac{2}{\mu}(1-a-c)\lambda'(\tau)-\frac{2}{\mu}(ab+cd)\lambda(\tau)
$$

Equation 3.7

$$\left(\frac{x_\alpha}{r_\alpha^2}-\frac{a_h}{\mu r_\alpha^2}\right)\xi''''(\tau)+\left(1+\frac{1}{8\mu r_\alpha^2}+\frac{a_h^2}{\mu r_\alpha^2}\right)\alpha''''(\tau)+\left(\frac{z_\beta}{r_\alpha^2}-\frac{1}{\mu\pi r_\alpha^2}\left[T_7+\{c_\beta-a_h\}T_1\right]\right)\beta''''(\tau)$$

$$+\left(\frac{2\zeta_\alpha}{U}+\frac{(0.5-a_h)}{\mu r_\alpha^2}\right)\alpha'''(\tau)+\frac{1}{\mu\pi r_\alpha^2}\left(T_1-T_8-[c_\beta-a_h]T_4+0.5T_{11}\right)\beta'''(\tau)+\frac{(T_4+T_{10})}{\mu\pi r_\alpha^2}\beta''(\tau)$$

$$+\frac{M''(\alpha)}{U^2}=-\frac{2C_1}{\mu r_\alpha^2}(0.5+a_h)(ab^2e^{-b\tau}+cd^2e^{-d\tau})+\frac{2}{\mu r_\alpha^2}(0.5+a_h)(ab+cd)\lambda(\tau)$$

$$-\frac{2}{\mu r_\alpha^2}(0.5+a_h)\int_0^\tau\left(abe^{-b\tau}e^{b\sigma}+cde^{-d\tau}e^{d\sigma}\right)\lambda(\sigma)d\sigma+.\frac{2}{\mu r_\alpha^2}(0.5+a_h)(1-a-c)\lambda'(\tau)$$

Equation 3.8

$$bd\left(1+\frac{1}{\mu}\right)\xi''(\tau)+bd\left(x_\alpha-\frac{a_h}{\mu}\right)\alpha''(\tau)-bd\left(\frac{m_\beta}{m}x_\beta-\frac{T_1}{\mu\pi}\right)\beta''(\tau)+\frac{bd}{\mu}\alpha'(\tau)+2bd\zeta_\xi\frac{\overline{\omega}_\xi}{U}\xi'(\tau)$$

$$-\frac{bdT_4}{\mu\pi}\beta'(\tau)+bd\left(\frac{\overline{\omega}_\xi}{U}\right)^2\xi(\tau)=-\frac{2bdC_1}{\mu}+\frac{2C_1}{\mu}\left(abde^{-b\tau}+bcde^{-d\tau}\right)$$

$$-\frac{2}{\mu}\int_0^\tau\left(bd-abde^{-b\tau}e^{b\sigma}-bcde^{-d\tau}e^{d\sigma}\right)\lambda(\sigma)d\sigma$$

Equation 3.9

$$\frac{bd}{r_\alpha^2}\left(x_\alpha-\frac{a_h}{\mu}\right)\xi''(\tau)+bd\left(1+\frac{1}{8\mu r_\alpha^2}+\frac{a_h^2}{\mu r_\alpha^2}\right)\alpha''(\tau)$$

$$+\left(\frac{bdz_\beta}{r_\alpha^2}-\frac{bd}{\mu\pi r_\alpha^2}\left[T_7+\{c_\beta-a_h\}T_1\right]\right)\beta''(\tau)+bd\left(\frac{2\zeta_\alpha}{U}+\frac{(0.5-a_h)}{\mu r_\alpha^2}\right)\alpha'(\tau)$$

$$+\frac{bd}{\mu\pi r_\alpha^2}\left(T_1-T_8-[c_\beta-a_h]T_4+\frac{T_{11}}{2}\right)\beta'(\tau)+\frac{bd(T_4+T_{10})}{\mu\pi r_\alpha^2}\beta(\tau)+\frac{bdM(\alpha)}{U^2}$$

$$=\frac{2bd}{\mu r_\alpha^2}C_1(0.5+a_h)(1-ae^{-b\tau}-ce^{-d\tau})$$

$$+\frac{2}{\mu r_\alpha^2}(0.5+a_h)\int_0^\tau\left(ab-abde^{-b\tau}e^{b\sigma}-bcde^{-d\tau}e^{d\sigma}\right)\lambda(\sigma)d\sigma$$

Equation 3.10

$$(b+d)\left(1+\frac{1}{\mu}\right)\xi'''(\tau)+(b+d)\left(x_\alpha-\frac{a_h}{\mu}\right)\alpha'''(\tau)+(b+d)\left(\frac{m_\beta}{m}x_\beta-\frac{T_1}{\mu\pi}\right)\beta'''(\tau)+\frac{(b+d)}{\mu}\alpha''(\tau)$$

$$+2(b+d)\zeta_\xi\frac{\overline{\omega}_\xi}{U}\xi''(\tau)-\frac{(b+d)T_4}{\mu\pi}\beta''(\tau)+(b+d)\left(\frac{\overline{\omega}_\xi}{U}\right)^2\xi'(\tau)$$

$$=-\frac{2C_1}{\mu}\left(ab^2e^{-b\tau}+abde^{-b\tau}+cd^2e^{-d\tau}++bcde^{-d\tau}\right)-\frac{2}{\mu}(b+d)(1-a-c)\lambda(\tau)$$

$$-\frac{2}{\mu}\int_0^\tau\left(ab^2e^{-b\tau}e^{b\sigma}+abde^{-b\tau}e^{b\sigma}+cd^2e^{-d\tau}e^{d\sigma}+bcde^{-d\tau}e^{d\sigma}\right)\lambda(\sigma)d\sigma$$

Equation 3.11

$$(b+d)\left(\frac{x_\alpha}{r_\alpha^2}-\frac{a_h}{\mu r_\alpha^2}\right)\xi'''(\tau)+(b+d)\left(1+\frac{1}{8\mu r_\alpha^2}+\frac{a_h^2}{\mu r_\alpha^2}\right)\alpha'''(\tau)$$

$$+(b+d)\left(\frac{\bar{z}_\beta}{r_\alpha^2}-\frac{1}{\mu\pi r_\alpha^2}\left[T_7+\left\{c_\beta-a_h\right\}T_1\right]\right)\beta'''(\tau)+(b+d)\left(\frac{2\zeta_\alpha}{U}+\frac{(0.5-a_h)}{\mu r_\alpha^2}\right)\alpha''(\tau)$$

$$+\frac{(b+d)}{\mu\pi r_\alpha^2}\left(T_1-T_8-\left[c_\beta-a_h\right]T_4+0.5T_{11}\right)\beta''(\tau)+\frac{(T_4+T_{10})}{\mu\pi r_\alpha^2}(b+d)\beta'(\tau)+(b+d)\frac{M'(\alpha)}{U^2}$$

$$=\frac{2C_1}{\mu r_\alpha^2}(0.5+a_h)\left(ab^2e^{-b\tau}+abde^{-b\tau}+bcde^{-d\tau}+cd^2e^{-d\tau}\right)$$

$$+.\frac{2}{\mu r_\alpha^2}(0.5+a_h)(b+d)(1-a-c)\lambda(\tau)$$

$$+\frac{2}{\mu r_\alpha^2}(0.5+a_h)\int_0^\tau\left(ab^2e^{-b\tau}e^{b\sigma}+abde^{-b\tau}e^{b\sigma}+bcde^{-d\tau}e^{d\sigma}+cd^2e^{-d\tau}e^{d\sigma}\right)\lambda(\sigma)d\sigma$$

Coefficients of Equations (3.12) and (3.13)

$$m_1=1+\frac{1}{\mu}$$

$$m_2=x_\alpha-\frac{a_h}{\mu}$$

$$m_3 = x_\beta - \frac{T_1}{\mu\pi}$$

$$m_4 = 2\zeta_\xi \frac{\overline{\omega}_\xi}{U} + (b+d)\left(1+\frac{1}{\mu}\right) + \frac{2}{\mu}(1-a-c)$$

$$m_5 = \frac{1}{\mu} + (b+d)\left(x_\alpha - \frac{a_h}{\mu}\right) + \frac{2}{\mu}(0.5-a_h)(1-a-c)$$

$$m_6 = (b+d)\left(x_\beta - \frac{T_1}{\mu\pi}\right) - \frac{T_4}{\mu\pi} + \frac{T_{11}}{\mu\pi}(1-a-c)$$

$$m_7 = \left(\frac{\overline{\omega}_\xi}{U}\right)^2 + bd\left(1+\frac{1}{\mu}\right) + 2(b+d)\zeta_\xi \frac{\overline{\omega}_\xi}{U} - \frac{2}{\mu}(ad+cb-b-d)$$

$$m_8 = bd\left(x_\alpha - \frac{a_h}{\mu}\right) + \frac{(b+d)}{\mu} + \frac{2}{\mu}(1-a-c) - \frac{2}{\mu}(0.5-a_h)(ad+bc-b-d)$$

$$m_9 = bd\left(x_\beta - \frac{T_1}{\mu\pi}\right) - (b+d)\frac{T_4}{\mu\pi} + \frac{2T_{10}}{\mu\pi}(1-a-c) - \frac{T_{11}}{\mu\pi}(ad+bc-b-d)$$

$$m_{10} = 2bd\zeta_\xi \frac{\overline{\omega}_\xi}{U} + (b+d)\left(\frac{\overline{\omega}_\xi}{U}\right)^2 + \frac{2}{\mu}bd$$

$$m_{11} = \frac{bd}{\mu} - \frac{2}{\mu}(ad+cb-b-d) + \frac{2}{\mu}bd(0.5-a_h)$$

$$m_{12} = \frac{bdT_{11}}{\mu\pi} - \frac{bdT_4}{\mu\pi} - \frac{2T_{10}}{\mu\pi}(ad+bc-b-d)$$

$$m_{13} = bd\left(\frac{\overline{\omega}_\xi}{U}\right)^2$$

$$m_{14} = \frac{2bd}{\mu}$$

$$m_{15} = \frac{2bdT_{10}}{\mu\pi}$$

$$n_1 = \frac{1}{r_\alpha^2}\left(x_\alpha - \frac{a_h}{\mu}\right)$$

$$n_2 = \frac{1}{\mu r_\alpha^2}\left(\mu r_\alpha^2 + \frac{1}{8} + a_h^2\right)$$

$$n_3 = \frac{z_\beta}{r_\alpha^2} - \frac{1}{\mu\pi r_\alpha^2}\left(T_7 + \left(c_\beta - a_h\right)T_1\right)$$

$$n_4 = \frac{x_\alpha}{r_\alpha^2}(b+d) - \frac{a_h}{\mu r_\alpha^2}(b+d) - \frac{2}{\mu r_\alpha^2}(0.5+a_h)(1-a-c)$$

$$n_5 = \frac{2\zeta_\alpha}{U} + \frac{(0.5-a_h)}{\mu r_\alpha^2} + \frac{(b+d)}{\mu r_\alpha^2}\left(\mu r_\alpha^2 + \frac{1}{8} + a_h^2\right) - \frac{2}{\mu r_\alpha^2}(0.5+a_h)(1-a-c)(0.5-a_h)$$

$$n_6 = \frac{z_\beta}{r_\alpha^2}(b+d) + \frac{1}{\mu\pi r_\alpha^2}\left[(b+d)\left(T_7 + \left(c_\beta - a_h\right)T_1\right) + T_1 - T_8 - \left(c_\beta - a_h\right)T_4\right]$$
$$+ \frac{1}{\mu\pi r_\alpha^2}\left[\frac{T_{11}}{2} - (0.5+a_h)(1-a-c)T_{11}\right]$$

$$n_7 = \frac{bdx_\alpha}{r_\alpha^2} - \frac{bda_h}{\mu r_\alpha^2} - \frac{2}{\mu r_\alpha^2}(0.5+a_h)(b+d-ad-bc)$$

$$n_8 = \frac{bd}{\mu r_\alpha^2}\left(\mu r_\alpha^2 + \frac{1}{8} + a_h^2\right) + \frac{2}{\mu}(b+d)\zeta_\alpha + \frac{(b+d)}{\mu r_\alpha^2}(0.5-a_h)$$
$$- \frac{2}{\mu r_\alpha^2}(0.5+a_h)(0.5-a_h)(b+d-ad-bc) - \frac{2}{\mu r_\alpha^2}(0.5+a_h)(1-a-c)$$

$$n_9 = \frac{1}{\mu\pi r_\alpha^2}\left[(b+d)\left(T_1 + T_8 - \left(c_\beta - a_h\right)T_4 + \frac{T_{11}}{2}\right) + bd\left(z_\beta \mu\pi\right) - T_7 - \left(c_\beta - a_h\right)T_1\right]$$
$$+ \frac{1}{\mu\pi r_\alpha^2}\left[T_4 + T_{10} - T_{11}(0.5+a_h)(b+d-ad-bc) - 2T_{10}(0.5+a_h)(1-a-c)\right]$$

$$n_{10} = -\frac{2bd}{\mu r_\alpha^2}(0.5+a_h)$$

$$n_{11} = \frac{2bd}{U}\zeta_\alpha + \frac{bd}{\mu r_\alpha^2}(0.5-a_h) - \frac{2bd}{\mu r_\alpha^2}(0.5+a_h)(0.5-a_h) - \frac{2}{\mu r_\alpha^2}(0.5+a_h)(b+d-ad-bc)$$

$$n_{12} = \frac{1}{\mu\pi r_\alpha^2}\left[bd\left(T_1 - T_8 - \left(c_\beta - a_h\right)T_4 + \frac{T_{11}}{2}\right) + (b+d)(T_4 + T_{10}) - bdT_{11}(0.5+a_h)\right]$$
$$- \frac{1}{\mu\pi r_\alpha^2}\left[2T_{10}(0.5+a_h)(b+d-ad-bc)\right]$$

$$n_{13} = 0$$

$$n_{14} = -\frac{2bd}{\mu r_\alpha^2}(0.5+a_h)$$

$$n_{15} = -\frac{2bdT_{10}}{\mu\pi r_\alpha^2}(0.5 + a_h)$$

Matrices in Equation (3.15)

$$[A] = \begin{bmatrix} 1 & 0 & 0 & 0 & 0 & 0 & 0 & 0 \\ 0 & 1 & 0 & 0 & 0 & 0 & 0 & 0 \\ 0 & 0 & 1 & 0 & 0 & 0 & 0 & 0 \\ 0 & 0 & 0 & 1 & 0 & 0 & 0 & 0 \\ 0 & 0 & 0 & 0 & 1 & 0 & 0 & 0 \\ 0 & 0 & 0 & 0 & 0 & 1 & 0 & 0 \\ 0 & 0 & 0 & 0 & 0 & 0 & m_1 & m_2 \\ 0 & 0 & 0 & 0 & 0 & 0 & n_1 & n_2 \end{bmatrix}$$

$$[B] = \begin{bmatrix} 0 & 0 & -1 & 0 & 0 & 0 & 0 & 0 \\ 0 & 0 & 0 & -1 & 0 & 0 & 0 & 0 \\ 0 & 0 & 0 & 0 & -1 & 0 & 0 & 0 \\ 0 & 0 & 0 & 0 & 0 & -1 & 0 & 0 \\ 0 & 0 & 0 & 0 & 0 & 0 & -1 & 0 \\ 0 & 0 & 0 & 0 & 0 & 0 & 0 & -1 \\ m_{13} & m_{14} & m_{10} & m_{11} & m_7 & m_8 & m_4 & m_5 \\ n_{13} & n_{14} & n_{10} & n_{11} & n_7 & n_8 & n_4 & n_5 \end{bmatrix}$$

First Mode									
				Recommended sweep rate		Actual rate (in # of times recommended rate)			
%U^*	ω	*f*	ζ	Hz/min	rad/s^2	0.000003	0.000006	0.000012	0.000024
59	0.233	0.0371	0.0357	0.000379	0.000040	0.08	0.15	0.30	0.61
64	0.219	0.0349	0.0375	0.000369	0.000039	0.08	0.16	0.31	0.62
68	0.208	0.0331	0.0391	0.000362	0.000038	0.08	0.16	0.32	0.63
73	0.198	0.0315	0.0402	0.000347	0.000036	0.08	0.17	0.33	0.66
77	0.19	0.0302	0.0407	0.000327	0.000034	0.09	0.18	0.35	0.70
82	0.184	0.0293	0.0404	0.000302	0.000032	0.09	0.19	0.38	0.76
86	0.179	0.0285	0.0386	0.000261	0.000027	0.11	0.22	0.44	0.88
91	0.177	0.0282	0.0343	0.000202	0.000021	0.14	0.28	0.57	1.14
96	0.173	0.0275	0.0244	0.000097	0.000010	0.29	0.59	1.18	2.35
98	0.173	0.0275	0.0152	0.000038	0.000004	0.76	1.51	3.03	6.06

Second Mode									
				Recommended sweep rate		Actual rate (in # of times recommended rate)			
%U^*	ω	*f*	ζ	Hz/min	rad/s^2	0.000003	0.000006	0.000012	0.000024
59	0.442	0.0703	0.038	0.001543	0.000162	0.02	0.04	0.07	0.15
64	0.406	0.0646	0.0429	0.001660	0.000174	0.02	0.03	0.07	0.14
68	0.374	0.0595	0.0483	0.001785	0.000187	0.02	0.03	0.06	0.13
73	0.346	0.0551	0.0543	0.001931	0.000202	0.01	0.03	0.06	0.12
77	0.32	0.0509	0.0611	0.002092	0.000219	0.01	0.03	0.05	0.11
82	0.296	0.0471	0.0691	0.002289	0.000240	0.01	0.03	0.05	0.10
86	0.274	0.0436	0.0787	0.002544	0.000266	0.01	0.02	0.05	0.09
91	0.252	0.0401	0.0911	0.002884	0.000302	0.01	0.02	0.04	0.08
96	0.232	0.0369	0.1094	0.003525	0.000369	0.01	0.02	0.03	0.07
98	0.221	0.0352	0.1231	0.004049	0.000424	0.01	0.01	0.03	0.06

Table 1. Comparison of the four sweep rates used in this study, .000003, .000006, .000012 and .000024 radians/(non-dimensional second)^2, with Ewin's recommended sweep rate, $216 f^2 \zeta^2$, at ten different values of non-dimensional airspeed. U^* is the linear flutter speed in non-dimensional units, ω is frequency in radians per non-dimensional second, ζ is damping factor, and f is frequency in Hz.

Parameter	Theory	Sweep rate in radians/(non-dimensional second)^2							
		.000003		.0000006		.000012		.000024	
		Time Domain	Spectral	Time Domain	Spectral	Time Domain	Spectral	Time Domain	Spectral
ω_1	.208	.208	.207	.209	.206	.211	.201	.214	.207
ζ_1 HPP	.0391	.0430	.0505	.0453	.0507	.0503	.0589	.0598	.0360
ζ_1 Nyquist		.0423	.0524	.0438	.0505	.0474	.0371	.0538	.0307
ω_2	.374	.376	.374	.375	.374	.376	.375	.377	.370
ζ_2 HPP	.0483	.0472	.0492	.0483	.0512	.0487	.0401	.0494	.0349
ζ_2 Nyquist		.0442	.0480	.0480	.0518	.0483	.0522	.0488	.0291

Table 2. Comparison of first and second mode frequency and damping values obtained at 68% of flutter speed using time-domain and spectral methods. ω_1 and ω_2 are the first and second mode natural frequencies in radians/non-dimensional second, ζ_1 HPP and ζ_2 HPP are the first and second mode half-power point damping values and ζ_1 Nyquist and ζ_2 Nyquist are the first and second mode Nyquist damping estimates.

Parameter	Theory	Sweep rate in radians/(non-dimensional second)^2							
		.000003		.0000006		.000012		.000024	
		Time Domain	Spectral	Time Domain	Spectral	Time Domain	Spectral	Time Domain	Spectral
ω_1	.173	.175	.172	.177	.173	.179	.165	.182	.176
ζ_1 HPP	.0244	.0298	.0347	.0348	.0413	.0189	.0288	.0588	.0634
ζ_1 Nyquist		.0281	.0342	.0312	.0348	.0259	.0281	.0331	.0207
ω_2	.232	.233	.233	.233	.233	.235	.233	.229	.235
ζ_2 HPP	.1094	.0929	.0977	.0862	.0988	n/a	.0567	n/a	.0892
ζ_2 Nyquist		.0866	.0867	.0916	.0919	.0872	.1276	.0907	.0899

Table 3. Comparison of first and second mode frequency and damping values obtained at 96% of flutter speed using time-domain and spectral methods. ω_1 and ω_2 are the first and second mode natural frequencies in radians/non-dimensional second, ζ_1 HPP and ζ_2 HPP are the first and second mode half-power point damping values and ζ_1 Nyquist and ζ_2 Nyquist are the first and second mode Nyquist damping estimates. n/a indicates applicable calculation not possible.

Parameter	Theoretical Value	$f=8s^{-1}$, $f_{max}=4$ Hz	$f= 4s^{-1}$, $f_{max}=2$ Hz	
		nw=9500, $\Delta f=0.0008$ Hz	nw=3500 $\Delta f=0.0012$ Hz	nw=4000 $\Delta f=0.0010$ Hz
ω_1	.173	.165	.170	.175
ζ_1 HPP	.0244	.0288	.0611	.0468
ζ_1 Nyquist		.0281	.0462	.0229
ω_2	.232	.233	.233	.233
ζ_2 HPP	.1094	.0567	.0972	.0939
ζ_2 Nyquist		.1276	.0929	.0874

Table 4. Comparison of first and second mode frequency and damping values obtained at 96% of flutter speed. f is the sampling frequency in s^{-1}; nw is the length of the window in number of samples. ω_1 and ω_2 are the first and second mode natural frequencies, ζ_1 HPP and ζ_2 HPP are the first and second mode half-power point damping values and ζ_1 Nyquist and ζ_2 Nyquist are the first and second mode Nyquist damping estimates. In all cases, a Hanning window was used with 50% overlap.

(a)

Percent of flutter speed	Transfer function, pitch with moment input				Transfer function, pitch with flap velocity input			
	Maximum value	Natural frequency	Half-power damping	Nyquist damping	Maximum value	Natural frequency	Half-power damping	Nyquist damping
59	677	0.233	0.039	0.038	4.3	0.233	0.038	0.038
64	815	0.219	0.041	0.041	5.1	0.220	0.040	0.040
68	968	0.208	0.043	0.042	5.9	0.208	0.042	0.042
73	1139	0.198	0.044	0.044	6.9	0.199	0.044	0.043
77	1334	0.190	0.045	0.044	8.0	0.191	0.045	0.044
82	1567	0.184	0.045	0.044	9.3	0.184	0.045	0.044
86	1869	0.179	0.044	0.042	11.0	0.179	0.043	0.042
91	2343	0.176	0.039	0.038	13.8	0.176	0.039	0.038
96	3477	0.175	0.030	0.028	20.4	0.175	0.029	0.028
98	5317	0.176	0.022	0.020	31.2	0.176	0.022	0.020

(b)

Percent of flutter speed	Transfer function, plunge with lift input				Transfer function, plunge with flap velocity input			
	Maximum value	Natural frequency	Half-power damping	Nyquist damping	Maximum value	Natural frequency	Half-power damping	Nyquist damping
59	2427	0.234	0.037	0.037	7.5	0.234	0.037	0.037
64	2765	0.220	0.039	0.039	8.5	0.220	0.039	0.039
68	3098	0.209	0.041	0.040	8.5	0.209	0.041	0.040
73	3422	0.199	0.042	0.042	10.5	0.199	0.042	0.042
77	3739	0.191	0.043	0.042	11.4	0.191	0.042	0.042
82	4059	0.185	0.042	0.042	12.4	0.185	0.042	0.042
86	4423	0.180	0.041	0.040	13.5	0.180	0.041	0.040
91	4970	0.176	0.037	0.036	15.2	0.176	0.037	0.036
96	6394	0.175	0.028	0.027	19.5	0.175	0.028	0.027
98	8871	0.176	0.021	0.020	27.1	0.176	0.021	0.020

Table 5. Estimated first mode frequency and damping values obtained using the time-domain approach at an increasing sweep-rate of .000003 radians/(non-dimensional second)^2. Linear system with airfoil parameters from Chapter 4.

(a)

Percent of flutter speed	Transfer function, pitch with moment input				Transfer function, pitch with flap velocity input			
	Maximum value	Natural frequency	Half-power damping	Nyquist damping	Maximum value	Natural frequency	Half-power damping	Nyquist damping
59	183.1	0.442	0.038	0.038	1.66	0.443	0.038	0.038
64	217.7	0.406	0.043	0.042	1.84	0.406	0.043	0.043
68	254.0	0.376	0.047	0.044	2.03	0.375	0.048	0.048
73	289.4	0.345	0.053	0.053	2.22	0.346	0.053	0.053
77	328.4	0.320	0.055	0.059	2.41	0.320	0.057	0.060
82	368.3	0.296	0.055	0.066	2.59	0.297	0.057	0.067
86	408.7	0.274	0.074	0.072	2.77	0.275	0.074	0.073
91	445.3	0.253	0.082	0.079	2.92	0.254	0.083	0.081
96	475.1	0.233	0.093	0.087	3.02	0.235	0.095	0.088
98	483.4	0.224	0.101	0.088	3.03	0.225	0.105	0.090

(b)

Percent of flutter speed	Transfer function, plunge with lift input				Transfer function, plunge with flap velocity input			
	Maximum value	Natural frequency	Half-power damping	Nyquist damping	Maximum value	Natural frequency	Half-power damping	Nyquist damping
59	136.5	0.439	0.051	0.051	0.49	0.439	0.048	0.048
64	157.0	0.400	0.069	0.070	0.54	0.402	0.069	0.069
68	172.5	0.369	0.058	0.071	0.58	0.369	0.059	0.068
73	190.6	0.338	0.079	0.117	0.63	0.339	0.080	0.112
77	210.2	0.310	0.043	0.079	0.68	0.310	0.044	0.076
82								
86								
91								
96								
98								

Table 6. Estimated second mode frequency and damping values obtained using the time-domain approach at an increasing sweep-rate of .000003 radians/(non-dimensional second)^2. Linear system with airfoil parameters from Chapter 4. Shaded areas indicate areas of the transfer function with mode definition too poor to calculate parameters.

(a)

Percent of flutter speed	Transfer function, pitch with moment input				Transfer function, pitch with flap velocity input			
	Maximum value	Natural frequency	Half-power damping	Nyquist damping	Maximum value	Natural frequency	Half-power damping	Nyquist damping
59	696.5	0.230	0.037	0.036	4.4	0.231	0.036	0.036
64	839.8	0.217	0.038	0.038	5.2	0.217	0.038	0.038
68	999.2	0.205	0.040	0.040	6.1	0.205	0.040	0.040
73	1178.1	0.195	0.041	0.041	7.1	0.195	0.041	0.041
77	1383.5	0.187	0.042	0.041	8.3	0.187	0.042	0.041
82	1630.2	0.181	0.041	0.041	9.6	0.181	0.041	0.041
86	1955.5	0.176	0.040	0.040	11.5	0.176	0.039	0.039
91	2473.5	0.172	0.035	0.034	14.5	0.172	0.035	0.034
96	3746.8	0.170	0.026	0.025	21.9	0.170	0.026	0.025
98	5859.2	0.169	0.020	0.018	34.2	0.169	0.020	0.018

(b)

Percent of flutter speed	Transfer function, plunge with lift input				Transfer function, plunge with flap velocity input			
	Maximum value	Natural frequency	Half-power damping	Nyquist damping	Maximum value	Natural frequency	Half-power damping	Nyquist damping
59	2464.8	0.231	0.036	0.036	7.6	0.231	0.036	0.036
64	2810.5	0.217	0.038	0.038	8.7	0.217	0.038	0.038
68	3151.3	0.206	0.040	0.039	9.7	0.206	0.040	0.039
73	3484.0	0.196	0.041	0.041	10.7	0.196	0.041	0.041
77	3810.2	0.188	0.041	0.041	11.7	0.188	0.041	0.041
82	4142.7	0.182	0.042	0.041	12.7	0.181	0.041	0.041
86	4524.7	0.176	0.039	0.039	13.8	0.176	0.039	0.039
91	5105.4	0.173	0.035	0.035	15.6	0.173	0.035	0.035
96	6643.8	0.170	0.027	0.026	20.3	0.170	0.027	0.026
98	9360.7	0.170	0.020	0.019	28.6	0.170	0.020	0.020

Table 7. Estimated first mode frequency and damping values obtained using the time-domain approach at a decreasing sweep-rate of .000003 radians/(non-dimensional second)^2. Linear system with airfoil parameters from Chapter 4.

(a)

Percent of flutter speed	Transfer function, pitch with moment input				Transfer function, pitch with flap velocity input			
	Maximum value	Natural frequency	Half-power damping	Nyquist damping	Maximum value	Natural frequency	Half-power damping	Nyquist damping
59	183.8	0.441	0.038	0.038	1.66	0.441	0.038	0.038
64	217.4	0.405	0.043	0.043	1.85	0.405	0.043	0.043
68	253.0	0.373	0.048	0.048	2.03	0.373	0.048	0.048
73	290.4	0.344	0.054	0.053	2.22	0.345	0.053	0.053
77	329.2	0.318	0.060	0.059	2.41	0.319	0.060	0.060
82	368.9	0.295	0.067	0.066	2.60	0.295	0.067	0.066
86	408.3	0.273	0.074	0.073	2.77	0.273	0.074	0.074
91	445.0	0.252	0.083	0.080	2.92	0.253	0.084	0.082
96	473.5	0.233	0.095	0.085	3.01	0.233	0.097	0.090
98	480.9	0.224		0.078	3.02	0.224		0.083

(b)

Percent of flutter speed	Transfer function, plunge with lift input				Transfer function, plunge with flap velocity input			
	Maximum value	Natural frequency	Half-power damping	Nyquist damping	Maximum value	Natural frequency	Half-power damping	Nyquist damping
59	137.9	0.438	0.049	0.049	0.50	0.438	0.047	0.046
64	159.0	0.400	0.065	0.063	0.54	0.401	0.065	0.064
68	174.3	0.368		0.059	0.59	0.368		0.057
73	192.6	0.337		0.075	0.64	0.338		0.071
77	212.3	0.309		0.103	0.69	0.310		0.098
82								
86								
91								
96								
98								

Table 8. Estimated second mode frequency and damping values obtained using the time-domain approach at a decreasing sweep-rate of .000003 radians/(non-dimensional second)^2. Linear system with airfoil parameters from Chapter 4. Shaded areas indicate areas of the transfer function with mode definition too poor to calculate parameters.

(a)

Percent of flutter speed	Transfer function, pitch with moment input				Transfer function, pitch with flap velocity input			
	Maximum value	Natural frequency	Half-power damping	Nyquist damping	Maximum value	Natural frequency	Half-power damping	Nyquist damping
59	664.5	0.234	0.041	0.040	4.2	0.235	0.040	0.039
64	799.3	0.220	0.043	0.040	5.0	0.221	0.042	0.039
68	947.4	0.209	0.045	0.044	5.8	0.209	0.044	0.044
73	1113.4	0.200	0.047	0.045	6.7	0.200	0.046	0.045
77	1302.1	0.191	0.048	0.046	7.8	0.192	0.047	0.046
82	1525.6	0.185	0.048	0.047	9.1	0.185	0.047	0.046
86	1813.9	0.181	0.043	0.042	10.7	0.181	0.043	0.042
91	2255.8	0.177	0.043	0.040	13.3	0.178	0.043	0.041
96	3263.6	0.177	0.035	0.031	19.2	0.177	0.034	0.031
98	4759.9	0.178	0.028	0.023	28.0	0.178	0.028	0.023

(b)

Percent of flutter speed	Transfer function, plunge with lift input				Transfer function, plunge with flap velocity input			
	Maximum value	Natural frequency	Half-power damping	Nyquist damping	Maximum value	Natural frequency	Half-power damping	Nyquist damping
59	2393.0	0.235	0.038	0.037	7.4	0.235	0.038	0.038
64	2724.8	0.221	0.040	0.042	8.4	0.222	0.040	0.042
68	3050.6	0.210	0.042	0.041	9.4	0.210	0.042	0.041
73	3366.8	0.200	0.043	0.043	10.3	0.201	0.043	0.043
77	3674.0	0.192	0.044	0.044	11.2	0.192	0.044	0.044
82	3982.2	0.186	0.044	0.043	12.2	0.186	0.044	0.044
86	4326.5	0.180	0.047	0.045	13.2	0.181	0.046	0.045
91	4829.3	0.178	0.040	0.039	14.7	0.178	0.039	0.039
96	6069.8	0.177	0.032	0.031	18.5	0.177	0.032	0.031
98	8039.1	0.178	0.026	0.024	24.5	0.178	0.026	0.024

Table 9. Estimated first mode frequency and damping values obtained using the time-domain approach at an increasing sweep-rate of .000006 radians/(non-dimensional second)^2. Linear system with airfoil parameters from Chapter 4.

(a)

Percent of flutter speed	Transfer function, pitch with moment input				Transfer function, pitch with flap velocity input			
	Maximum value	Natural frequency	Half-power damping	Nyquist damping	Maximum value	Natural frequency	Half-power damping	Nyquist damping
59	182.7	0.443	0.039	0.038	1.66	0.443	0.038	0.038
64	216.1	0.407	0.043	0.043	1.84	0.407	0.043	0.043
68	251.5	0.375	0.048	0.048	2.03	0.375	0.048	0.048
73	288.9	0.346	0.054	0.053	2.22	0.347	0.053	0.053
77	327.9	0.320	0.060	0.059	2.41	0.321	0.059	0.059
82	367.8	0.296	0.067	0.066	2.59	0.297	0.066	0.066
86	407.7	0.274	0.074	0.072	2.77	0.275	0.074	0.073
91	445.3	0.254	0.082	0.079	2.92	0.255	0.083	0.081
96	475.6	0.233	0.086	0.092	3.03	0.235	0.090	0.093
98	484.5	0.225	0.071	0.108	3.04	0.225	0.076	0.111

(b)

Percent of flutter speed	Transfer function, plunge with lift input				Transfer function, plunge with flap velocity input			
	Maximum value	Natural frequency	Half-power damping	Nyquist damping	Maximum value	Natural frequency	Half-power damping	Nyquist damping
59	135.8	0.440	0.047	0.049	0.49	0.440	0.047	0.048
64	153.7	0.402	0.042	0.052	0.54	0.403	0.043	0.051
68	171.5	0.369	0.056	0.069	0.58	0.370	0.056	0.067
73	189.6	0.338		0.070	0.63	0.339		0.068
77								
82								
86								
91								
96								
98								

Table 10. Estimated second mode frequency and damping values obtained using the time-domain approach at an increasing sweep-rate of .000006 radians/(non-dimensional second)^2. Linear system with airfoil parameters from Chapter 4. Shaded areas indicate areas of the transfer function with mode definition too poor to calculate parameters.

(a)

Percent of flutter speed	Transfer function, pitch with moment input				Transfer function, pitch with flap velocity input			
	Maximum value	Natural frequency	Half-power damping	Nyquist damping	Maximum value	Natural frequency	Half-power damping	Nyquist damping
59	2464.3	0.230	0.037	0.036	7.6	0.230	0.037	0.036
64	2810.3	0.216	0.039	0.039	8.7	0.216	0.039	0.038
68	3151.4	0.204	0.040	0.039	9.7	0.204	0.040	0.040
73	3483.8	0.195	0.042	0.041	10.7	0.195	0.042	0.041
77	3809.1	0.187	0.042	0.041	11.7	0.186	0.042	0.041
82	4138.7	0.180	0.042	0.041	12.7	0.180	0.042	0.041
86	4513.3	0.175	0.041	0.040	13.8	0.175	0.041	0.040
91	5070.2	0.171	0.037	0.037	15.5	0.171	0.037	0.037
96	6476.9	0.169	0.031	0.029	19.8	0.168	0.031	0.029
98	8745.3	0.168	0.026	0.023	26.7	0.167	0.026	0.024

(b)

Percent of flutter speed	Transfer function, plunge with lift input				Transfer function, plunge with flap velocity input			
	Maximum value	Natural frequency	Half-power damping	Nyquist damping	Maximum value	Natural frequency	Half-power damping	Nyquist damping
59	700.9	0.229	0.036	0.036	4.4	0.229	0.036	0.036
64	845.6	0.215	0.038	0.038	5.2	0.215	0.038	0.037
68	1006.6	0.204	0.040	0.039	6.1	0.204	0.040	0.039
73	1187.4	0.094	0.041	0.040	7.1	0.194	0.041	0.040
77	1394.8	0.186	0.042	0.041	8.3	0.186	0.042	0.041
82	1643.8	0.179	0.041	0.040	9.7	0.179	0.041	0.040
86	1970.4	0.174	0.040	0.038	11.6	0.174	0.040	0.038
91	2488.3	0.170	0.036	0.035	14.6	0.170	0.036	0.035
96	3704.9	0.168	0.029	0.027	21.6	0.168	0.029	0.028
98	5547.8	0.167	0.025	0.022	32.3	0.167	0.025	0.022

Table 11. Estimated first mode frequency and damping values obtained using the time-domain approach at a decreasing sweep-rate of .000006 radians/(non-dimensional second)^2. Linear system with airfoil parameters from Chapter 4.

(a)

Percent of flutter speed	Transfer function, pitch with moment input				Transfer function, pitch with flap velocity input			
	Maximum value	Natural frequency	Half-power damping	Nyquist damping	Maximum value	Natural frequency	Half-power damping	Nyquist damping
59	185.6	0.442	0.037	0.036	1.66	0.441	0.038	0.038
64	217.7	0.404	0.043	0.043	1.85	0.404	0.043	0.043
68	253.3	0.372	0.048	0.048	2.04	0.373	0.048	0.048
73	290.8	0.344	0.054	0.053	2.22	0.344	0.054	0.054
77	329.7	0.318	0.060	0.059	2.41	0.318	0.060	0.060
82	369.3	0.294	0.067	0.066	2.60	0.295	0.067	0.067
86	408.6	0.272	0.074	0.073	2.77	0.273	0.075	0.074
91	445.4	0.252	0.083	0.080	2.92	0.252	0.084	0.083
96	473.4	0.232	0.096	0.085	3.01	0.233	0.097	0.090
98	480.4	0.223		0.092	3.01	0.224		0.096

(b)

Percent of flutter speed	Transfer function, plunge with lift input				Transfer function, plunge with flap velocity input			
	Maximum value	Natural frequency	Half-power damping	Nyquist damping	Maximum value	Natural frequency	Half-power damping	Nyquist damping
59	138.6	0.437	0.048	0.048	0.50	0.437	0.046	0.045
64	157.0	0.400		0.049	0.55	0.400		0.046
68	175.3	0.367		0.059	0.59	0.368		0.055
73	193.7	0.337		0.074	0.64	0.337		0.070
77	213.4	0.309		0.103	0.69	0.309		0.095
82								
86								
91								
96								
98								

Table 12. Estimated second mode frequency and damping values obtained using the time-domain approach at a decreasing sweep-rate of .000006 radians/(non-dimensional second)^2. Linear system with airfoil parameters from Chapter 4. Shaded areas indicate areas of the transfer function with mode definition too poor to calculate parameters.

(a)

Percent of flutter speed	Transfer function, pitch with moment input				Transfer function, pitch with flap velocity input			
	Maximum value	Natural frequency	Half-power damping	Nyquist damping	Maximum value	Natural frequency	Half-power damping	Nyquist damping
59	639.6	0.236	0.045	0.042	4.1	0.237	0.044	0.042
64	768.2	0.222	0.048	0.045	4.8	0.223	0.047	0.044
68	910.1	0.211	0.050	0.047	5.6	0.212	0.049	0.047
73	1067.4	0.201	0.052	0.049	6.5	0.202	0.051	0.049
77	1245.0	0.193	0.054	0.051	7.5	0.194	0.053	0.050
82	1453.1	0.187	0.044	0.048	8.6	0.187	0.046	0.049
86	1716.5	0.182	0.032	0.043	10.1	0.183	0.033	0.044
91	2107.8	0.179	0.022	0.034	12.4	0.180	0.024	0.037
96	2939.9	0.179	0.019	0.026	17.3	0.180	0.020	0.027
98	4050.7	0.180	0.021	0.022	23.9	0.181	0.022	0.024

(b)

Percent of flutter speed	Transfer function, plunge with lift input				Transfer function, plunge with flap velocity input			
	Maximum value	Natural frequency	Half-power damping	Nyquist damping	Maximum value	Natural frequency	Half-power damping	Nyquist damping
59	2322.9	0.237	0.041	0.040	7.2	0.237	0.041	0.040
64	2642.7	0.223	0.044	0.042	8.1	0.224	0.043	0.043
68	2955.2	0.212	0.046	0.044	9.1	0.212	0.046	0.044
73	3257.5	0.202	0.048	0.046	10.0	0.202	0.047	0.046
77	3547.4	0.194	0.049	0.047	10.8	0.195	0.048	0.047
82	3833.9	0.188	0.046	0.047	11.7	0.188	0.047	0.047
86	4144.1	0.183	0.033	0.043	12.6	0.183	0.034	0.043
91	4576.4	0.180	0.023	0.036	13.9	0.180	0.024	0.037
96	5563.1	0.179	0.019	0.030	17.0	0.179	0.020	0.031
98	6968.9	0.180	0.019	0.024	21.2	0.180	0.020	0.025

Table 13. Estimated first mode frequency and damping values obtained using the time-domain approach at an increasing sweep-rate of .000012 radians/(non-dimensional second)^2. Linear system with airfoil parameters from Chapter 4.

(a)

Percent of flutter speed	Transfer function, pitch with moment input				Transfer function, pitch with flap velocity input			
	Maximum value	Natural frequency	Half-power damping	Nyquist damping	Maximum value	Natural frequency	Half-power damping	Nyquist damping
59	181.6	0.444	0.039	0.038	1.65	0.445	0.038	0.038
64	214.9	0.408	0.044	0.043	1.83	0.409	0.043	0.043
68	250.3	0.376	0.049	0.048	2.02	0.376	0.048	0.048
73	287.7	0.347	0.054	0.054	2.21	0.348	0.053	0.053
77	326.7	0.321	0.060	0.059	2.40	0.322	0.060	0.059
82	366.8	0.297	0.067	0.065	2.60	0.298	0.066	0.066
86	407.0	0.275	0.074	0.072	2.77	0.276	0.073	0.072
91	445.4	0.255	0.082	0.078	2.92	0.255	0.082	0.080
96	476.8	0.235	0.093	0.082	3.03	0.236	0.095	0.086
98								

(b)

Percent of flutter speed	Transfer function, plunge with lift input				Transfer function. plunge with flap velocity input			
	Maximum value	Natural frequency	Half-power damping	Nyquist damping	Maximum value	Natural frequency	Half-power damping	Nyquist damping
59	134.3	0.440	0.054	0.054	0.49	0.441	0.050	0.050
64	152.1	0.403		0.054	0.53	0.404		0.053
68	169.8	0.369		0.066	0.58	0.370		0.064
73	188.1	0.340		0.074	0.62	0.340		0.081
77	207.4	0.308		0.152	0.67	0.310		0.127
82								
86								
91								
96								
98								

Table 14. Estimated second mode frequency and damping values obtained using the time-domain approach at an increasing sweep-rate of .000012 radians/(non-dimensional second)^2. Linear system with airfoil parameters from Chapter 4. Shaded areas indicate areas of the transfer function with mode definition too poor to calculate parameters.

(a)

Percent of flutter speed	Transfer function, pitch with moment input				Transfer function, pitch with flap velocity input			
	Maximum value	Natural frequency	Half-power damping	Nyquist damping	Maximum value	Natural frequency	Half-power damping	Nyquist damping
59	704.8	0.226	0.038	0.037	4.4	0.226	0.038	0.037
64	851.3	0.212	0.041	0.038	5.2	0.213	0.040	0.039
68	1014.3	0.201	0.042	0.039	6.2	0.201	0.042	0.041
73	1197.4	0.191	0.043	0.041	7.2	0.191	0.045	0.042
77	1407.0	0.183	0.044	0.042	8.3	0.183	0.045	0.042
82	1657.4	0.176	0.044	0.042	9.7	0.176	0.045	0.042
86	1982.8	0.171	0.043	0.041	11.6	0.171	0.044	0.041
91	2483.4	0.167	0.041	0.038	14.5	0.167	0.041	0.038
96	3595.7	0.164	0.036	0.031	20.9	0.164	0.036	0.032
98	5110.4	0.163	0.032	0.027	29.6	0.163	0.033	0.027

(b)

Percent of flutter speed	Transfer function, plunge with lift input				Transfer function, plunge with flap velocity input			
	Maximum value	Natural frequency	Half-power damping	Nyquist damping	Maximum value	Natural frequency	Half-power damping	Nyquist damping
59	2451.2	0.227	0.039	0.038	7.6	0.227	0.039	0.038
64	2796.2	0.214	0.041	0.040	8.6	0.213	0.042	0.041
68	3136.0	0.202	0.043	0.042	9.6	0.202	0.043	0.043
73	3466.5	0.192	0.044	0.043	10.6	0.192	0.045	0.044
77	3779.5	0.184	0.046	0.044	11.5	0.184	0.046	0.044
82	4100.0	0.178	0.046	0.044	12.5	0.177	0.046	0.045
86	4456.5	0.172	0.046	0.044	13.6	0.172	0.046	0.044
91	4966.4	0.168	0.043	0.041	15.2	0.168	0.043	0.042
96	6160.8	0.166	0.038	0.035	18.8	0.165	0.038	0.036
98	7910.9	0.164	0.034	0.029	24.2	0.164	0.034	0.029

Table 15. Estimated first mode frequency and damping values obtained using the time-domain approach at a decreasing sweep-rate of .000012 radians/(non-dimensional second)^2. Linear system with airfoil parameters from Chapter 4.

(a)

Percent of flutter speed	Transfer function, pitch with moment input				Transfer function, pitch with flap velocity input			
	Maximum value	Natural frequency	Half-power damping	Nyquist damping	Maximum value	Natural frequency	Half-power damping	Nyquist damping
59	184.6	0.439	0.038	0.038	1.66	0.439	0.038	0.038
64	218.3	0.402	0.043	0.043	1.85	0.403	0.043	0.043
68	254.1	0.371	0.048	0.048	2.04	0.371	0.048	0.048
73	291.7	0.342	0.054	0.053	2.23	0.343	0.054	0.054
77	330.6	0.316	0.060	0.059	2.41	0.317	0.060	0.060
82	370.3	0.293	0.067	0.066	2.60	0.293	0.068	0.067
86	409.5	0.271	0.075	0.073	2.77	0.271	0.076	0.075
91	445.6	0.251	0.084	0.081	2.91	0.251	0.085	0.083
96	472.6	0.231	0.097	0.086	3.00	0.232	0.098	0.091
98	478.7	0.222		0.105	3.00	0.222		0.110

(b)

Percent of flutter speed	Transfer function, plunge with lift input				Transfer function, plunge with flap velocity input			
	Maximum value	Natural frequency	Half-power damping	Nyquist damping	Maximum value	Natural frequency	Half-power damping	Nyquist damping
59	139.9	0.436	0.047	0.046	0.50	0.436	0.045	0.044
64	158.6	0.399		0.046	0.55	0.399		0.045
68	177.2	0.366		0.055	0.60	0.366		0.054
73	196.0	0.335		0.067	0.65	0.336		0.066
77	215.8	0.308		0.093	0.70	0.309		0.083
82								
86								
91								
96								
98								

Table 16. Estimated second mode frequency and damping values obtained using the time-domain approach at a decreasing sweep-rate of .000012 radians/(non-dimensional second)^2. Linear system with airfoil parameters from Chapter 4. Shaded areas indicate areas of the transfer function with mode definition too poor to calculate parameters.

(a)

Percent of flutter speed	Transfer function, pitch with moment input				Transfer function, pitch with flap velocity input			
	Maximum value	Natural frequency	Half-power damping	Nyquist damping	Maximum value	Natural frequency	Half-power damping	Nyquist damping
59	599.9	0.239	0.053	0.048	3.8	0.240	0.051	0.048
64	719.2	0.225	0.056	0.051	4.5	0.226	0.055	0.051
68	850.4	0.213	0.060	0.054	5.2	0.214	0.058	0.052
73	994.7	0.203	0.063	0.056	6.0	0.205	0.060	0.054
77	1156.1	0.196	0.065	0.057	6.9	0.197	0.063	0.055
82	1342.0	0.190	0.066	0.056	8.0	0.190	0.064	0.056
86	1571.1	0.185	0.066	0.056	9.3	0.186	0.064	0.056
91	1894.3	0.181	0.065	0.050	11.2	0.183	0.062	0.051
96	2522.5	0.182	0.059	0.033	14.8	0.183	0.057	0.036
98	3268.7	0.184	0.054	0.020	19.3	0.185	0.053	0.020

(b)

Percent of flutter speed	Transfer function, plunge with lift input				Transfer function, plunge with flap velocity input			
	Maximum value	Natural frequency	Half-power damping	Nyquist damping	Maximum value	Natural frequency	Half-power damping	Nyquist damping
59	2202.0	0.239	0.048	0.045	6.8	0.240	0.047	0.046
64	2502.7	0.226	0.051	0.048	7.7	0.227	0.050	0.048
68	2794.8	0.214	0.053	0.051	8.6	0.215	0.053	0.051
73	3075.1	0.205	0.055	0.052	9.4	0.206	0.055	0.053
77	3347.3	0.197	0.057	0.052	10.2	0.197	0.057	0.054
82	3594.7	0.190	0.058	0.055	10.9	0.191	0.057	0.055
86	3858.0	0.186	0.058	0.053	11.7	0.186	0.057	0.053
91	4197.0	0.183	0.055	0.050	12.8	0.184	0.055	0.051
96	4898.2	0.182	0.050	0.041	14.9	0.183	0.050	0.415
98	5783.6	0.183	0.046	0.030	17.6	0.184	0.046	0.030

Table 17. Estimated first mode frequency and damping values obtained using the time-domain approach at an increasing sweep-rate of .000024 radians/(non-dimensional second)^2. Linear system with airfoil parameters from Chapter 4.

(a)

Percent of flutter speed	Transfer function, pitch with moment input				Transfer function, pitch with flap velocity input			
	Maximum value	Natural frequency	Half-power damping	Nyquist damping	Maximum value	Natural frequency	Half-power damping	Nyquist damping
59	179.4	0.446	0.040	0.039	1.63	0.447	0.039	0.038
64	212.6	0.410	0.045	0.044	1.87	0.411	0.044	0.043
68	248.0	0.377	0.049	0.049	2.01	0.379	0.049	0.048
73	285.5	0.349	0.041	0.053	2.20	0.350	0.042	0.053
77	324.7	0.323	0.034	0.056	2.39	0.324	0.036	0.057
82	365.3	0.299	0.062	0.067	2.58	0.300	0.064	0.066
86	385.8	0.277	0.044	0.072	2.76	0.278	0.047	0.072
91	446.4	0.256	0.044	0.079	2.93	0.257	0.047	0.081
96								
98								

(b)

Percent of flutter speed	Transfer function, plunge with lift input				Transfer function, plunge with flap velocity input			
	Maximum value	Natural frequency	Half-power damping	Nyquist damping	Maximum value	Natural frequency	Half-power damping	Nyquist damping
59	132.3	0.437	0.058	0.051	0.48	0.443	0.054	0.054
64	149.2	0.404	0.056	0.063	0.52	0.405	0.056	0.062
68	166.6	0.371	0.043	0.061	0.57	0.372	0.044	0.061
73	184.6	0.340	0.032	0.060	0.61	0.342	0.033	0.060
77								
82								
86								
91								
96								
98								

Table 18. Estimated second mode frequency and damping values obtained using the time-domain approach at an increasing sweep-rate of .000024 radians/(non-dimensional second)^2. Linear system with airfoil parameters from Chapter 4. Shaded areas indicate areas of the transfer function with mode definition too poor to calculate parameters.

(a)

Percent of flutter speed	Transfer function, pitch with moment input				Transfer function, pitch with flap velocity input			
	Maximum value	Natural frequency	Half-power damping	Nyquist damping	Maximum value	Natural frequency	Half-power damping	Nyquist damping
59	703.2	0.222	0.044	0.041	4.4	0.222	0.044	0.042
64	850.5	0.208	0.046	0.043	5.2	0.208	0.047	0.045
68	1014.5	0.197	0.048	0.046	6.1	0.196	0.049	0.046
73	1198.7	0.186	0.050	0.046	7.1	0.186	0.051	0.047
77	1408.5	0.178	0.052	0.048	8.3	0.178	0.053	0.049
82	1656.7	0.171	0.046	0.049	9.7	0.172	0.048	0.052
86	1974.7	0.166	0.053	0.046	11.5	0.166	0.053	0.050
91	2449.7	0.162	0.038	0.046	14.2	0.162	0.405	0.047
96	3425.7	0.159	0.045	0.040	19.8	0.159	0.048	0.041
98	4603.4	0.157	0.045	0.034	26.5	0.157	0.045	0.035

(b)

Percent of flutter speed	Transfer function, plunge with lift input				Transfer function, plunge with flap velocity input			
	Maximum value	Natural frequency	Half-power damping	Nyquist damping	Maximum value	Natural frequency	Half-power damping	Nyquist damping
59	2397.0	0.224	0.045	0.043	7.4	0.223	0.046	0.044
64	2735.0	0.210	0.048	0.046	8.4	0.209	0.049	0.046
68	3066.1	0.198	0.051	0.047	9.4	0.197	0.051	0.048
73	3386.7	0.189	0.053	0.049	10.9	0.188	0.053	0.050
77	3695.8	0.180	0.054	0.051	11.3	0.180	0.055	0.053
82	3999.8	0.174	0.042	0.052	12.3	0.173	0.045	0.053
86	4325.0	0.168	0.055	0.051	13.3	0.167	0.056	0.052
91	4758.9	0.165	0.031	0.042	14.6	0.163	0.035	0.047
96	5679.7	0.162	0.044	0.043	17.4	0.161	0.047	0.044
98	6897.8	0.161	0.045	0.036	21.2	0.160	0.047	0.037

Table 19. Estimated first mode frequency and damping values obtained using the time-domain approach at a decreasing sweep-rate of .000024 radians/(non-dimensional second)^2. Linear system with airfoil parameters from Chapter 4.

(a)

Percent of flutter speed	Transfer function, pitch with moment input				Transfer function, pitch with flap velocity input			
	Maximum value	Natural frequency	Half-power damping	Nyquist damping	Maximum value	Natural frequency	Half-power damping	Nyquist damping
59	184.8	0.436	0.039	0.038	1.66	0.436	0.039	0.039
64	218.7	0.400	0.043	0.043	1.84	0.400	0.044	0.043
68	254.6	0.368	0.049	0.048	2.03	0.369	0.049	0.049
73	292.4	0.340	0.055	0.053	2.22	0.340	0.055	0.055
77	331.4	0.314	0.061	0.060	2.41	0.314	0.062	0.061
82	371.1	0.291	0.068	0.067	2.59	0.291	0.069	0.068
86	410.0	0.269	0.076	0.074	2.76	0.269	0.077	0.076
91	445.2	0.248	0.086	0.082	2.90	0.249	0.088	0.085
96	470.4	0.229	0.099	0.088	2.98	0.230	0.101	0.092
98	475.0	0.220		0.078	2.97	0.221		0.085

(b)

Percent of flutter speed	Transfer function, plunge with lift input				Transfer function, plunge with flap velocity input			
	Maximum value	Natural frequency	Half-power damping	Nyquist damping	Maximum value	Natural frequency	Half-power damping	Nyquist damping
59	141.6	0.433	0.058	0.044	0.51	0.433	0.044	0.041
64	160.9	0.396	0.056	0.064	0.56	0.396	0.058	0.054
68	180.2	0.364		0.055	0.61	0.363		0.054
73	199.7	0.334		0.068	0.66	0.333		0.065
77	220.5	0.306		0.091	0.71	0.306		0.085
82								
86								
91								
96								
98								

Table 20. Estimated second mode frequency and damping values obtained using the time-domain approach at a decreasing sweep-rate of .000024 radians/(non-dimensional second)^2. Linear system with airfoil parameters from Chapter 4. Shaded areas indicate areas of the transfer function with mode definition too poor to calculate parameters.

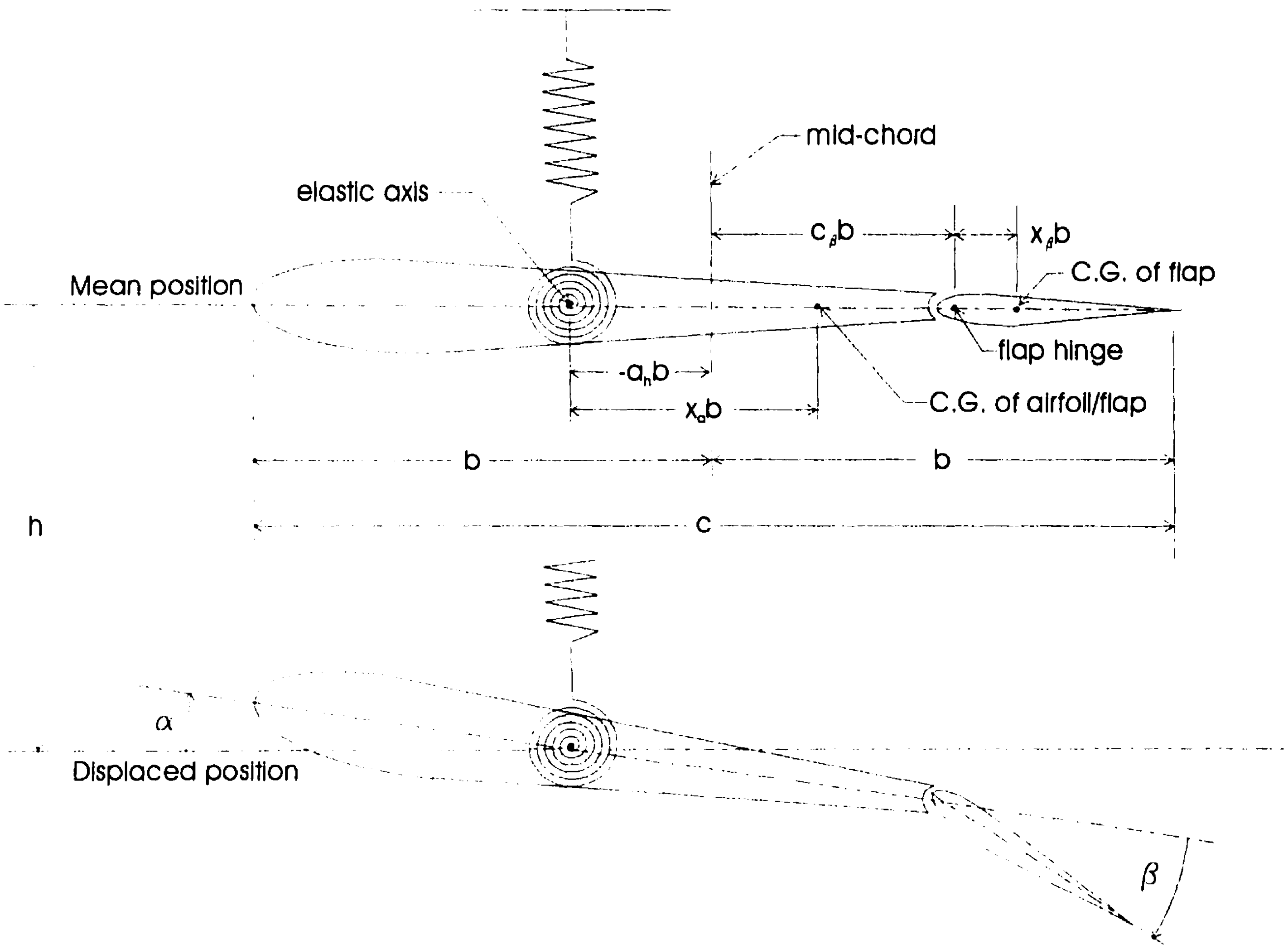

Figure 1. Two-dimensional, three degree of freedom airfoil section with flap

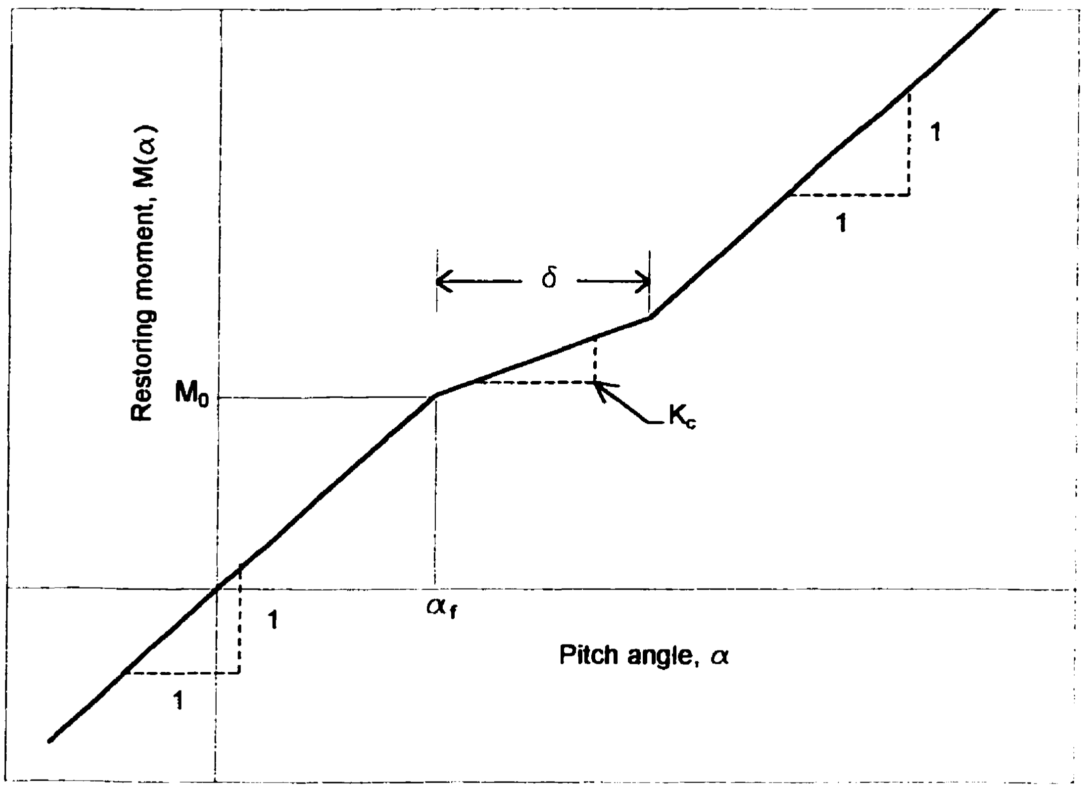

Figure 2. Schematic of a typical freeplay nonlinearity. M_0 is the preload, α_f is the beginning of the freeplay region, and δ is the length of the freeplay region.

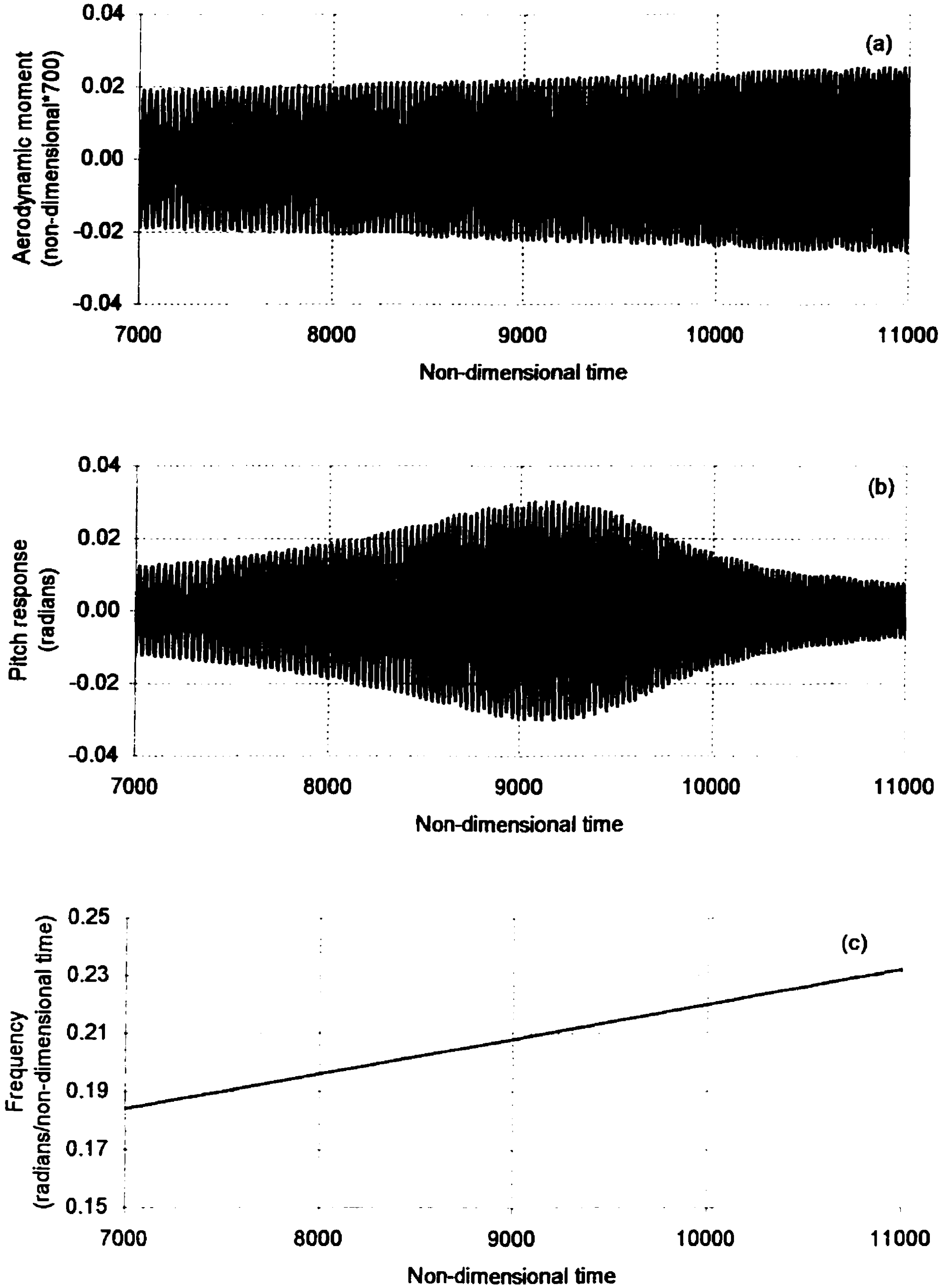

Figure 3. Simulated sine sweep of one mode of the two-degree-of-freedom linear system subject to an increasing frequency sweep at 68% of linear flutter speed and a sweep-rate of .000006 radians/(non-dimensional second)^2. (a) aerodynamic moment or input function. (b) pitch response, (c) frequency of input and response.

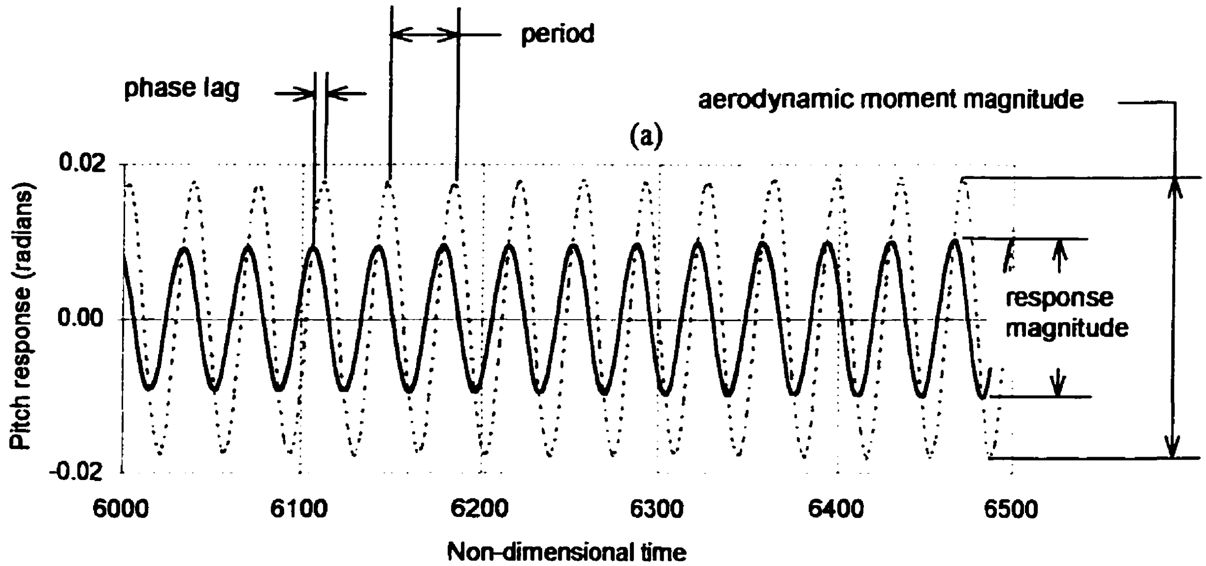

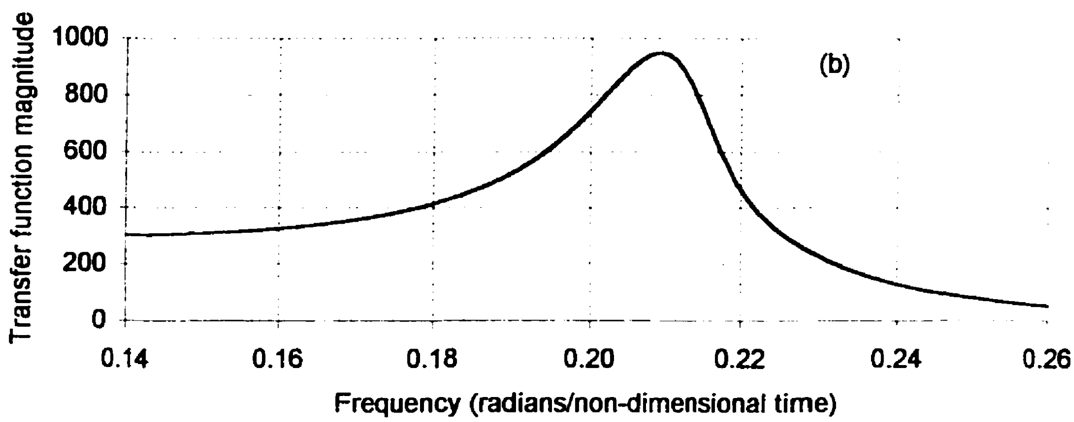

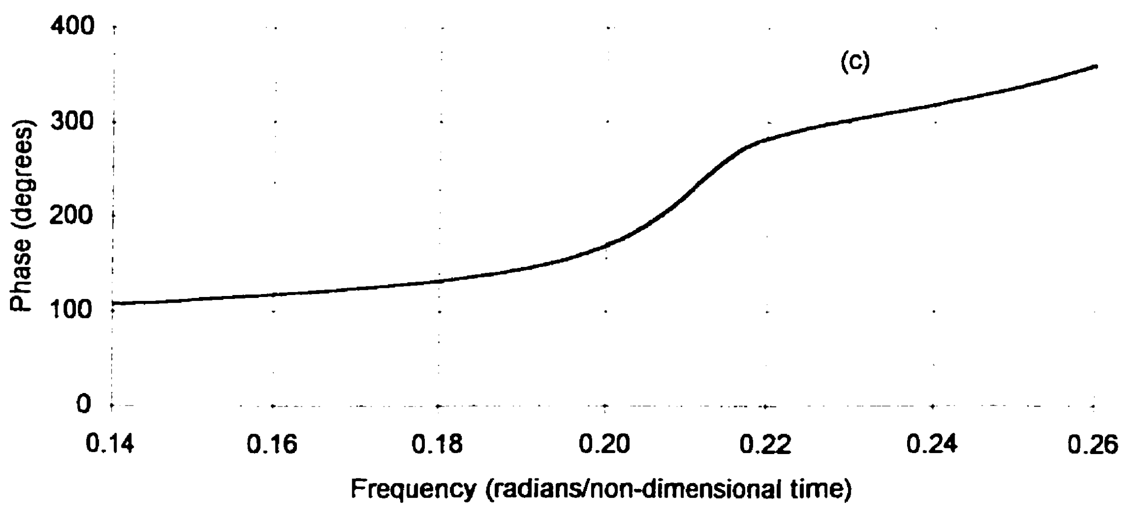

Figure 4. (a) Method used to obtain magnitude and phase lag for transfer function. (b)&(c) Frequency transfer function, obtained from the time domain approach, for the frequency sweep presented in Figure 3. (b) magnitude, (c) phase.

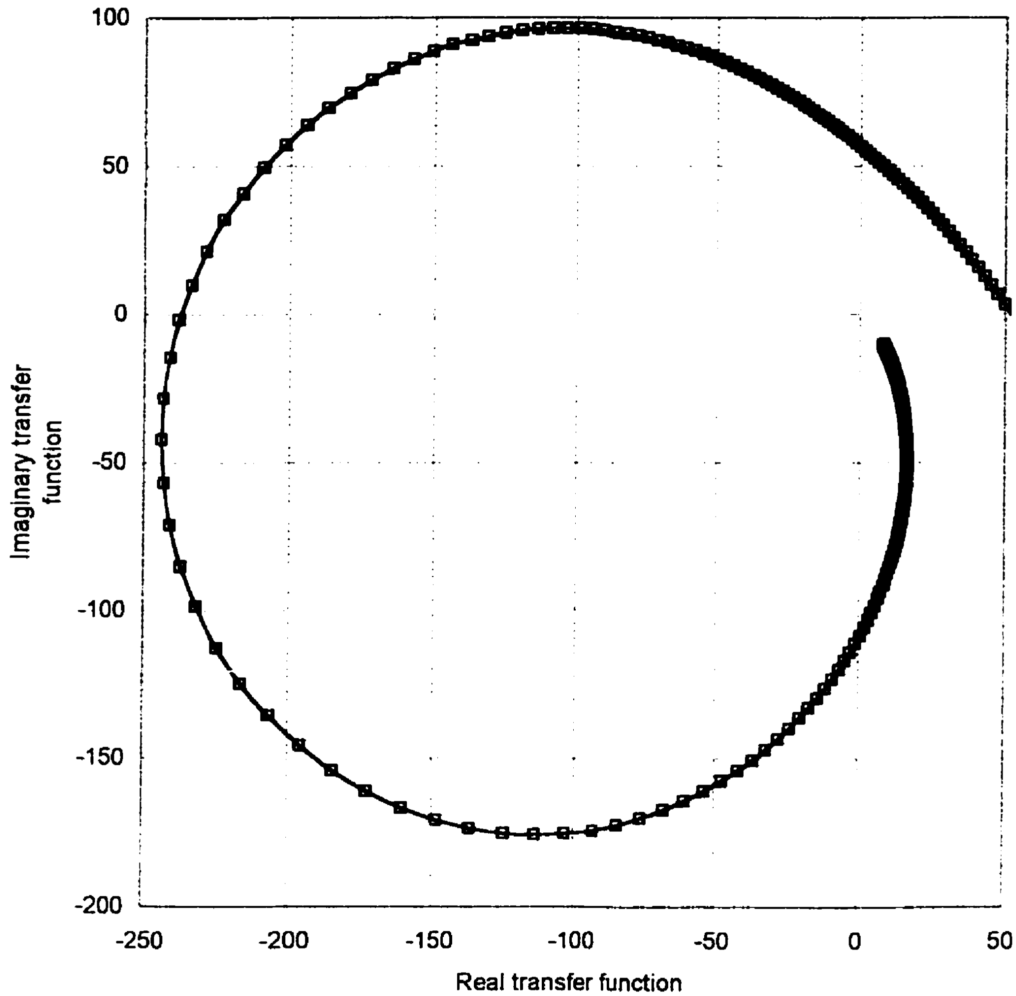

Figure 5. Nyquist plot representation of the transfer function presented in Figure 4.

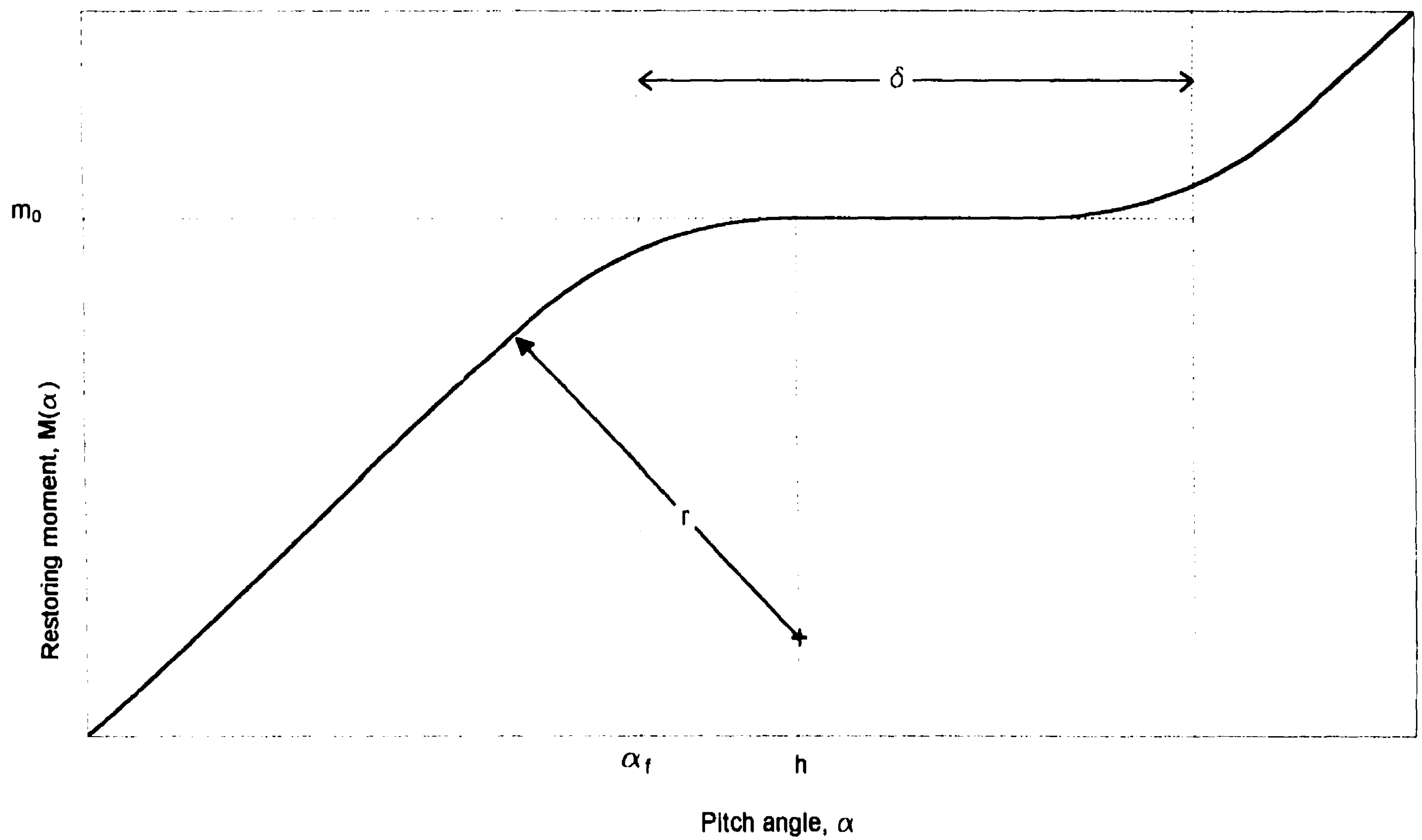

Figure 6. Schematic of terms defining nonlinear restoring moment in pitch degree of freedom.

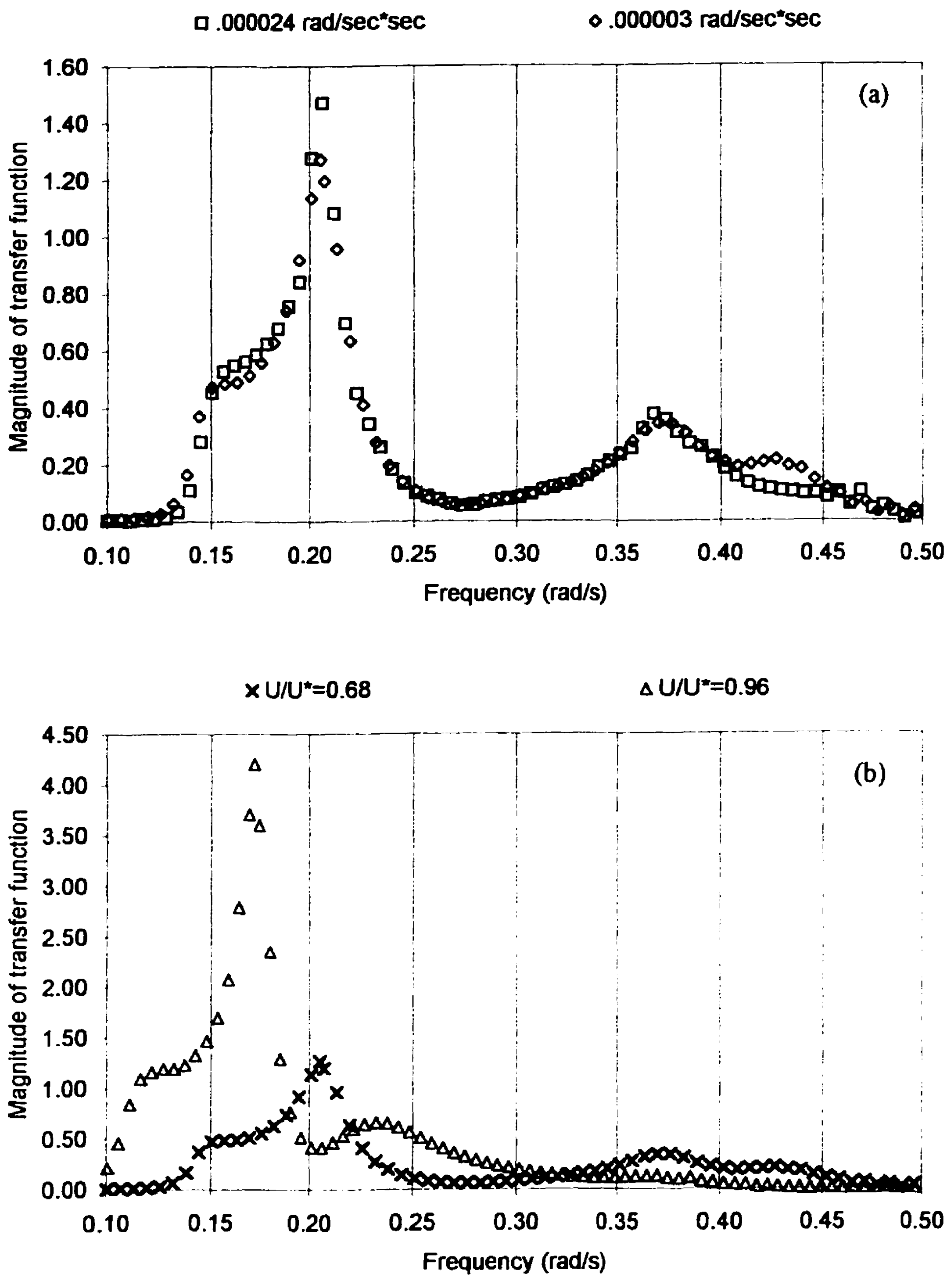

Figure 7. Comparison of transfer functions obtained using Fourier transform (spectral) methods. (a) Data obtained at 68% of linear flutter speed and sweep rates of .000003 and .000024 radians/(non-dimensional second)^2, (b) Data obtained at .000003 radians/(non-dimensional second)^2 and 68% and 96% of linear flutter speed.

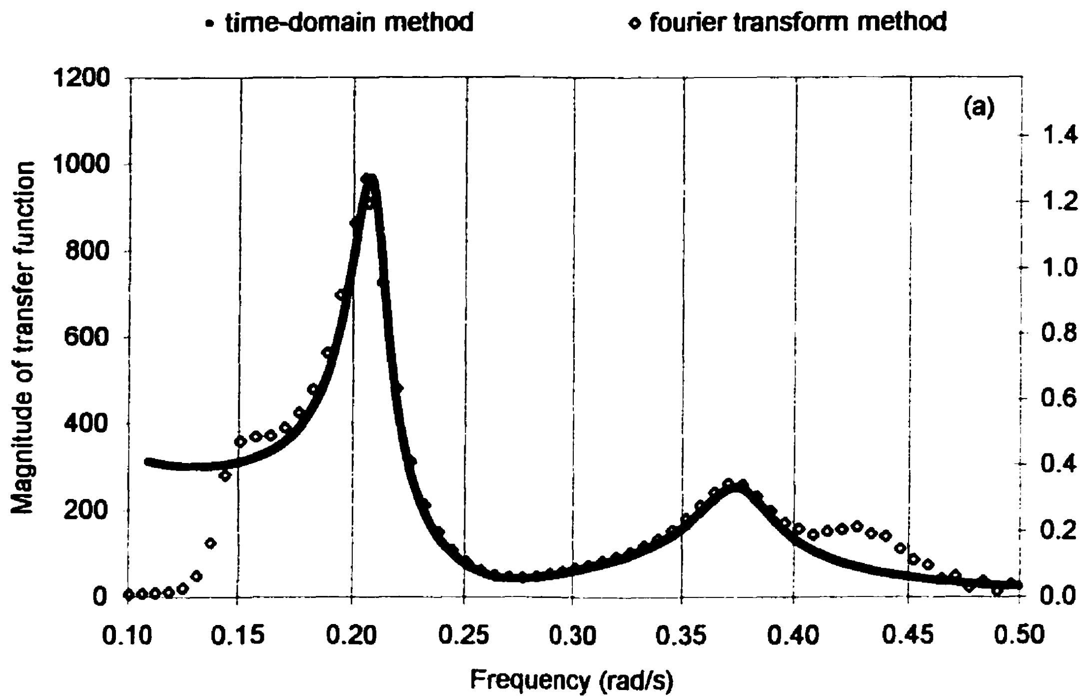

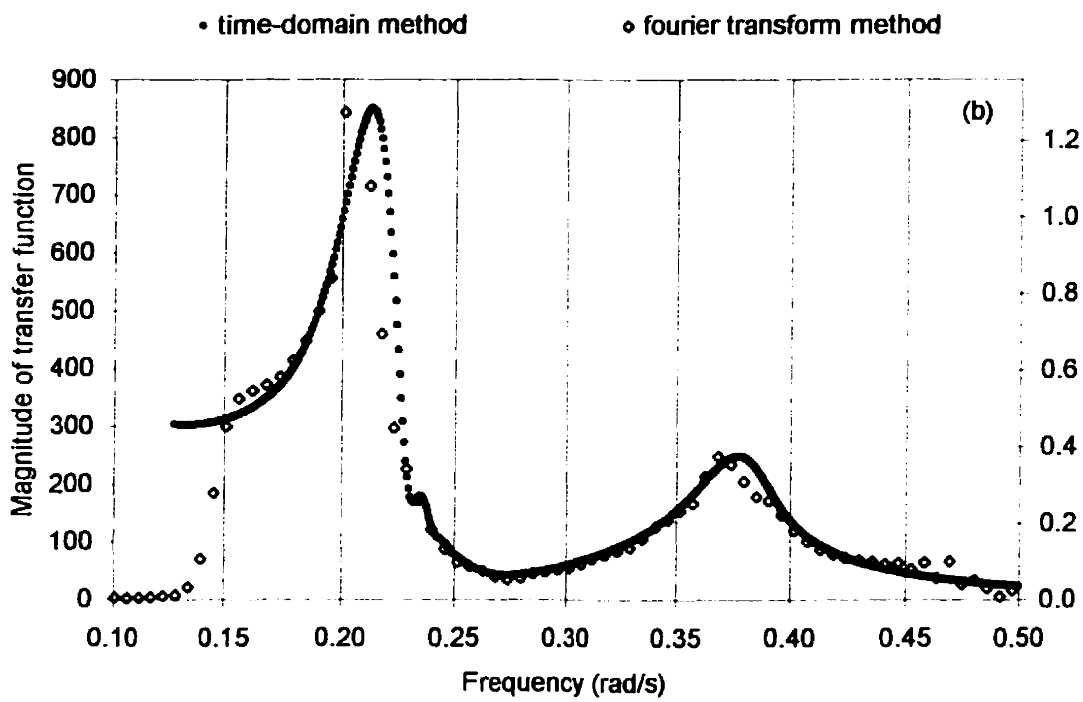

Figure 8. Comparison of transfer functions obtained using time domain and Fourier transform (spectral) methods. Data obtained at 68% of flutter speed and at increasing frequency sweeps (a) sweep-rate .000003 radians/(non-dimensional second)^2, (b) sweep-rate .000024 radians/(non-dimensional second)^2.

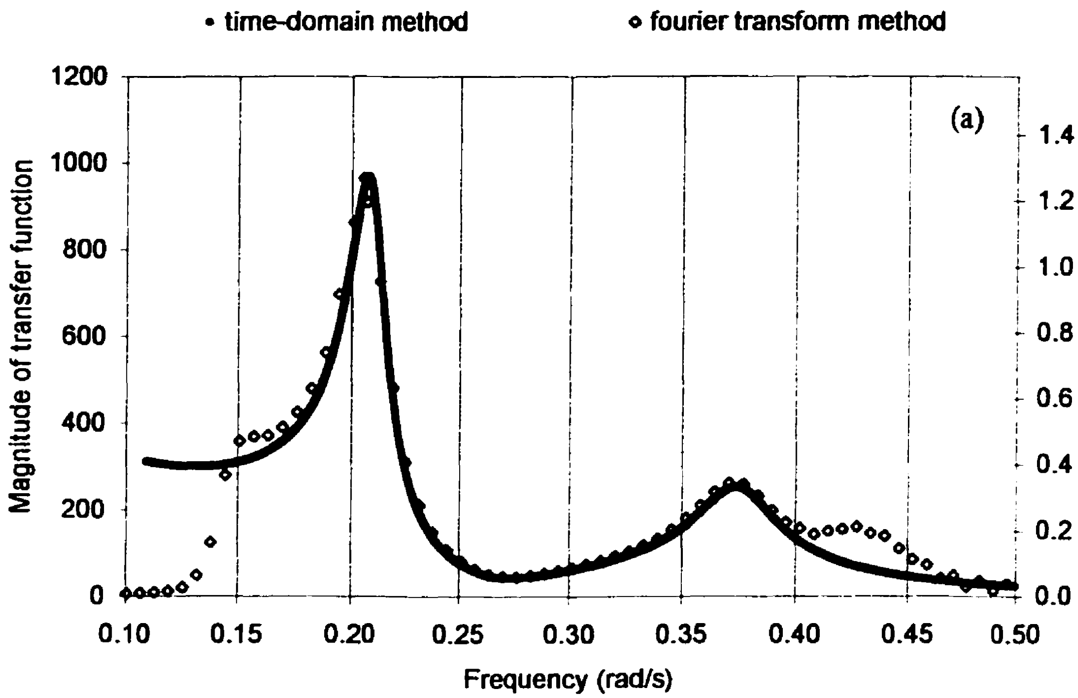

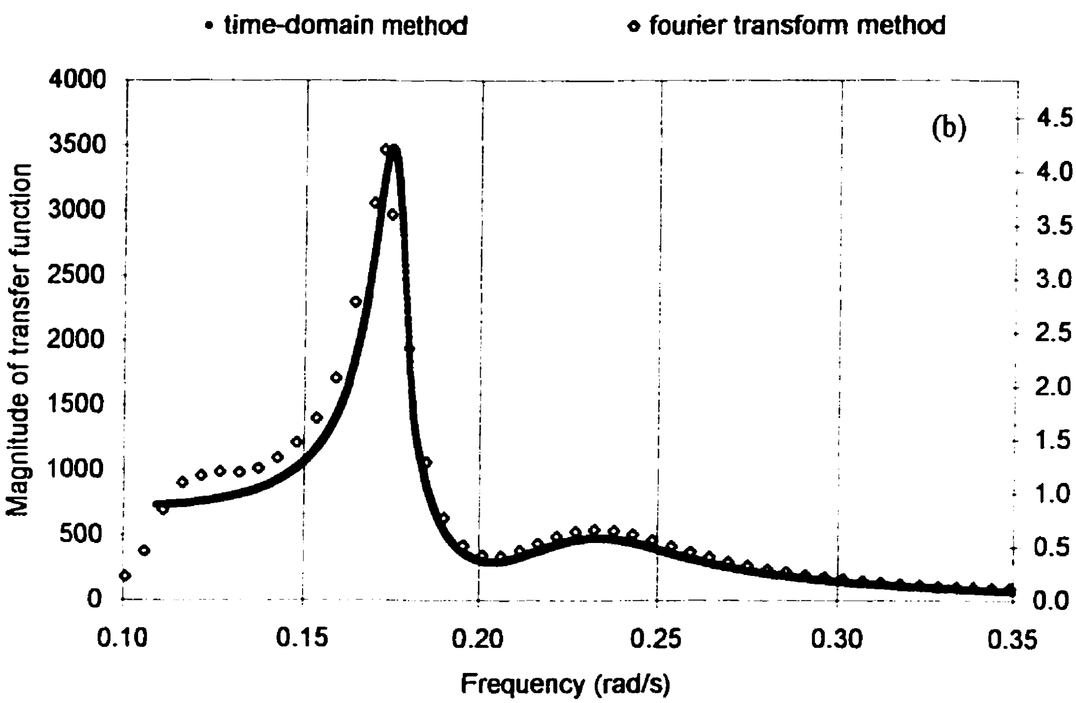

Figure 9. Comparison of transfer functions obtained using time domain and Fourier transform (spectral) methods at an increasing sweep-rate of .000003 radians/(non-dimensional second)^2 and at (a) 68% of the linear flutter speed, (b) 96% of the linear flutter speed.

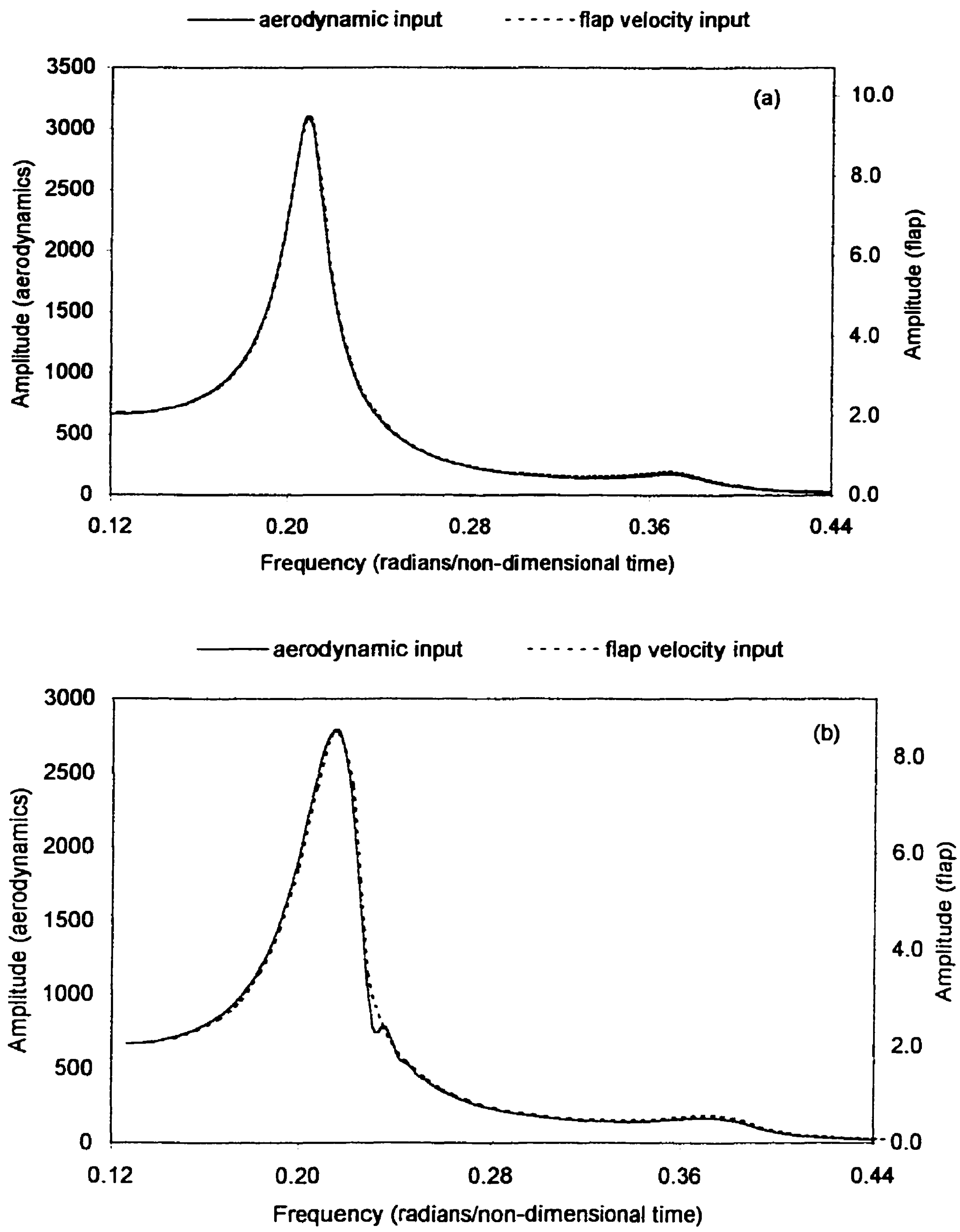

Figure 10. Comparison of plunge response transfer functions obtained using aerodynamic lift input and aileron velocity input, at 68% of flutter speed. (a) sweep-rate .000003 radians/(non-dimensional second)^2, (b) sweep-rate .000024 radians/(non-dimensional second)^2.

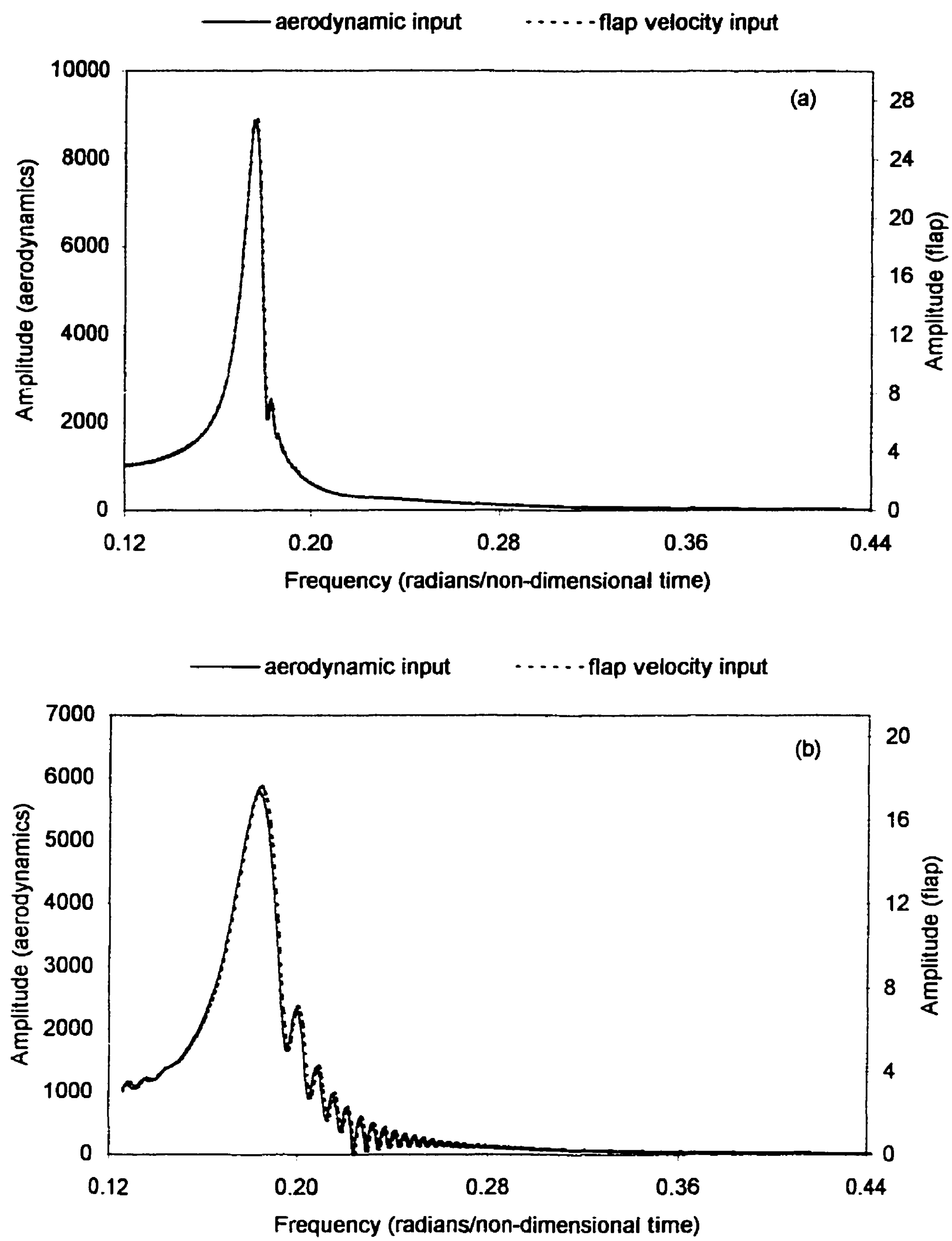

Figure 11. Comparison of plunge response transfer functions obtained using aerodynamic lift input and aileron velocity input, at 98% of flutter speed. (a) sweep-rate .000003 radians/(non-dimensional second)^2, (b) sweep-rate .000024 radians/(non-dimensional second)^2.

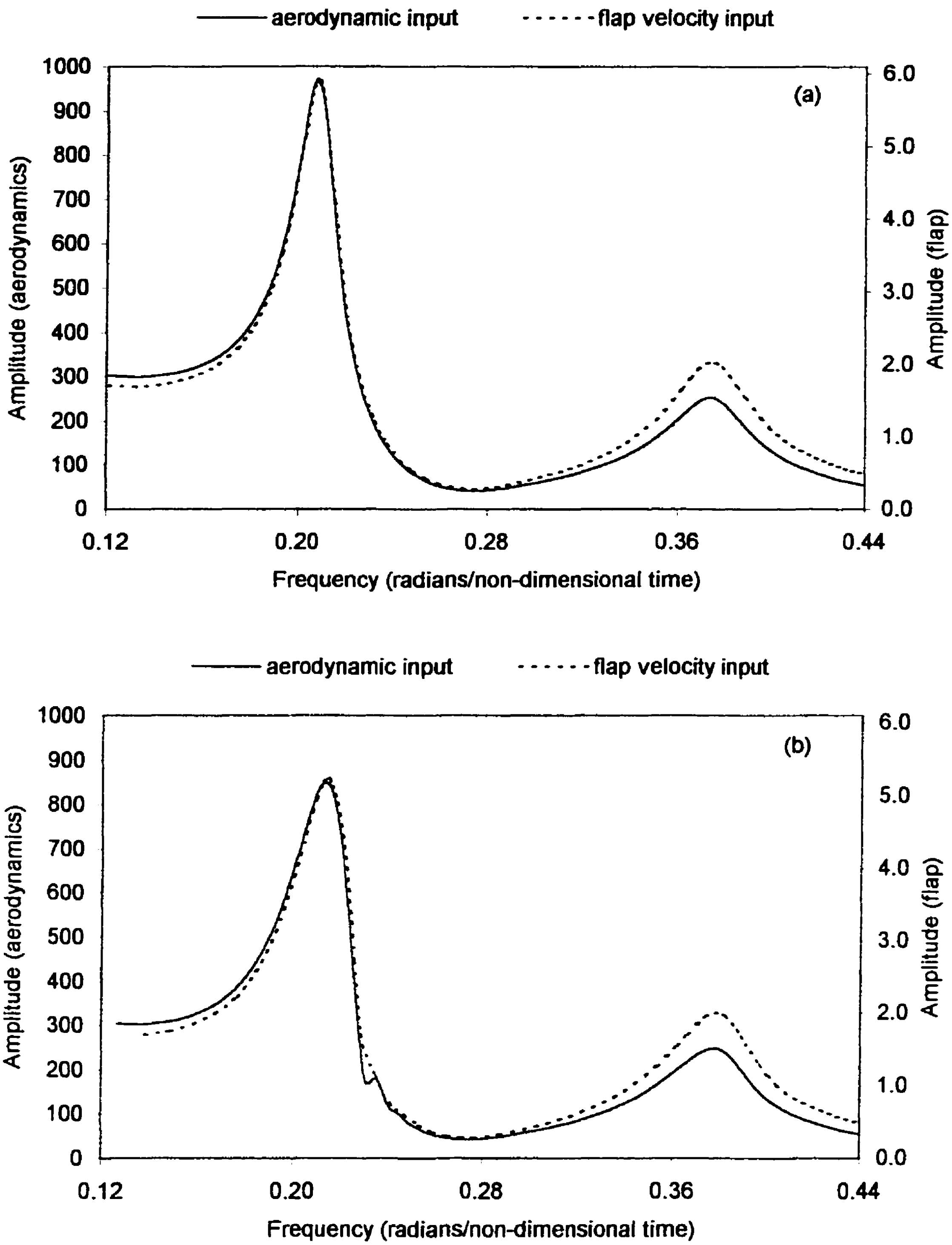

Figure 12. Comparison of pitch response transfer functions obtained using aerodynamic moment input and aileron velocity input, at 68% of flutter speed. (a) sweep-rate .000003 radians/(non-dimensional second)^2, (b) sweep-rate .000024 radians/(non-dimensional second)^2.

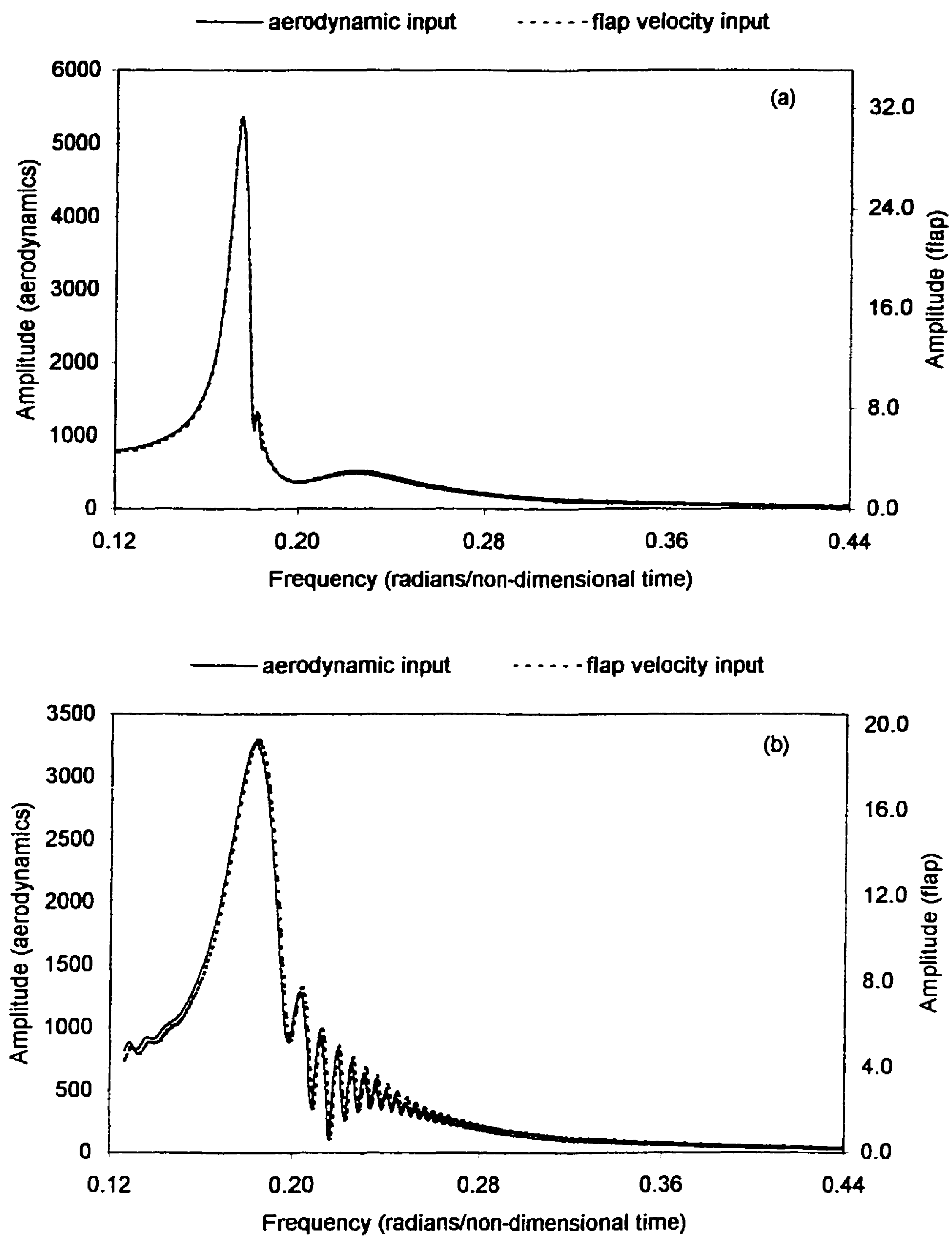

Figure 13. Comparison of pitch response transfer functions obtained using aerodynamic moment input and aileron velocity input, at 98% of flutter speed. (a) sweep-rate .000003 radians/(non-dimensional second)^2, (b) sweep-rate .000024 radians/(non-dimensional second)^2.

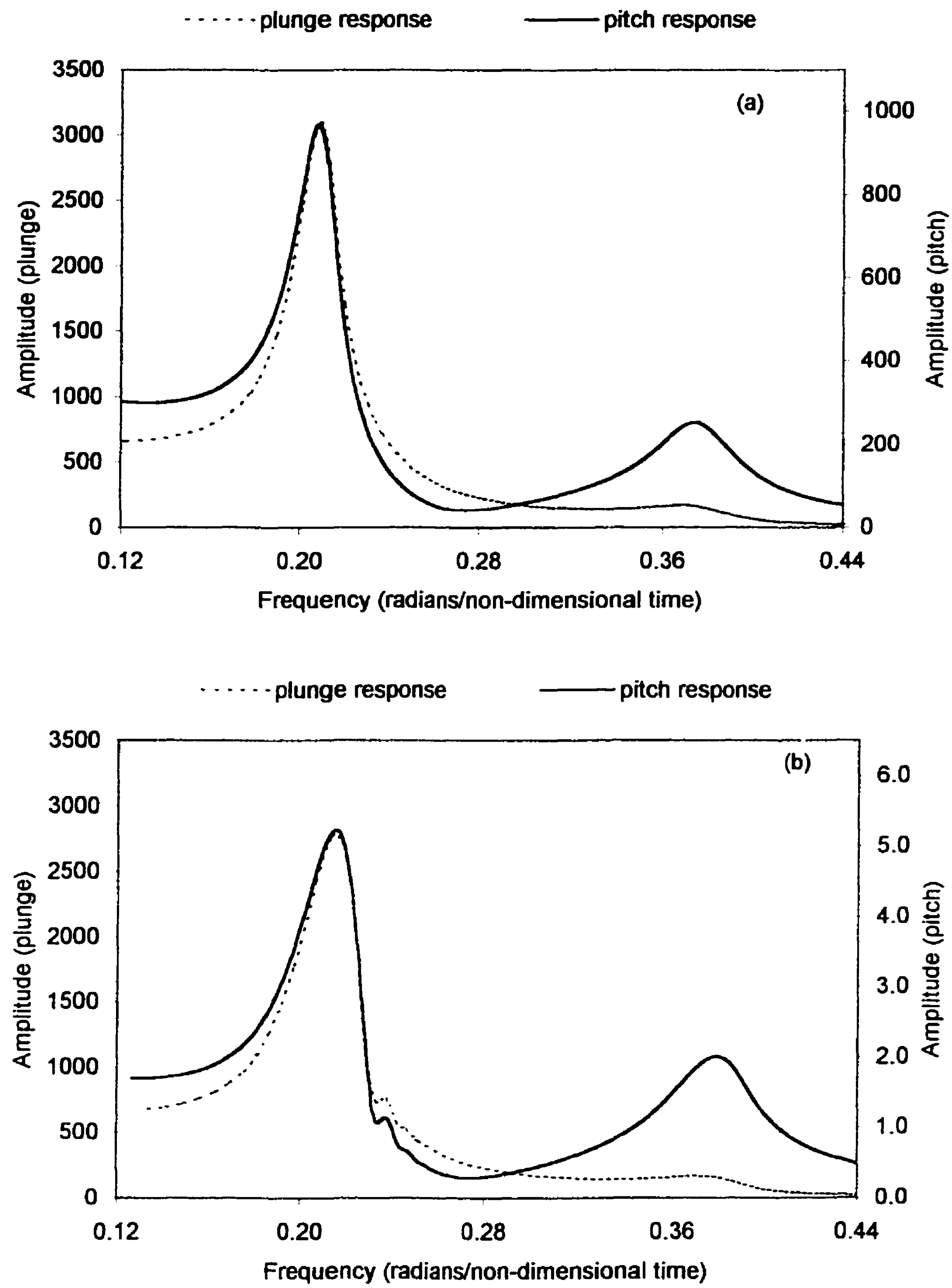

Figure 14. Comparison of plunge response and pitch response transfer functions obtained at 68% of flutter speed, (a) sweep-rate .000003 radians/(non-dimensional second)^2, (b) sweep-rate .000024 radians/(non-dimensional second)^2.

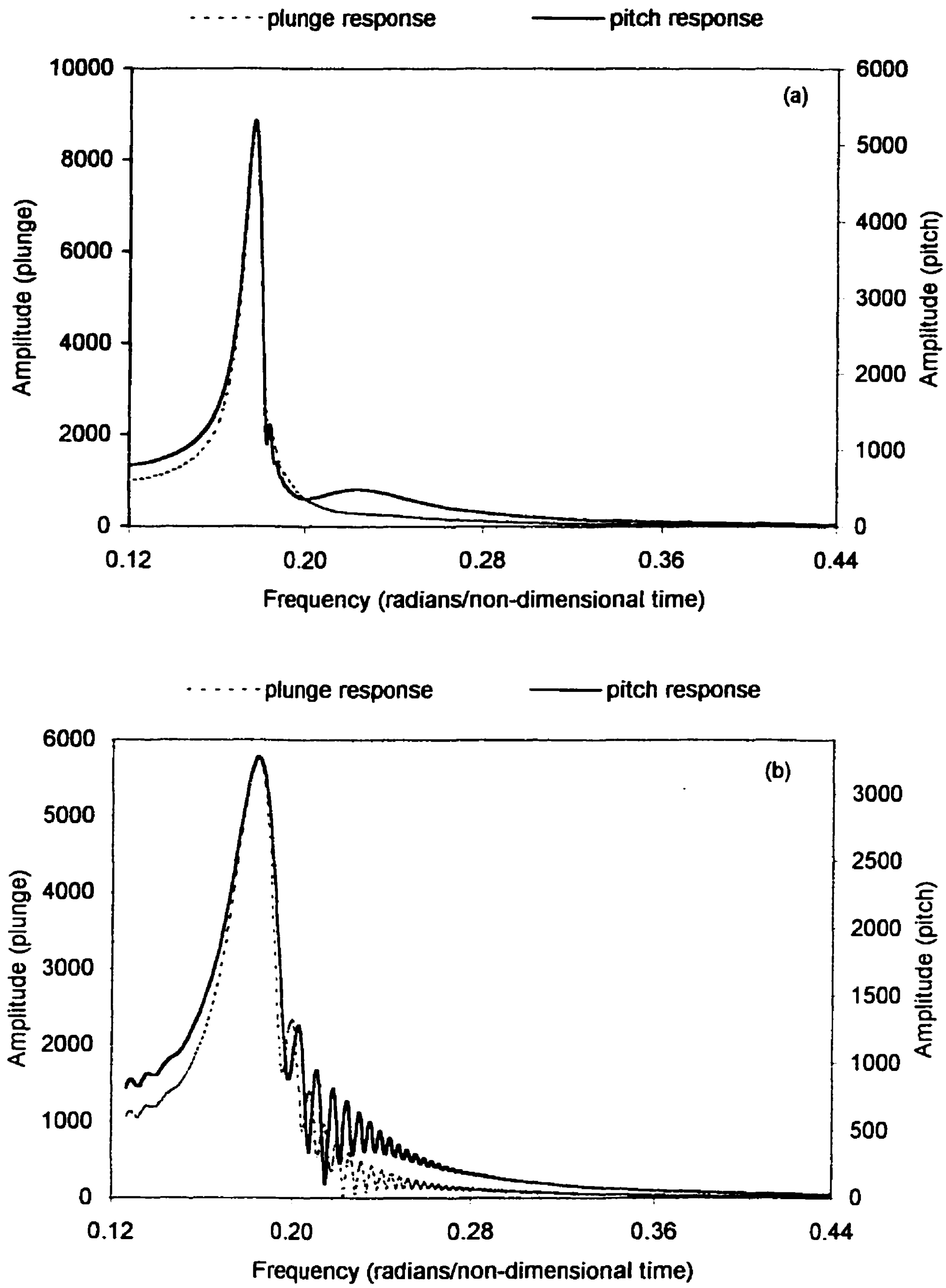

Figure 15. Comparison of plunge response and pitch response transfer functions obtained at 98% of flutter speed, (a) sweep-rate .000003 radians/(non-dimensional second)^2, (b) sweep-rate .000024 radians/(non-dimensional second)^2.

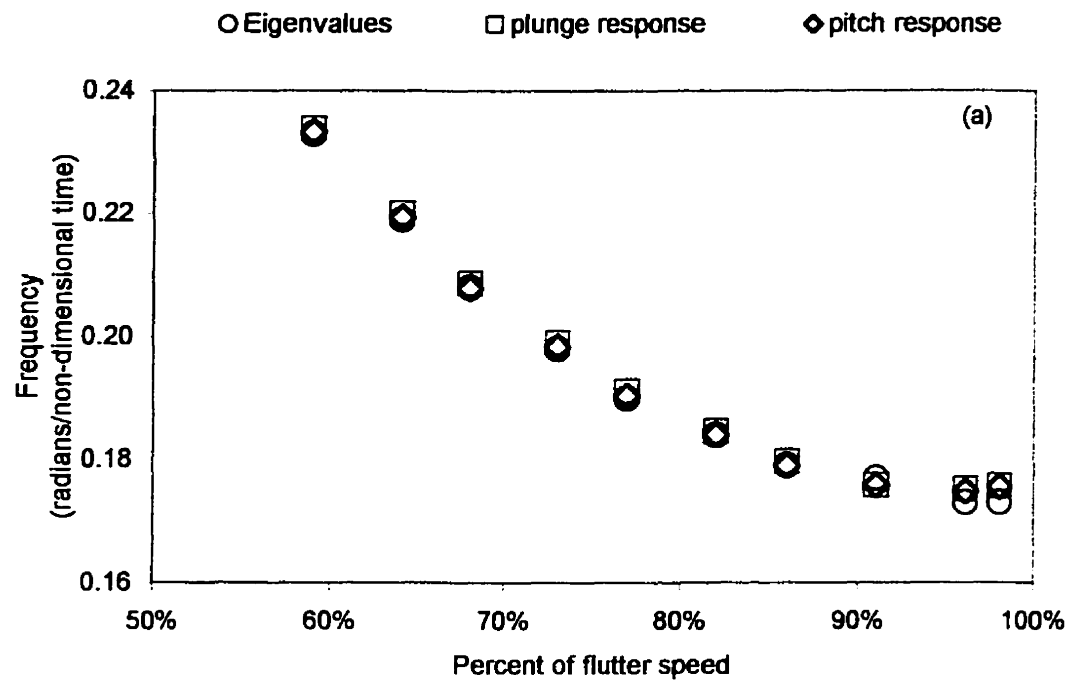

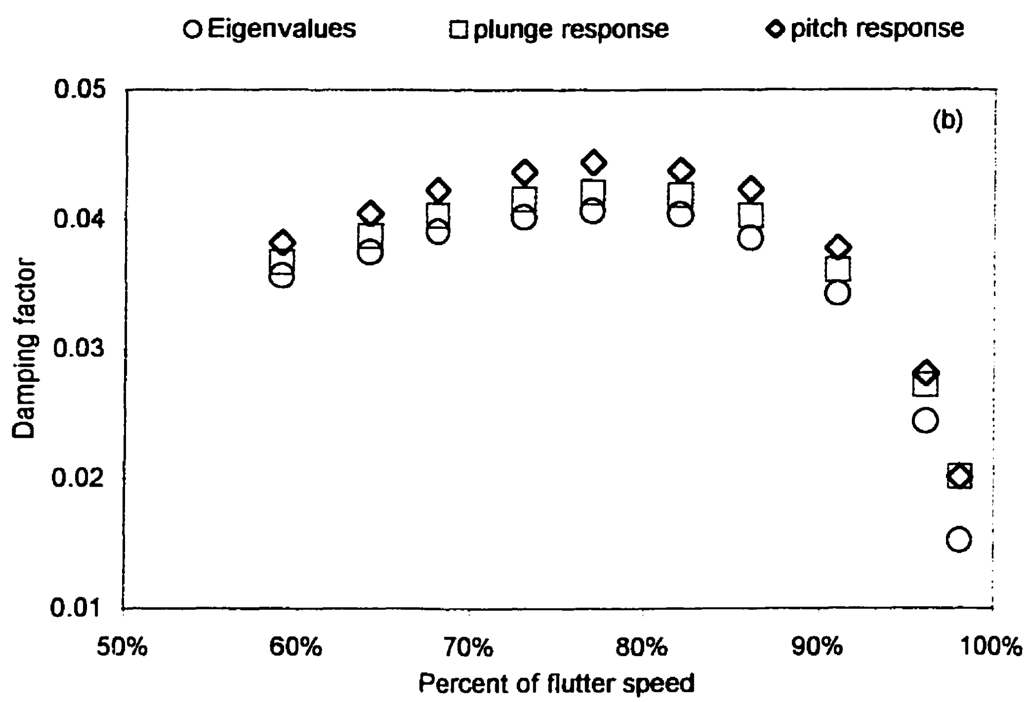

Figure 16. Comparison of the first mode damping and frequency estimates obtained using plunge and pitch response data at an increasing sweep-rate of .000003 radians/(non-dimensional second)^2. (a) frequency, (b) damping.

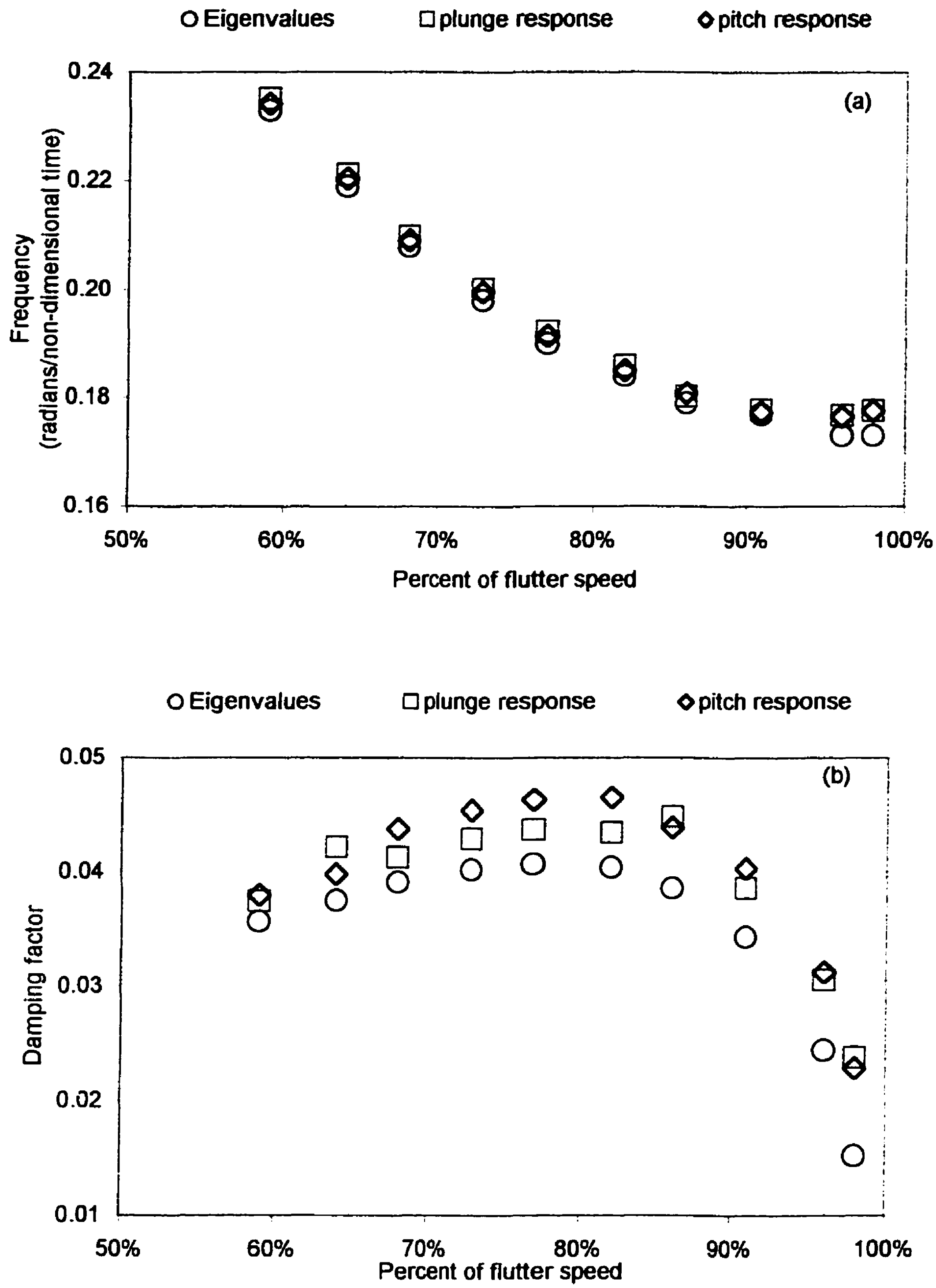

Figure 17. Comparison of the first mode damping and frequency estimates obtained using plunge and pitch response data at an increasing sweep-rate of .000006 radians/(non-dimensional second)^2, (a) frequency, (b) damping.

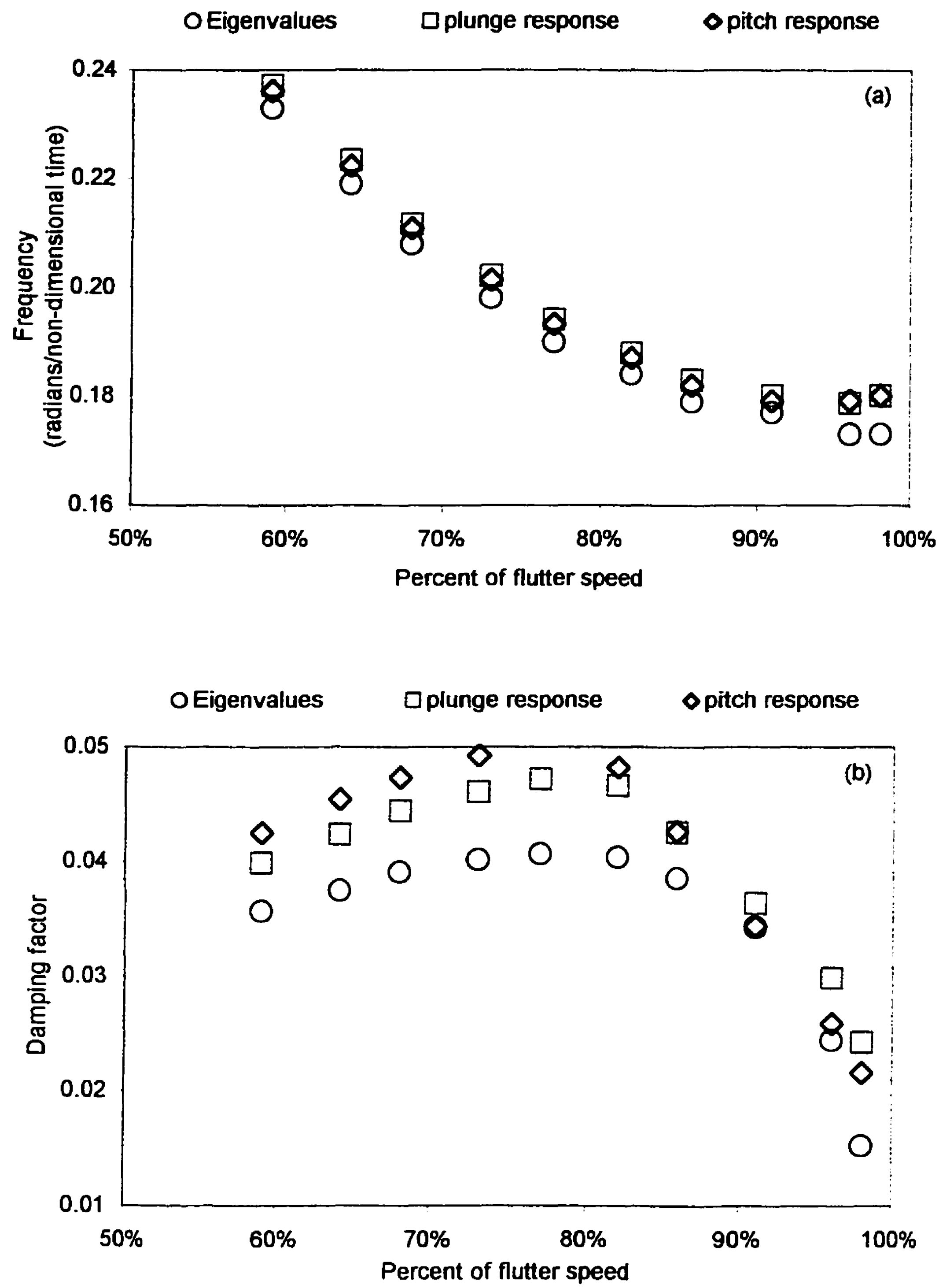

Figure 18. Comparison of the first mode damping and frequency estimates obtained using plunge and pitch response data at an increasing sweep-rate of .000012 radians/(non-dimensional second)^2, (a) frequency, (b) damping.

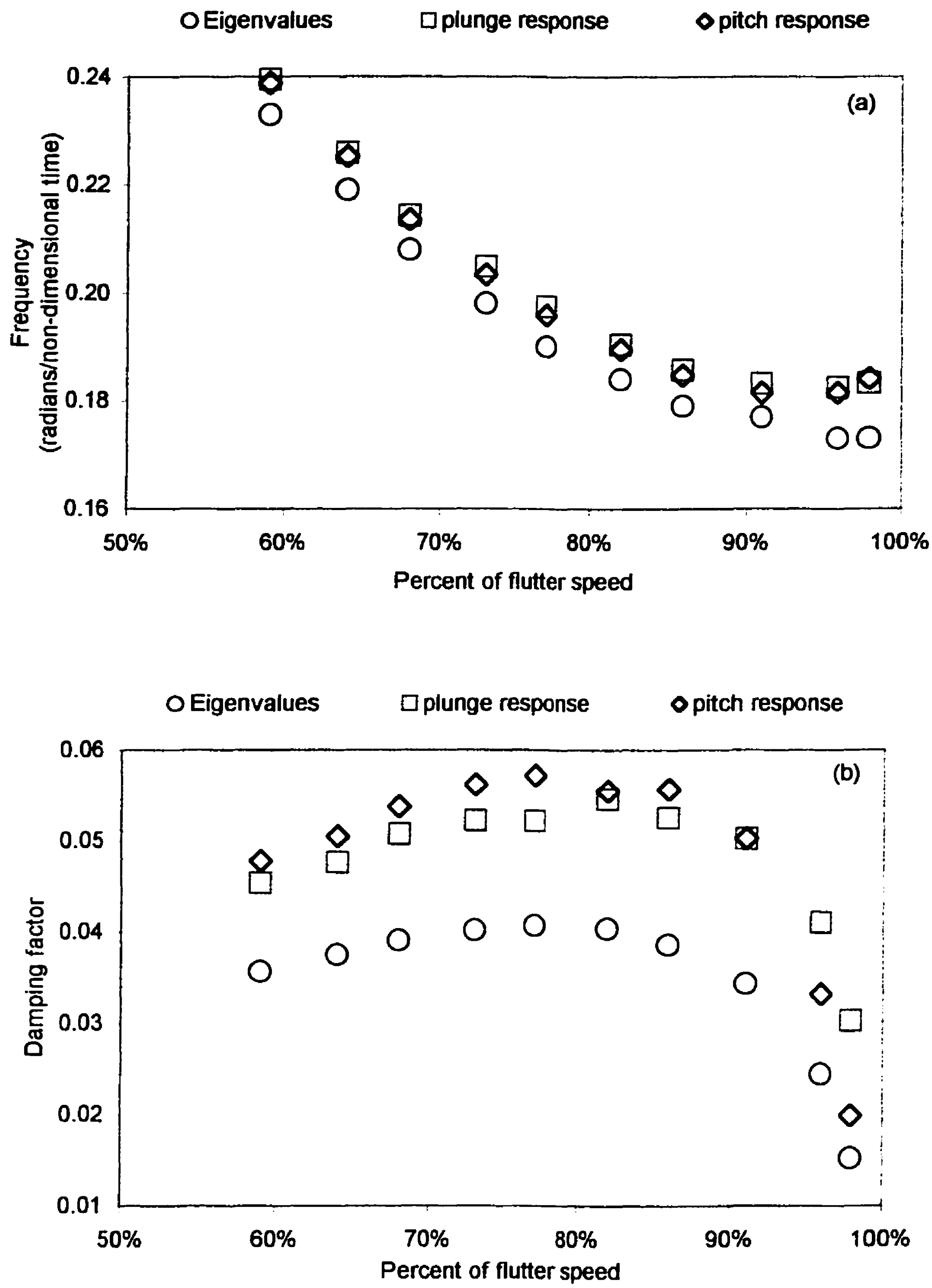

Figure 19. Comparison of the first mode damping and frequency estimates obtained using plunge and pitch response data at an increasing sweep-rate of .000024 radians/(non-dimensional second)^2, (a) frequency, (b) damping.

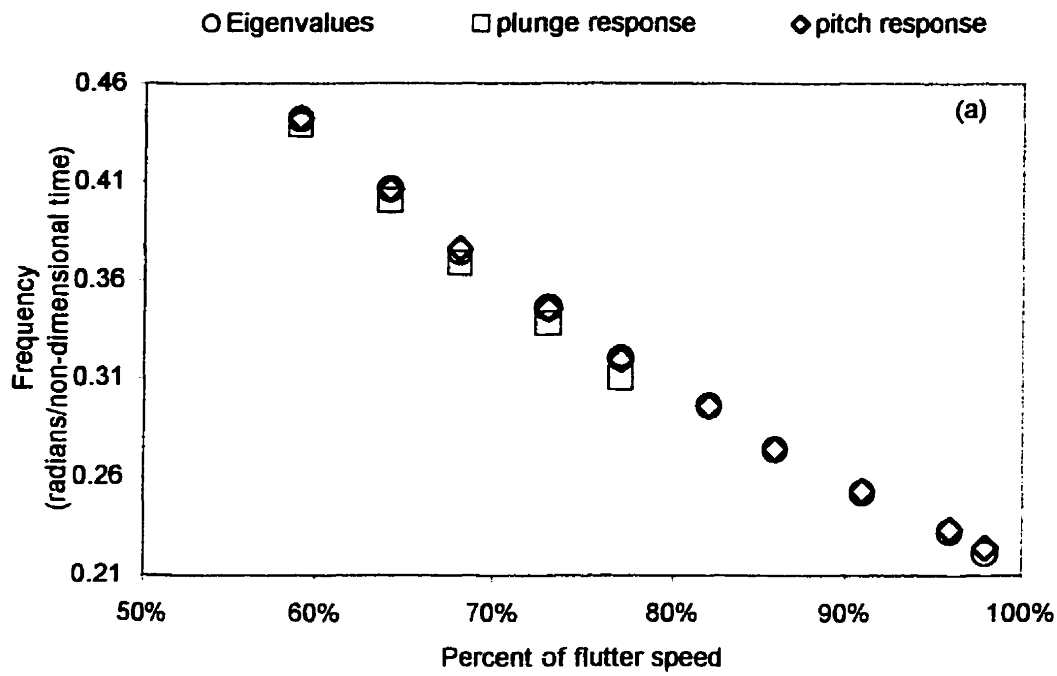

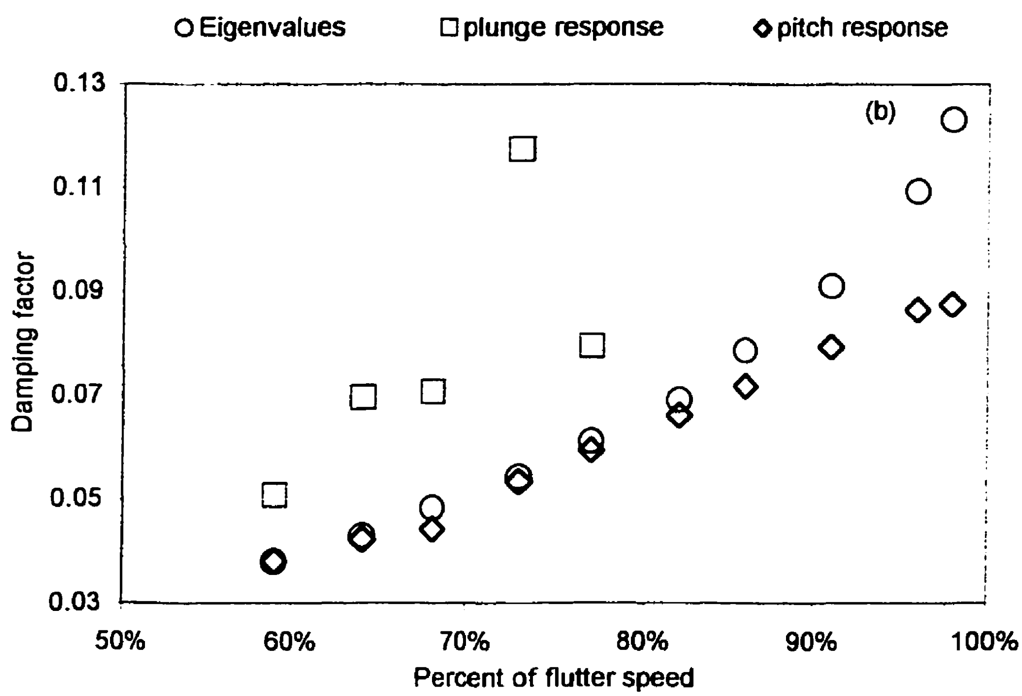

Figure 20. Comparison of the second mode damping and frequency estimates obtained using plunge and pitch response data at an increasing sweep-rate of .000003 radians/(non-dimensional second)^2, (a) frequency, (b) damping.

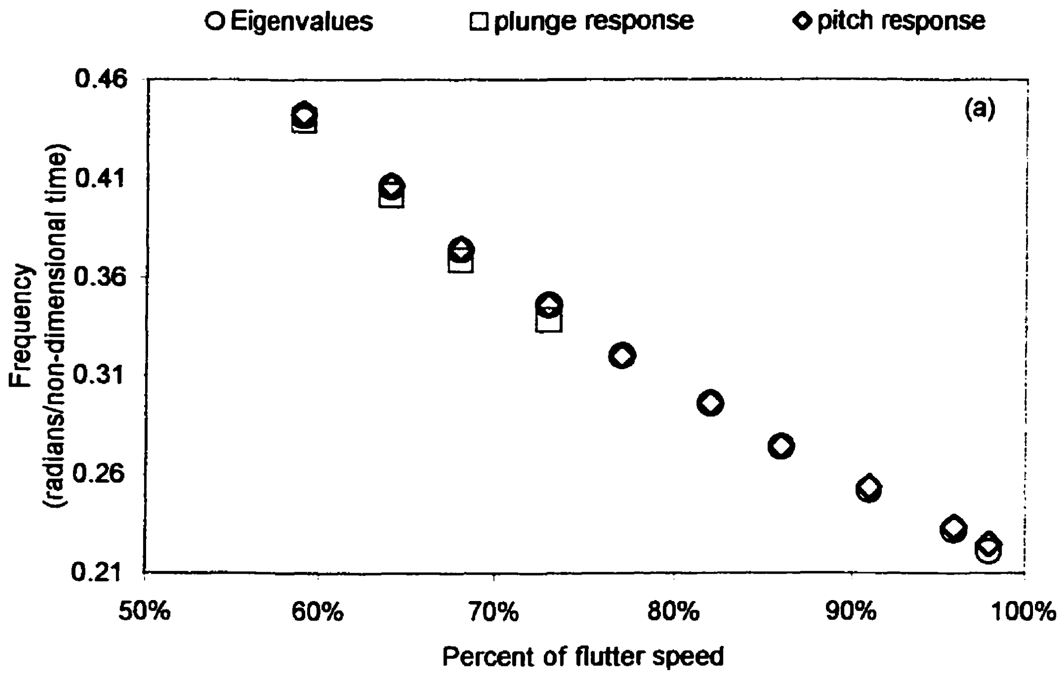

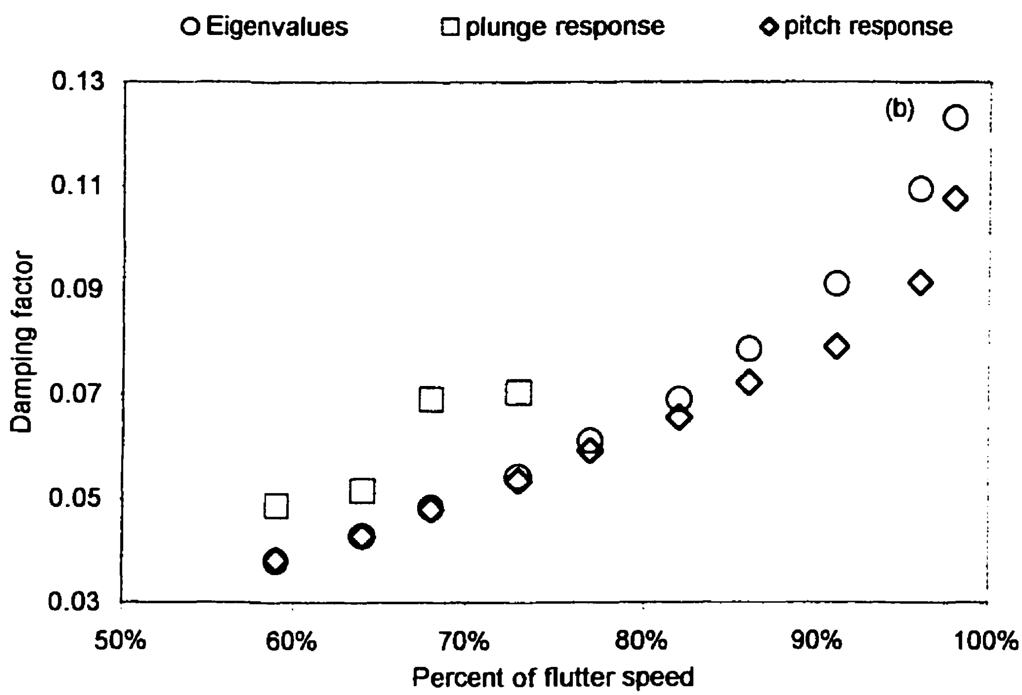

Figure 21. Comparison of the second mode damping and frequency estimates obtained using plunge and pitch response data at an increasing sweep-rate of .000006 radians/(non-dimensional second)^2, (a) frequency, (b) damping.

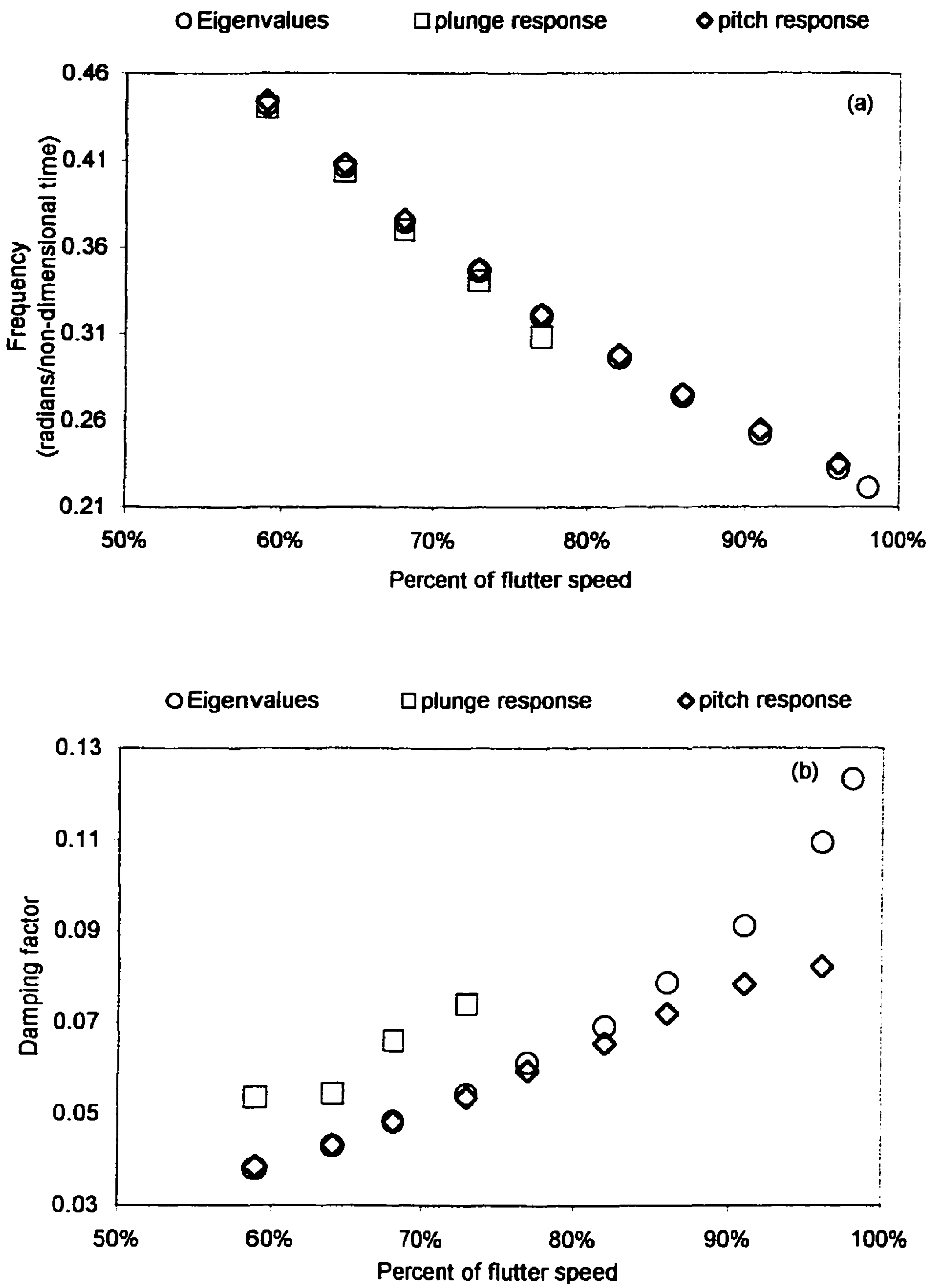

Figure 22. Comparison of the second mode damping and frequency estimates obtained using plunge and pitch response data at an increasing sweep-rate of .000012 radians/(non-dimensional second)^2, (a) frequency, (b) damping.

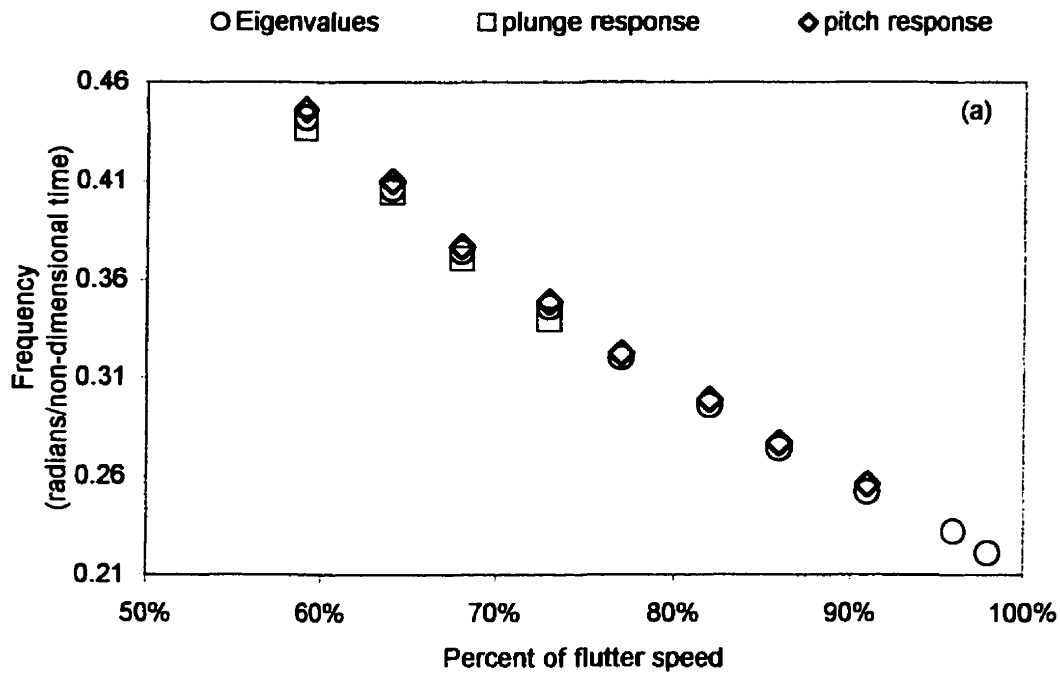

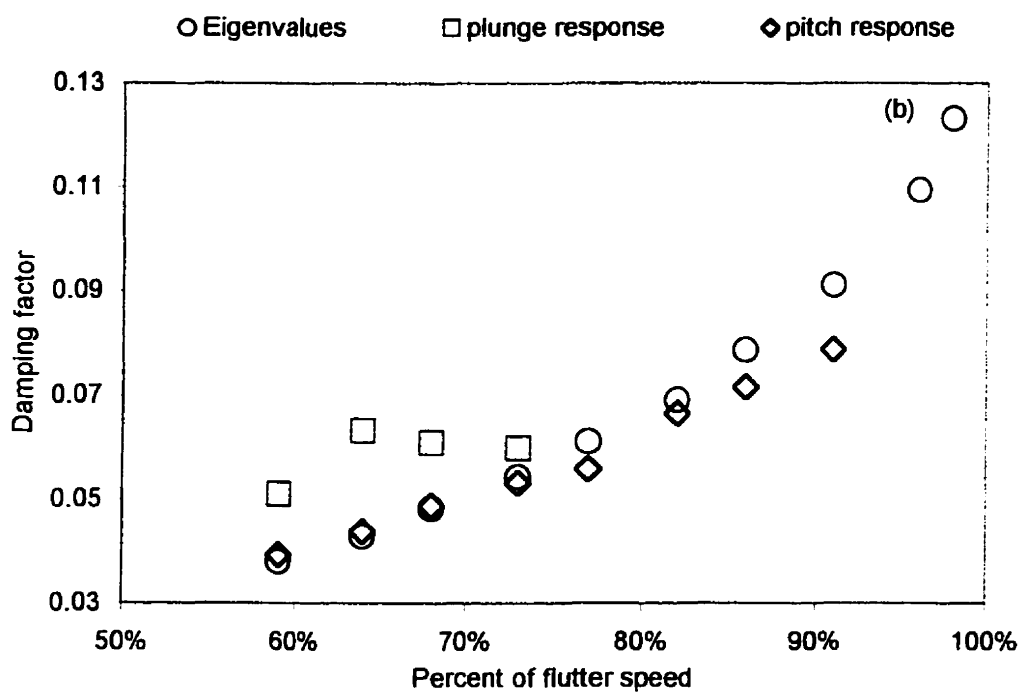

Figure 23. Comparison of the second mode damping and frequency estimates obtained using plunge and pitch response data at an increasing sweep-rate of .000024 radians/(non-dimensional second)^2, (a) frequency, (b) damping.

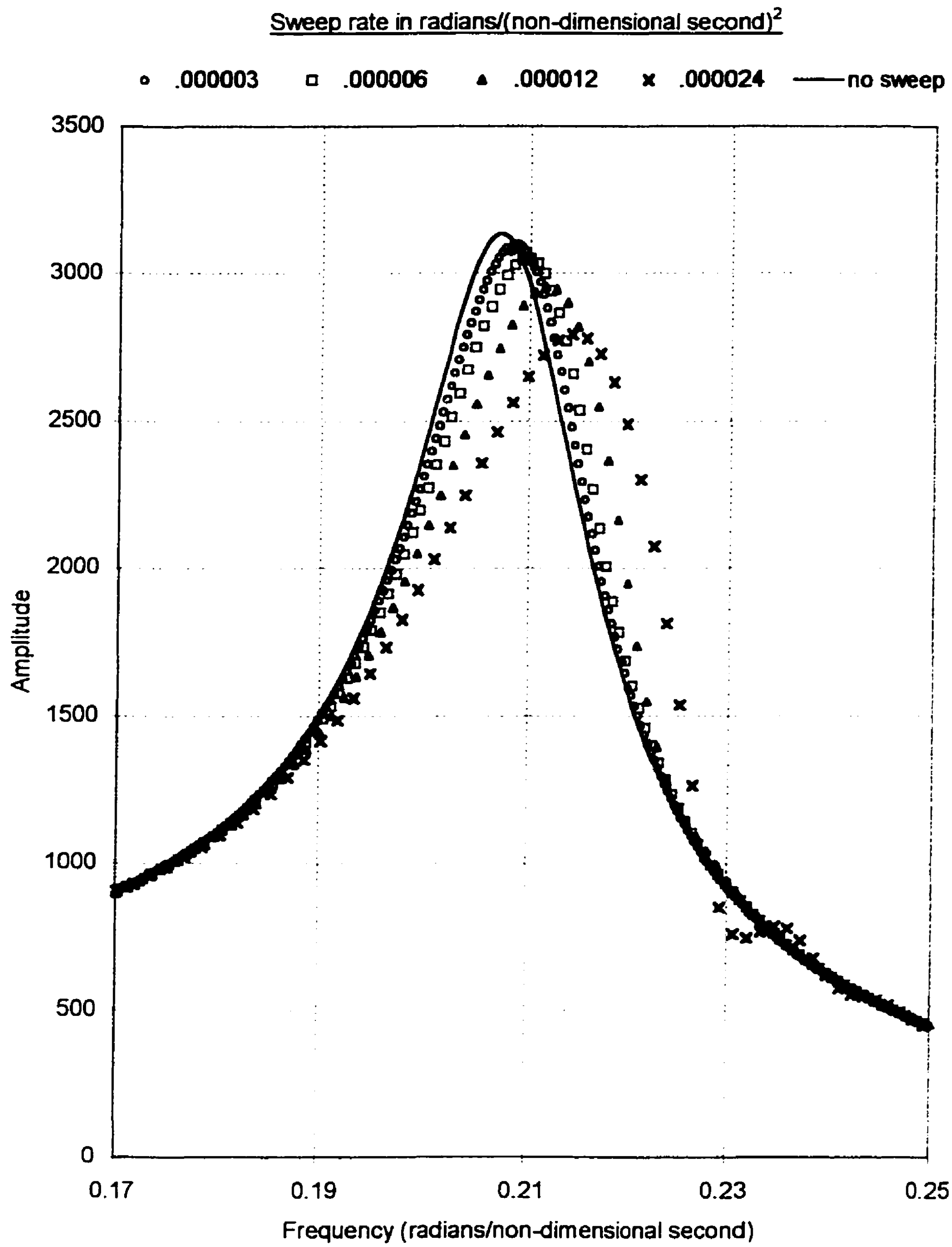

Figure 24. First mode transfer functions obtained from aerodynamic lift input and plunge response at 68% of the linear flutter speed, at four different sweep-rates and without sweep.

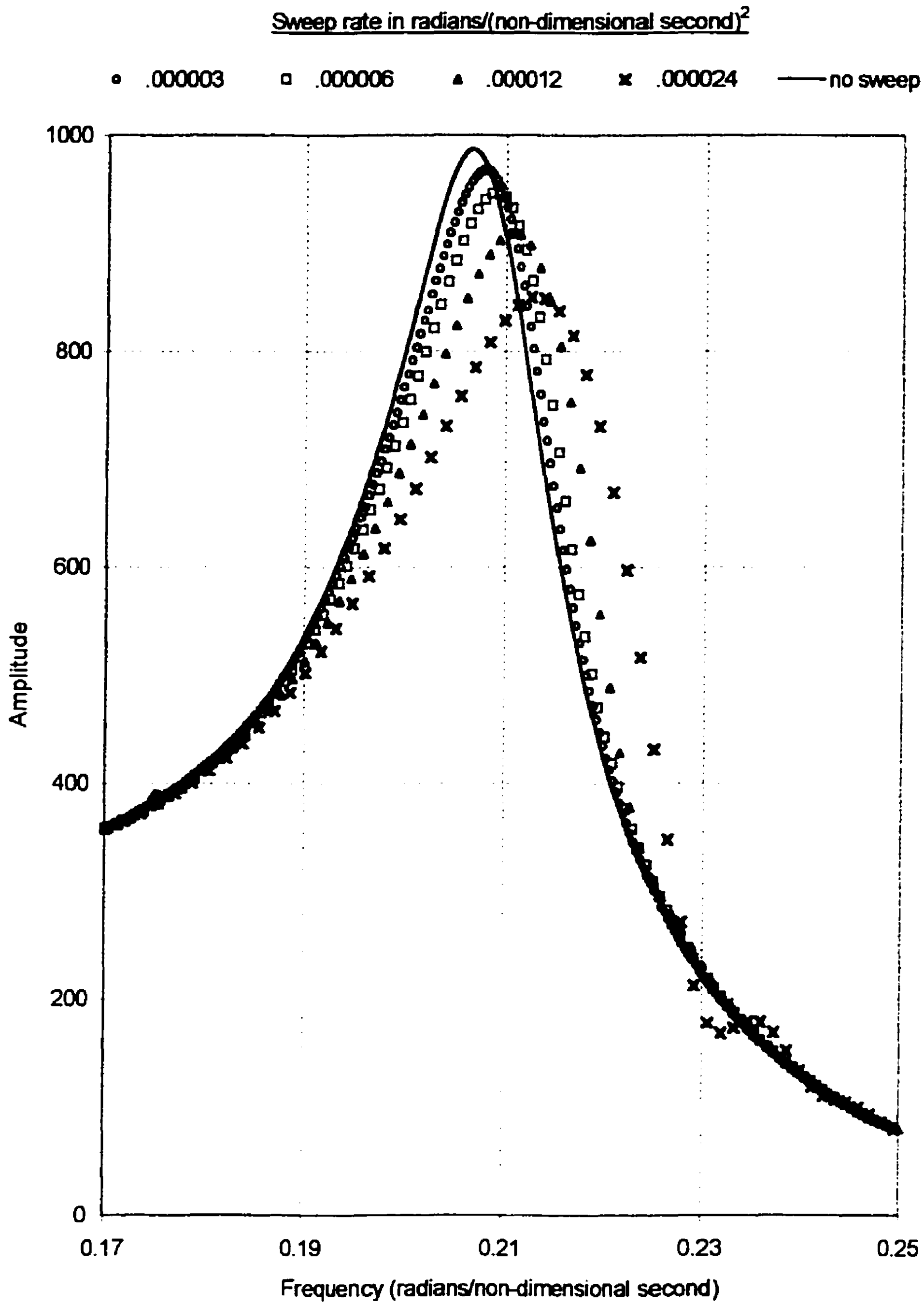

Figure 25. First mode frequency transfer functions obtained from aerodynamic moment input and pitch response at 68% of the linear flutter speed, at four different increasing sweep-rates and without sweep.

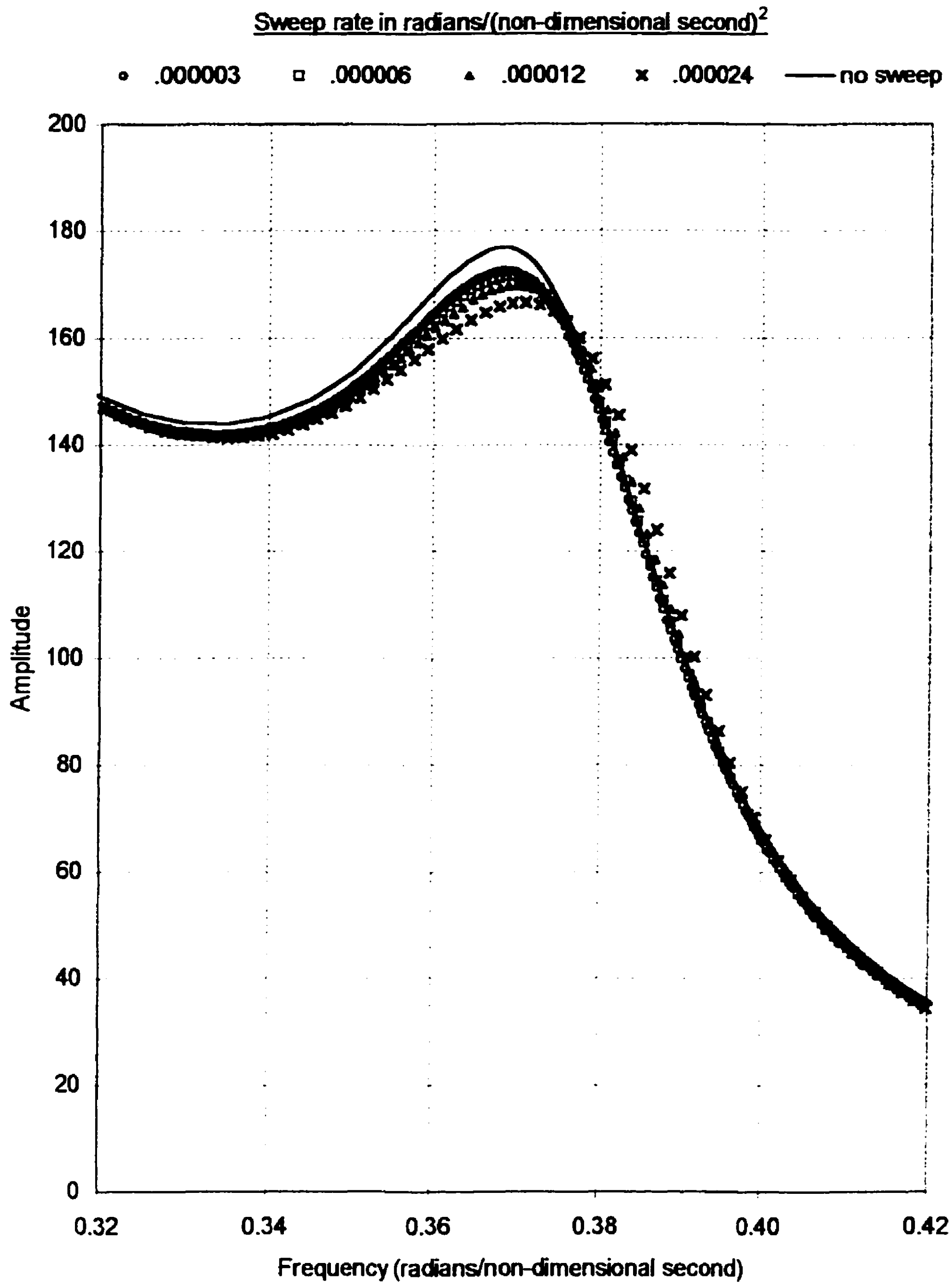

Figure 26. Second mode frequency transfer functions obtained from aerodynamic lift input and plunge response at 68% of the linear flutter speed, at four different increasing sweep-rates and without sweep.

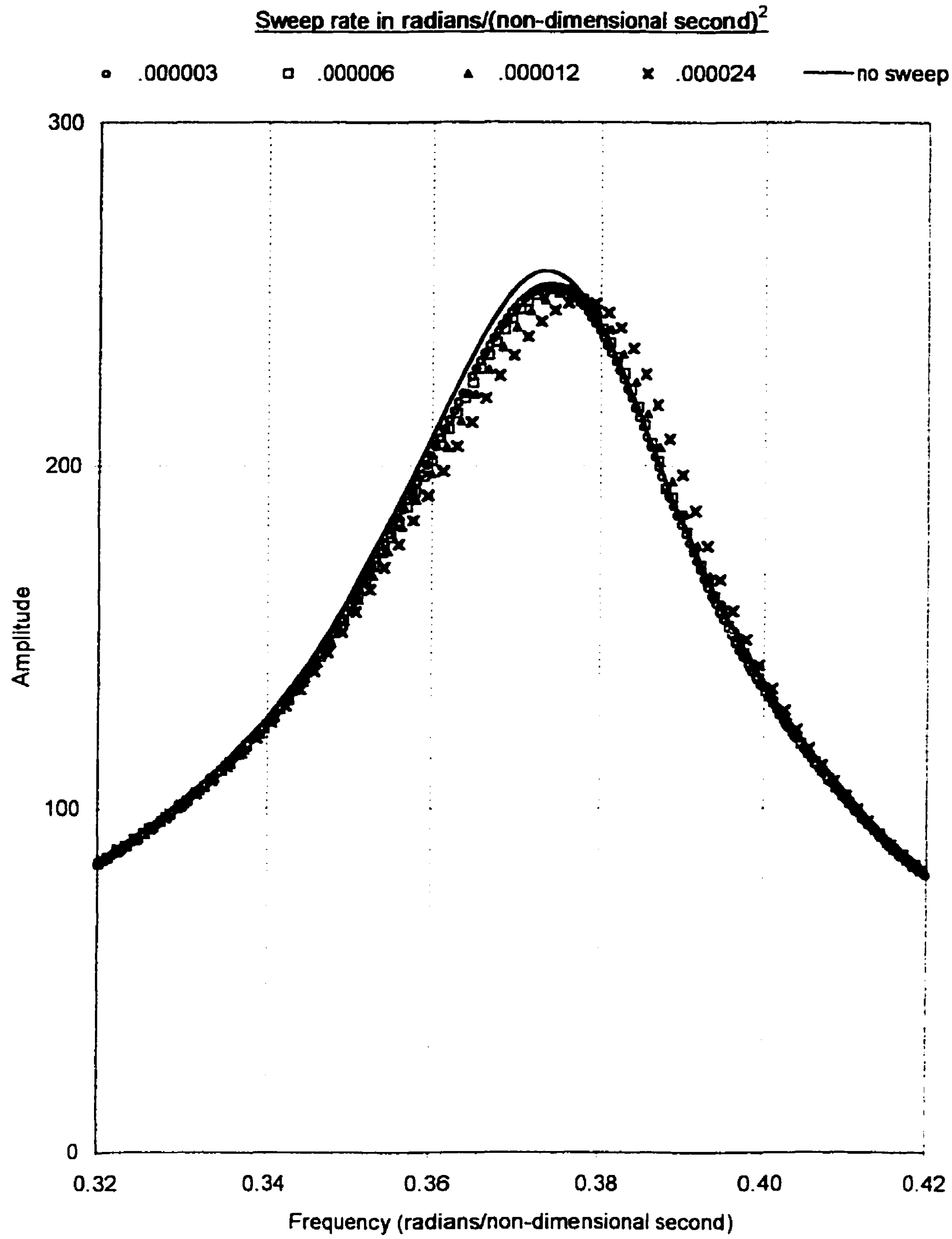

Figure 27. Second mode frequency transfer functions obtained from aerodynamic moment input and pitch response at 68% of the linear flutter speed, at four different increasing sweep-rates and without sweep.

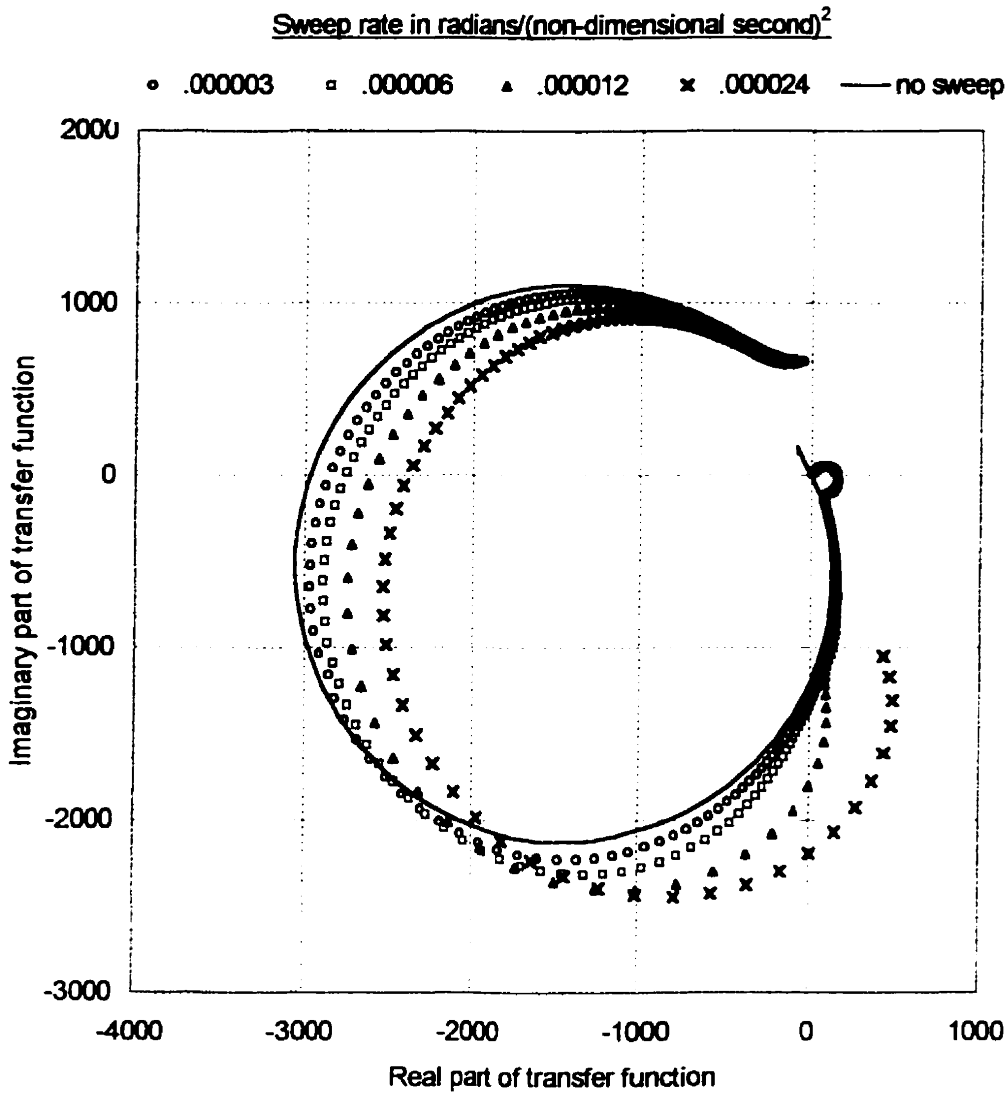

Figure 28. First mode Nyquist diagram obtained from aerodynamic lift input and plunge response at 68% of the linear flutter speed, at four different increasing sweep-rates and without sweep.

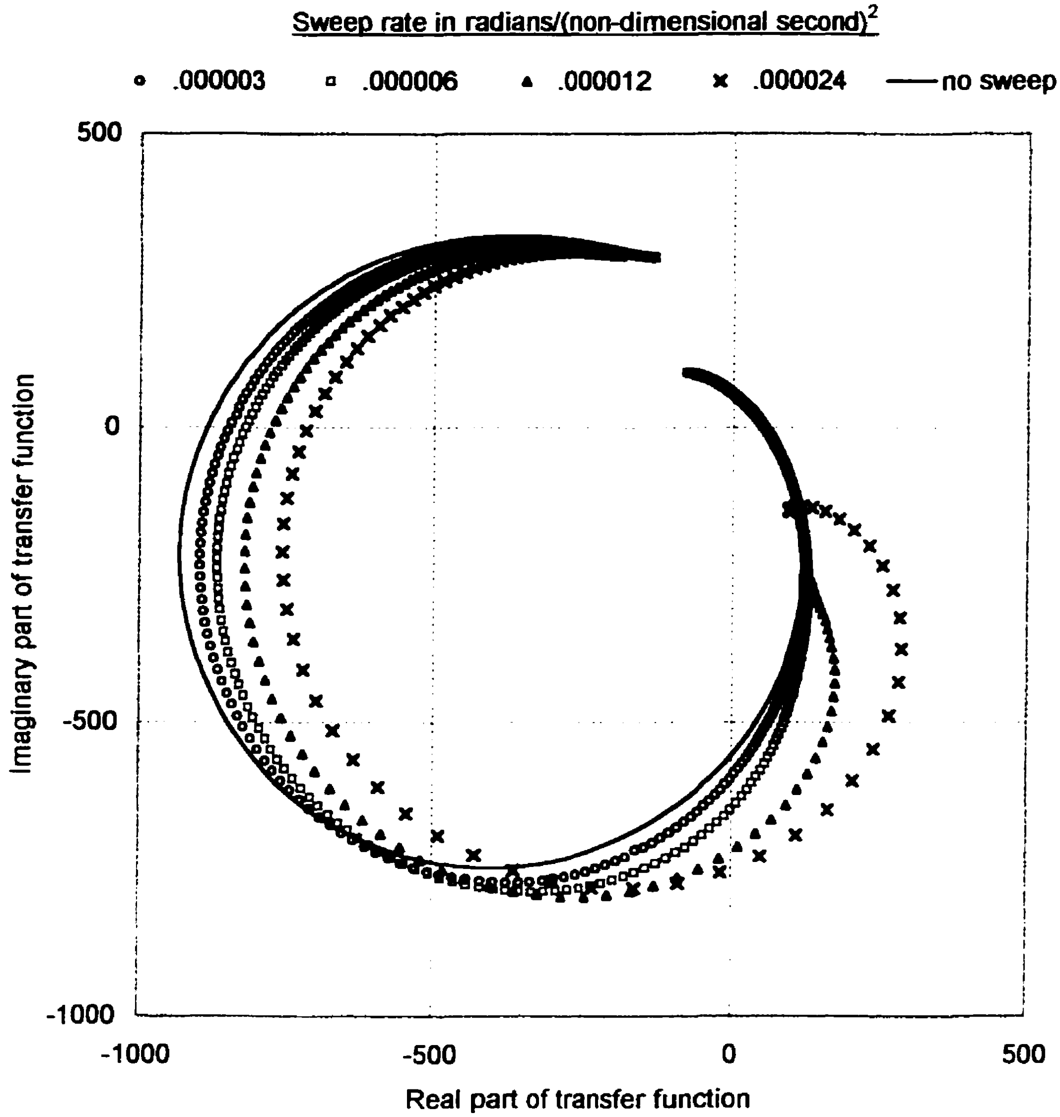

Figure 29. First mode Nyquist diagram obtained from aerodynamic moment input and pitch response at 68% of the linear flutter speed, at four increasing sweep-rates and without sweep.

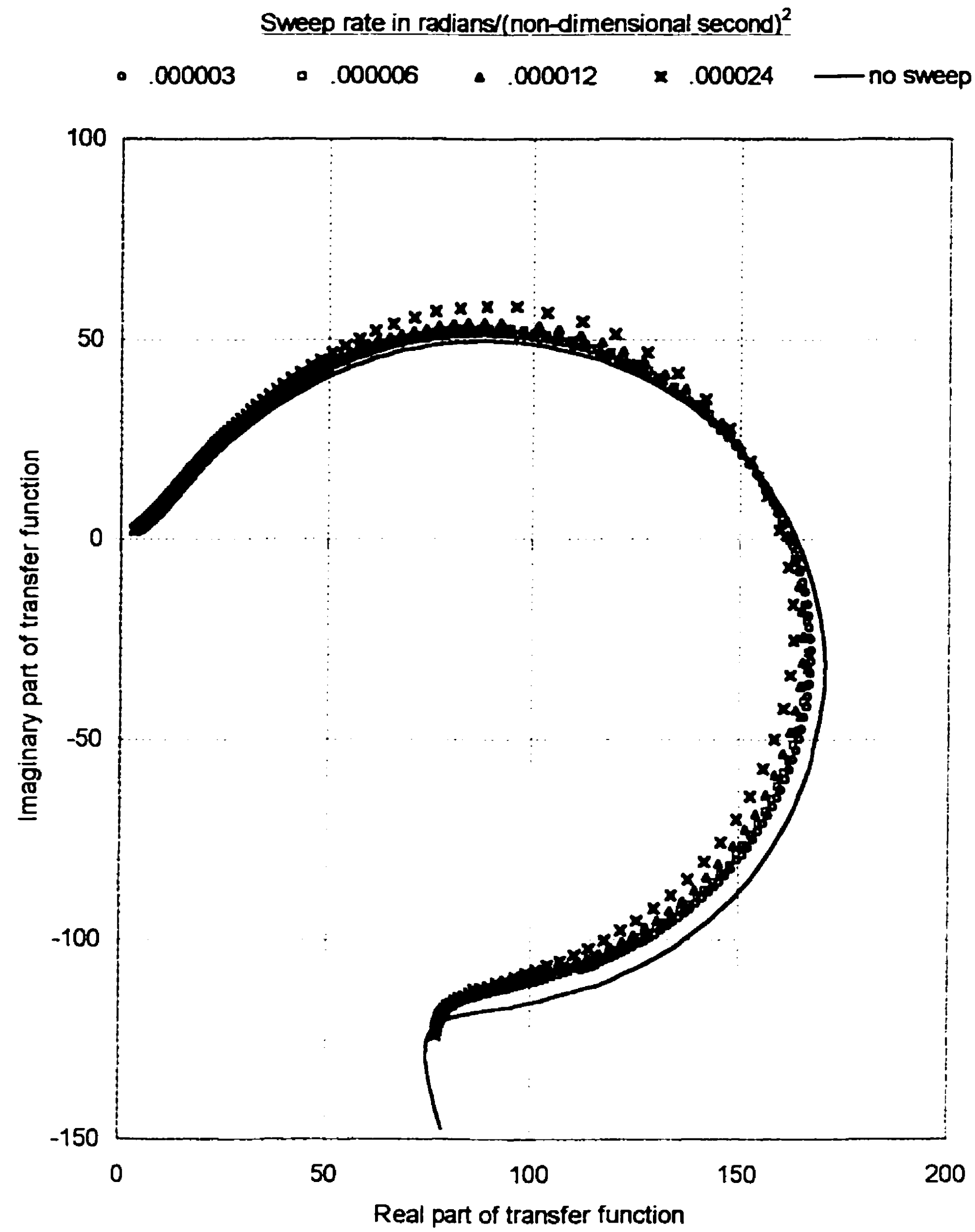

Figure 30. Second mode Nyquist diagram obtained from aerodynamic lift input and plunge response at 68% of the linear flutter speed, at four increasing sweep-rates and without sweep.

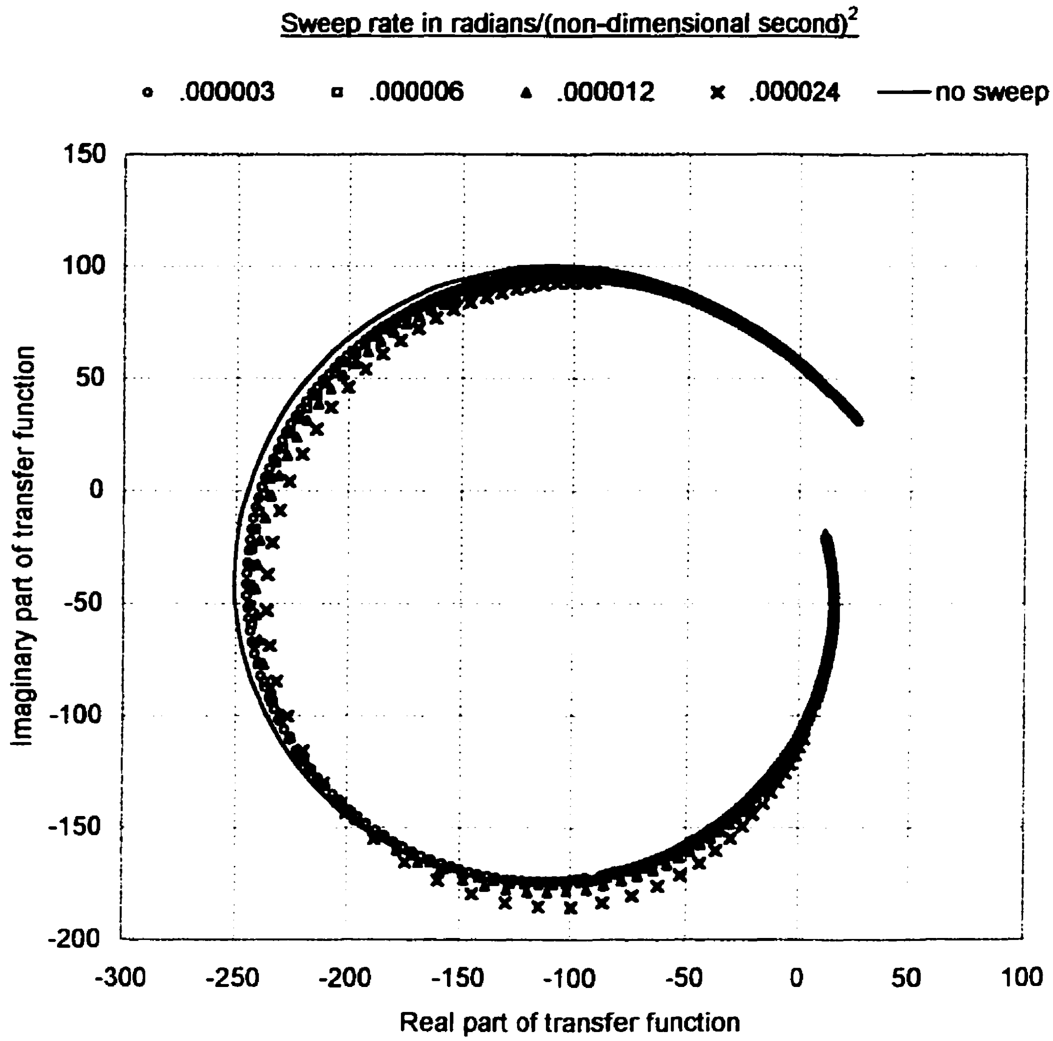

Figure 31. Second mode Nyquist diagram obtained from aerodynamic moment input and pitch response at 68% of the linear flutter speed, at four increasing sweep-rates and without sweep.

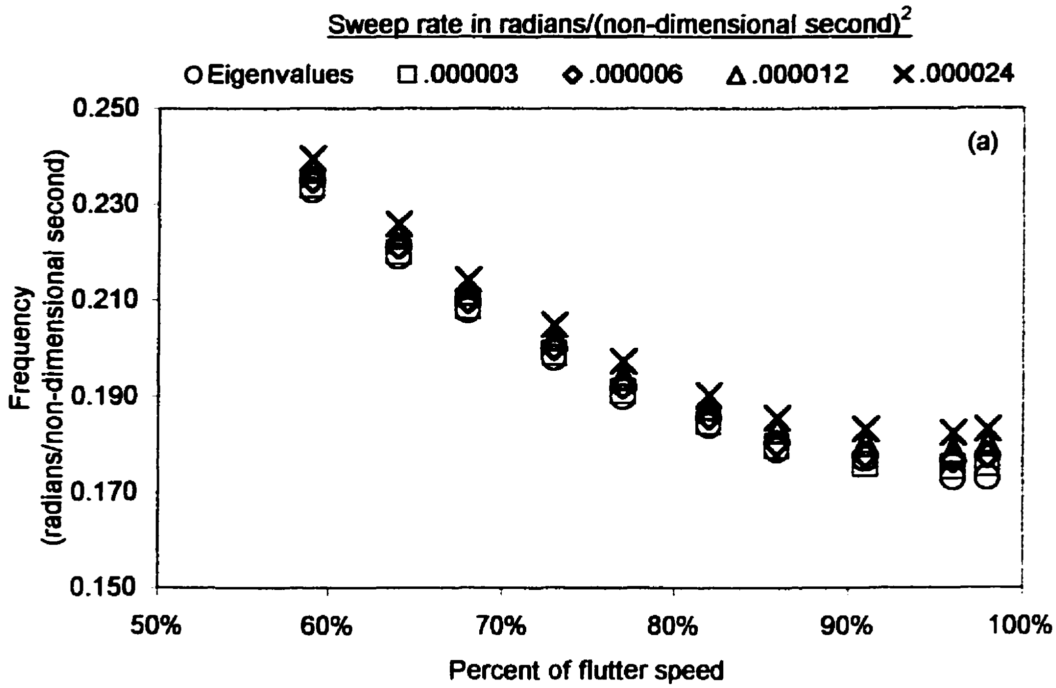

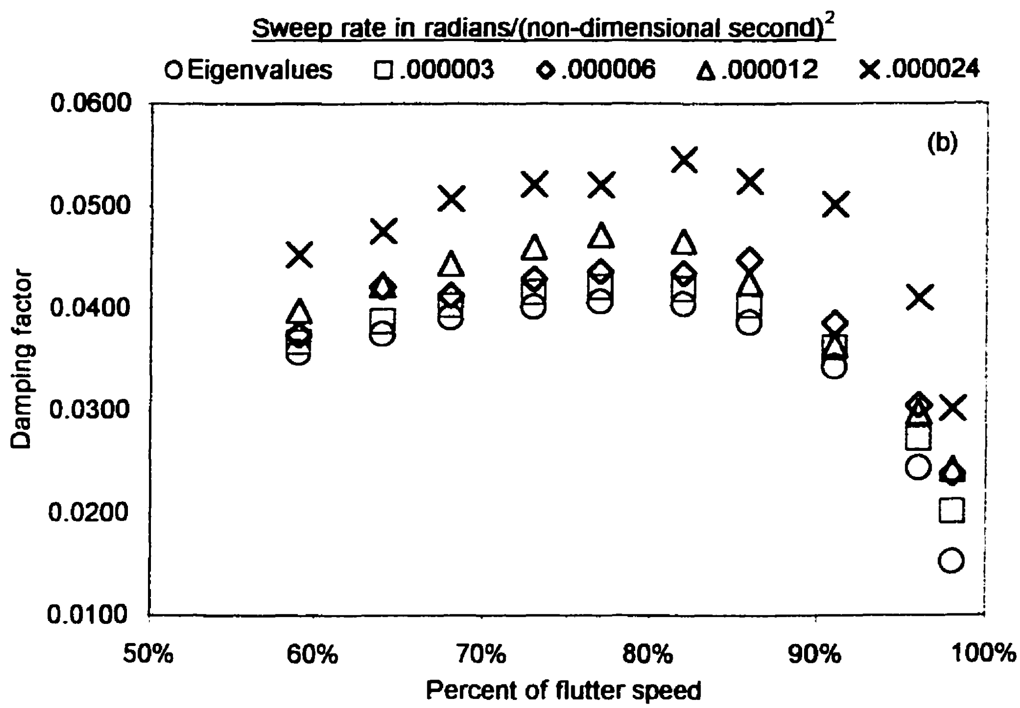

Figure 32. Effect of sweep-rate on the first mode damping and frequency estimates obtained using plunge response to an increasing frequency sweep, (a) frequency, (b) damping.

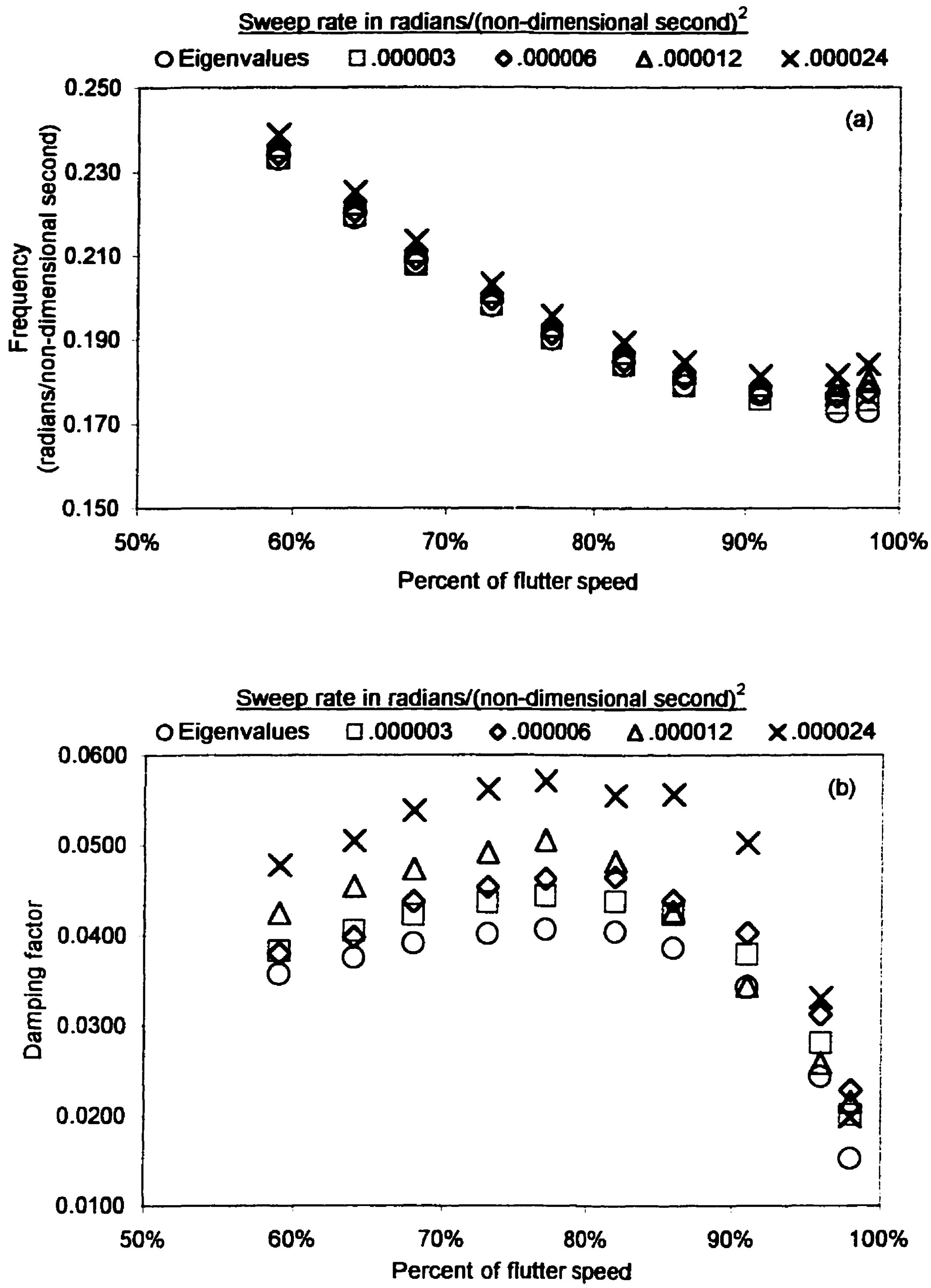

Figure 33. Effect of sweep rate on the first mode damping and frequency estimates obtained using pitch response to an increasing frequency sweep. (a) frequency, (b) damping.

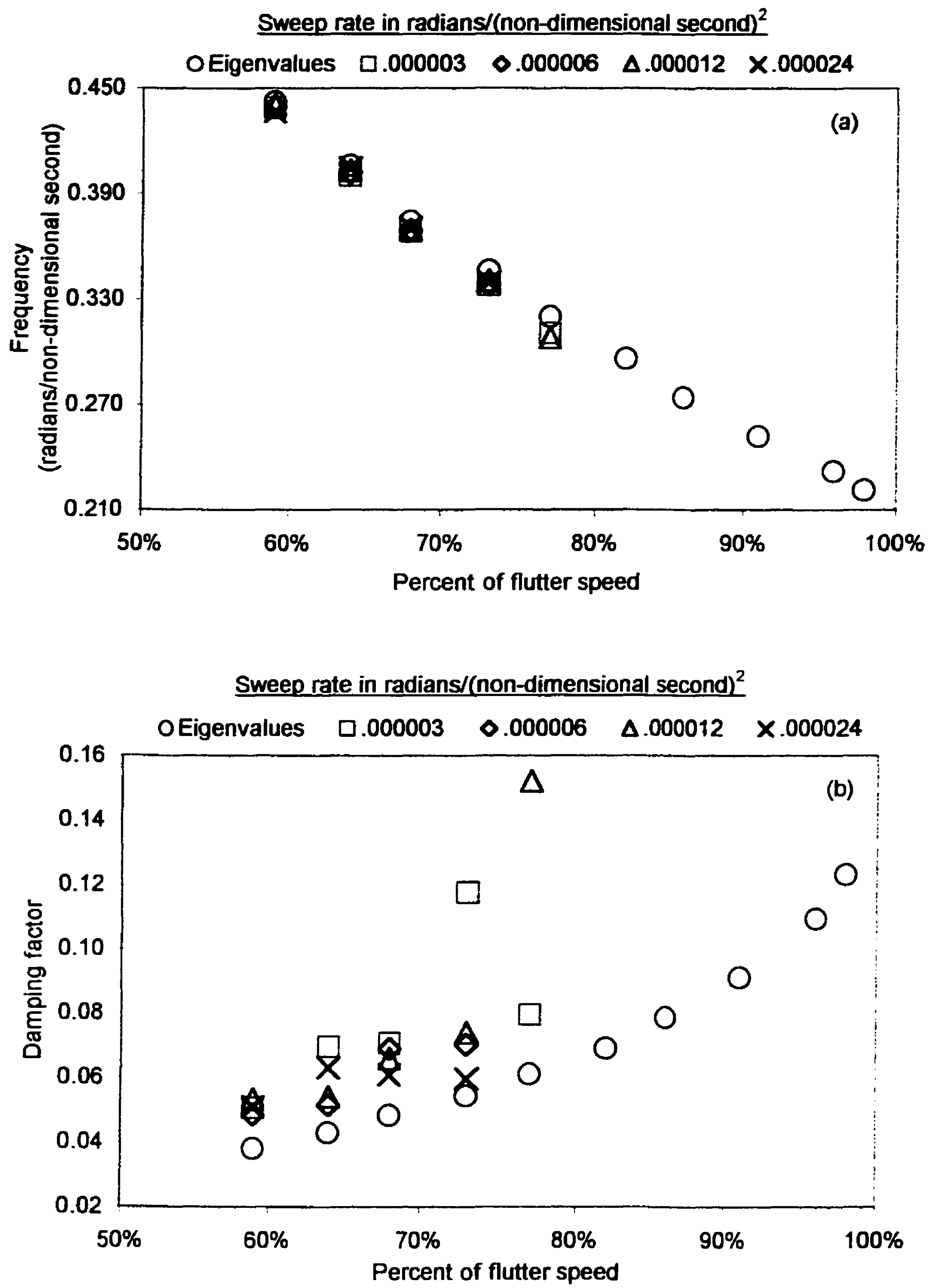

Figure 34. Effect of sweep rate on the second mode damping and frequency estimates obtained using plunge response to an increasing frequency sweep, (a) frequency, (b) damping.

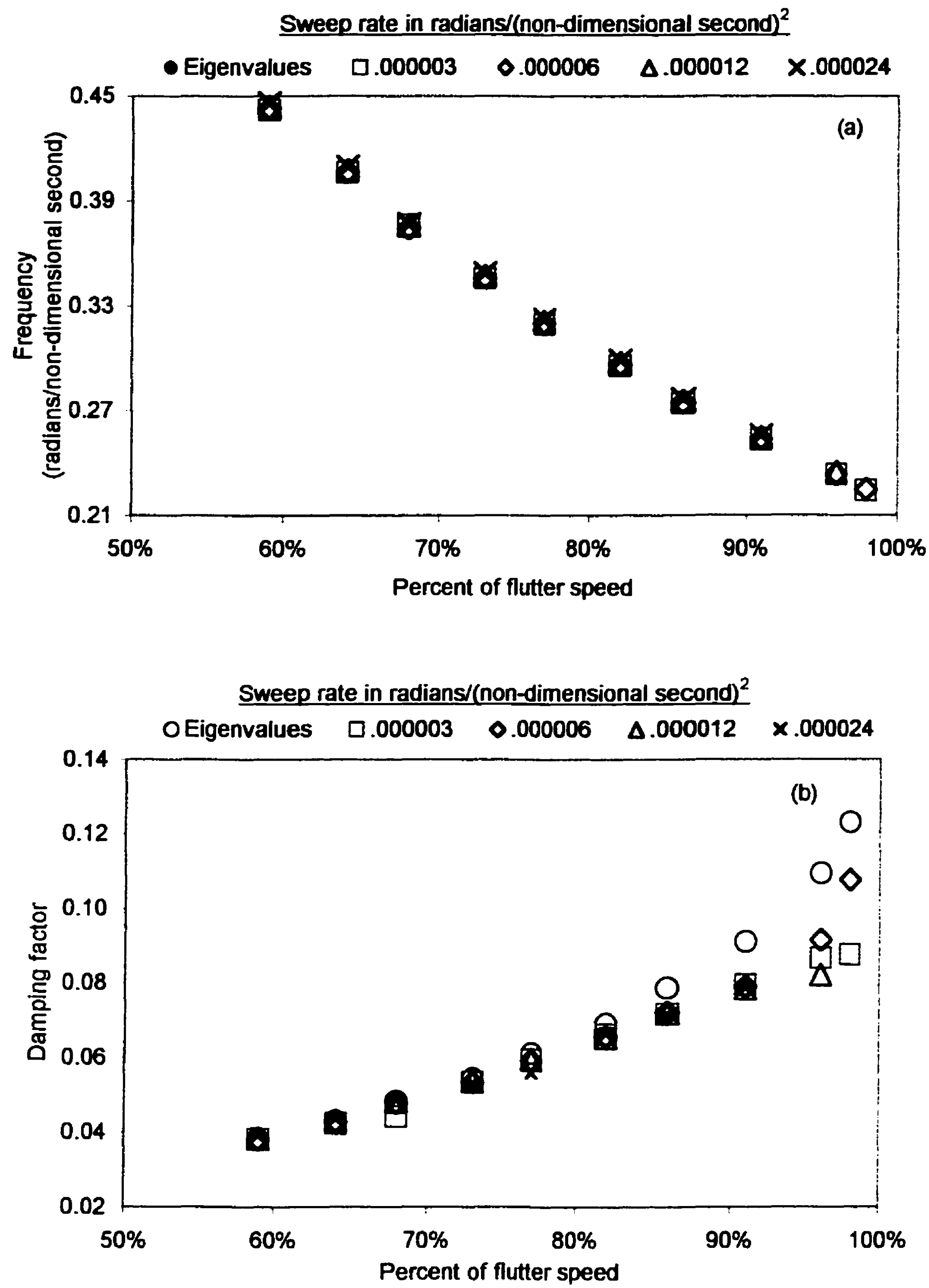

Figure 35. Effect of sweep rate on the second mode damping and frequency estimates obtained using pitch response to an increasing frequency sweep, (a) frequency,(b) damping.

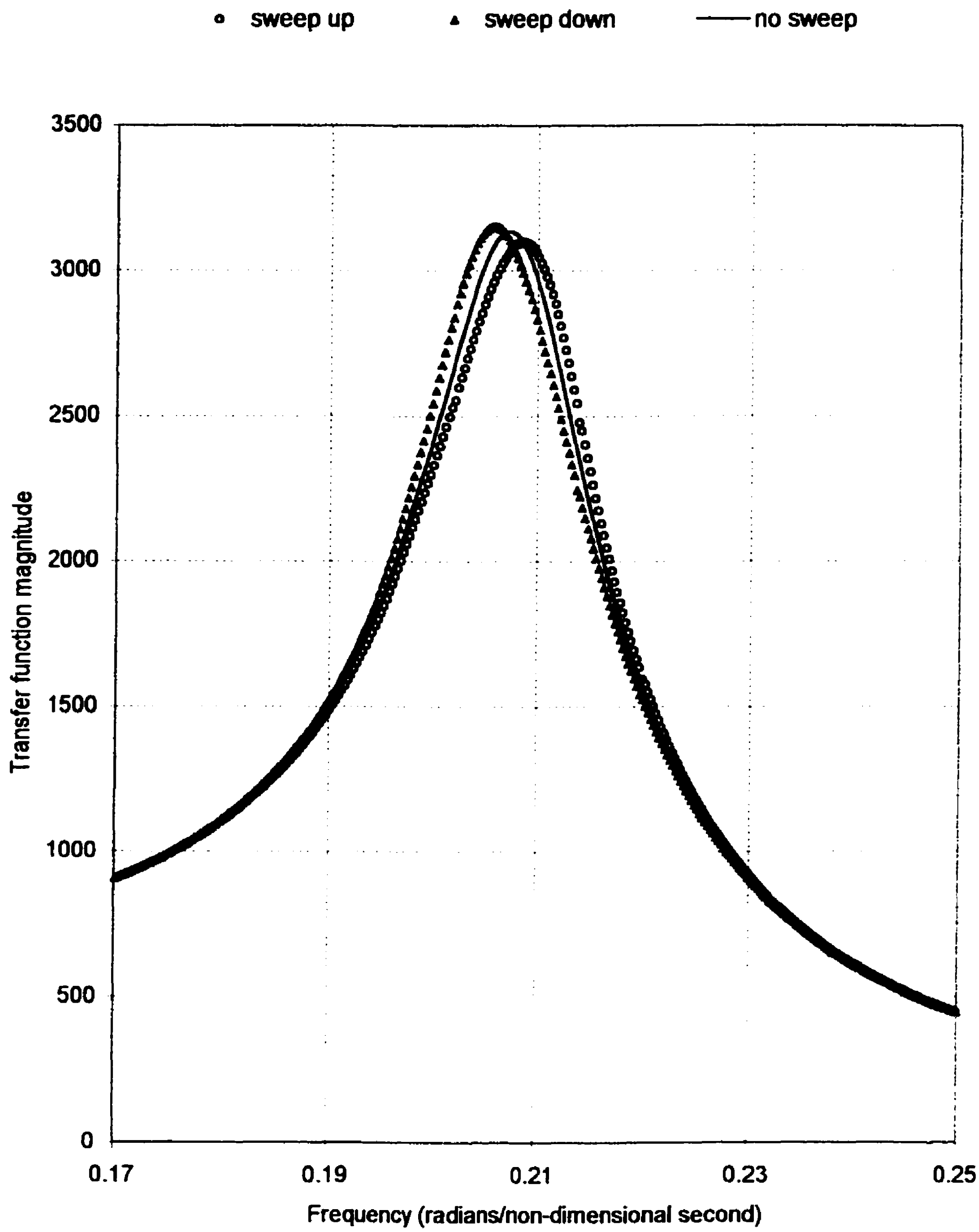

Figure 36. First mode frequency transfer functions for increasing and decreasing sweep-rates. Aerodynamic lift input and plunge response at 68% of the linear flutter speed and a sweep-rate of .000003 radians/(non-dimensional second)^2.

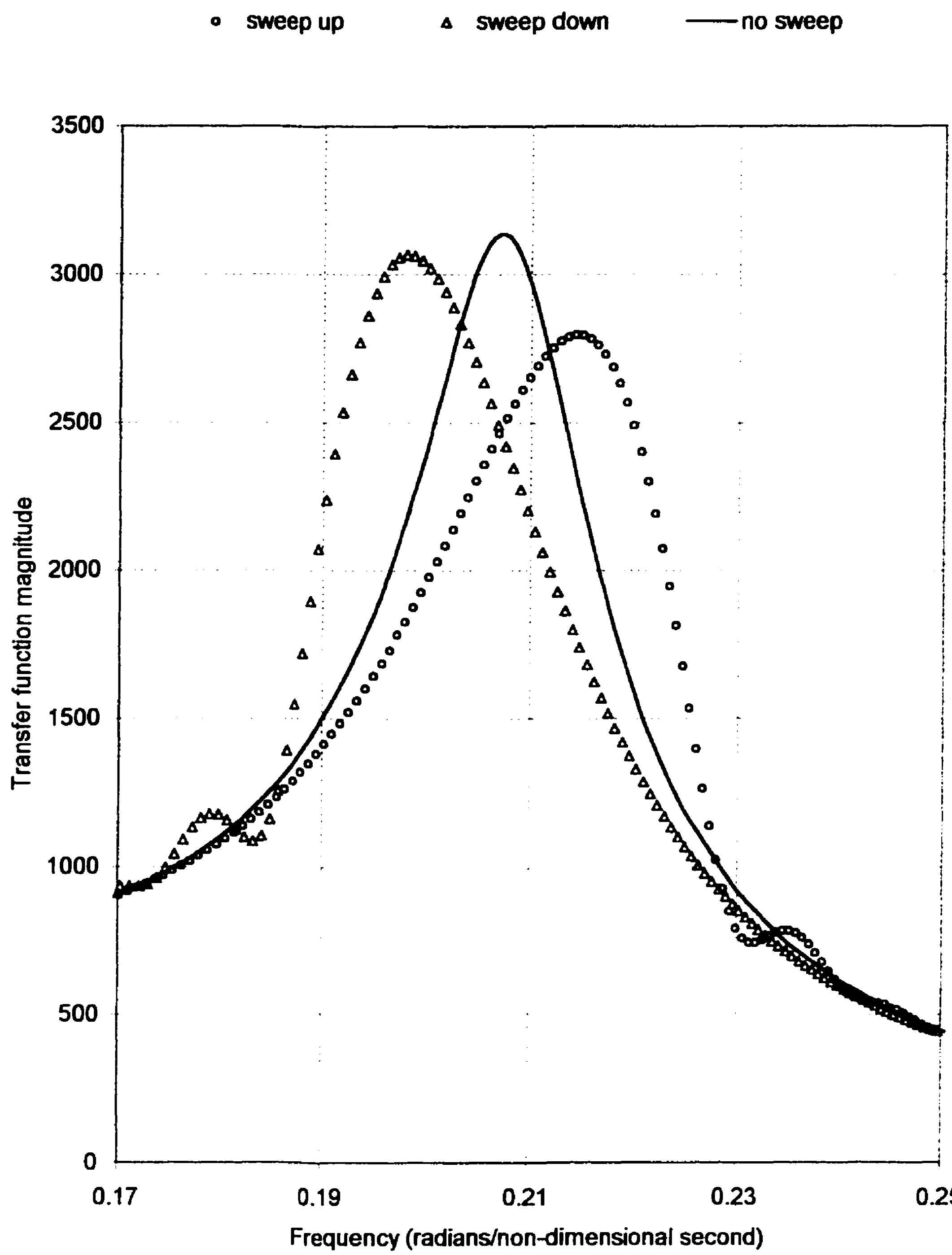

Figure 37. First mode frequency transfer functions for increasing and decreasing sweep rates. Aerodynamic lift input and plunge response at 68% of the linear flutter speed and a sweep-rate of .000024 radians/(non-dimensional second)^2.

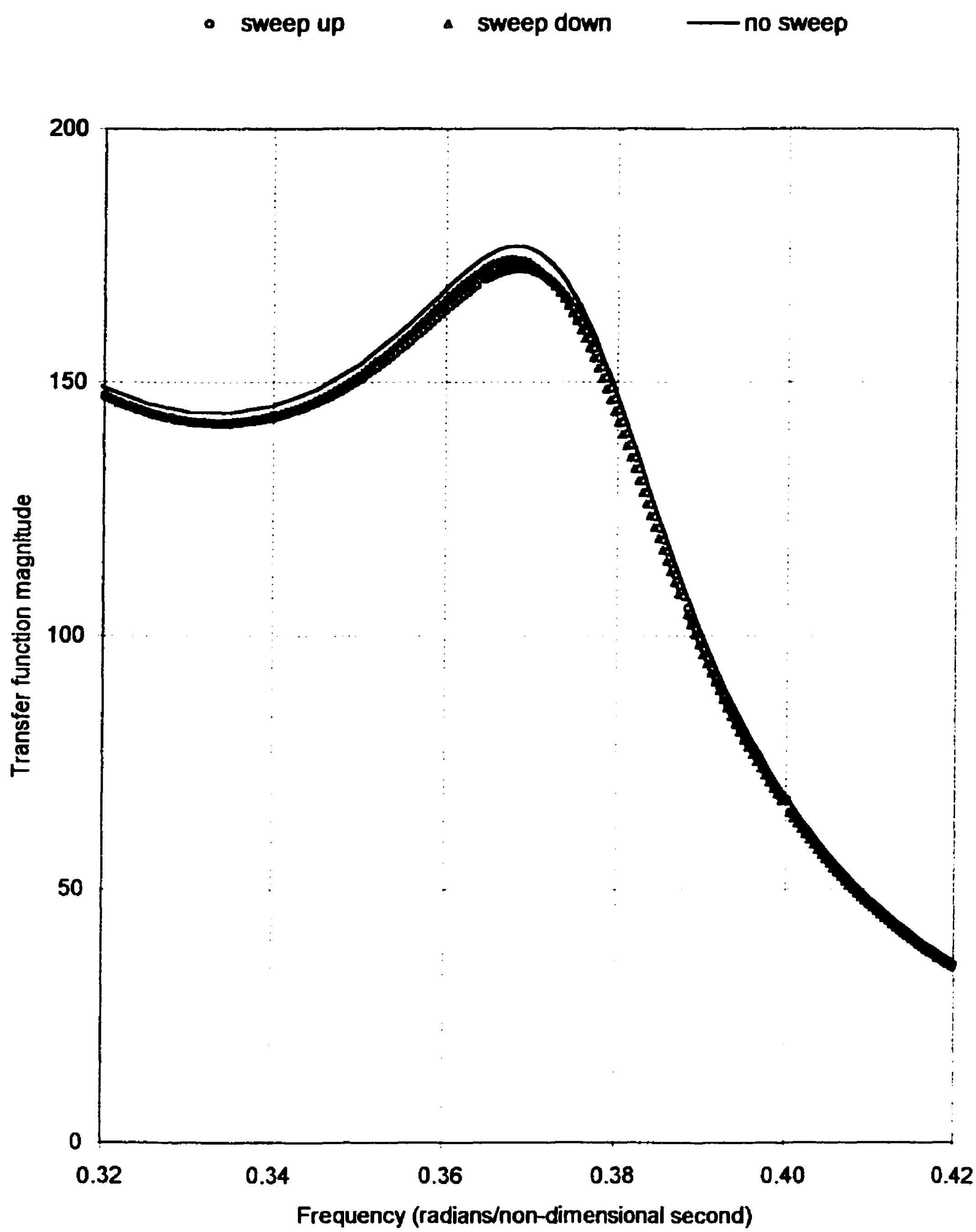

Figure 38. Second mode frequency transfer functions at increasing and decreasing sweep rates. Aerodynamic lift input and plunge response at 68% of the linear flutter speed and a sweep-rate of .000003 radians/(non-dimensional second)^2.

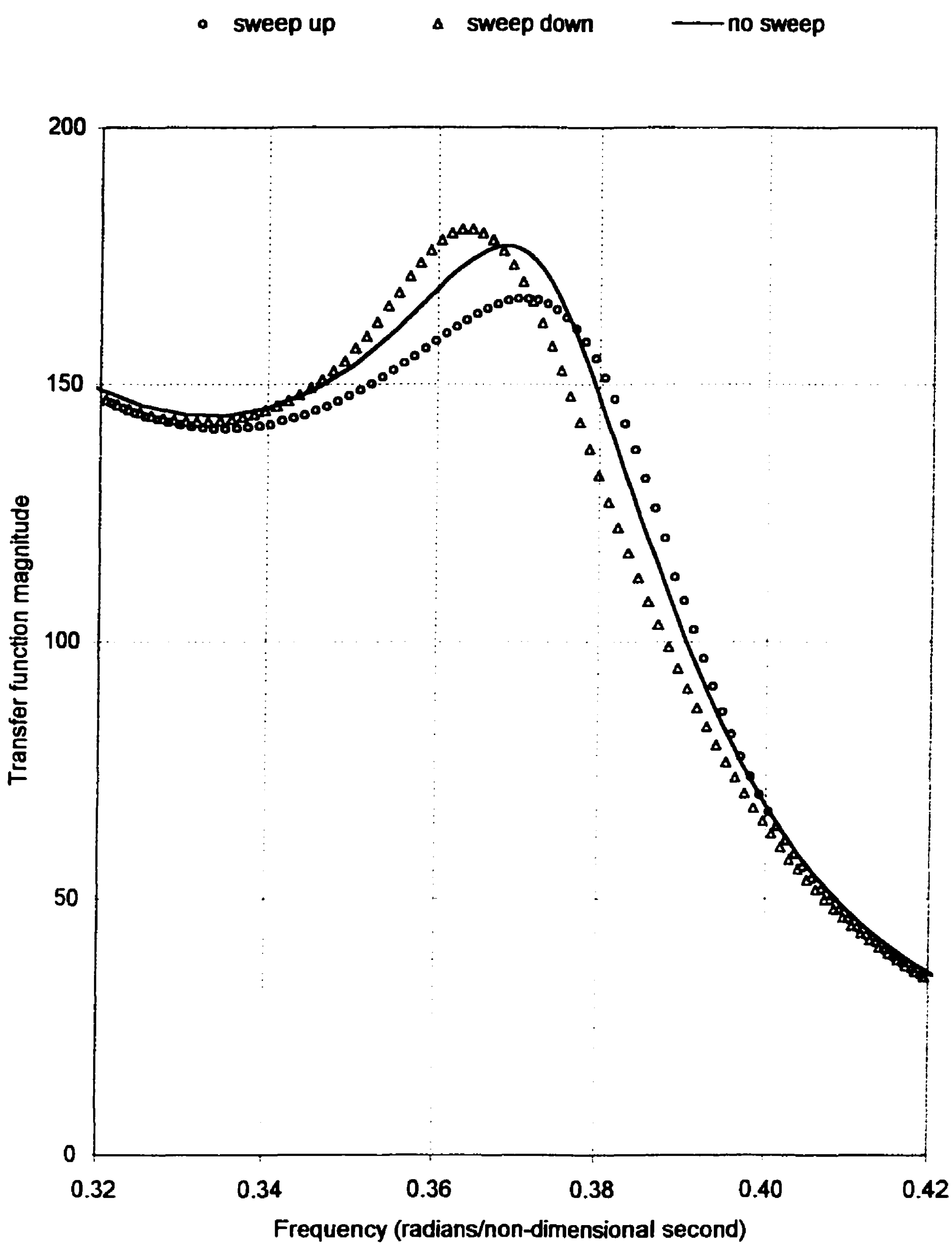

Figure 39. Second mode frequency transfer functions at increasing and decreasing sweep rates. Aerodynamic lift input and plunge response at 68% of the linear flutter speed and a sweep-rate of .000024 radians/(non-dimensional second)^2.

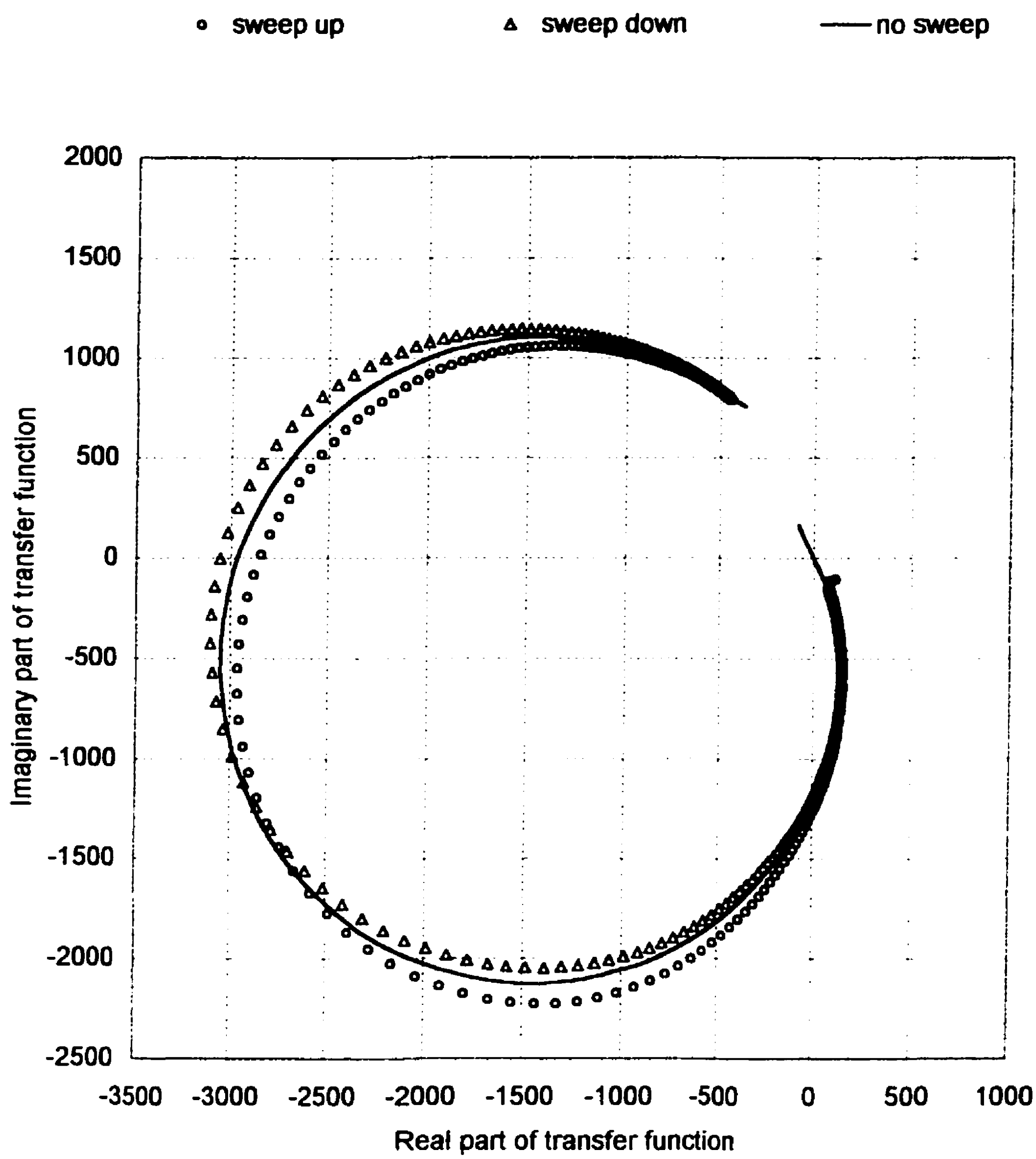

Figure 40. First mode Nyquist diagrams for increasing and decreasing sweep-rates. Aerodynamic lift input and plunge response at 68% of the linear flutter speed and a sweep-rate of .000003 radians/(non-dimensional second)^2.

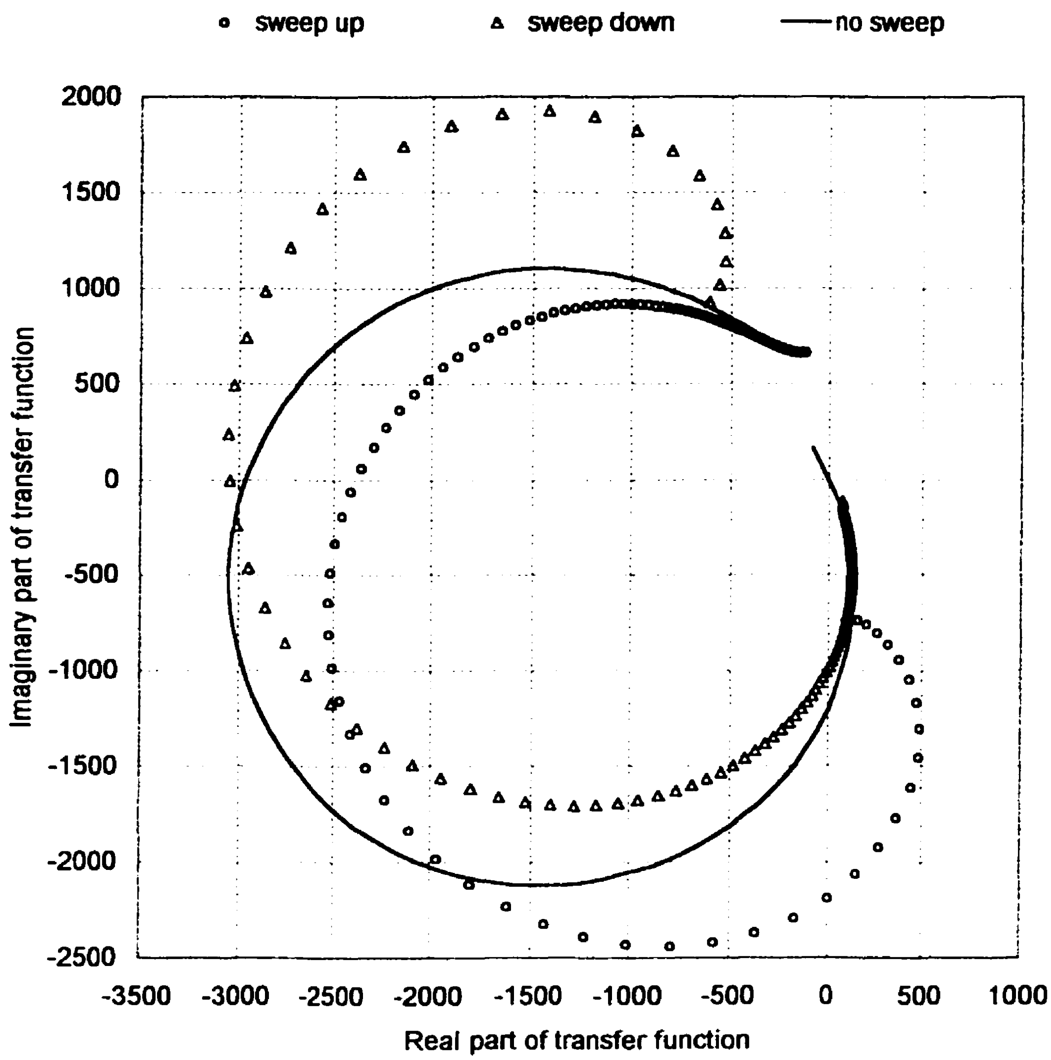

Figure 41. First mode Nyquist diagrams for increasing and decreasing sweep-rates. Aerodynamic lift input and plunge response at 68% of the linear flutter speed and a sweep-rate of .000024 radians/(non-dimensional second)^2.

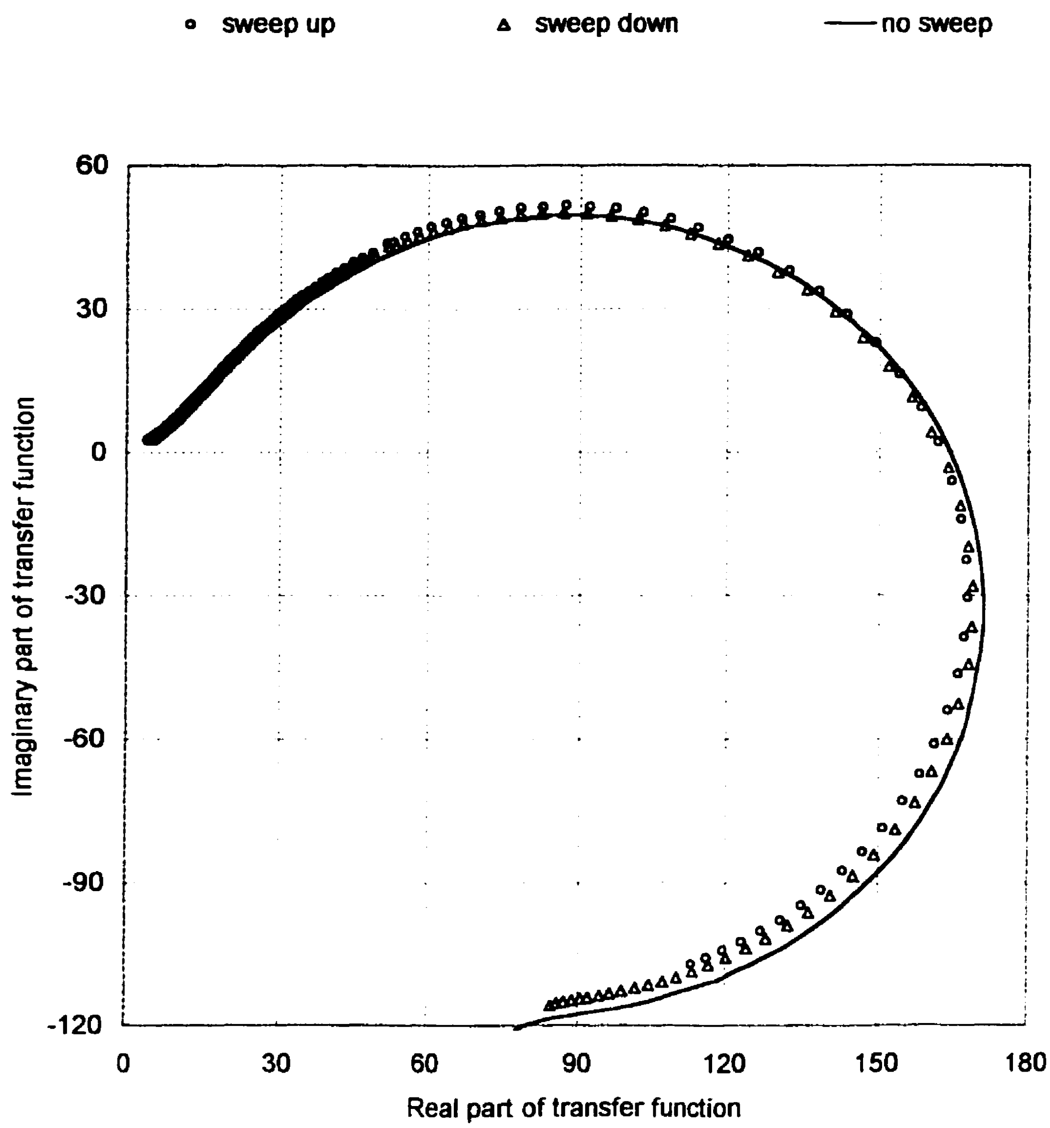

Figure 42. Second mode Nyquist diagrams for increasing and decreasing sweep-rates. Aerodynamic lift input and plunge response at 68% of the linear flutter speed and a sweep-rate of .000003 radians/(non-dimensional second)^2.

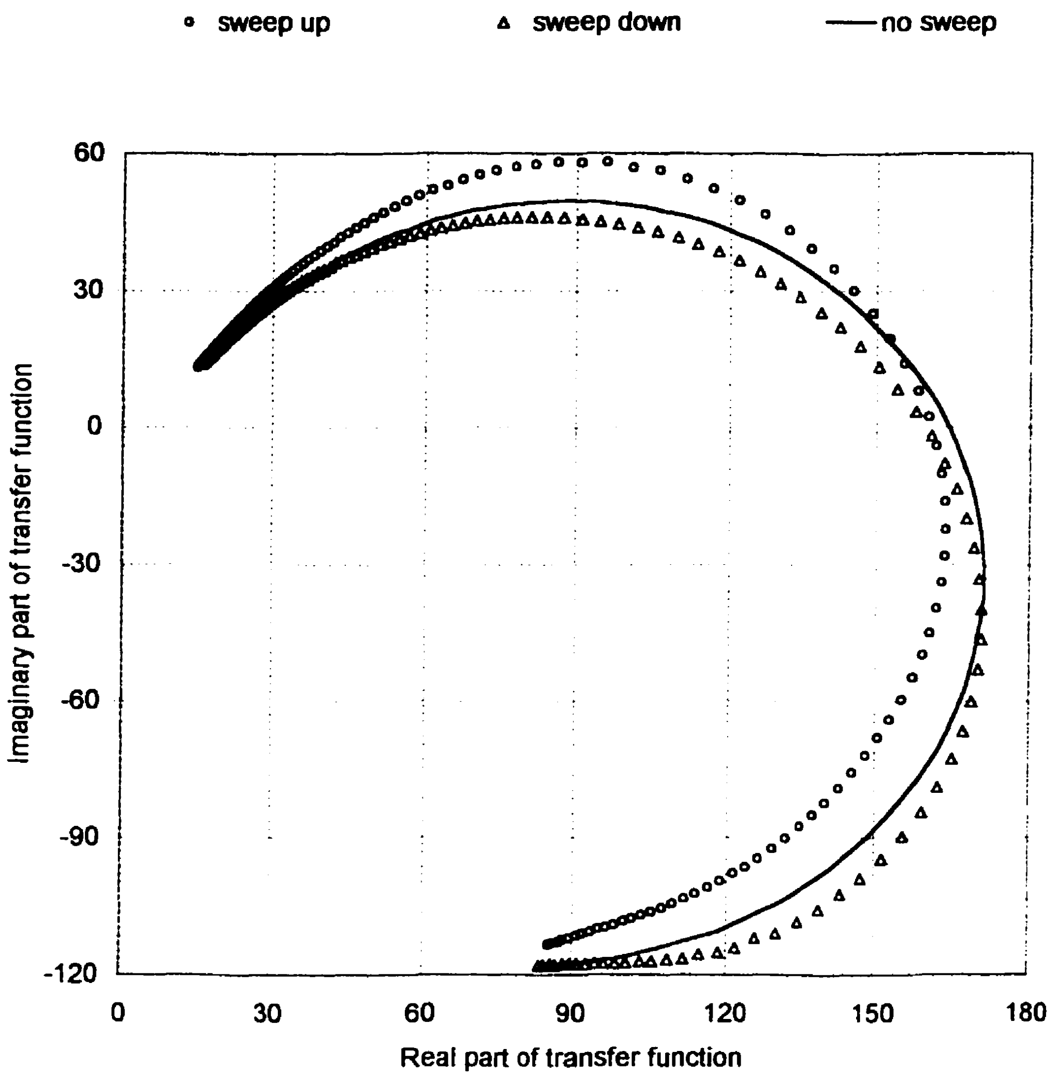

Figure 43. Second mode Nyquist diagrams for increasing and decreasing sweep-rates. Aerodynamic lift input and plunge response at 68% of the linear flutter speed and a sweep-rate of .000024 radians/(non-dimensional second)^2.

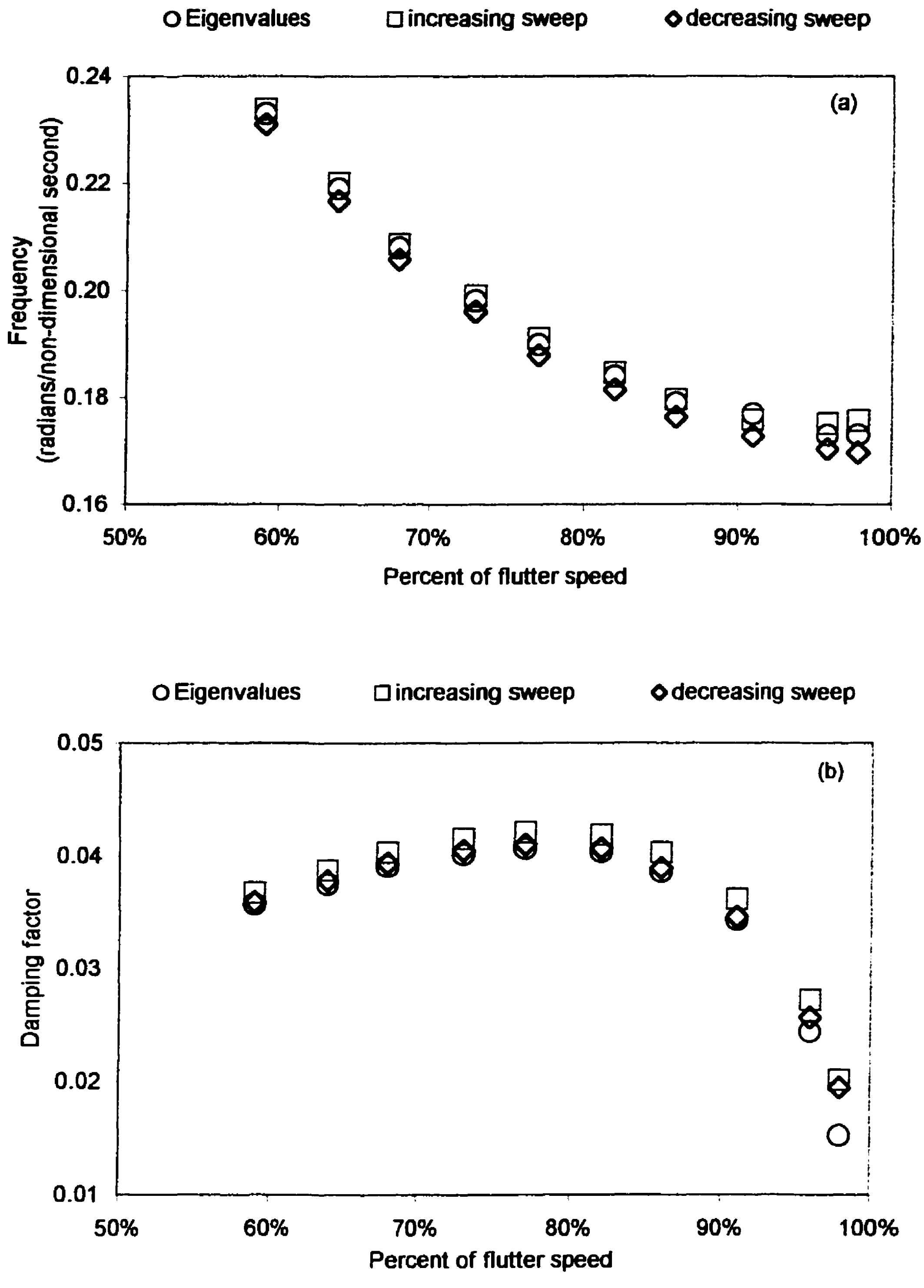

Figure 44. First mode damping and frequency estimates obtained using plunge response to increasing and decreasing frequency sweeps. Transfer functions obtained using aerodynamic lift input and plunge response at a sweep-rate of .000003 radians/(non-dimensional second)^2. (a) frequency, (b) damping.

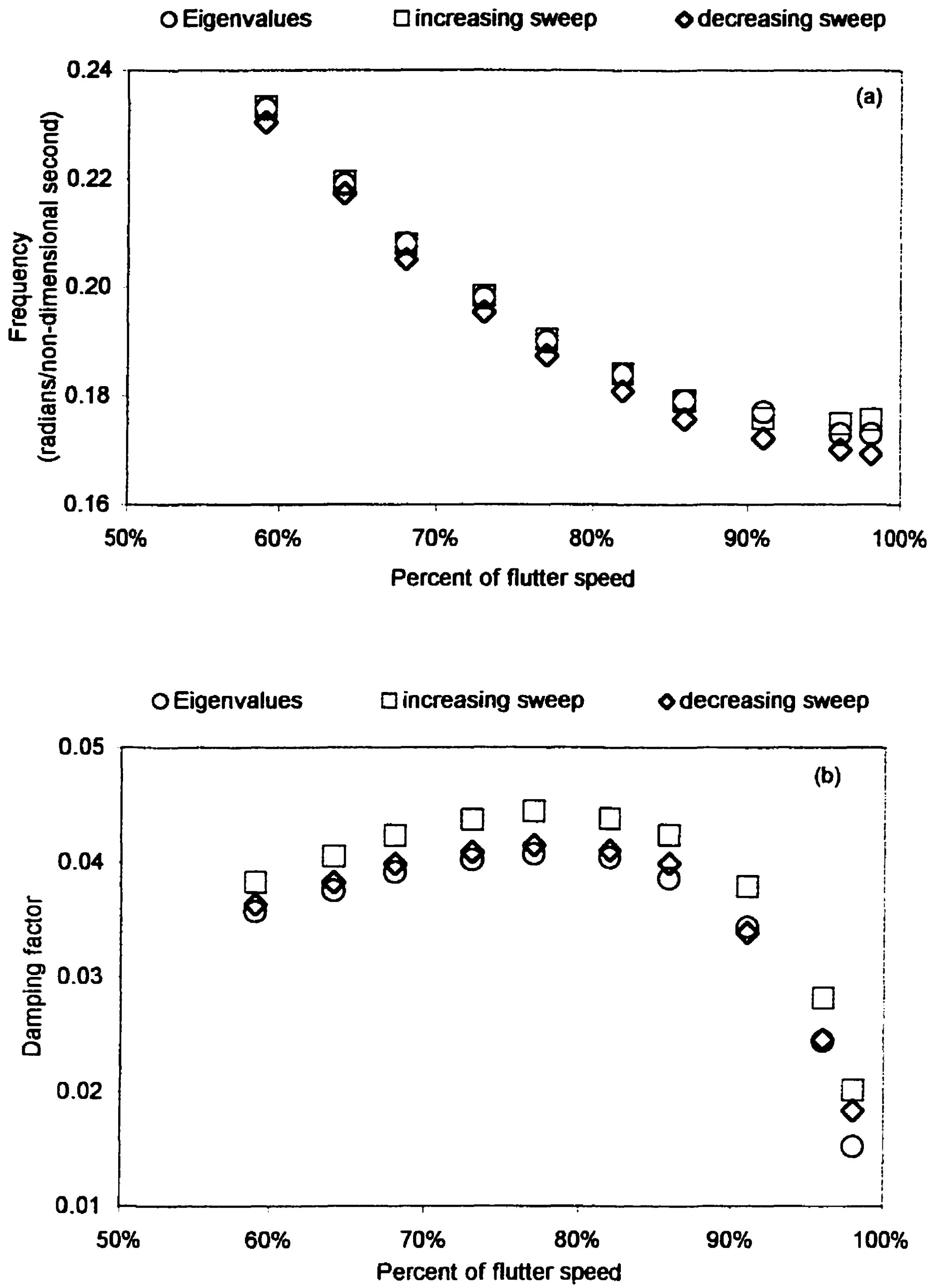

Figure 45. First mode damping and frequency estimates obtained using pitch response to increasing and decreasing frequency sweeps. Transfer functions obtained using aerodynamic lift input and plunge response at a sweep-rate of .000003 radians/(non-dimensional second)^2, (a) frequency, (b) damping.

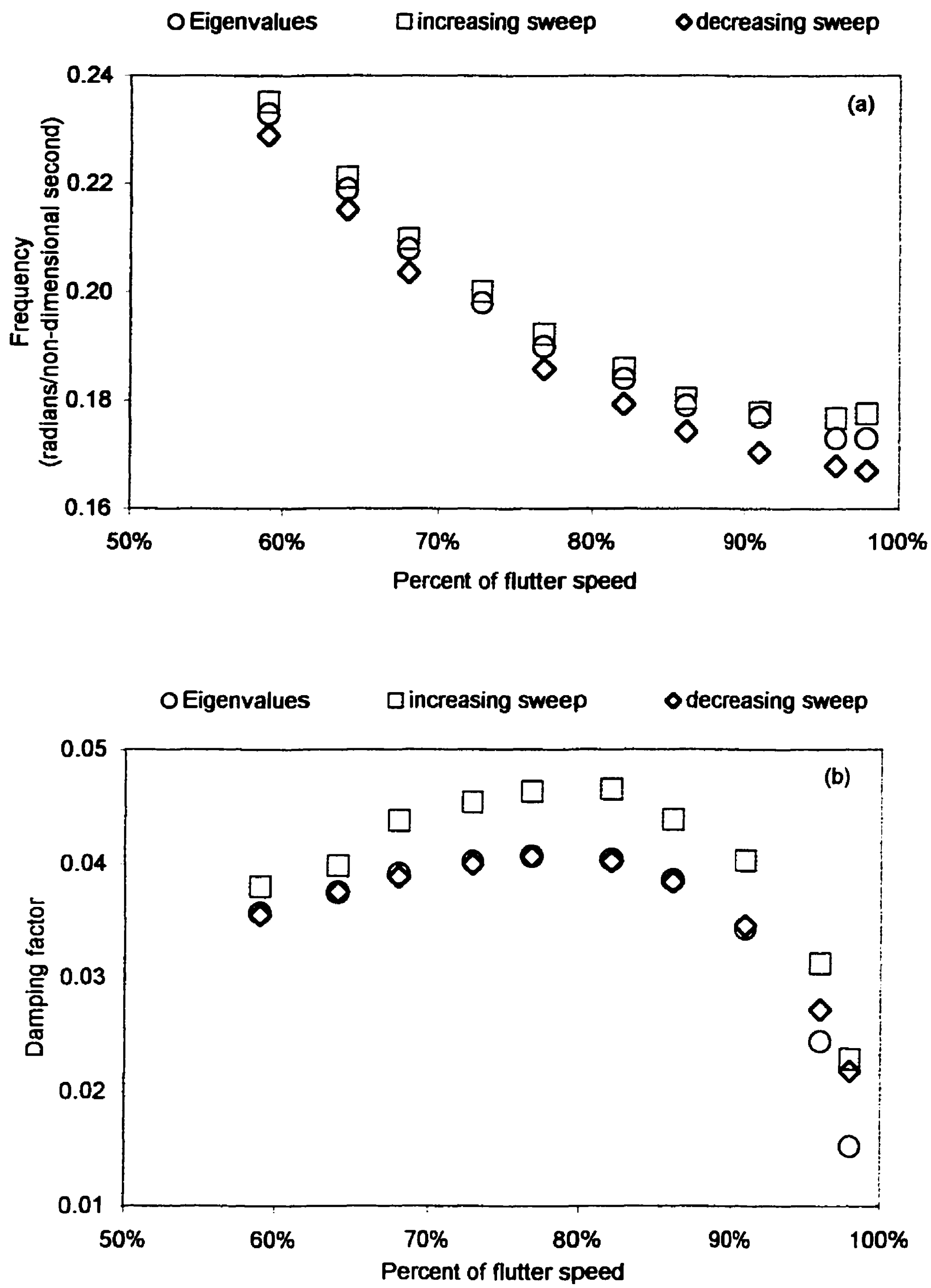

Figure 46. First mode damping and frequency estimates obtained using plunge response to increasing and decreasing frequency sweeps. Transfer functions obtained using aerodynamic lift input and plunge response at a sweep-rate of .000006 radians/(non-dimensional second)^2. (a) frequency, (b) damping.

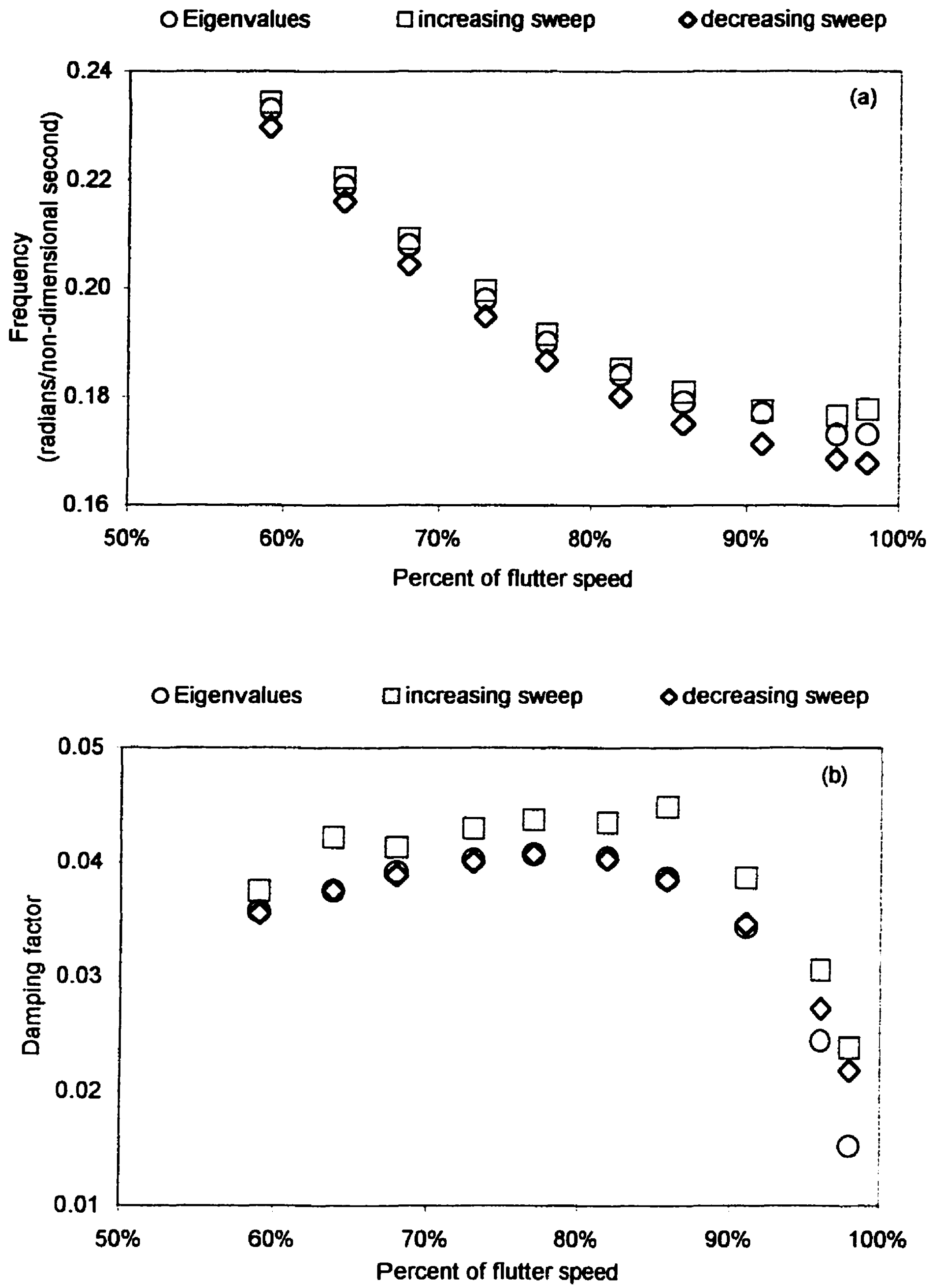

Figure 47. First mode damping and frequency estimates obtained using pitch response to increasing and decreasing frequency sweeps. Transfer functions obtained using aerodynamic lift input and plunge response at a sweep-rate of .000006 radians/(non-dimensional second)^2, (a) frequency, (b) damping.

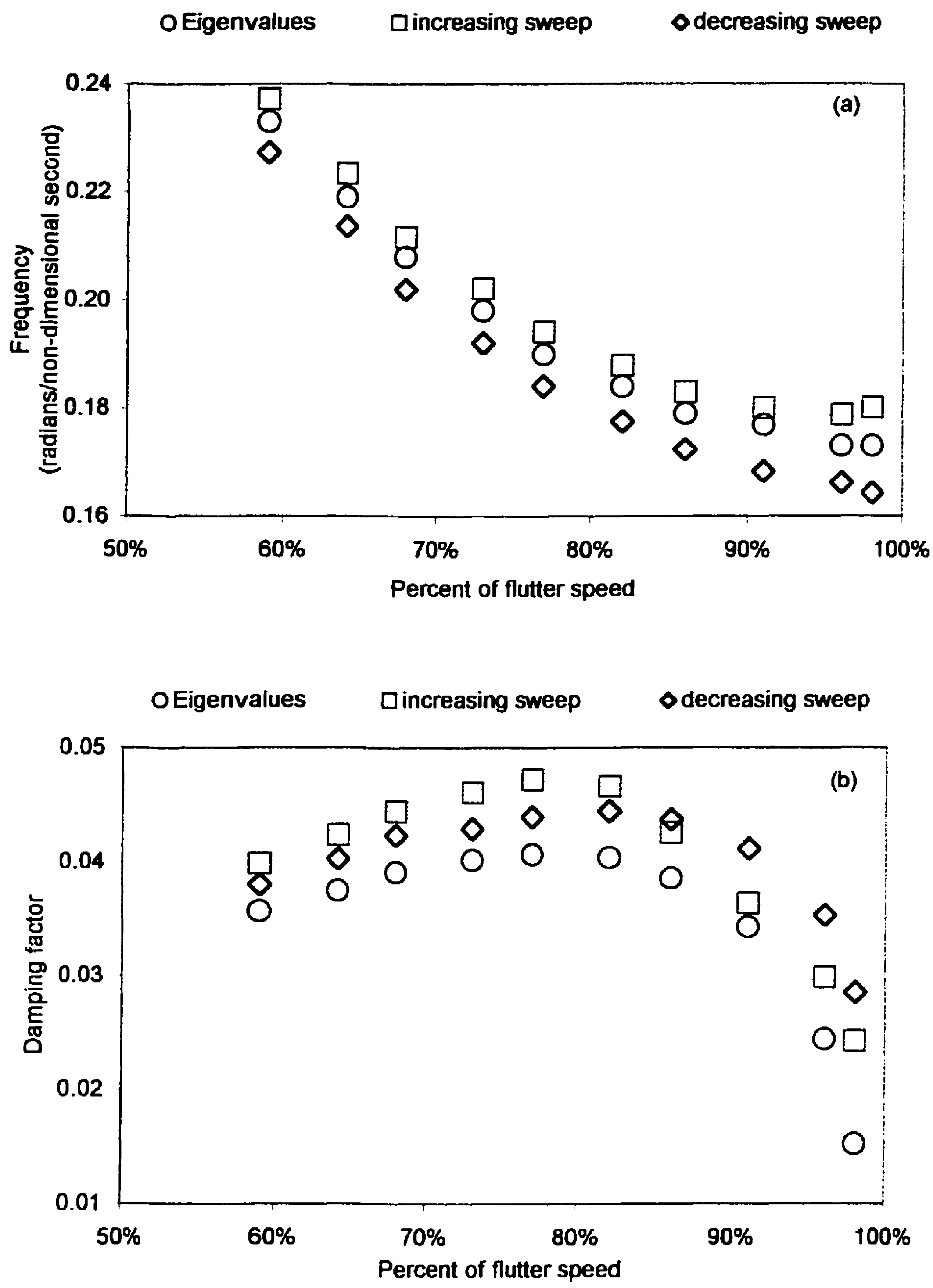

Figure 48. First mode damping and frequency estimates obtained using plunge response to increasing and decreasing frequency sweeps. Transfer functions obtained using aerodynamic lift input and plunge response at a sweep-rate of .000012 radians/(non-dimensional second)^2. (a) frequency, (b) damping.

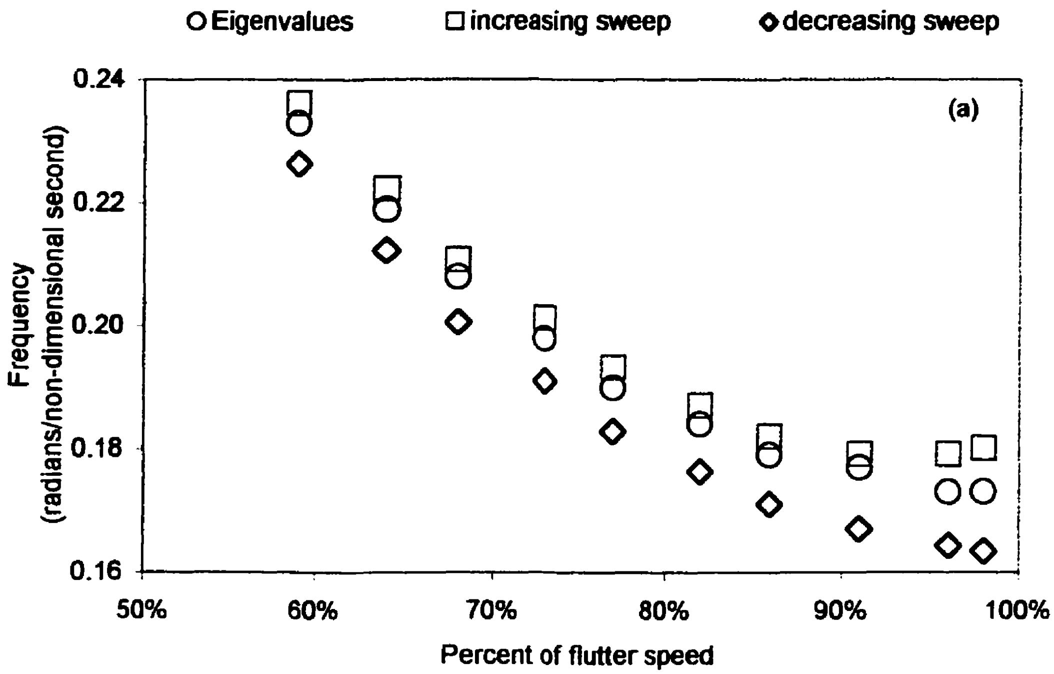

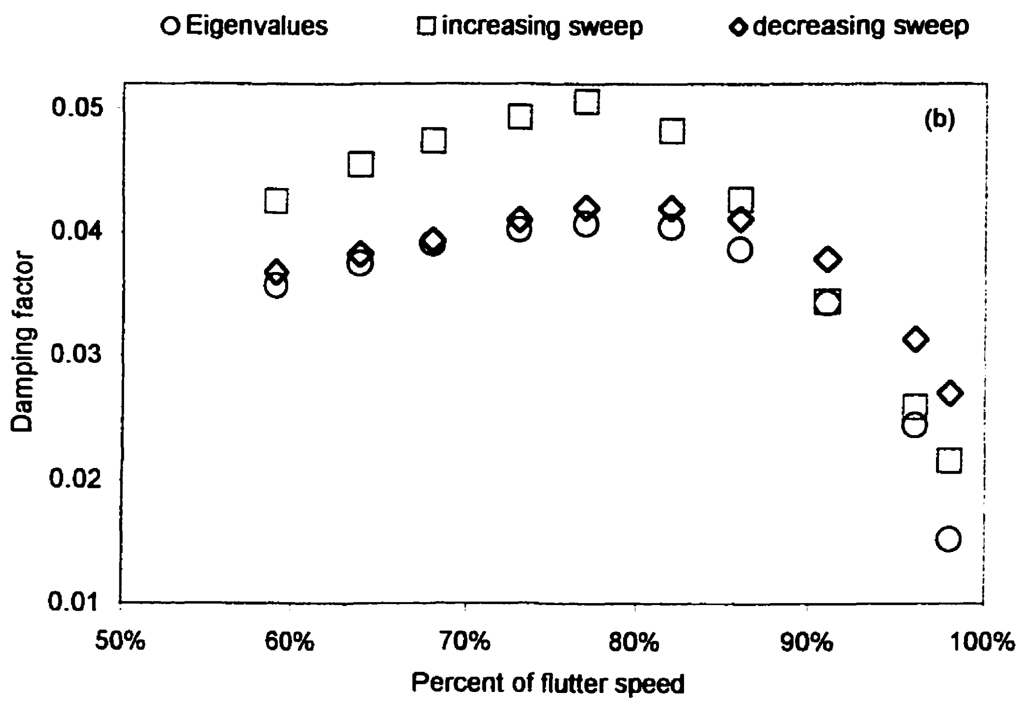

Figure 49. First mode damping and frequency estimates obtained using pitch response to increasing and decreasing frequency sweeps. Transfer functions obtained using aerodynamic lift input and plunge response at a sweep-rate of .000012 radians/(non-dimensional second)^2, (a) frequency, (b) damping.

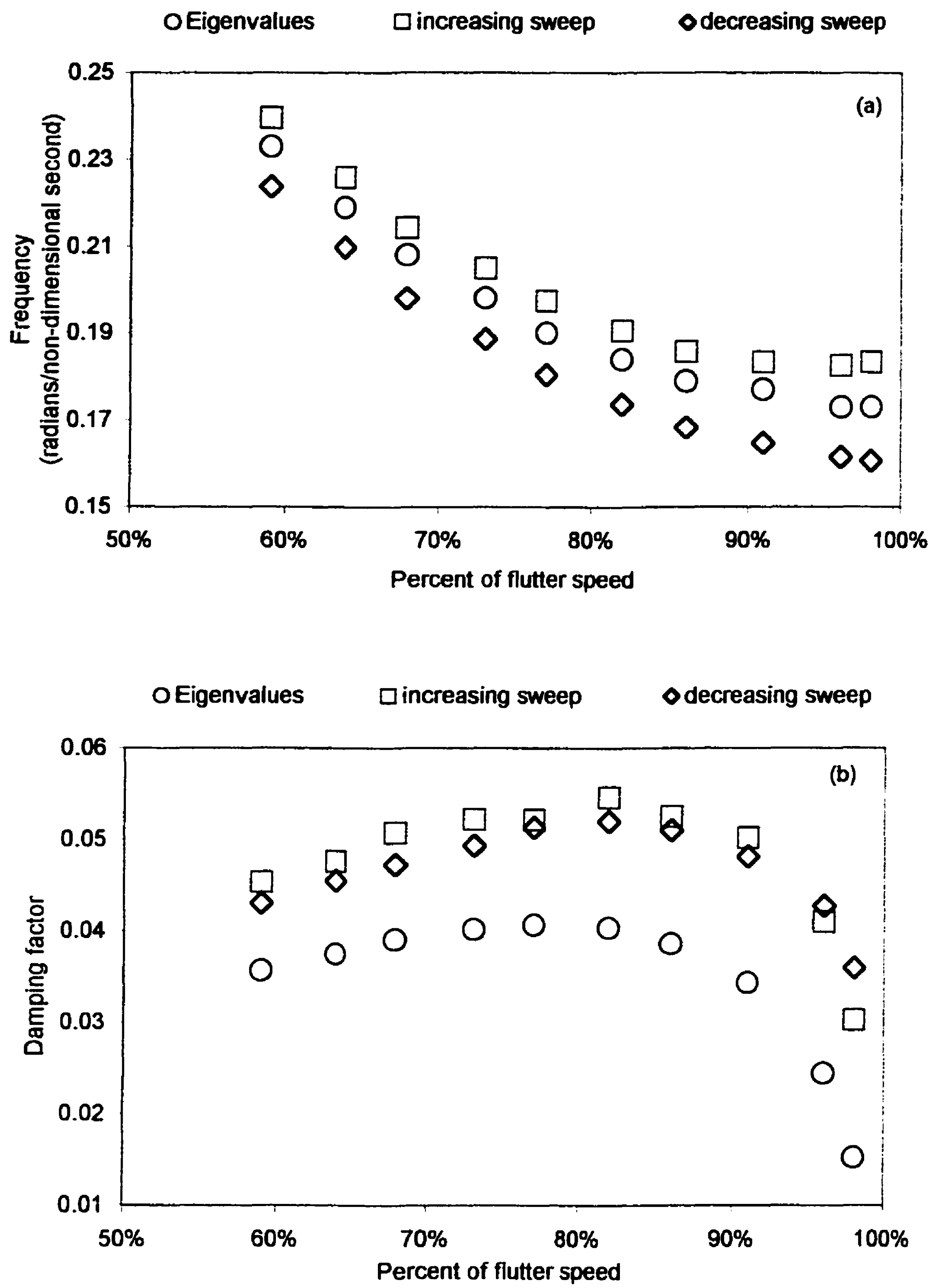

Figure 50. First mode damping and frequency estimates obtained using plunge response to increasing and decreasing frequency sweeps. Transfer functions obtained using aerodynamic lift input and plunge response at a sweep-rate of .000024 radians/(non-dimensional second)^2, (a) frequency, (b) damping.

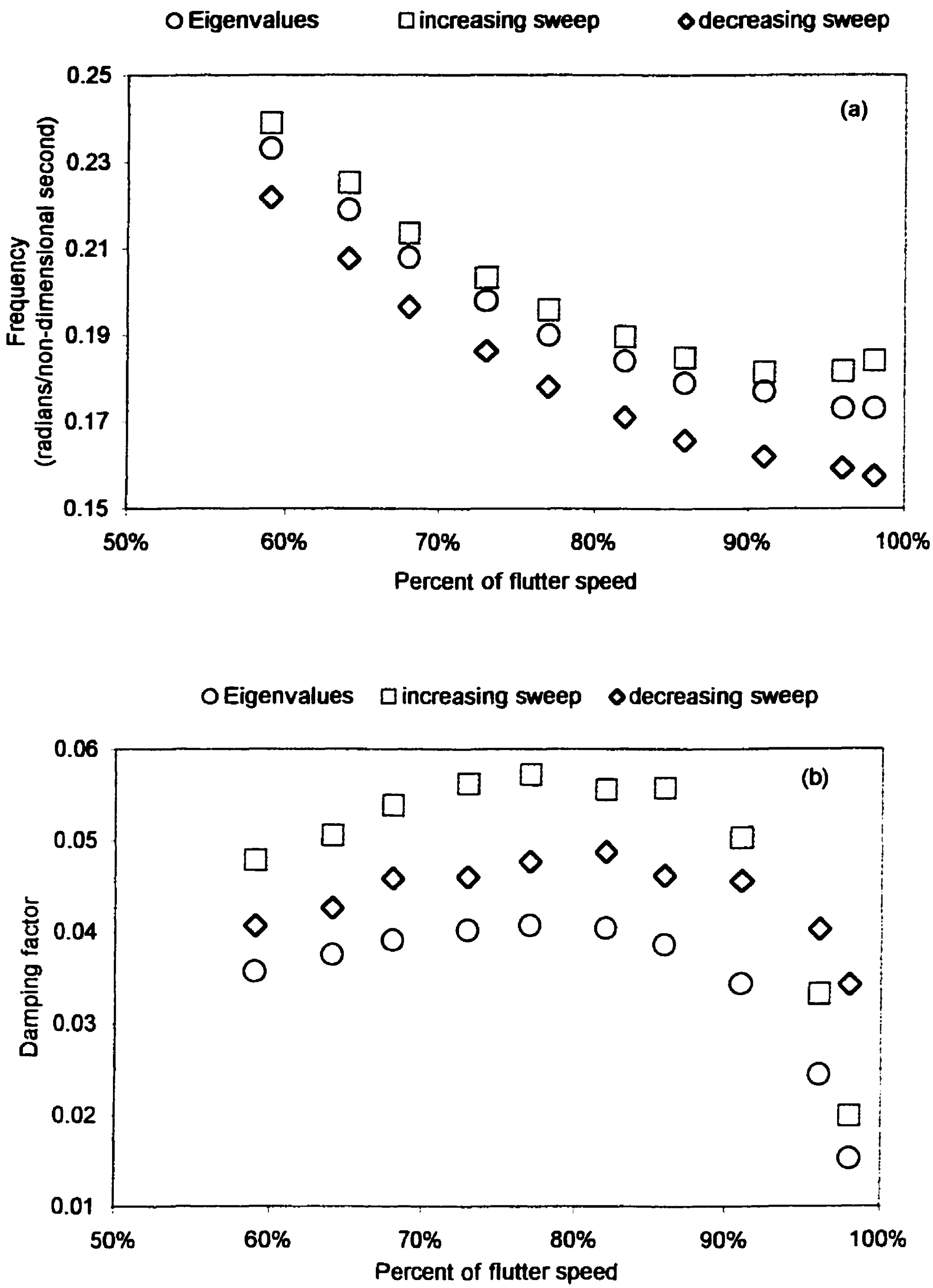

Figure 51. First mode damping and frequency estimates obtained using pitch response to increasing and decreasing frequency sweep. Transfer functions obtained from aerodynamic lift input and plunge response at a sweep-rate of .000024 radians/(non-dimensional second)^2, (a) frequency, (b) damping.

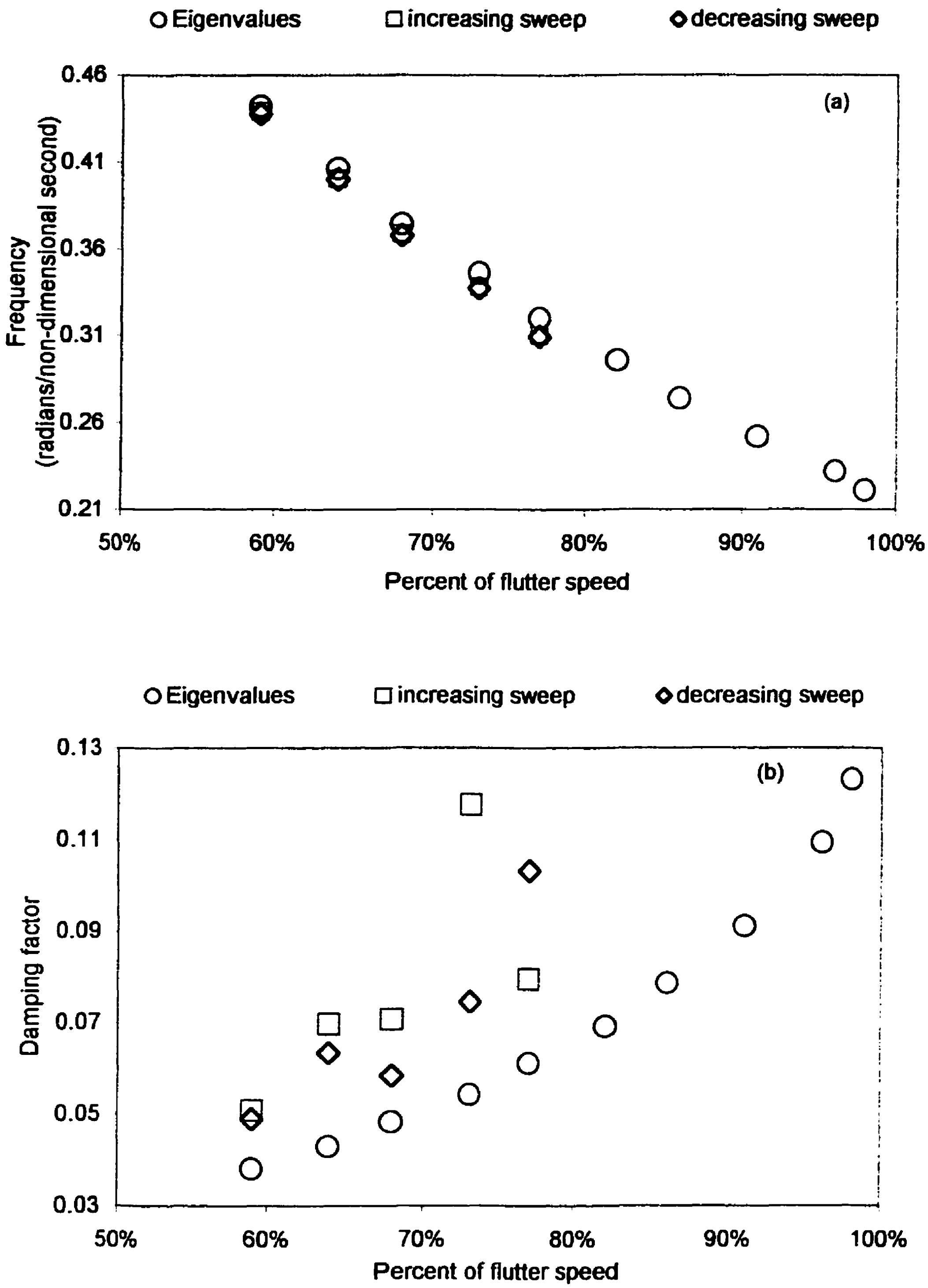

Figure 52. Second mode damping and frequency estimates obtained using plunge response to increasing and decreasing frequency sweeps. Transfer functions obtained from aerodynamic lift input and plunge response at a sweep-rate of .000003 radians/(non-dimensional second)^2, (a) frequency, (b) damping.

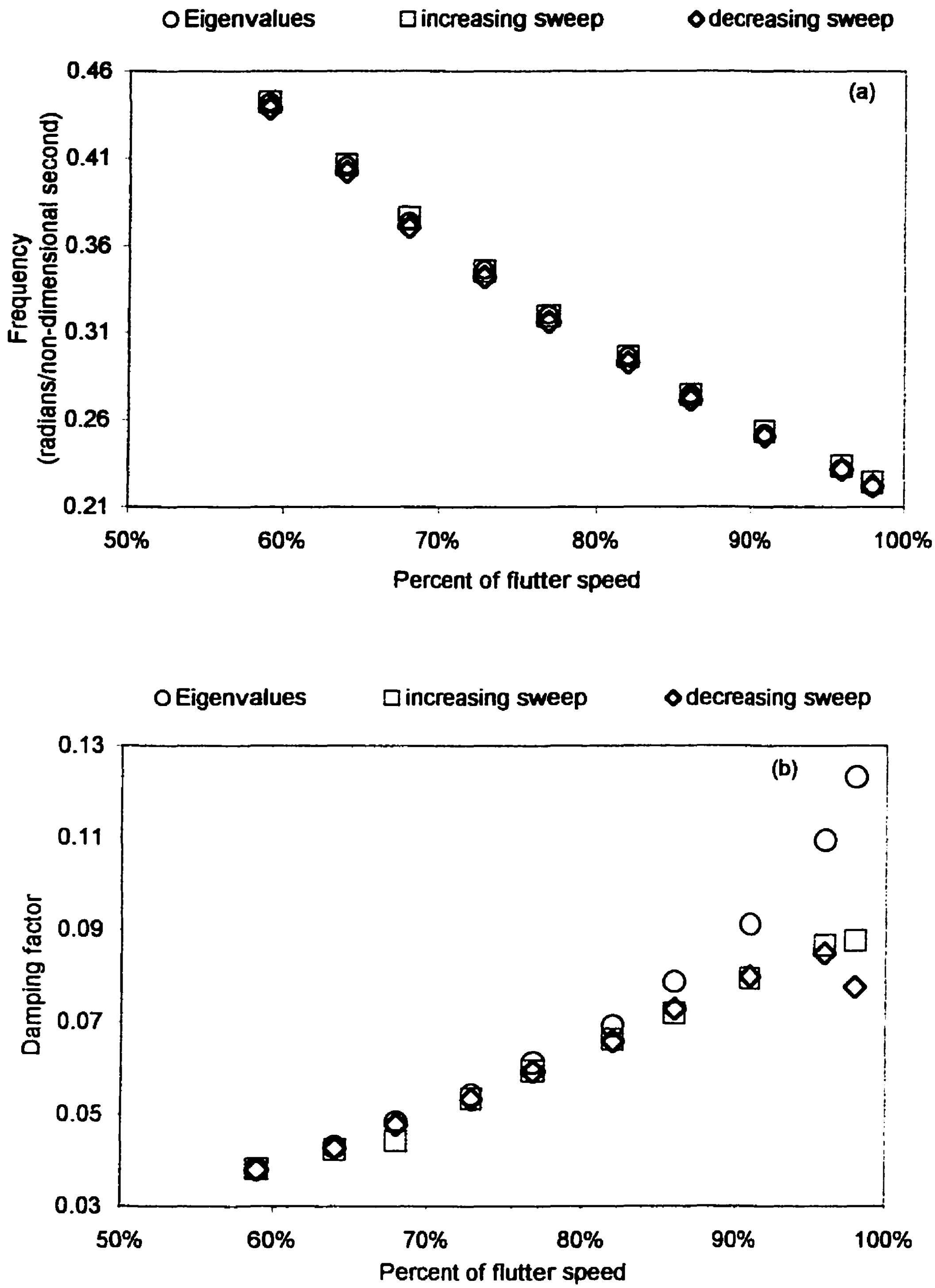

Figure 53. Second mode damping and frequency estimates obtained using pitch response to increasing and decreasing frequency sweeps. Transfer functions obtained from aerodynamic moment input and pitch response at a sweep-rate of .000003 radians/(non-dimensional second)^2, (a) frequency, (b) damping.

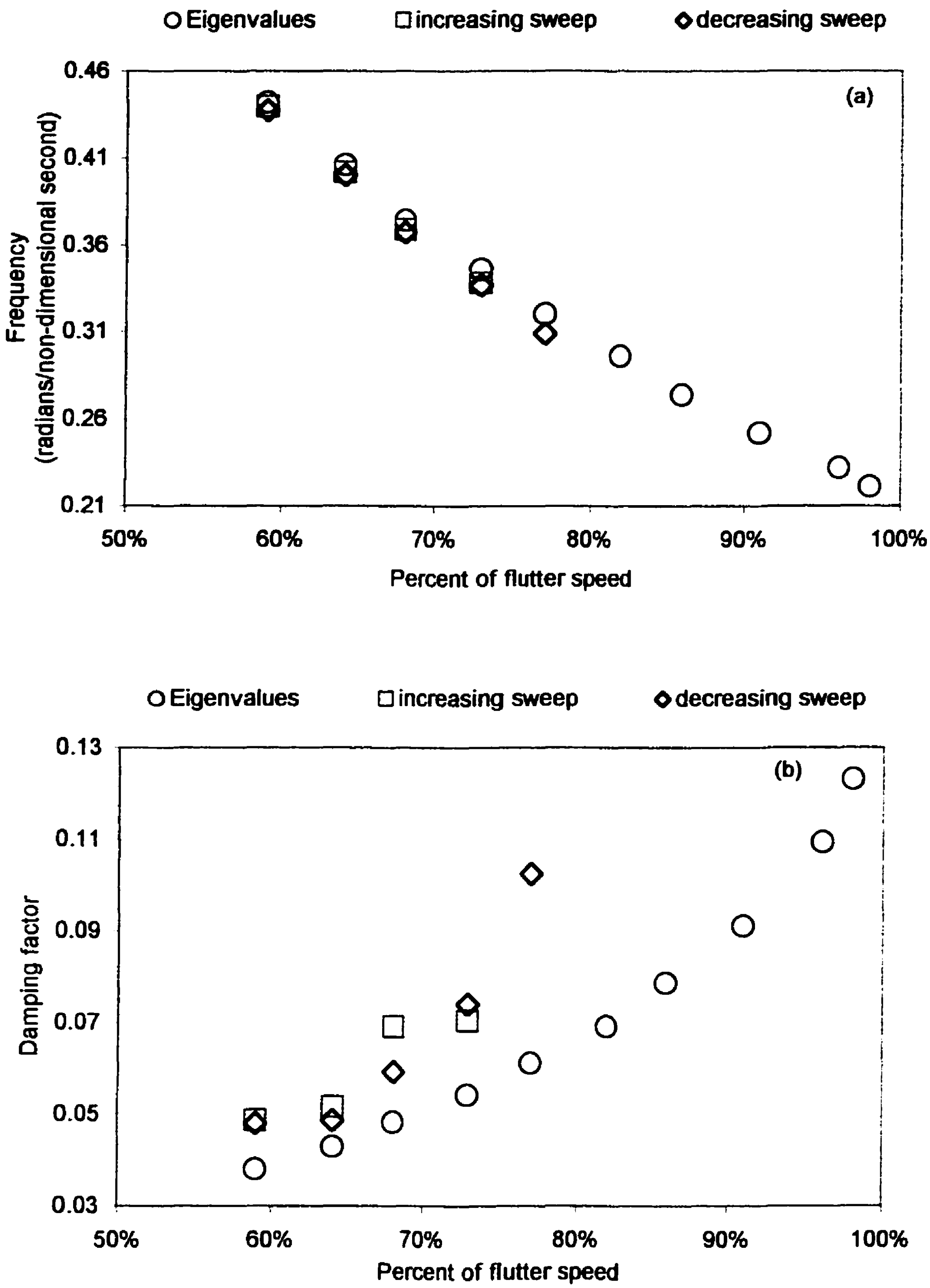

Figure 54. Second mode damping and frequency estimates obtained using plunge response to increasing and decreasing frequency sweeps. Transfer functions obtained from aerodynamic lift input and plunge response at a sweep-rate of .000006 radians/(non-dimensional second)^2, (a) frequency, (b) damping.

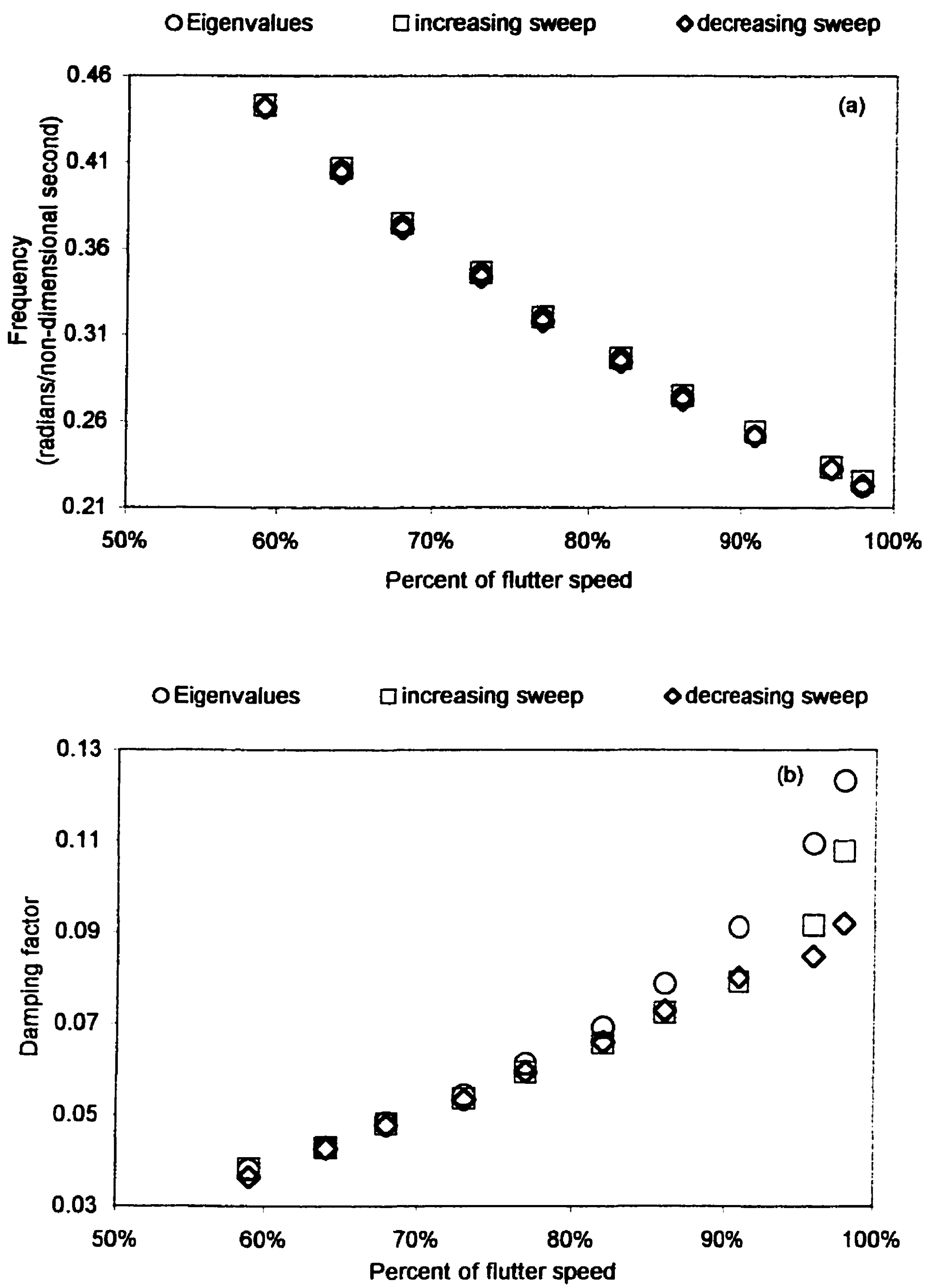

Figure 55. Second mode damping and frequency estimates obtained using pitch response to increasing and decreasing frequency sweeps. Transfer functions obtained from aerodynamic moment input and pitch response at a sweep-rate of .000006 radians/(non-dimensional second)^2, (a) frequency, (b) damping.

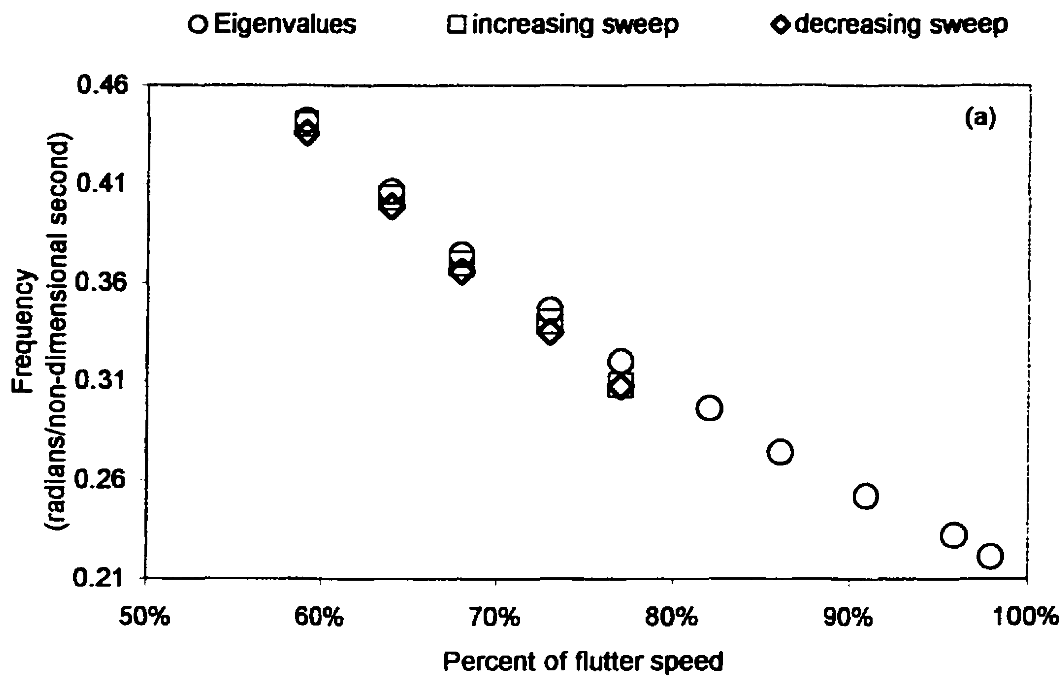

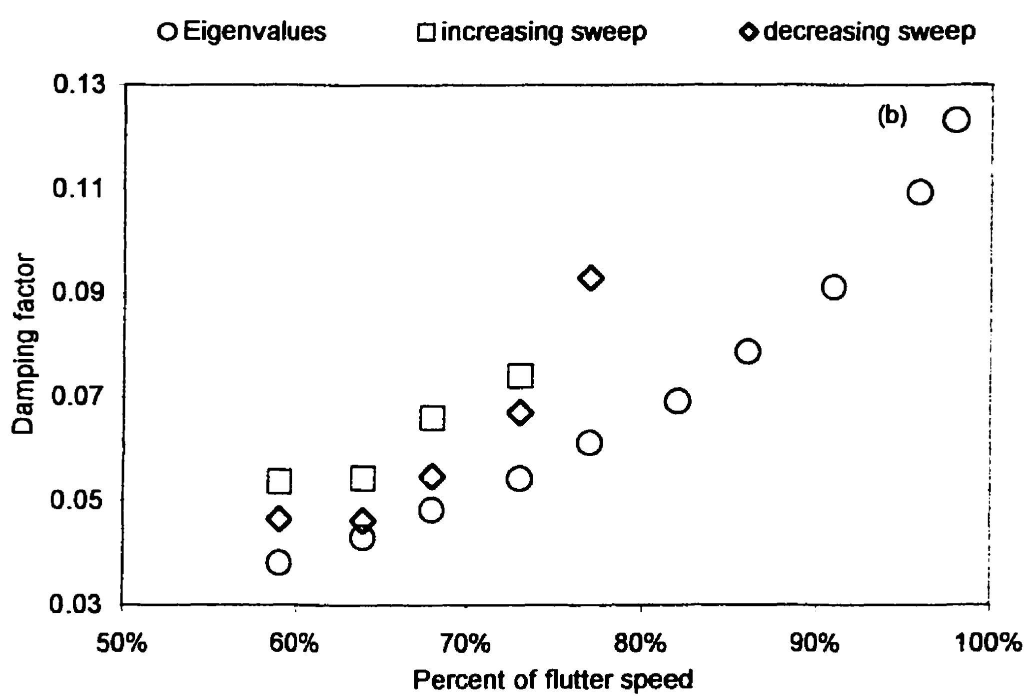

Figure 56. Second mode damping and frequency estimates obtained using plunge response to increasing and decreasing frequency sweeps. Transfer functions obtained from aerodynamic lift input and plunge response at a sweep-rate of .000012 radians/(non-dimensional second)^2, (a) frequency, (b) damping.

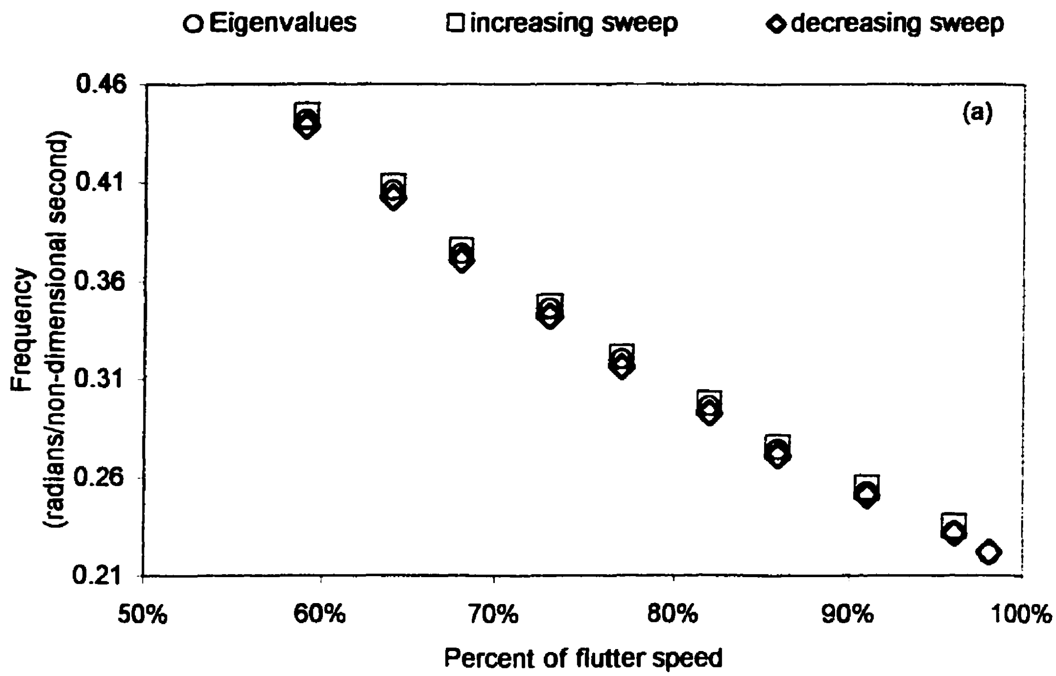

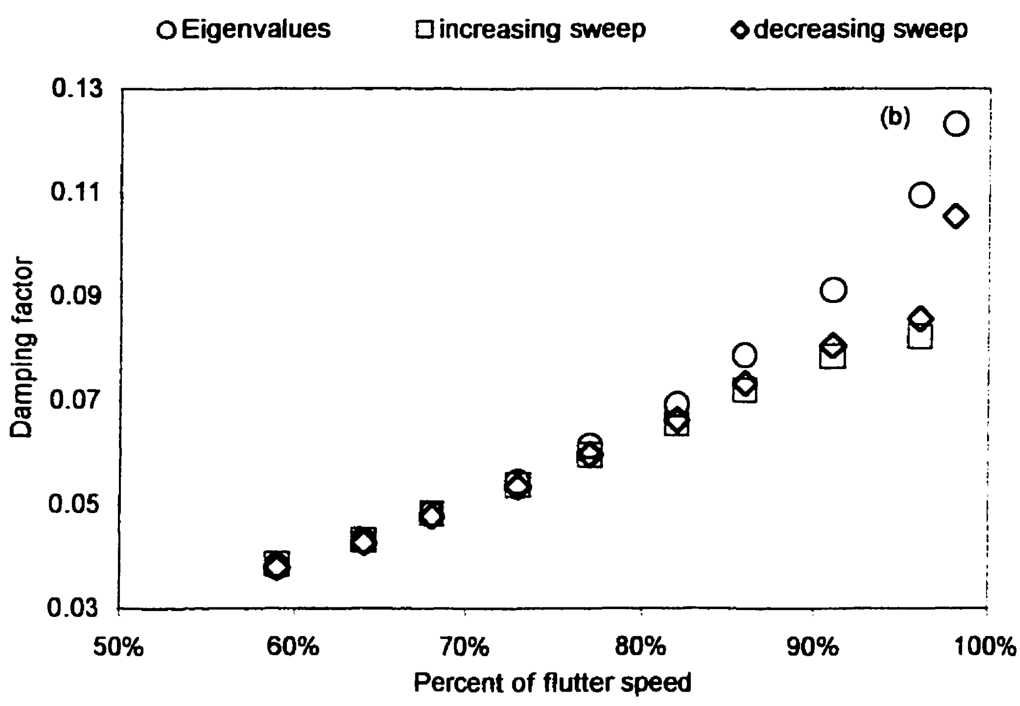

Figure 57. Second mode damping and frequency estimates obtained using pitch response to increasing and decreasing frequency sweeps. Transfer functions obtained from aerodynamic moment input and pitch response at a sweep-rate of .000012 radians/(non-dimensional second)^2, (a) frequency, (b) damping.

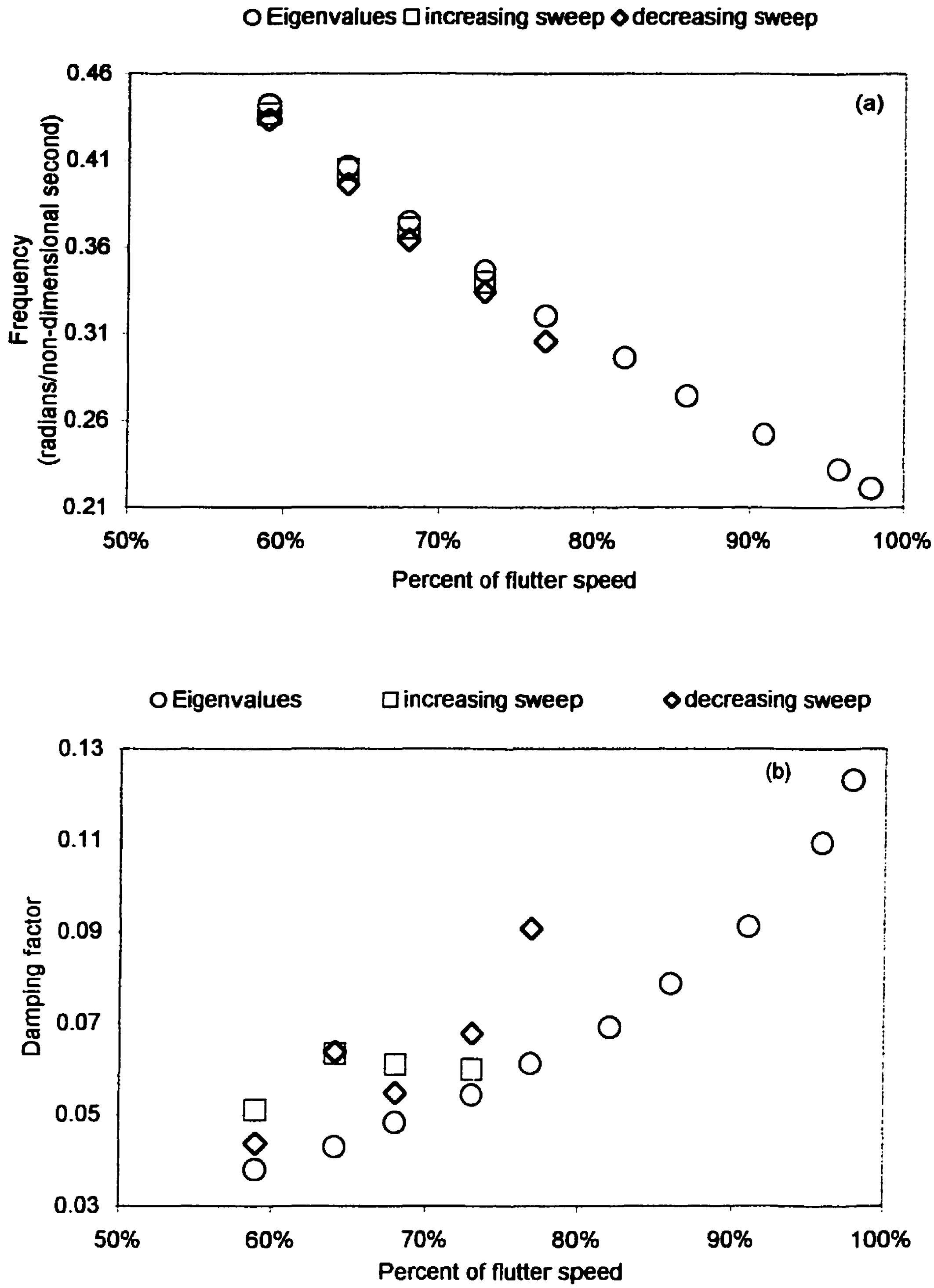

Figure 58. Second mode damping and frequency estimates obtained using plunge response to increasing and decreasing frequency sweeps. Transfer functions obtained from aerodynamic lift input and plunge response at a sweep-rate of .000024 radians/(non-dimensional second)^2, (a) frequency, (b) damping.

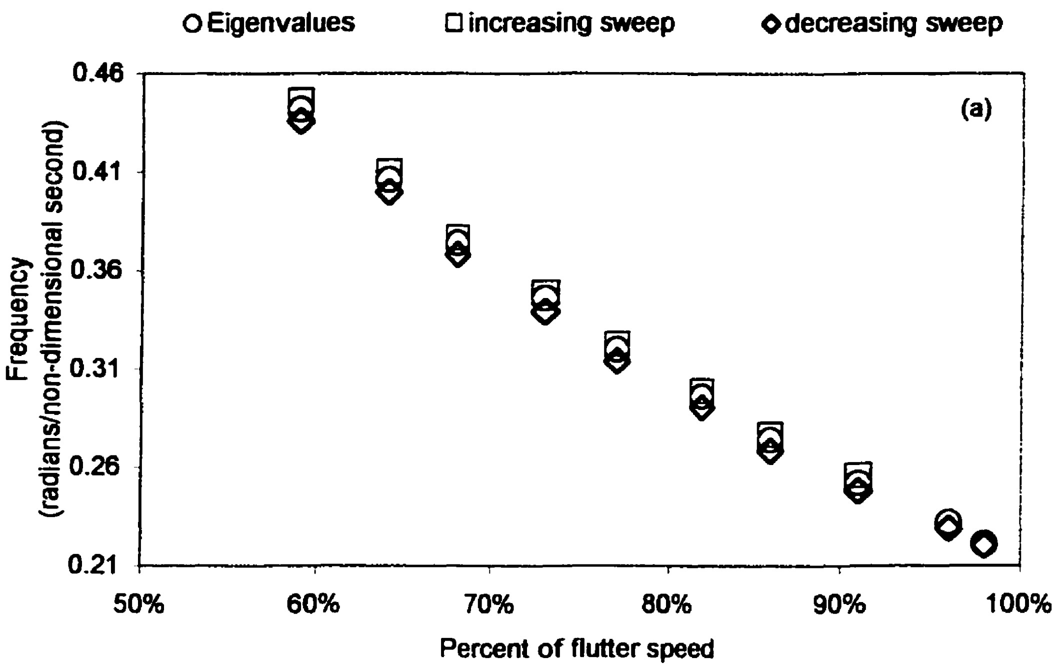

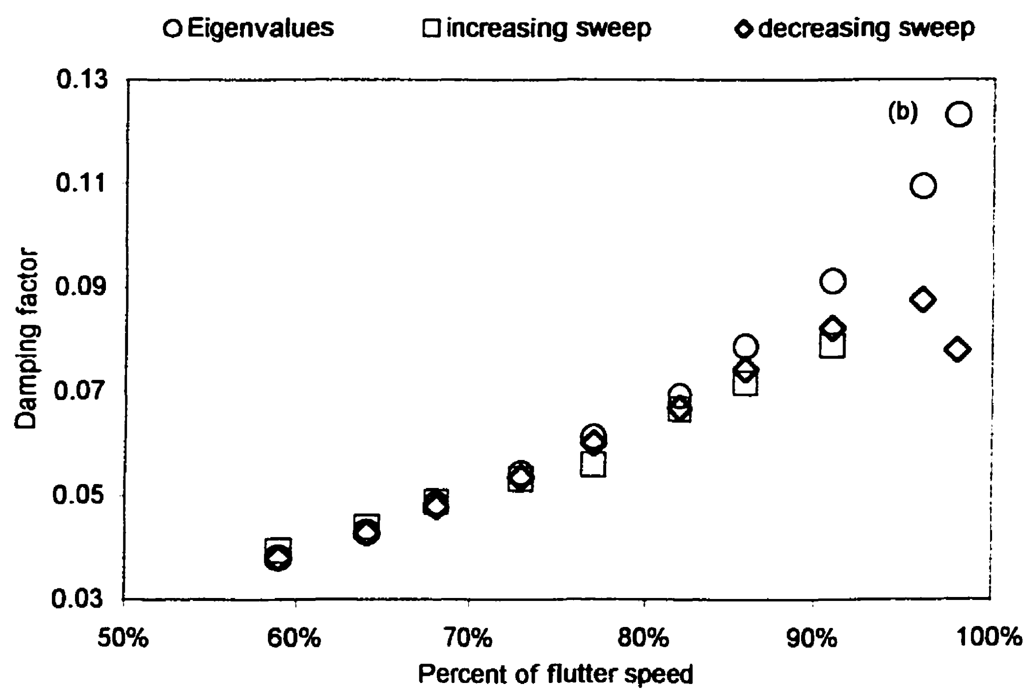

Figure 59. Second mode damping and frequency estimates obtained using pitch response to increasing and decreasing frequency sweep. Transfer functions obtained from aerodynamic moment input and pitch response at a sweep-rate of .000024 radians/(non-dimensional second)^2, (a) frequency, (b) damping.

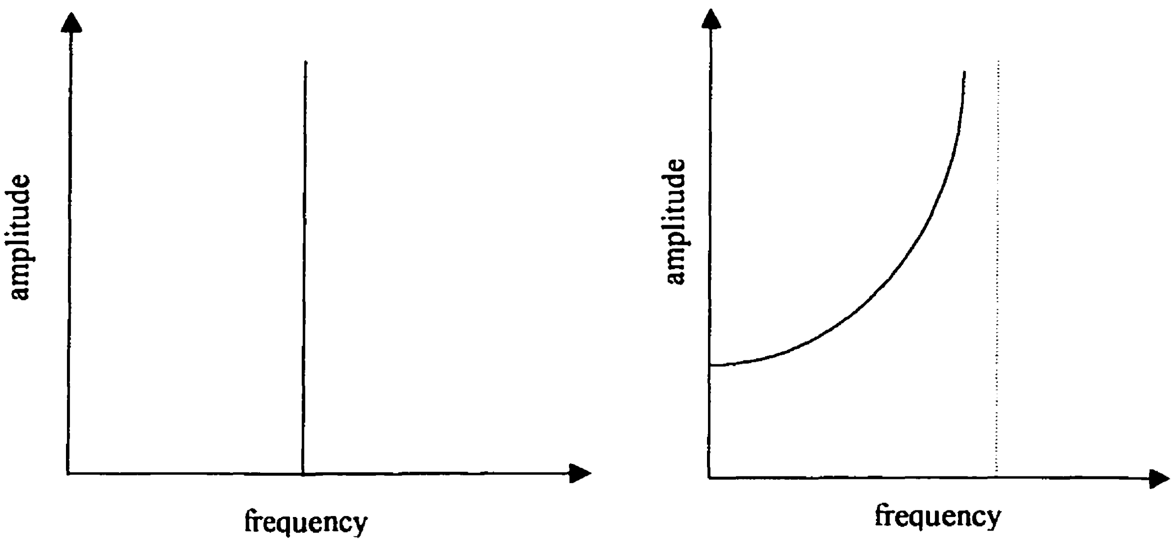

Figure 60. Amplitude vs. frequency for undamped free vibrations of one degree of freedom mechanical system (a) linear, (b) with a nonlinear hardening spring with freeplay.

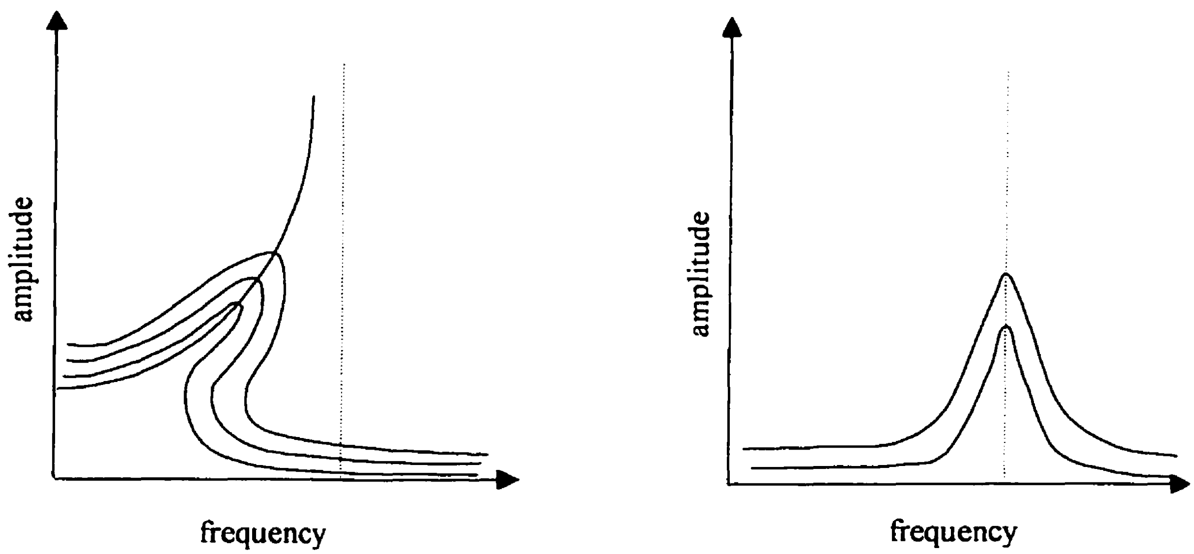

Figure 61. Typical response curves at resonance for various levels of excitation for the systems of Figure 60, (a) nonlinear spring (b) linear system.

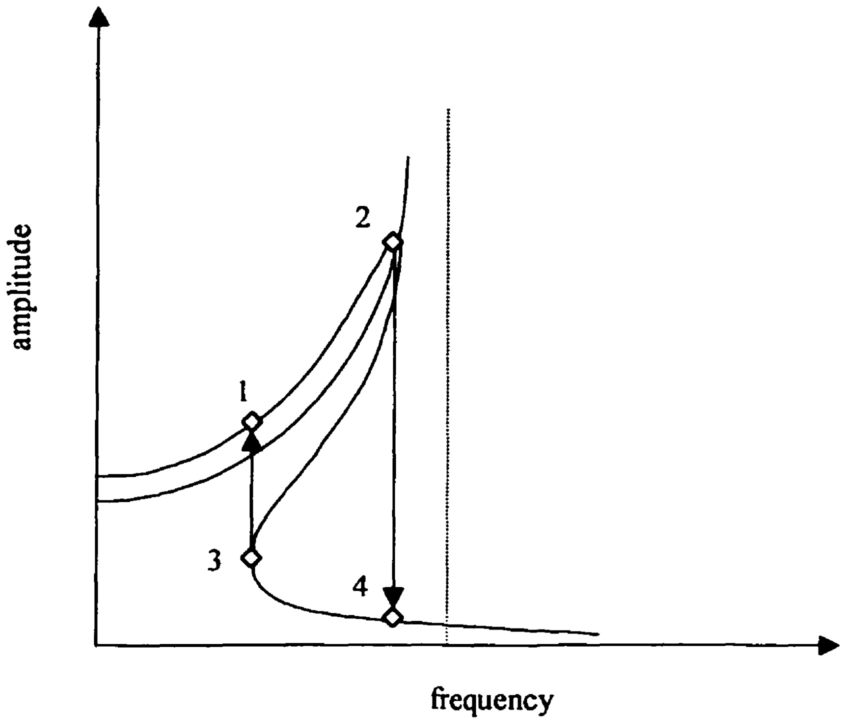

Figure 62. Theoretical frequency response curve for nonlinear hardening spring showing regions of instability.

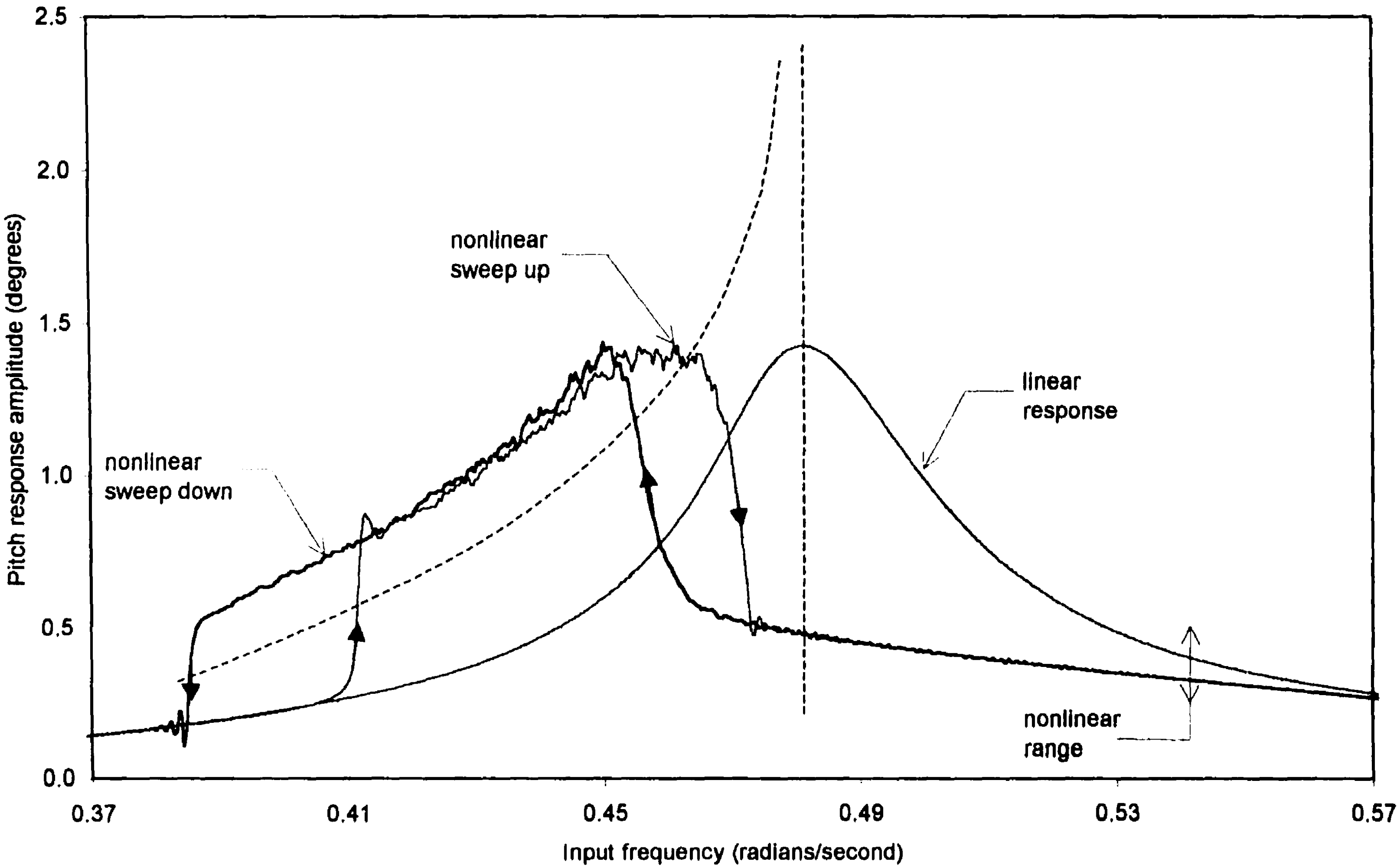

Figure 63. Second mode linear and nonlinear frequency responses to increasing and decreasing frequency sweeps at a sweep-rate of .000012 radians/(non-dimensional second)^2, at U/U*=0.55. Dashed lines indicate linear and nonlinear "backbones". Arrows indicate "jumps" in frequency response.

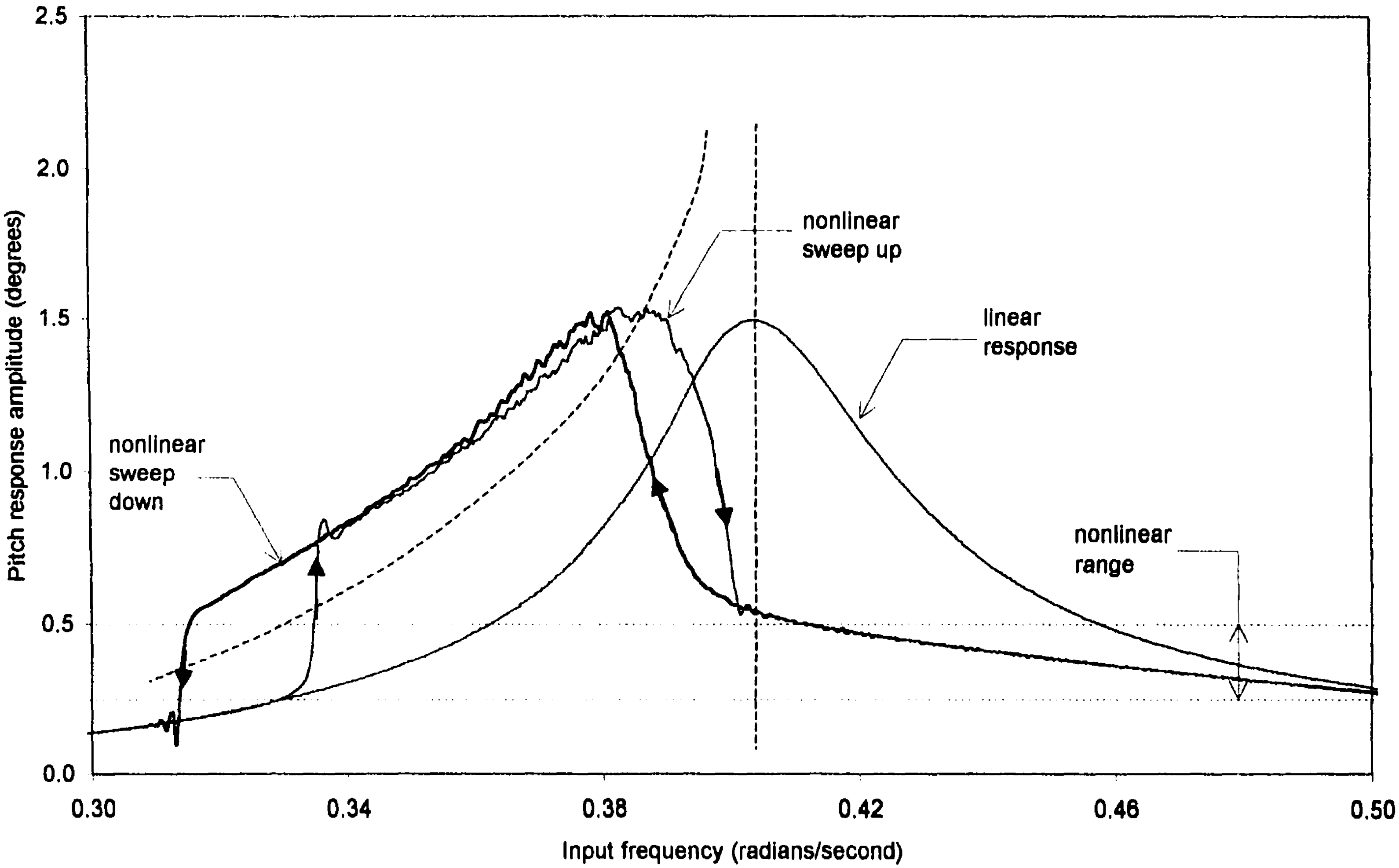

Figure 64. Second mode linear and nonlinear frequency responses to increasing and decreasing frequency sweeps at a sweep-rate of .000012 radians/(non-dimensional second)^2, at U/U*=0.64. Dashed lines indicate linear and nonlinear "backbones". Arrows indicate "jumps" in frequency response.

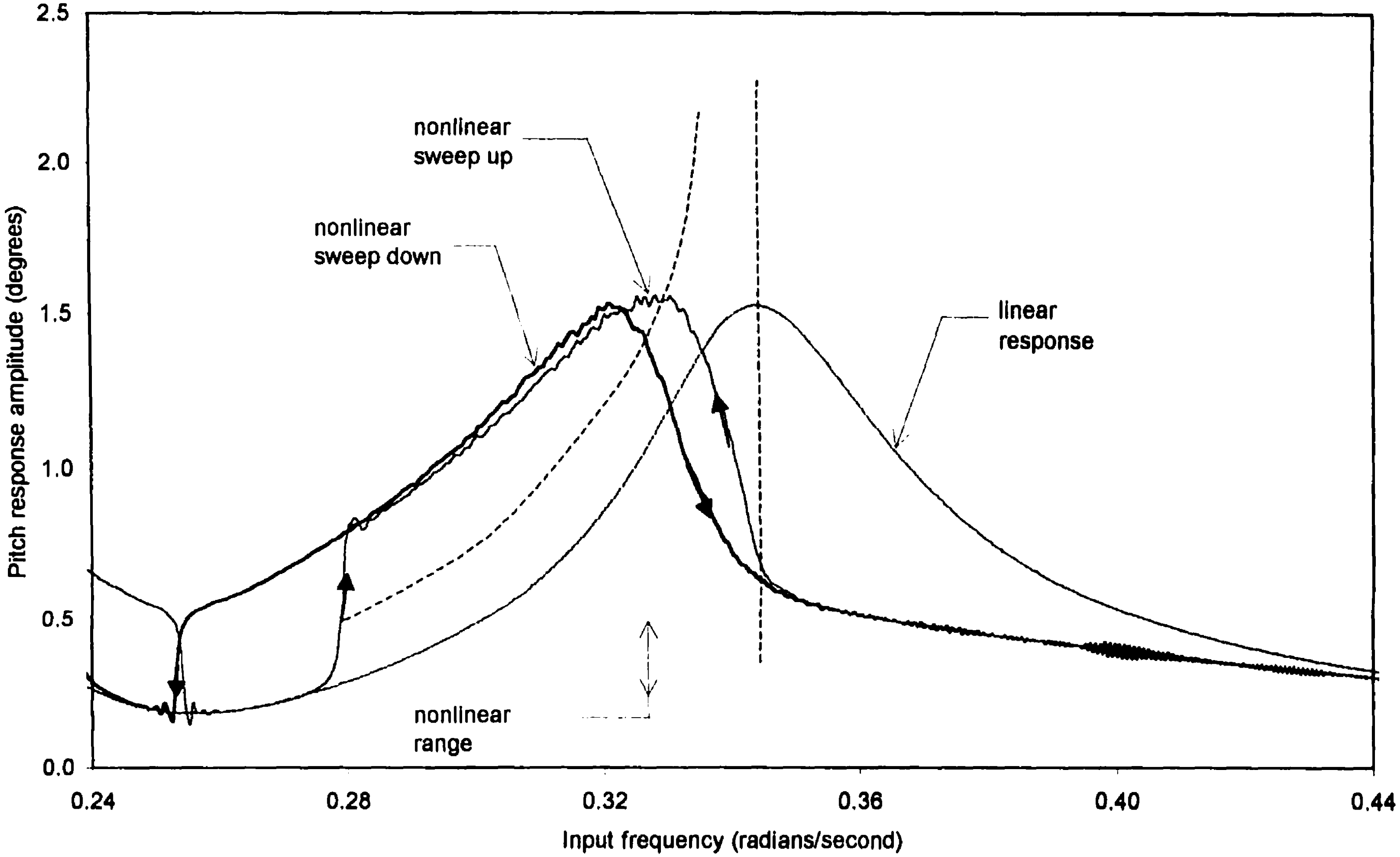

Figure 65. Second mode linear and nonlinear frequency responses to increasing and decreasing frequency sweeps at a sweep-rate of .000012 radians/(non-dimensional second)^2, at U/U*=0.73. Dashed lines indicate linear and nonlinear "backbones". Arrows indicate "jumps" in frequency response.

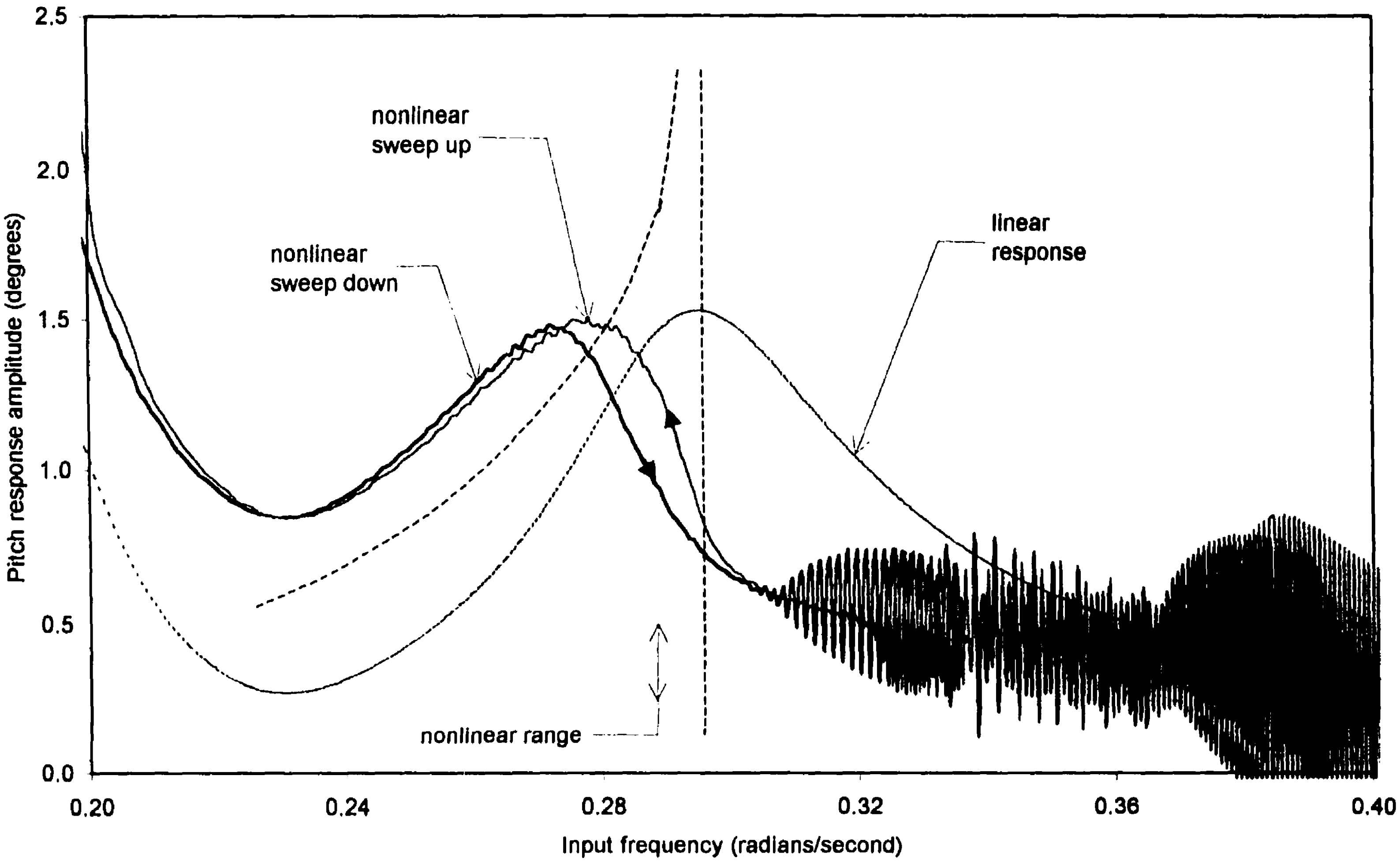

Figure 66. Second mode linear and nonlinear frequency responses to increasing and decreasing frequency sweeps at a sweep-rate of .000012 radians/(non-dimensional second)^2, at U/U*=0.82. Dashed lines indicate linear and nonlinear "backbones". Arrows indicate "jumps" in frequency response.

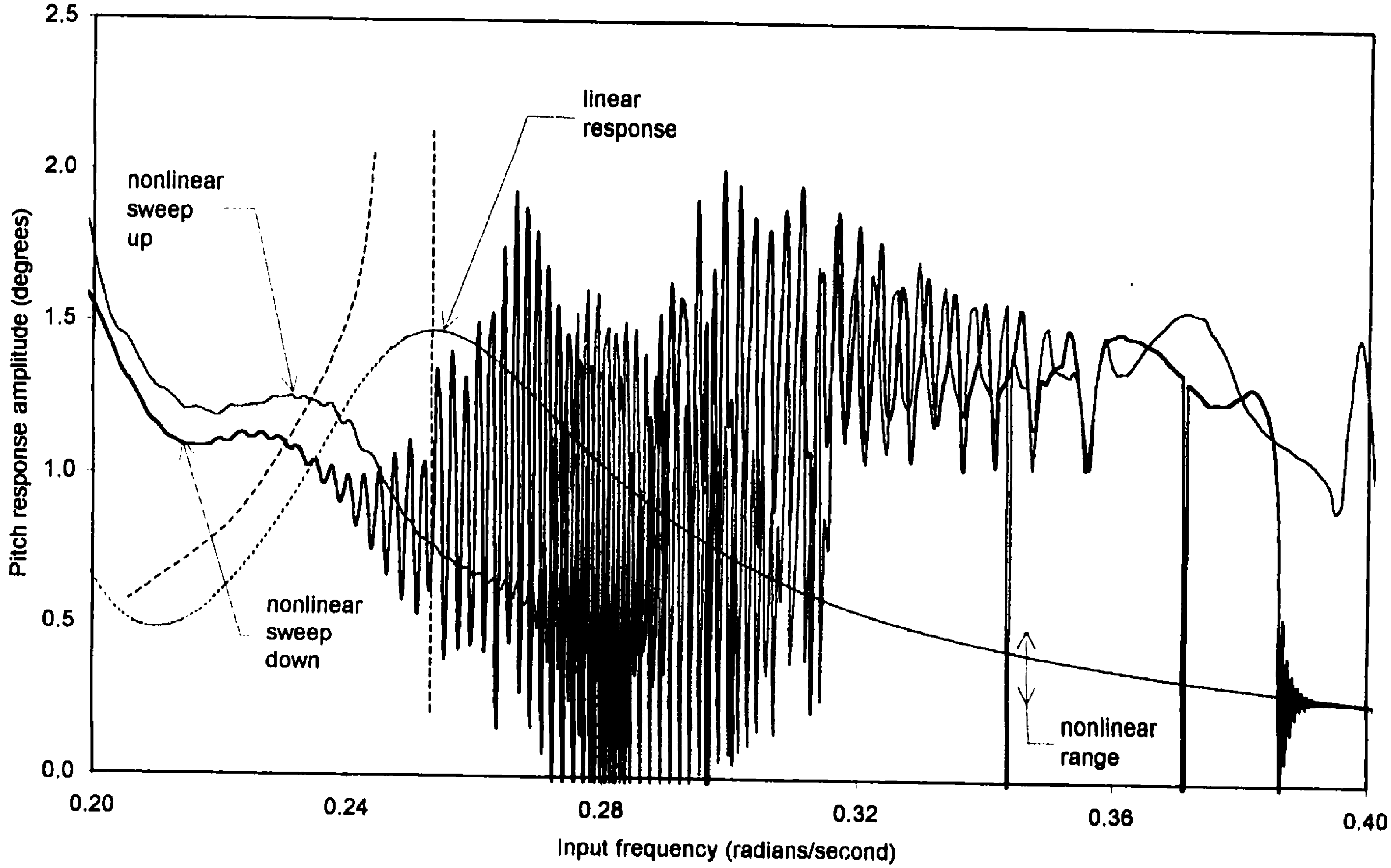

Figure 67. Second mode linear and nonlinear frequency responses to increasing and decreasing frequency sweeps at a sweep-rate of .000012 radians/(non-dimensional second)^2, at U/U*=0.91. Dashed lines indicate linear and nonlinear "backbones". Arrows indicate "jumps" in frequency response.

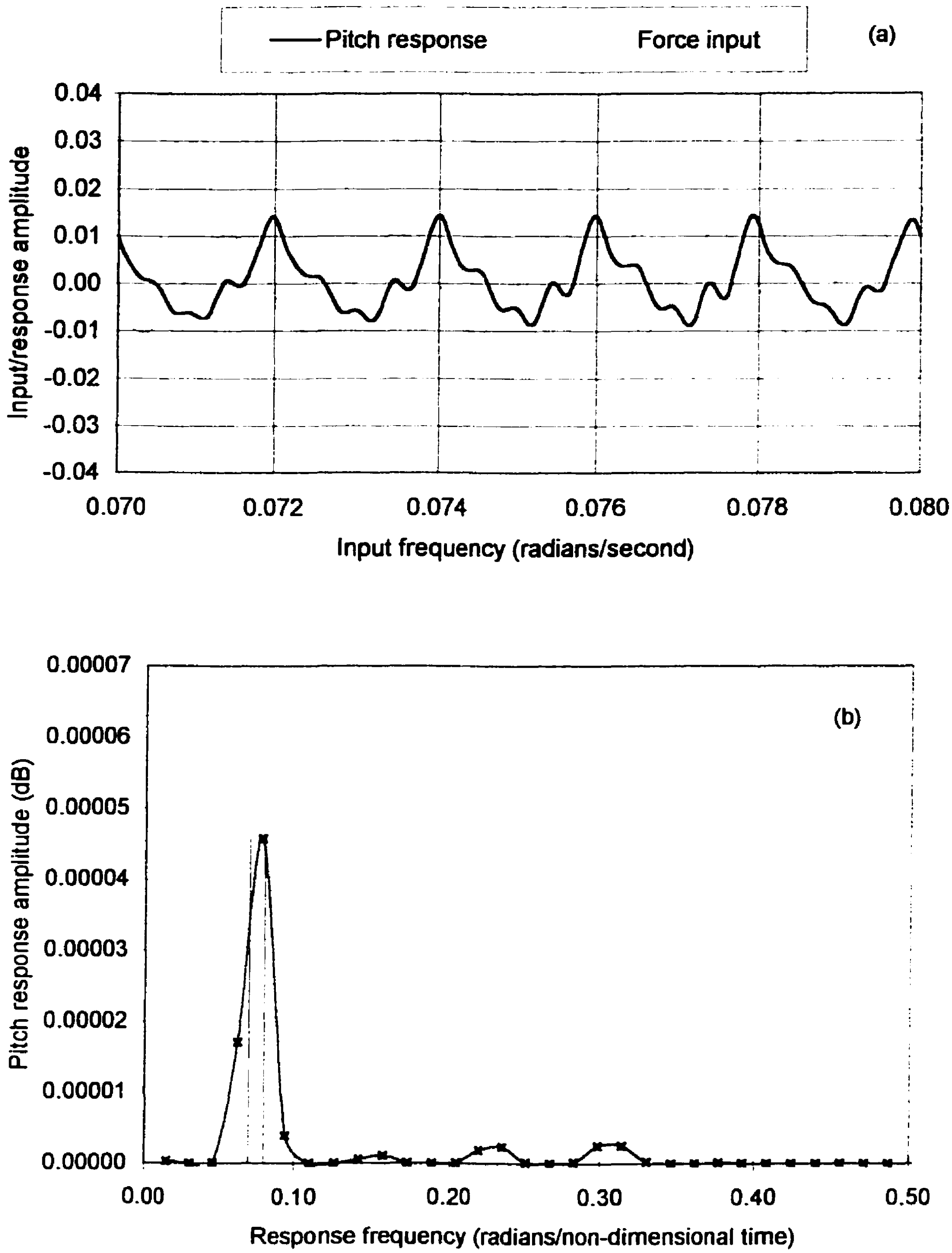

Figure 68. (a) Typical superharmonic waveform response at four times the forcing frequency. Pitch response to a decreasing sweep-rate of .000012 radians/(non-dimensional second)^2 at U/U*=73%. (b) Power spectral density plot of frequency response shown in (a). Vertical lines indicate input frequency range.

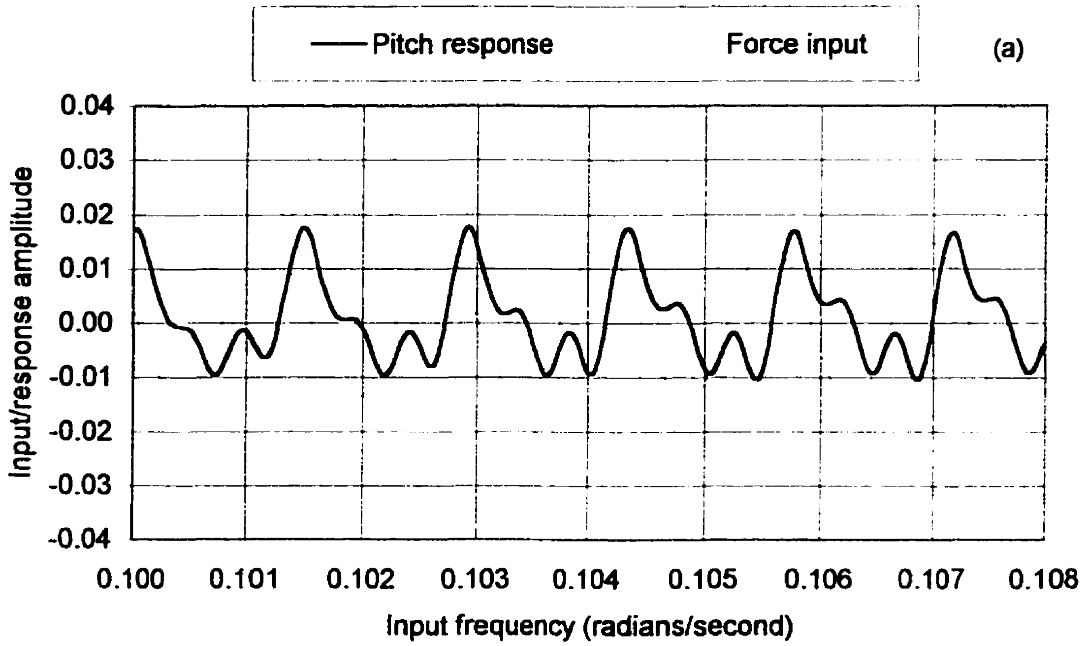

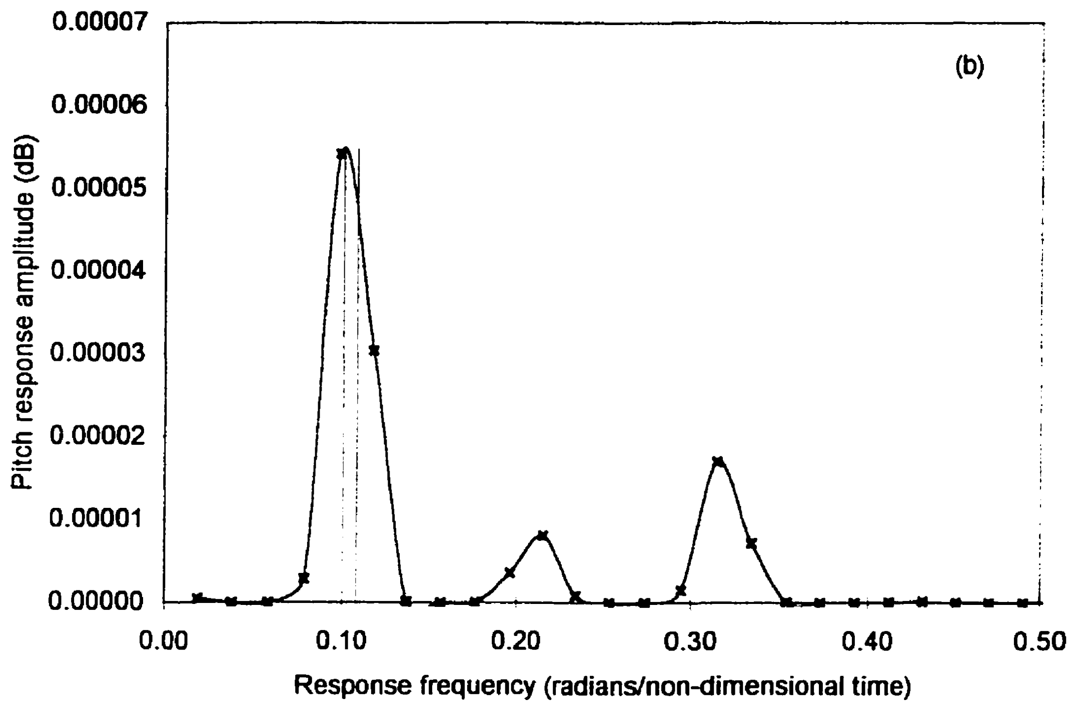

Figure 69. (a) Typical superharmonic waveform response at three times the forcing frequency. Pitch response to a decreasing sweep-rate of .000012 radians/(non-dimensional second)^2 at U/U*=73%. (b) Power spectral density plot of frequency response shown in (a). Vertical lines indicate input frequency range.

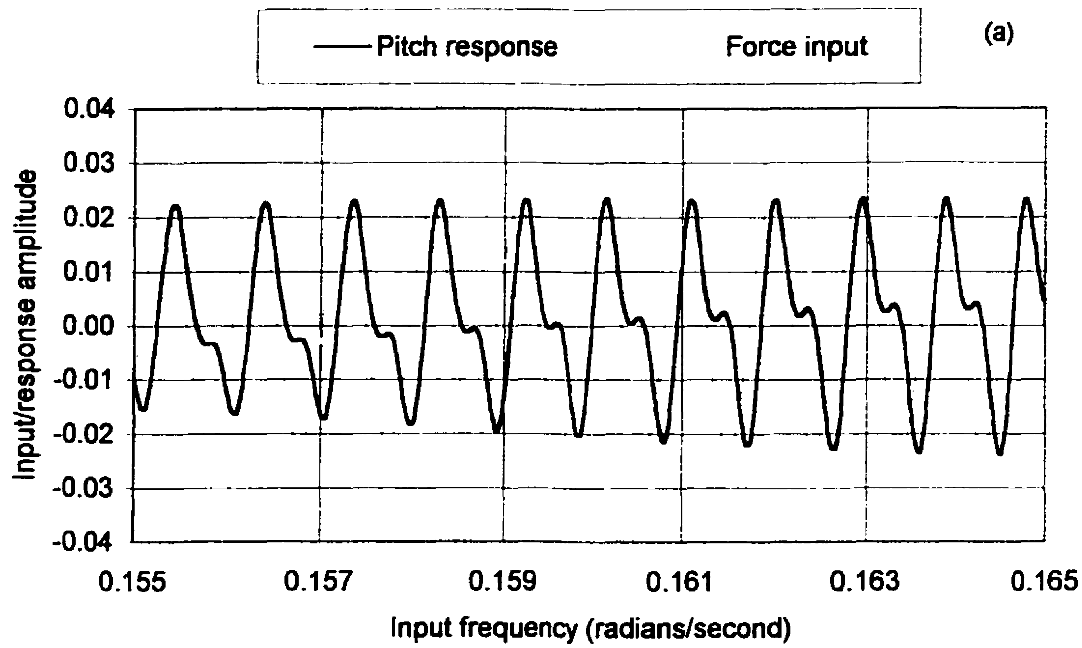

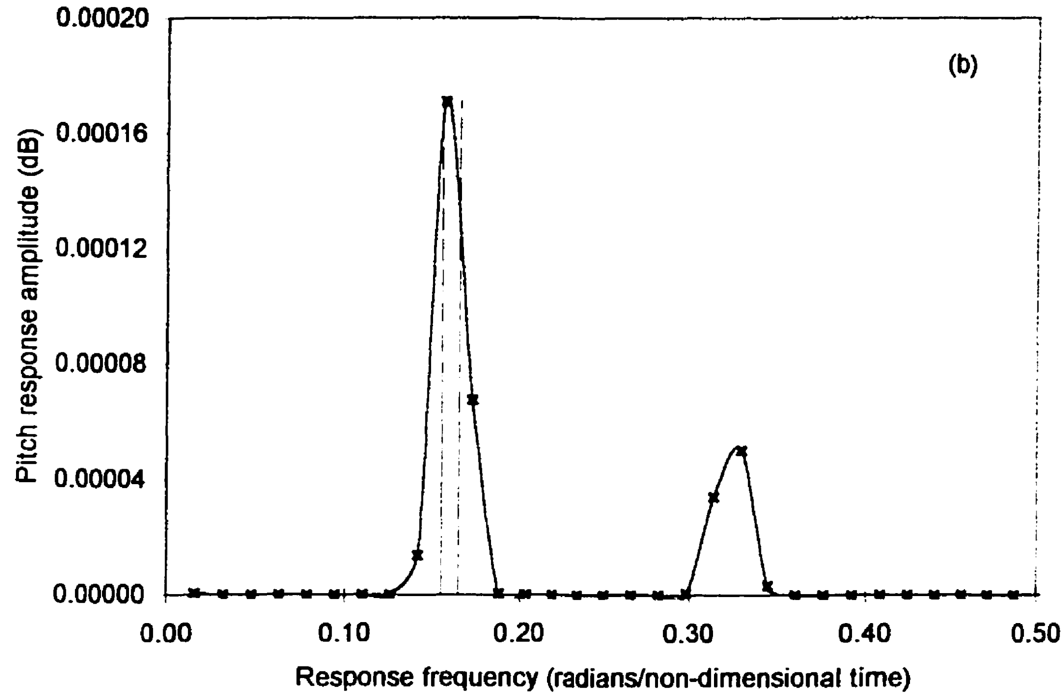

Figure 70. (a) Typical superharmonic waveform response at two times the forcing frequency. Pitch response to a decreasing sweep-rate of .000012 radians/(non-dimensional second)^2 at U/U*=73%. (b) Power spectral density plot of frequency response shown in (a). Vertical lines indicate input frequency range.

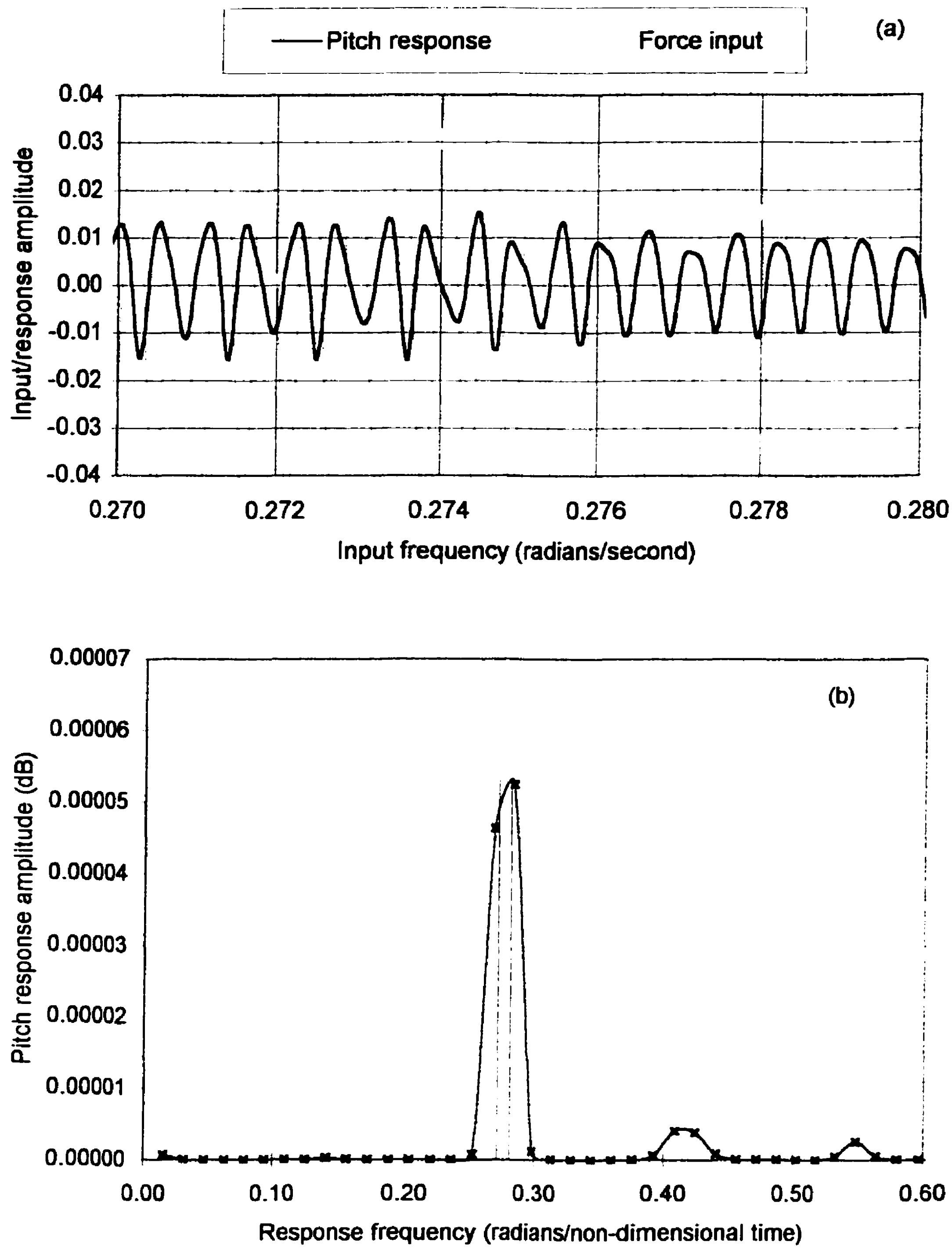

Figure 71. (a) Typical harmonic waveform response at one-and-a-half and two times the input frequency. Pitch response to a decreasing sweep-rate of .000012 radians/(non-dimensional second)^2 at U/U*=55%. (b) Power spectral density plot of frequency response shown in (a). Vertical lines indicate input frequency range.

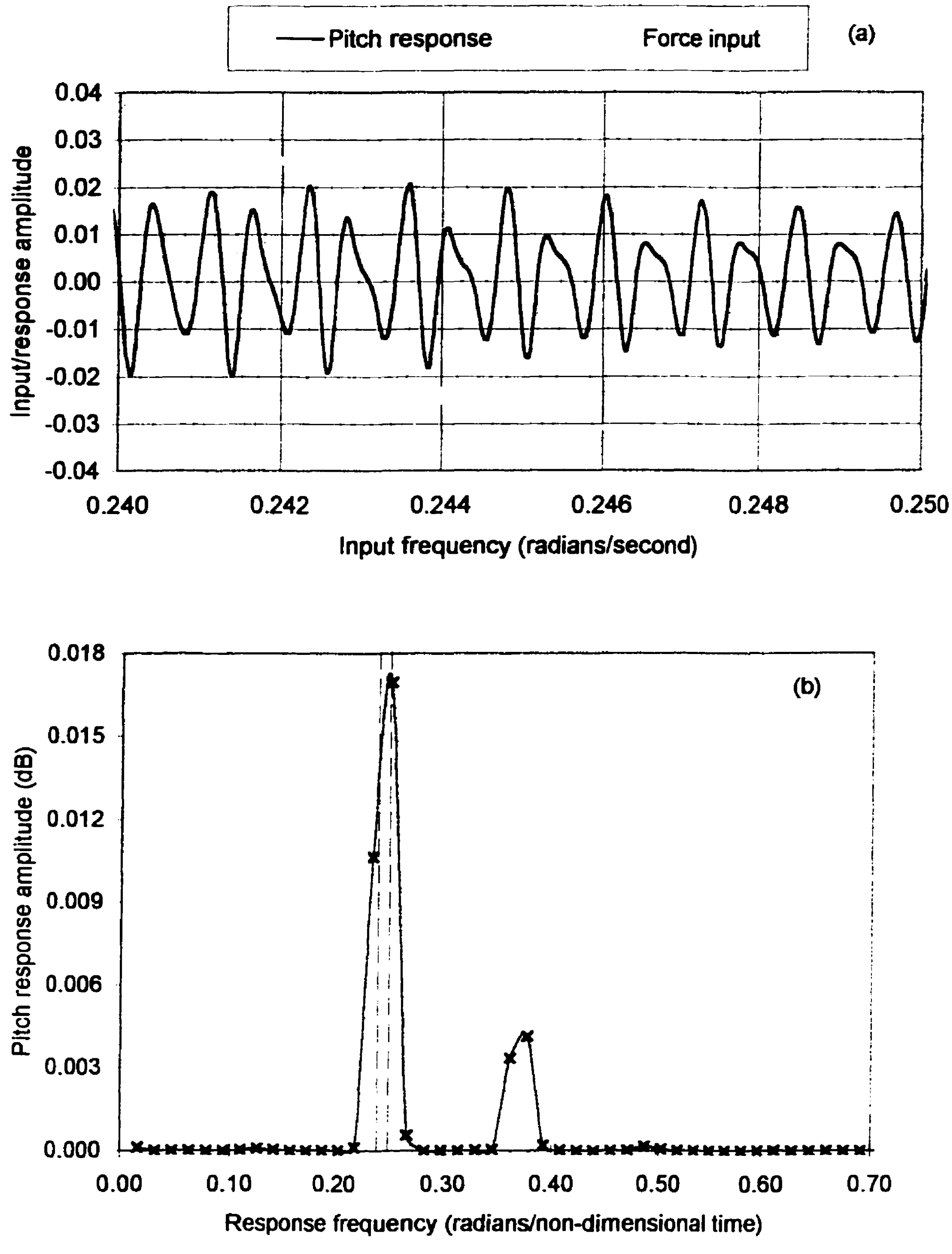

Figure 72. (a) Typical harmonic waveform response at one and a half times the input frequency. Pitch response to a decreasing sweep-rate of .000012 radians/(non-dimensional second)^2 at U/U*=64%. (b) Power spectral density plot of frequency response shown in (a). Vertical lines indicate input frequency range.

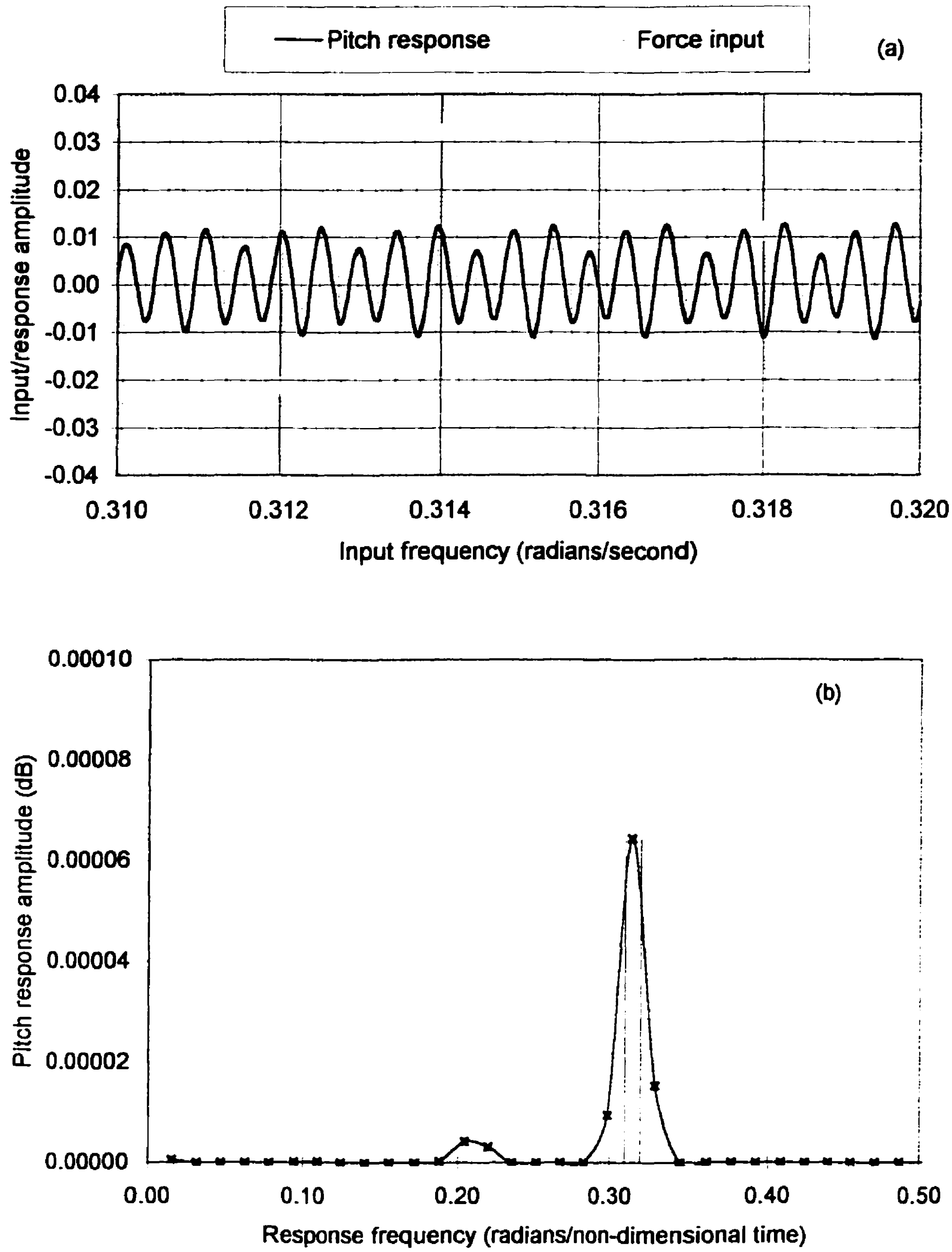

Figure 73. (a) Typical subharmonic waveform response at two thirds of the input frequency. Pitch response to a decreasing sweep-rate of .000012 radians/(non-dimensional second)^2 at U/U*=82%. (b) Power spectral density plot of frequency response shown in (a). Vertical lines indicate input frequency range.

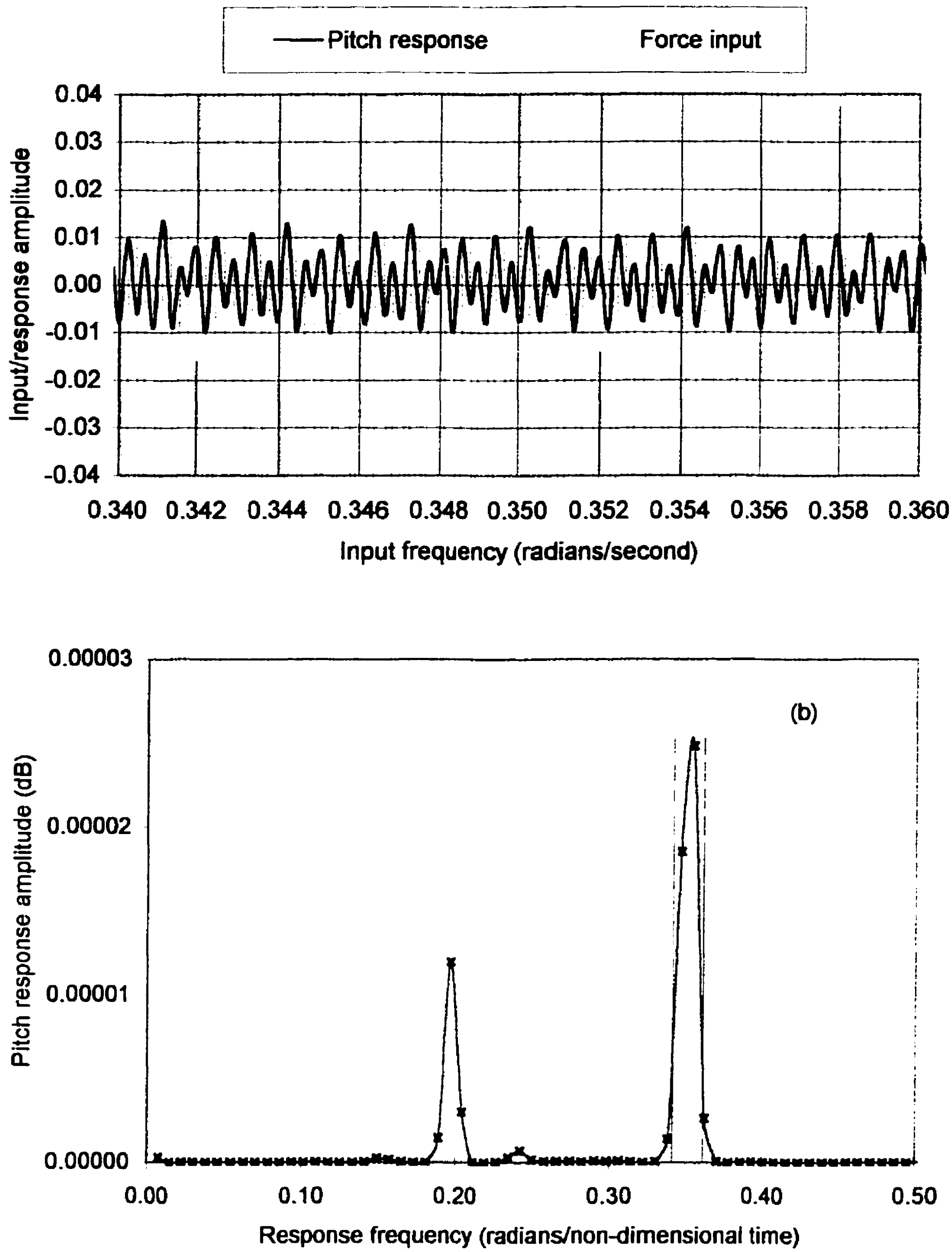

Figure 74. (a) Subharmonic waveform response at first mode natural frequency. Pitch response to a decreasing sweep-rate of .000012 radians/(non-dimensional second)^2 at U/U*=82%. (b) Power spectral density plot of frequency response shown in (a). Vertical lines indicate input frequency range.

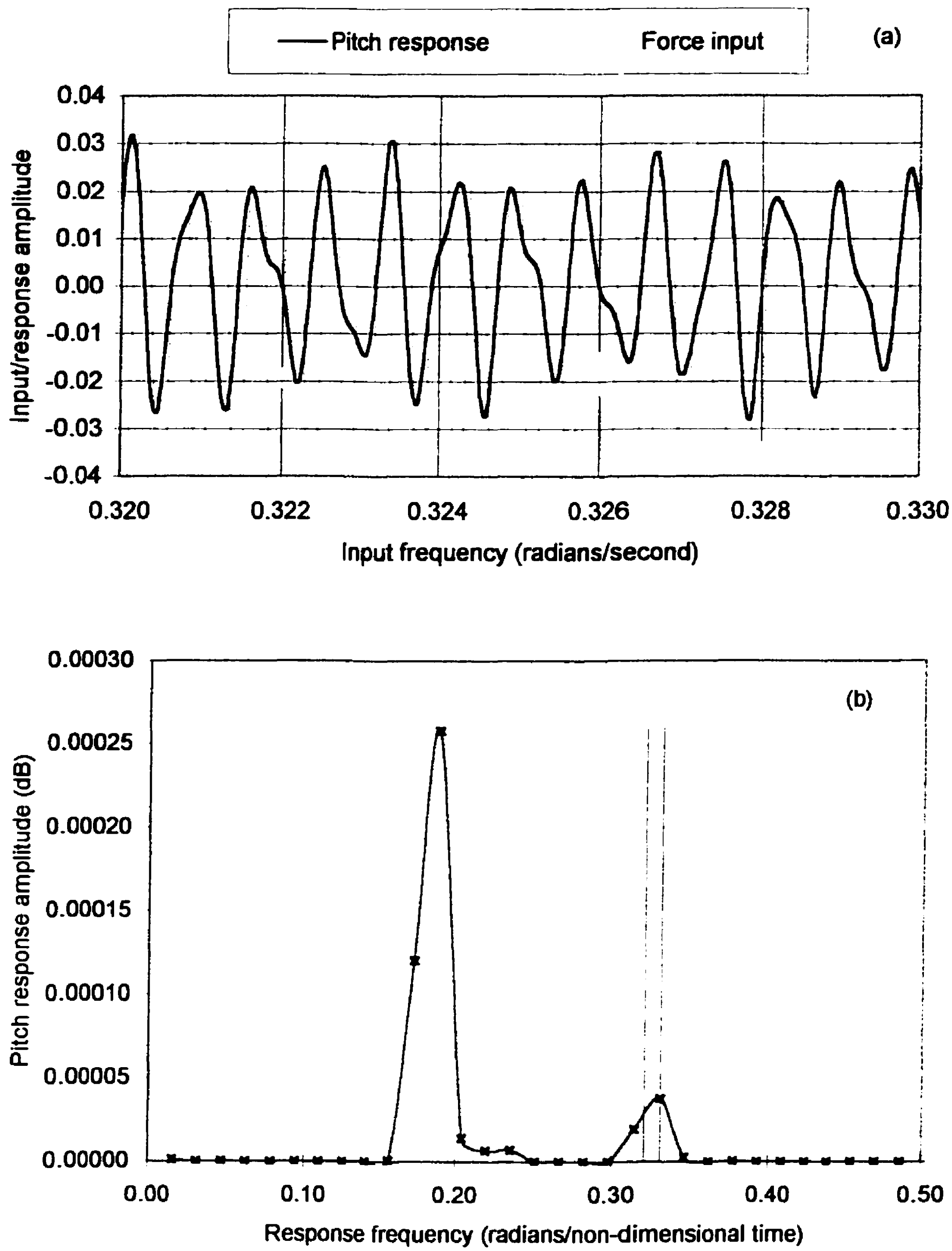

Figure 77. (a) Subharmonic waveform response at first mode natural frequency. Pitch response to a decreasing sweep-rate of .000012 radians/(non-dimensional second)^2 at U/U*=91%. (b) Power spectral density plot of frequency response shown in (a). Vertical lines indicate input frequency range.

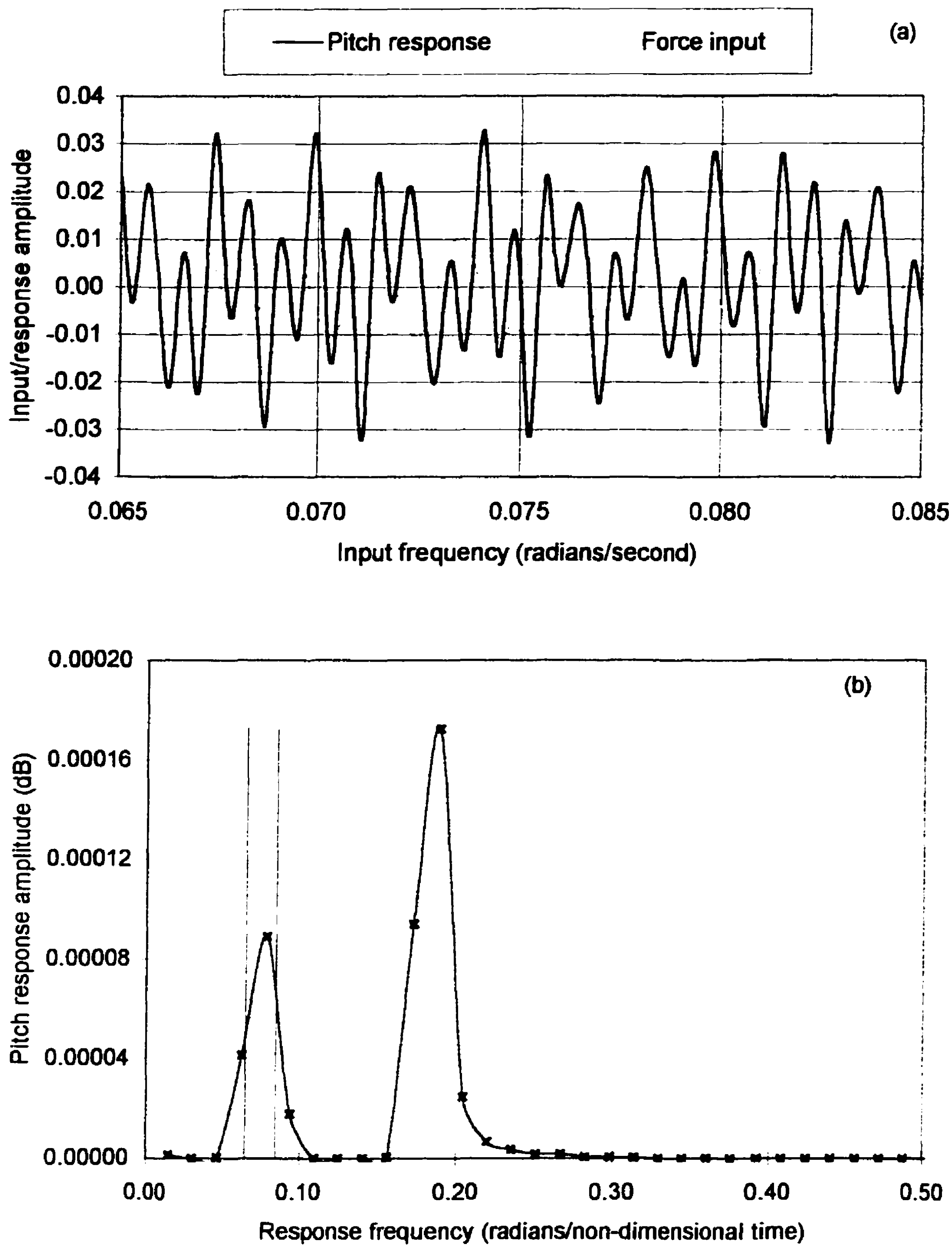

Figure 76. (a) Superharmonic waveform response at two and a half times the input frequency. Pitch response to a decreasing sweep-rate of .000012 radians/(non-dimensional second)^2 at U/U*=91%. (b) Power spectral density plot of frequency response shown in (a). Vertical lines indicate input frequency range.

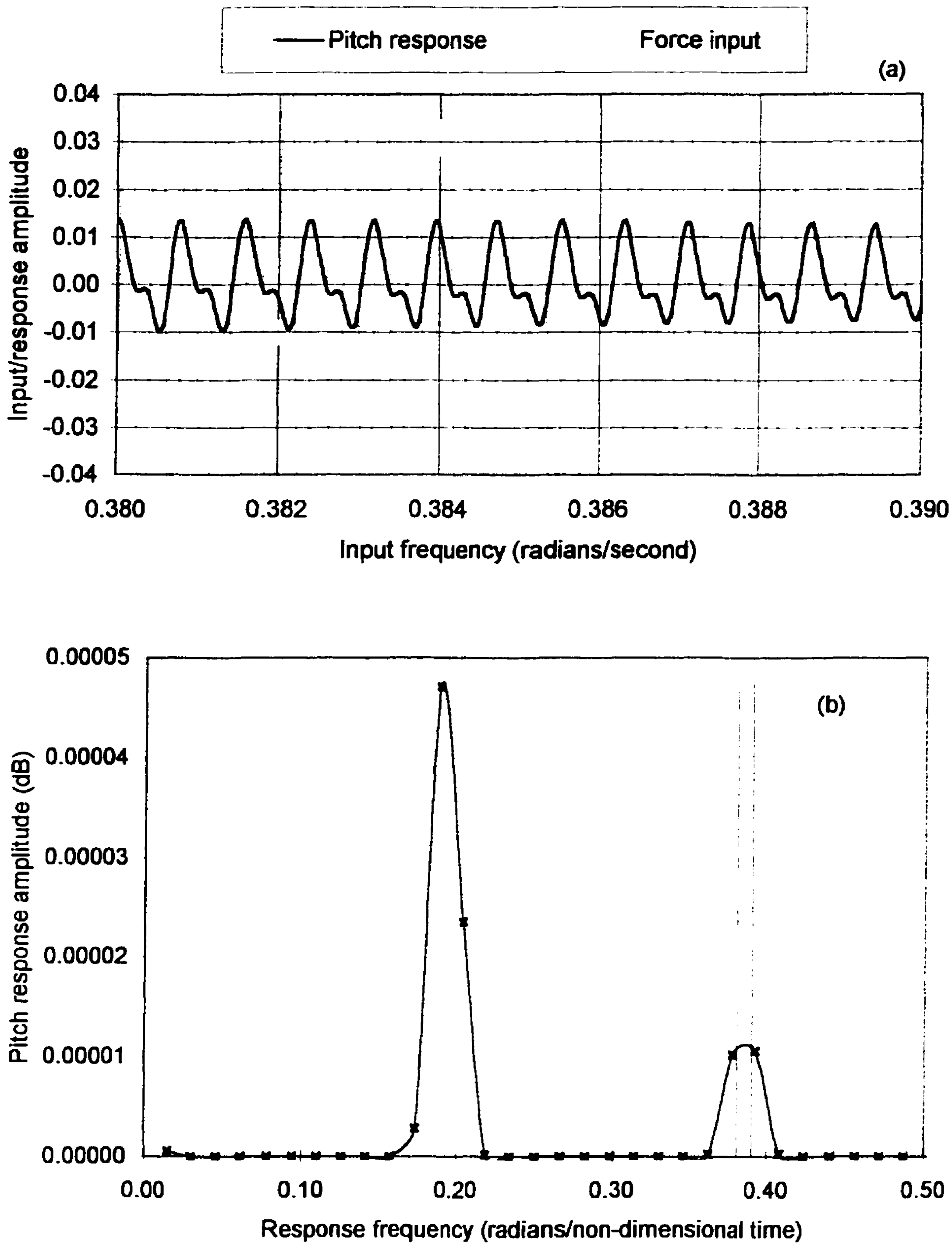

Figure 75. Subharmonic waveform response at first mode natural frequency. Pitch response to a decreasing sweep-rate of .000012 radians/(non-dimensional second)^2 at U/U*=82%. (b) Power spectral density plot of frequency response shown in (a). Vertical lines indicate input frequency range.

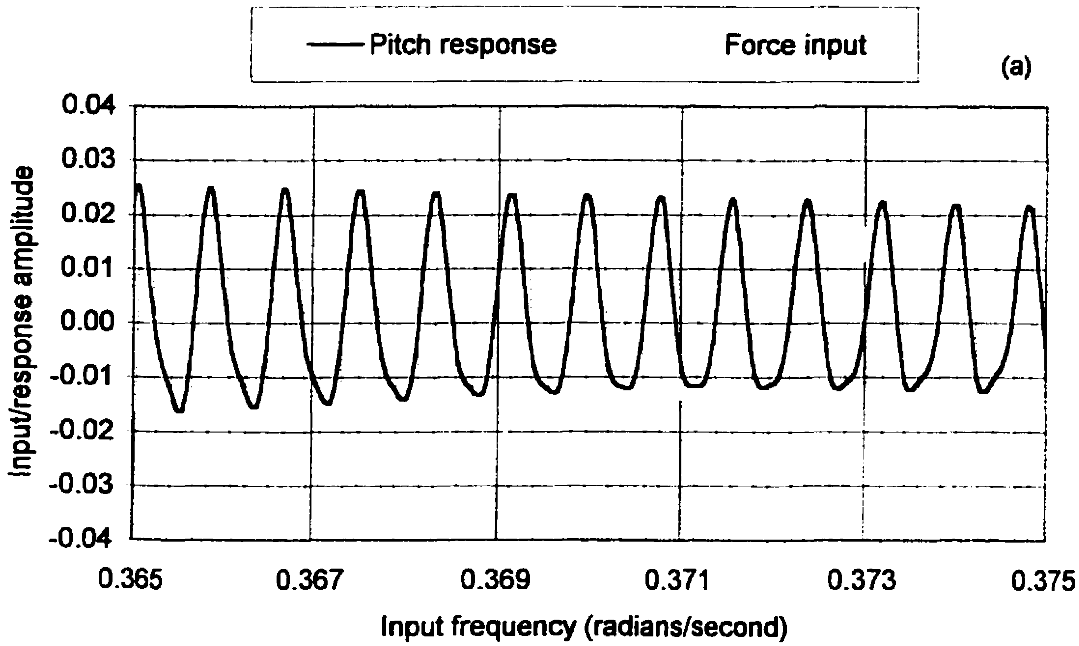

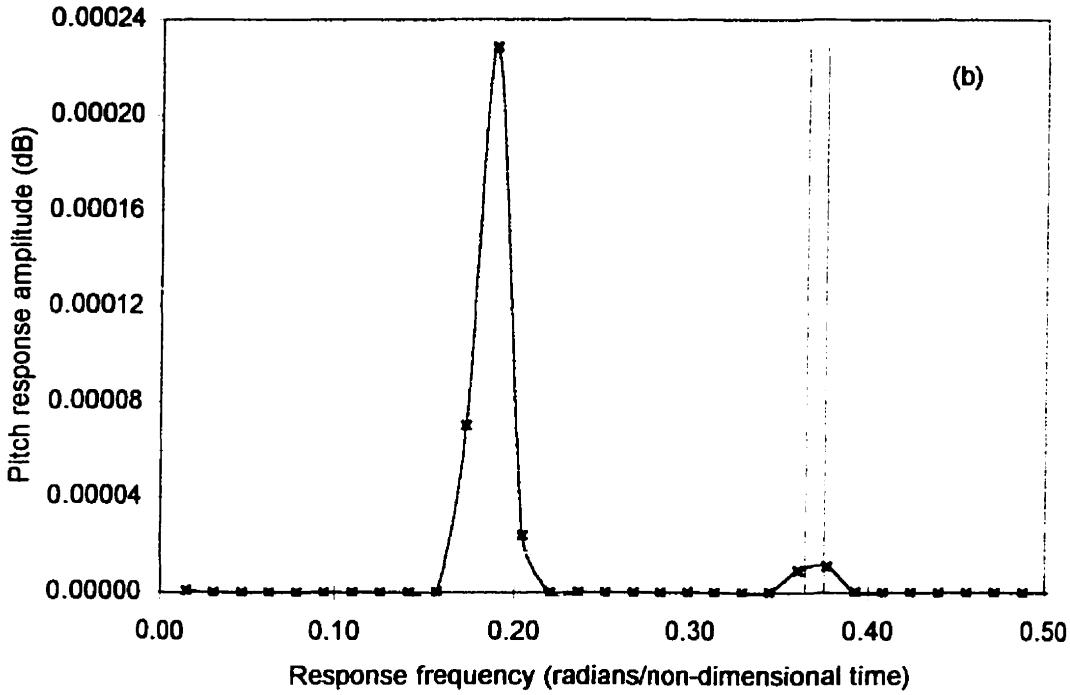

Figure 78. Subharmonic waveform response at first mode natural frequency. Pitch response to a decreasing sweep-rate of .000012 radians/(non-dimensional second)^2 at U/U*=91%. (b) Power spectral density plot of frequency response shown in (a). Vertical lines indicate input frequency range.

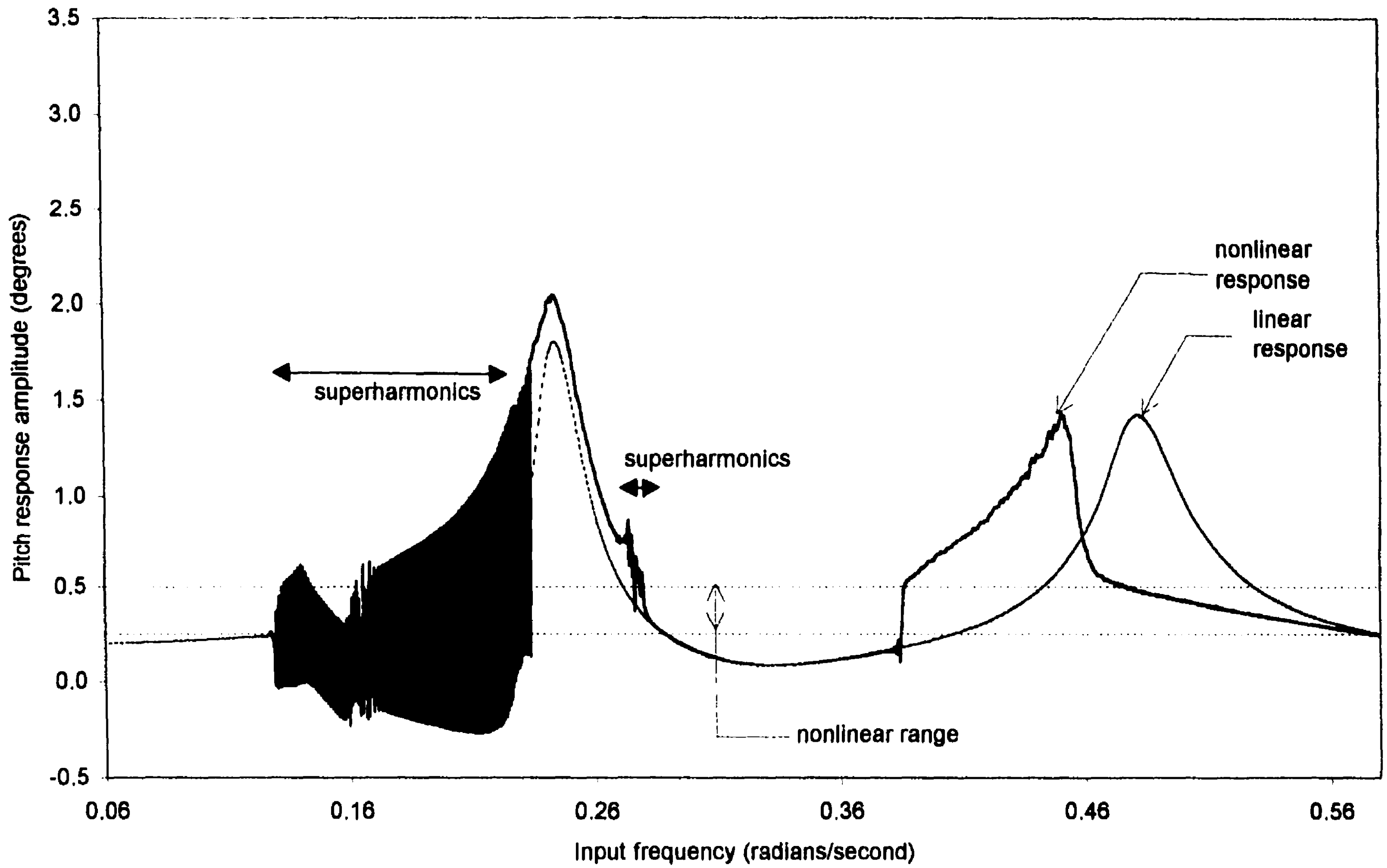

Figure 79. Linear and nonlinear pitch motion frequency response to a decreasing frequency sweep at a sweep-rate of .000012 radians/(non-dimensional second)^2, at U/U*=0.55. Dashed lines indicate upper and lower limits of freeplay region.

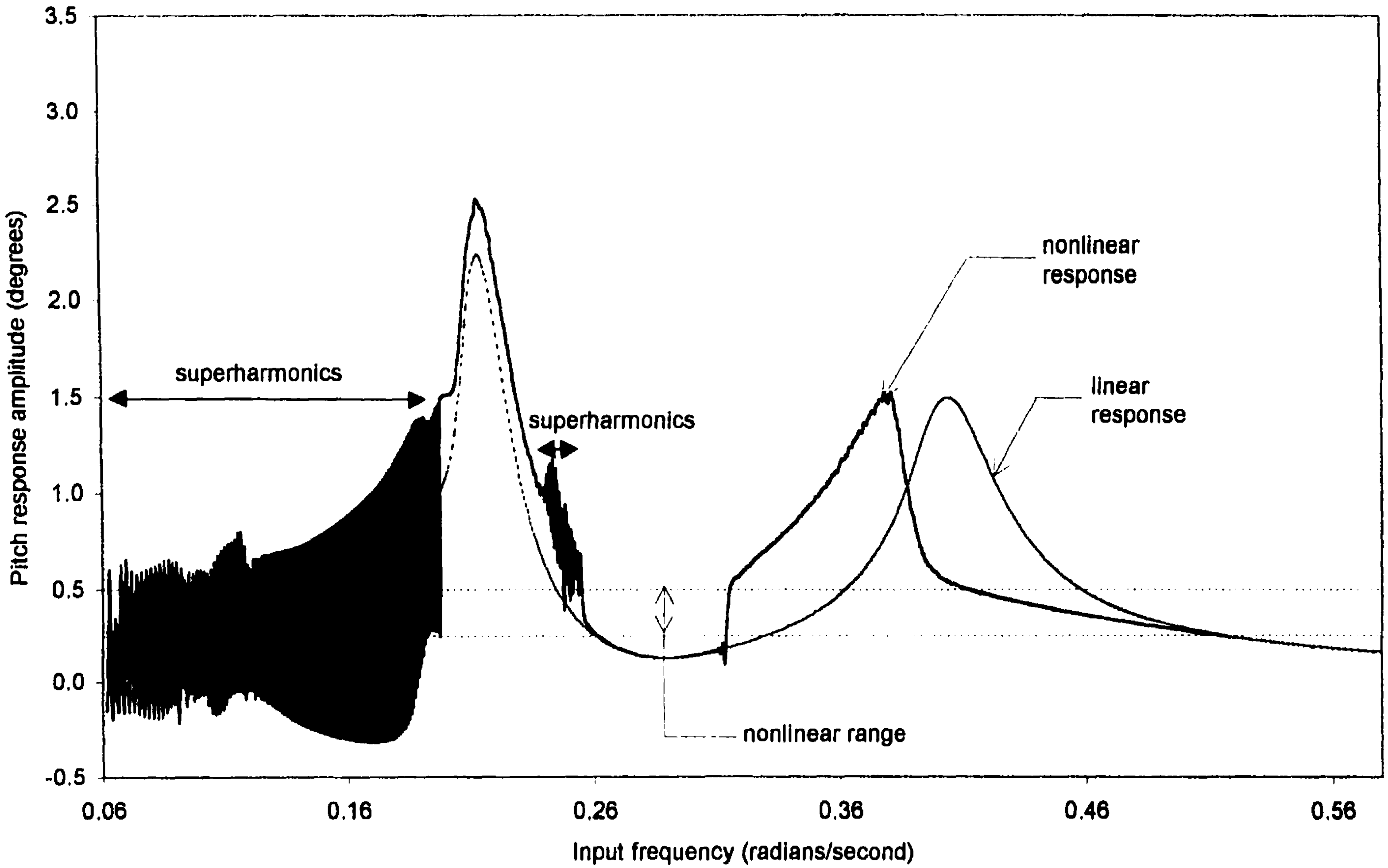

Figure 80. Linear and nonlinear pitch motion frequency response to a decreasing frequency sweep at a sweep-rate of .000012 radians/(non-dimensional second)^2, at U/U*=0.64. Dashed lines indicate upper and lower limits of freeplay region.

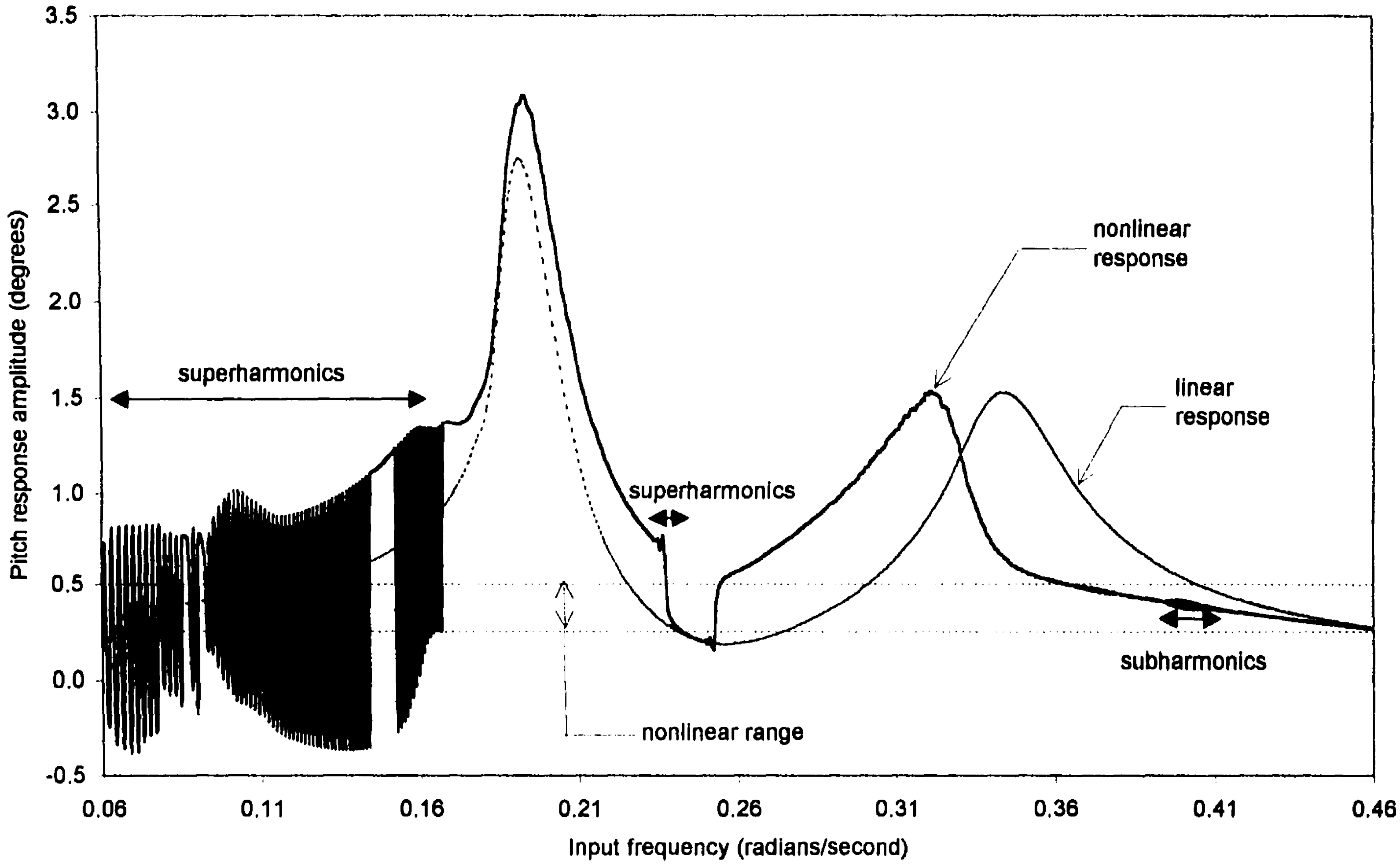

Figure 81. Linear and nonlinear pitch motion frequency response to a decreasing frequency sweep at a sweep-rate of .000012 radians/(non-dimensional second)^2, at U/U*=0.73. Dashed lines indicate upper and lower limits of freeplay region.

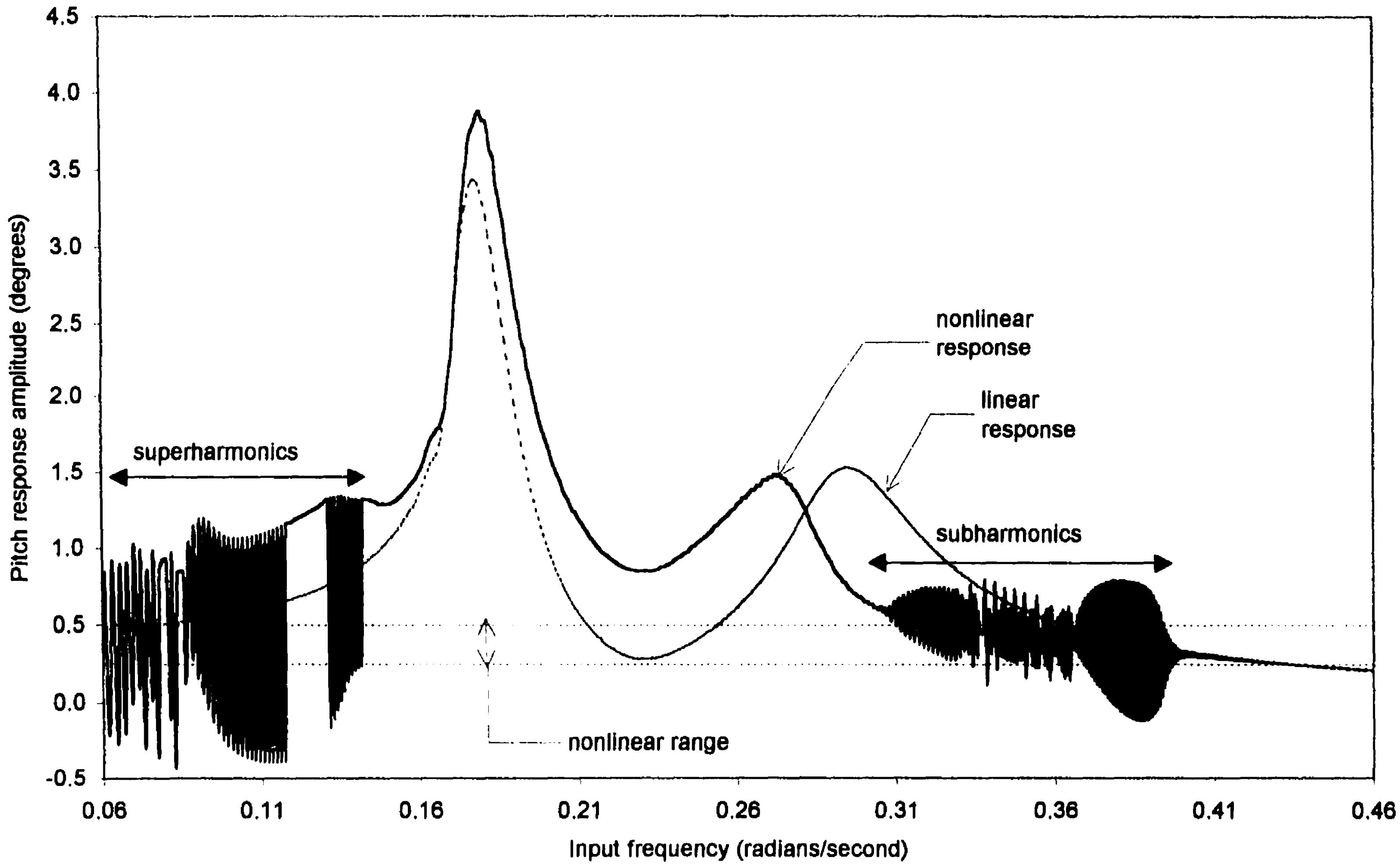

Figure 82. Linear and nonlinear pitch motion frequency response to a decreasing frequency sweep at a sweep-rate of .000012 radians/(non-dimensional second)^2, at U/U*=0.82. Dashed lines indicate upper and lower limits of freeplay region.

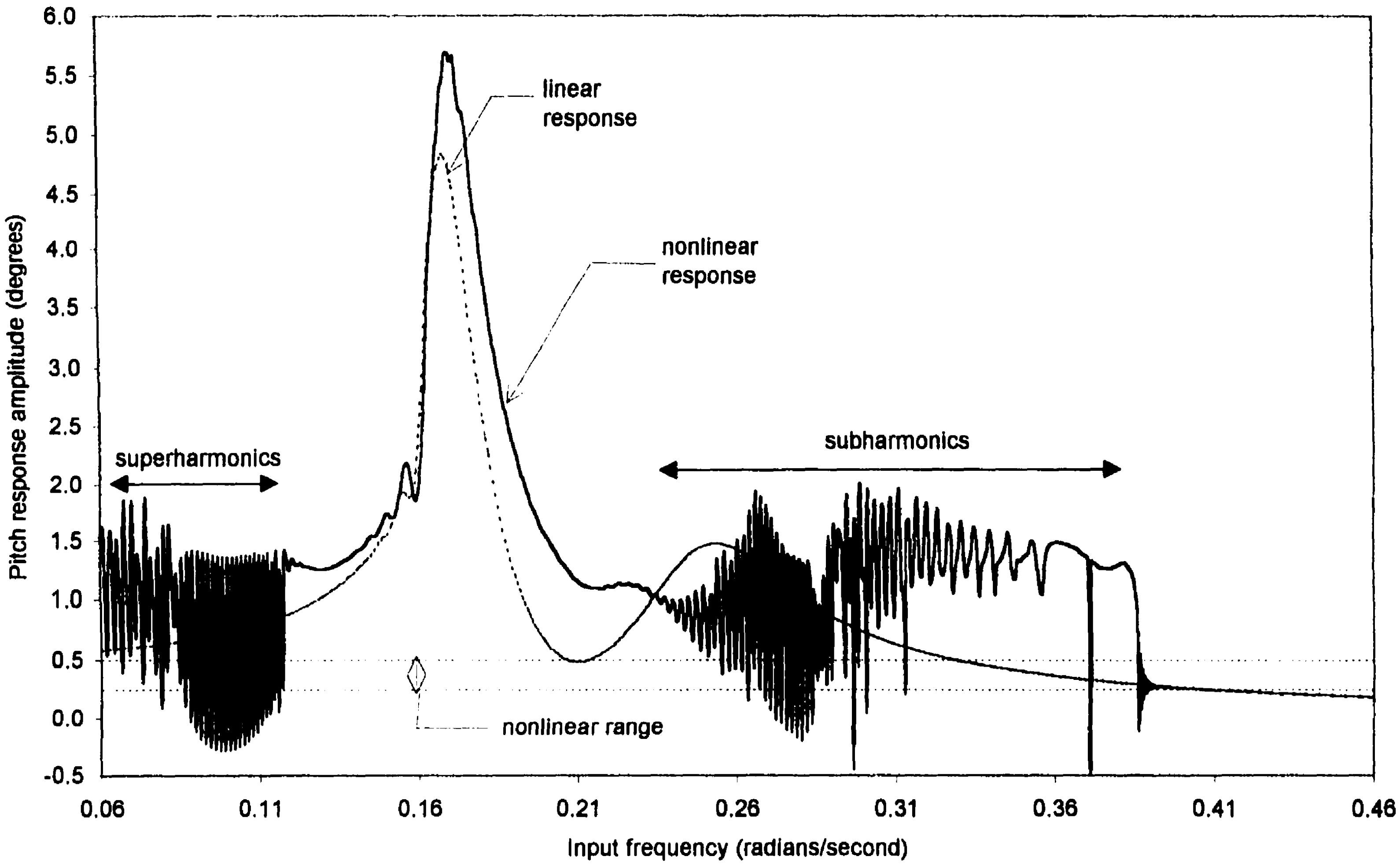

Figure 83. Linear and nonlinear pitch motion frequency response to a decreasing frequency sweep at a sweep-rate of .000012 radians/(non-dimensional second)^2, at U/U*=0.91. Dashed lines indicate upper and lower limits of freeplay region.

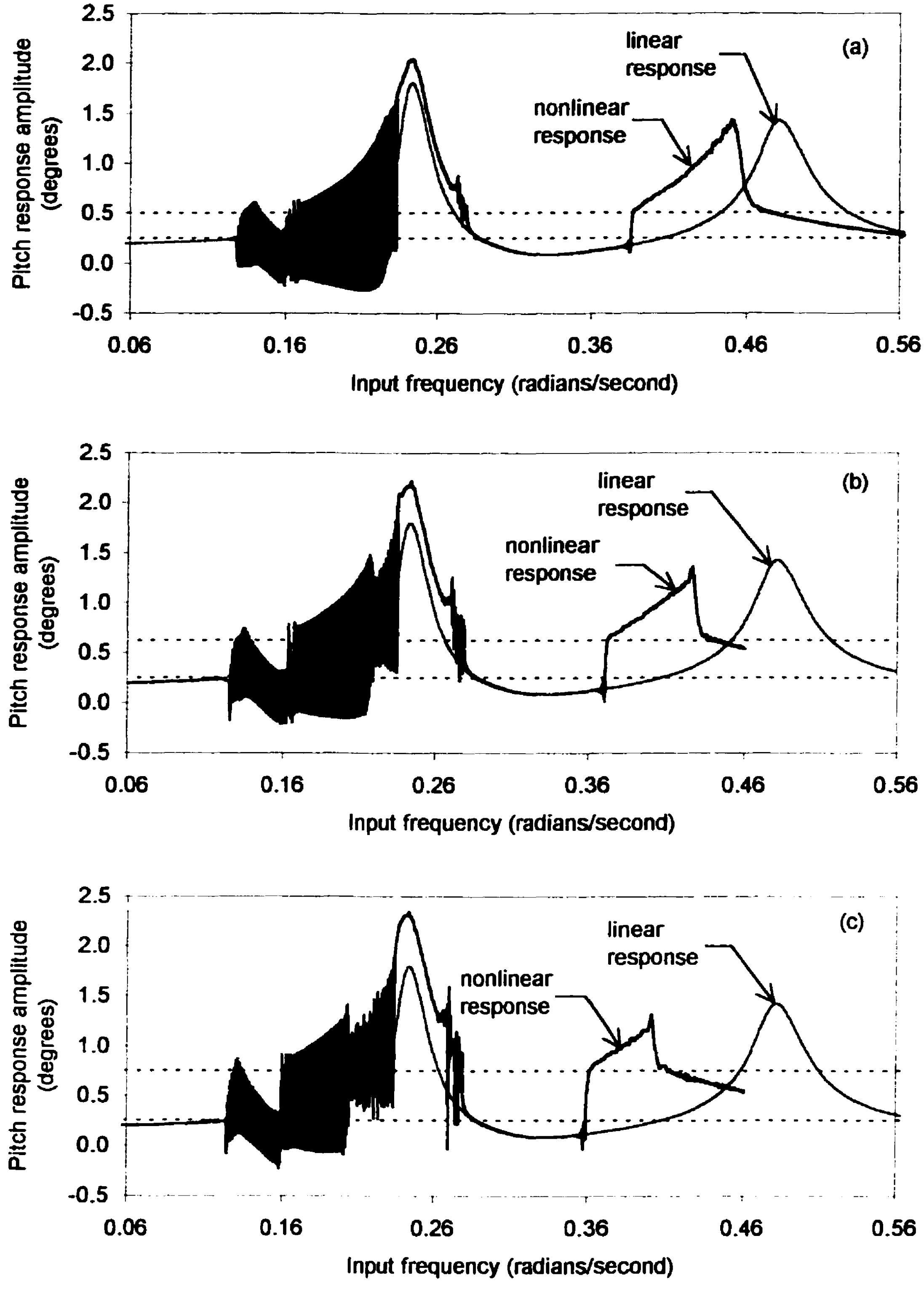

Figure 84. Linear and nonlinear frequency response to a decreasing frequency sweep at a sweep-rate of .000012 radians/(non-dimensional second)^2, and a non-dimensional airspeed ratio of U/U*=0.55. Nonlinear curves obtained for nonlinear region lengths of (a) .25 degrees, (b) .5 degrees and (c) .75 degrees.

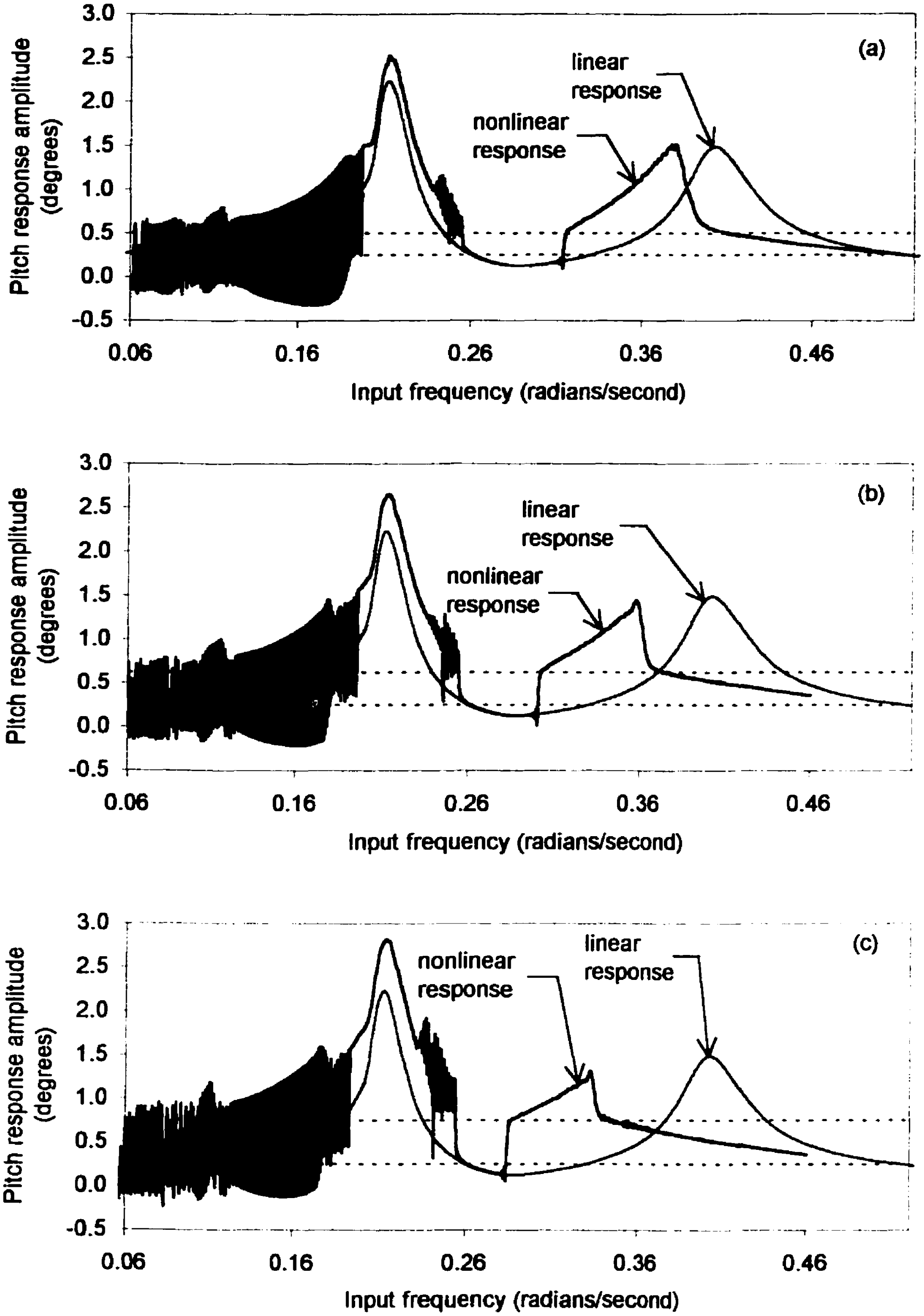

Figure 85. Linear and nonlinear frequency response to a decreasing frequency sweep at a sweep-rate of .000012 radians/(non-dimensional second)^2, and a non-dimensional airspeed equivalent to U/U*=0.64. Nonlinear curves obtained for nonlinear region lengths of (a) .25 degrees, (b) .5 degrees and (c) .75 degrees.

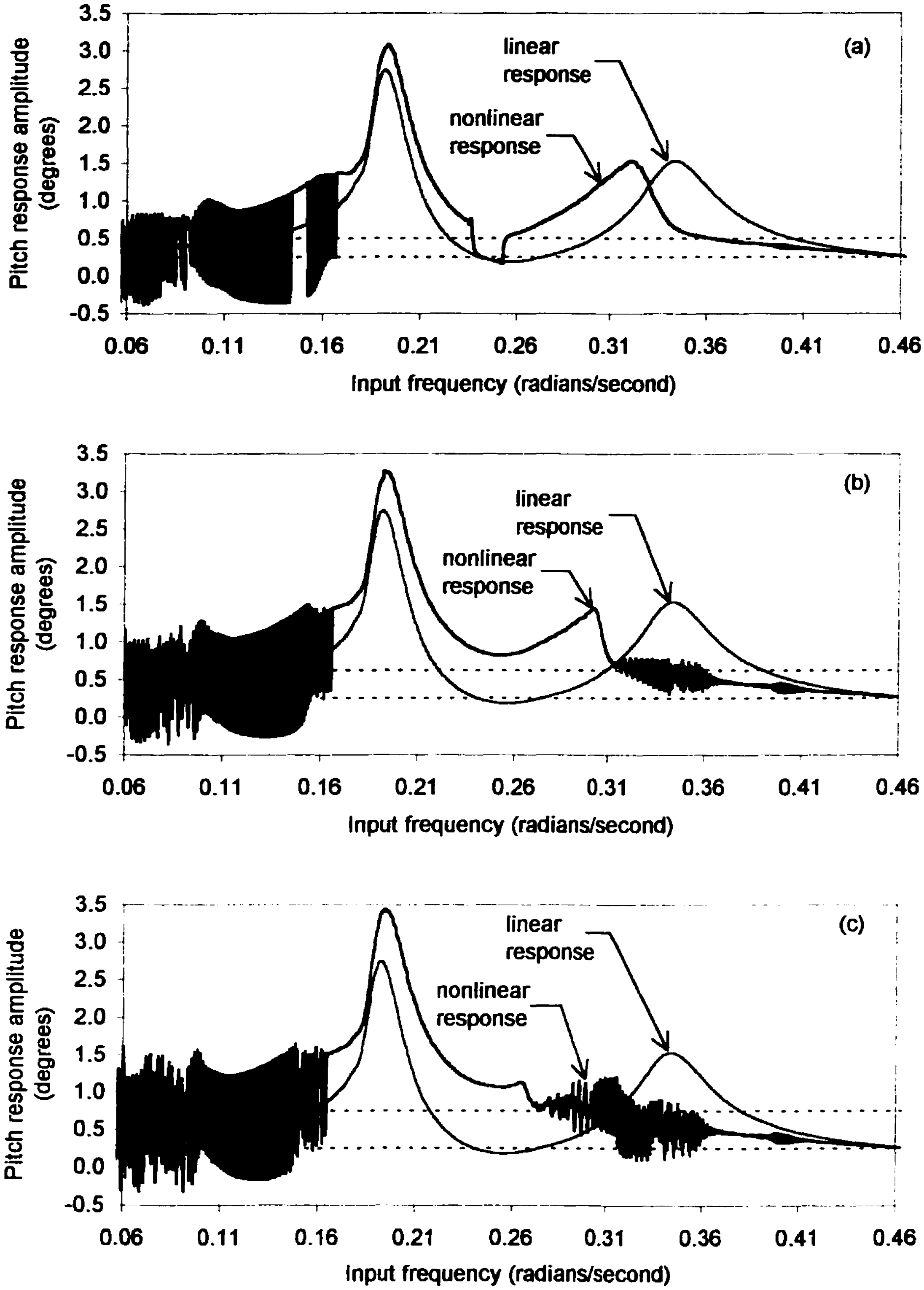

Figure 86. Linear and nonlinear frequency response to a decreasing frequency sweep at a sweep-rate of .000012 radians/(non-dimensional second)^2, and a non-dimensional airspeed equivalent to U/U*=0.73. Nonlinear curves obtained for nonlinear region lengths of (a) .25 degrees, (b) .5 degrees and (c) .75 degrees.

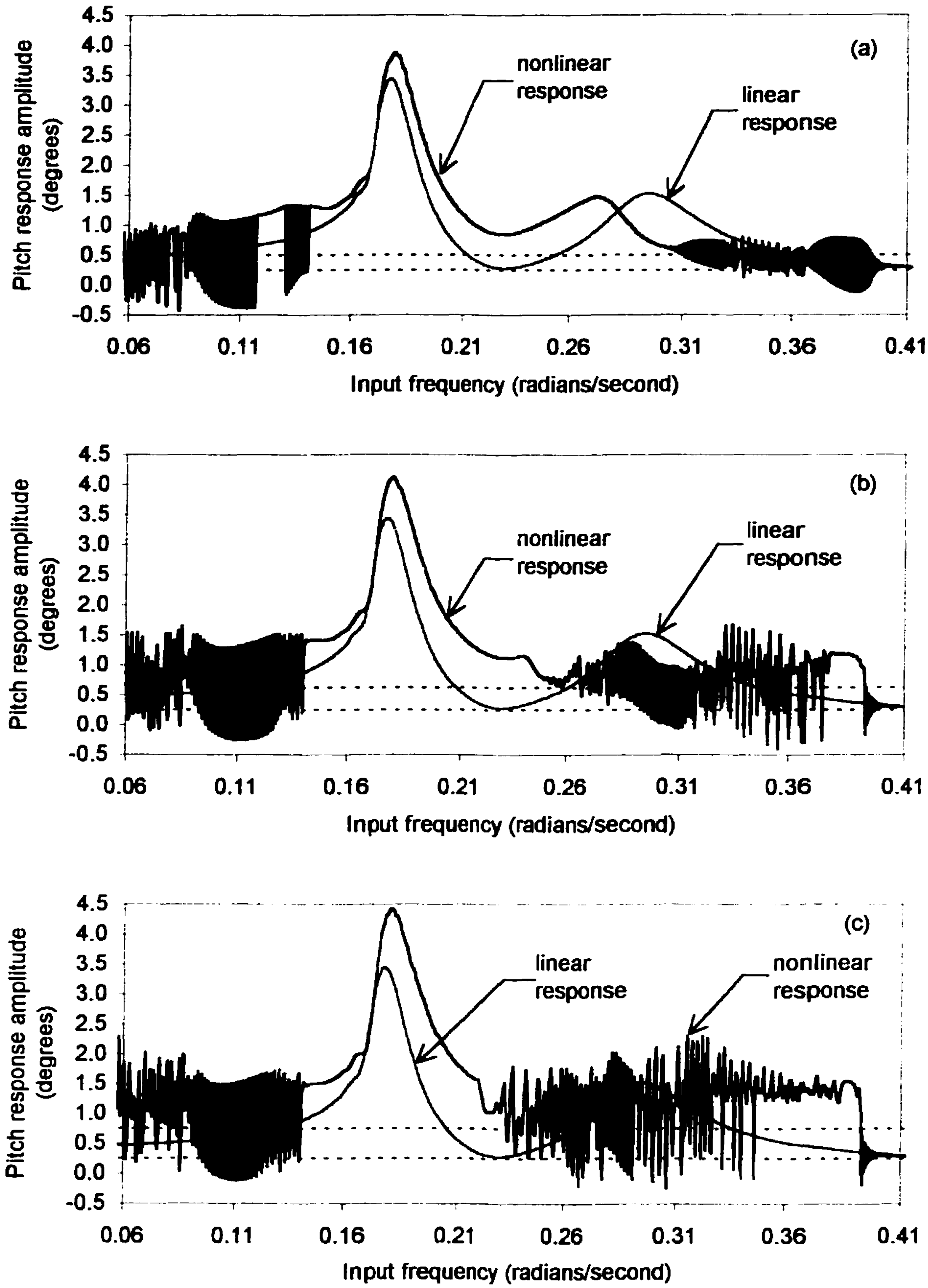

Figure 87. Linear and nonlinear frequency response to a decreasing frequency sweep at a sweep-rate of .000012 radians/(non-dimensional second)^2, and a non-dimensional airspeed equivalent to U/U*=0.82. Nonlinear curves obtained for nonlinear region lengths of (a) .25 degrees, (b) .5 degrees and (c) .75 degrees.

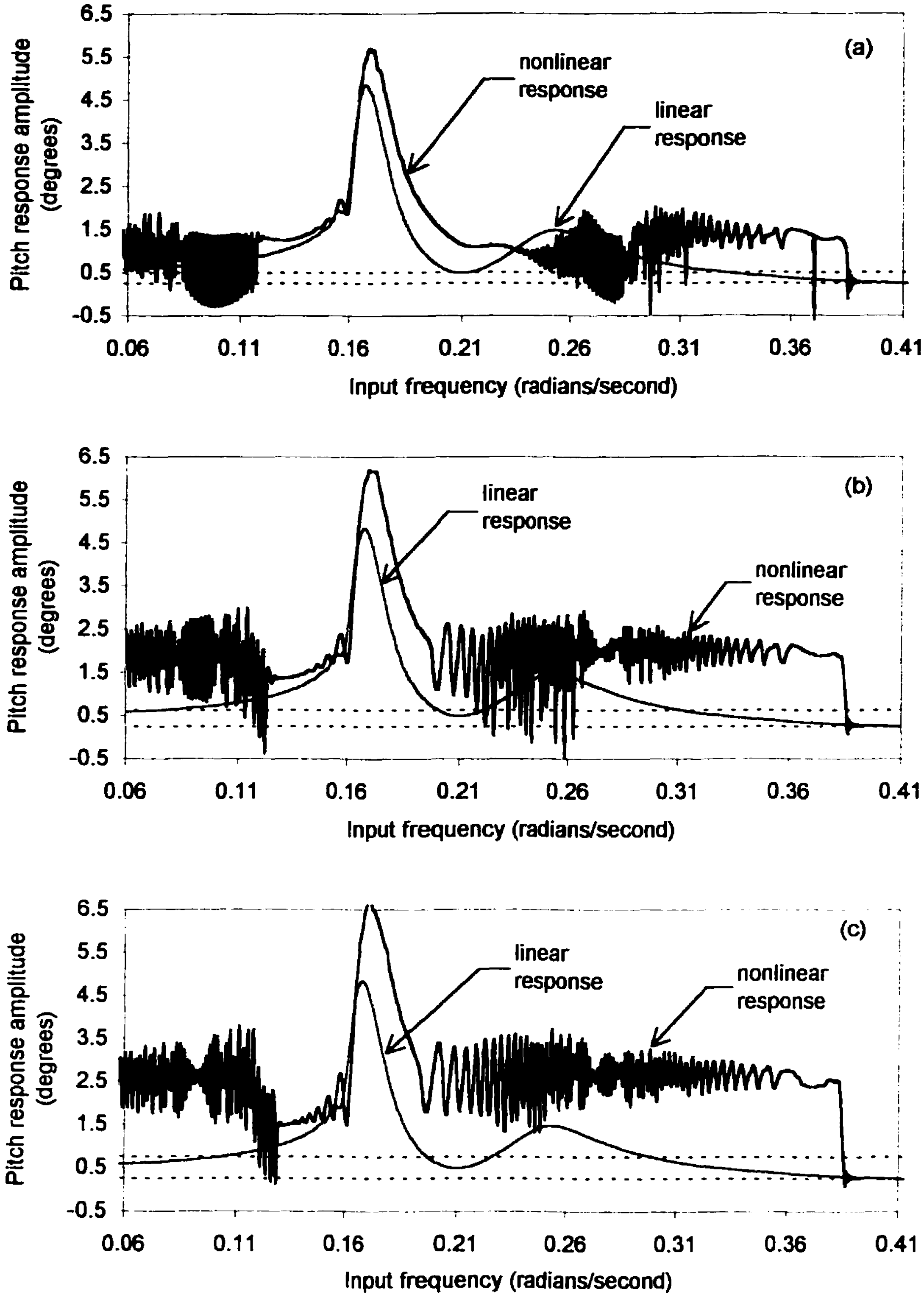

Figure 88. Linear and nonlinear frequency response to a decreasing frequency sweep at a sweep-rate of .000012 radians/(non-dimensional second)^2, and a non-dimensional airspeed of U/U*=0.91. Nonlinear curves obtained for nonlinear region lengths of (a) .25 degrees, (b) .5 degrees and (c) .75 degrees.

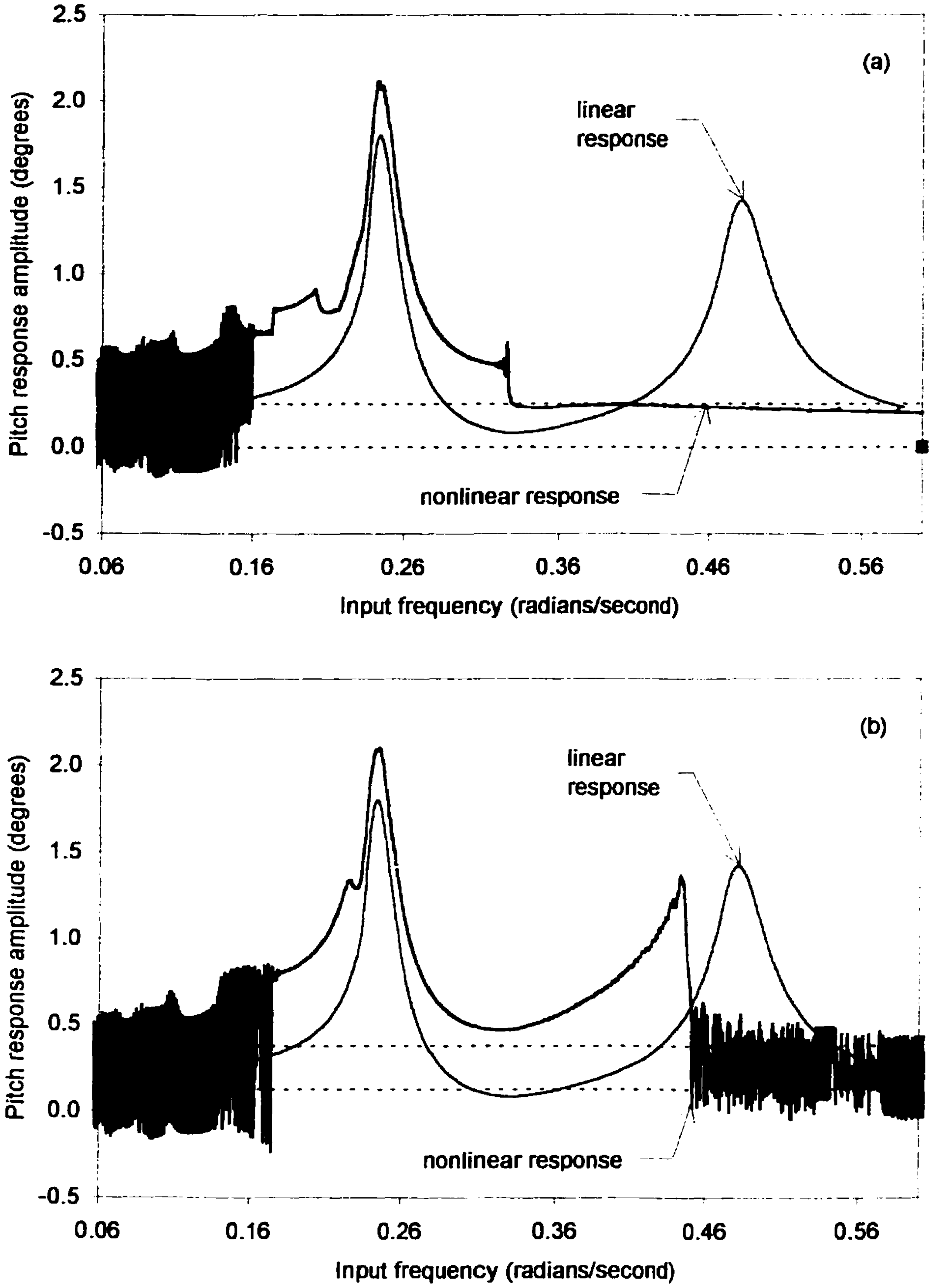

Figure 89. Linear and nonlinear frequency responses to a decreasing frequency sweep at a sweep-rate of .000012 radians/(non-dimensional second)^2, and a non-dimensional airspeed equivalent to U/U*=0.55. Nonlinear curves obtained for a nonlinear region length of 0.25 degrees and a preload of (a) 0.0 degrees, and (b) 0.125 degrees.

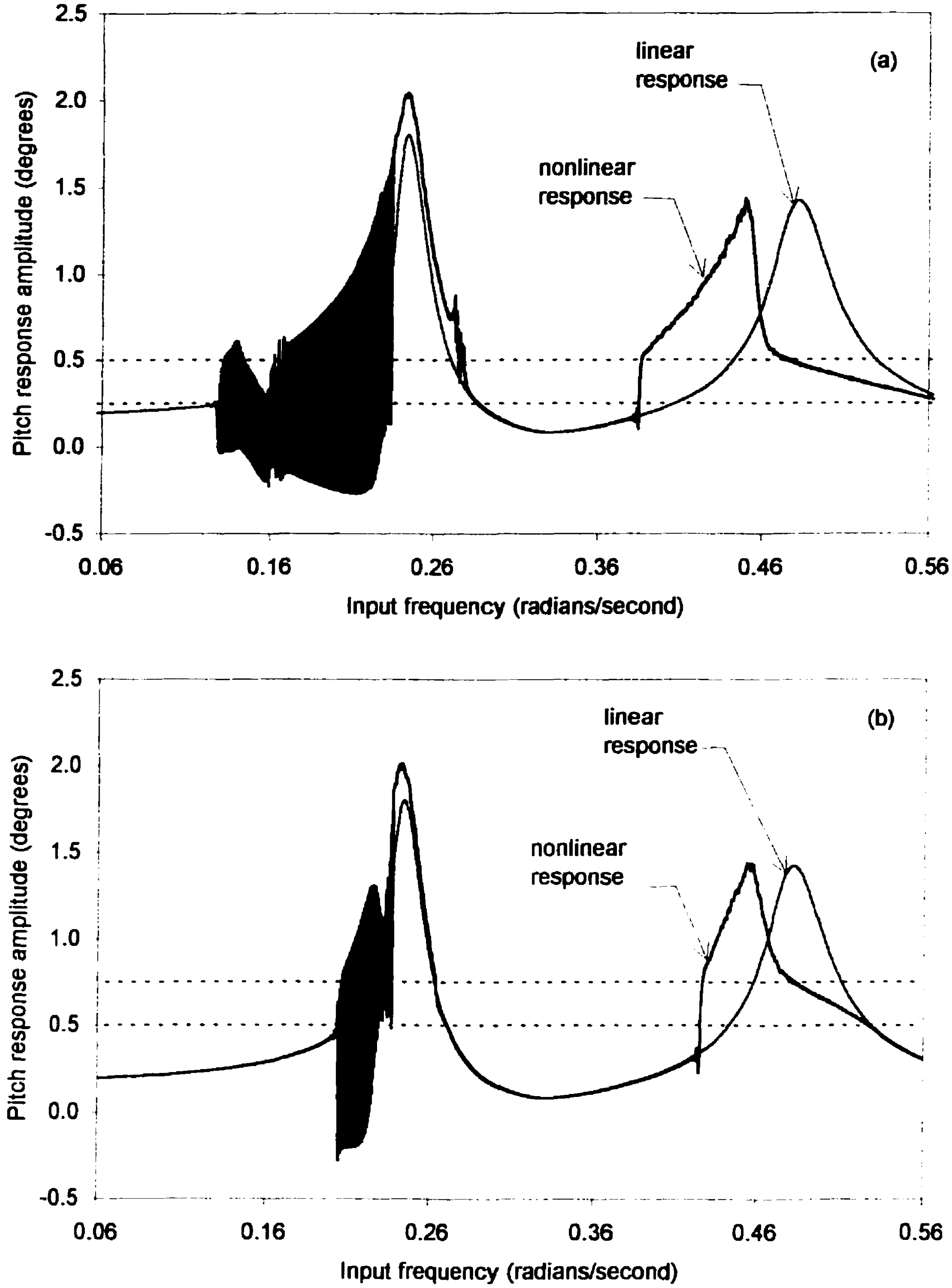

Figure 90. Linear and nonlinear frequency responses to a decreasing frequency sweep at a sweep-rate of .000012 radians/(non-dimensional second)^2, and a non-dimensional airspeed equivalent to U/U*=0.55. Nonlinear curves obtained for a nonlinear region length of 0.25 degrees and a preload of (a) 0.25 degrees, and (b) 0.50 degrees.

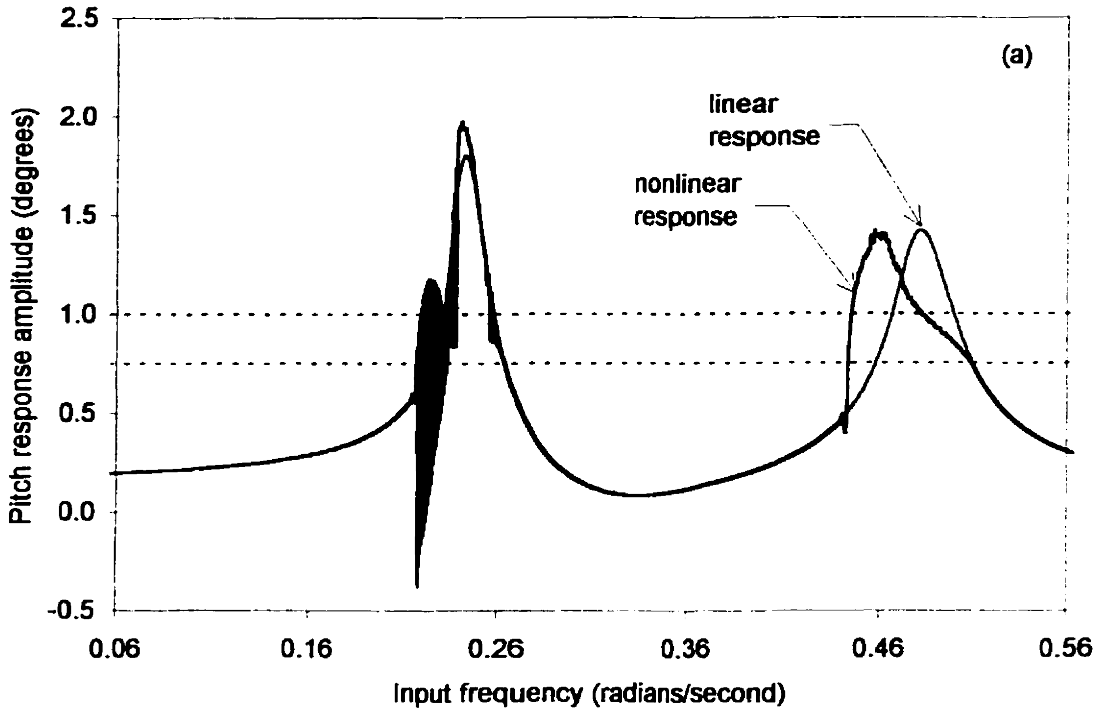

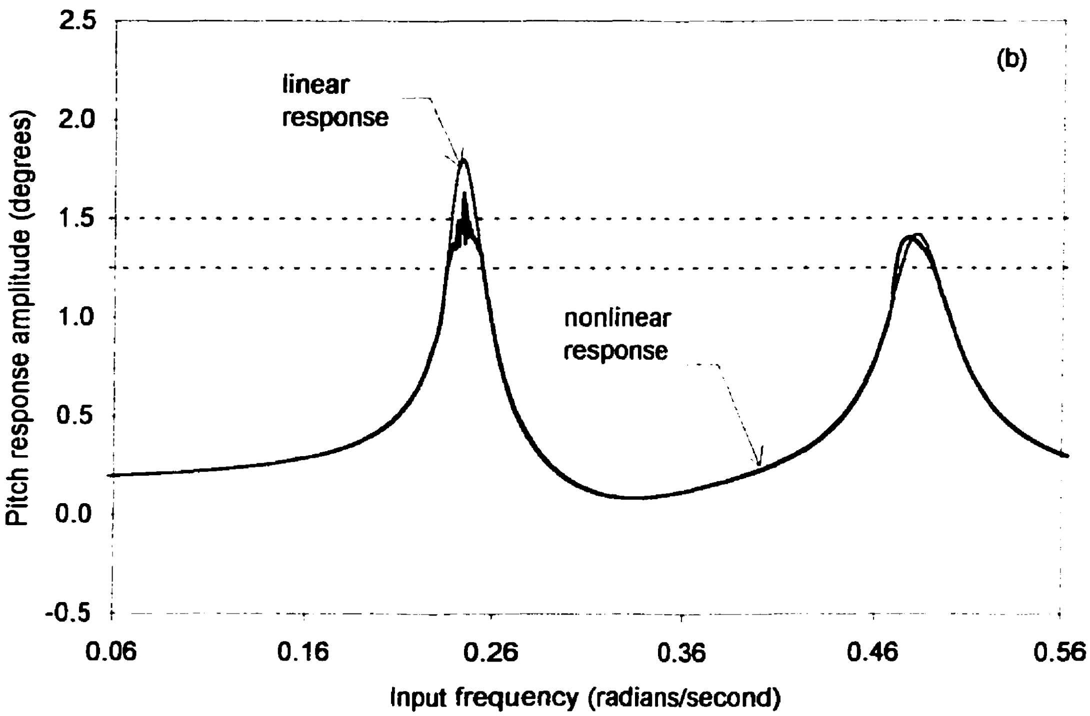

Figure 91. Linear and nonlinear frequency responses to a decreasing frequency sweep at a sweep-rate of .000012 radians/(non-dimensional second)^2, and a non-dimensional airspeed equivalent to U/U*=0.55. Nonlinear curves obtained for a nonlinear region length of 0.25 degrees and a preload of (a) 0.75 degrees, and (b) 1.25 degrees.

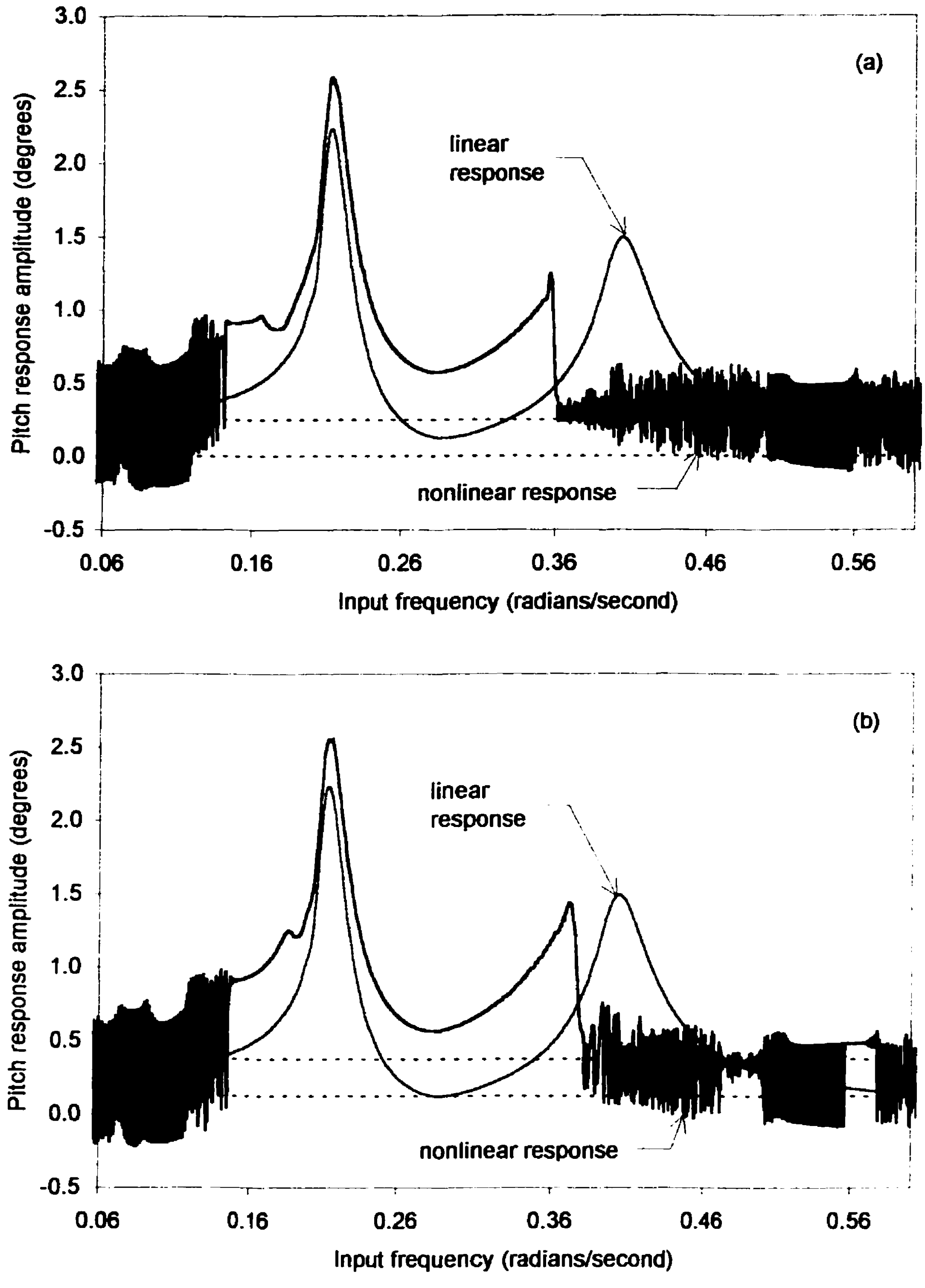

Figure 92. Linear and nonlinear frequency responses to a decreasing frequency sweep at a sweep-rate of .000012 radians/(non-dimensional second)^2, and a non-dimensional airspeed equivalent to U/U*=0.64. Nonlinear curves obtained for a nonlinear region length of 0.25 degrees and a preload of (a) 0.0 degrees, and (b) 0.125 degrees.

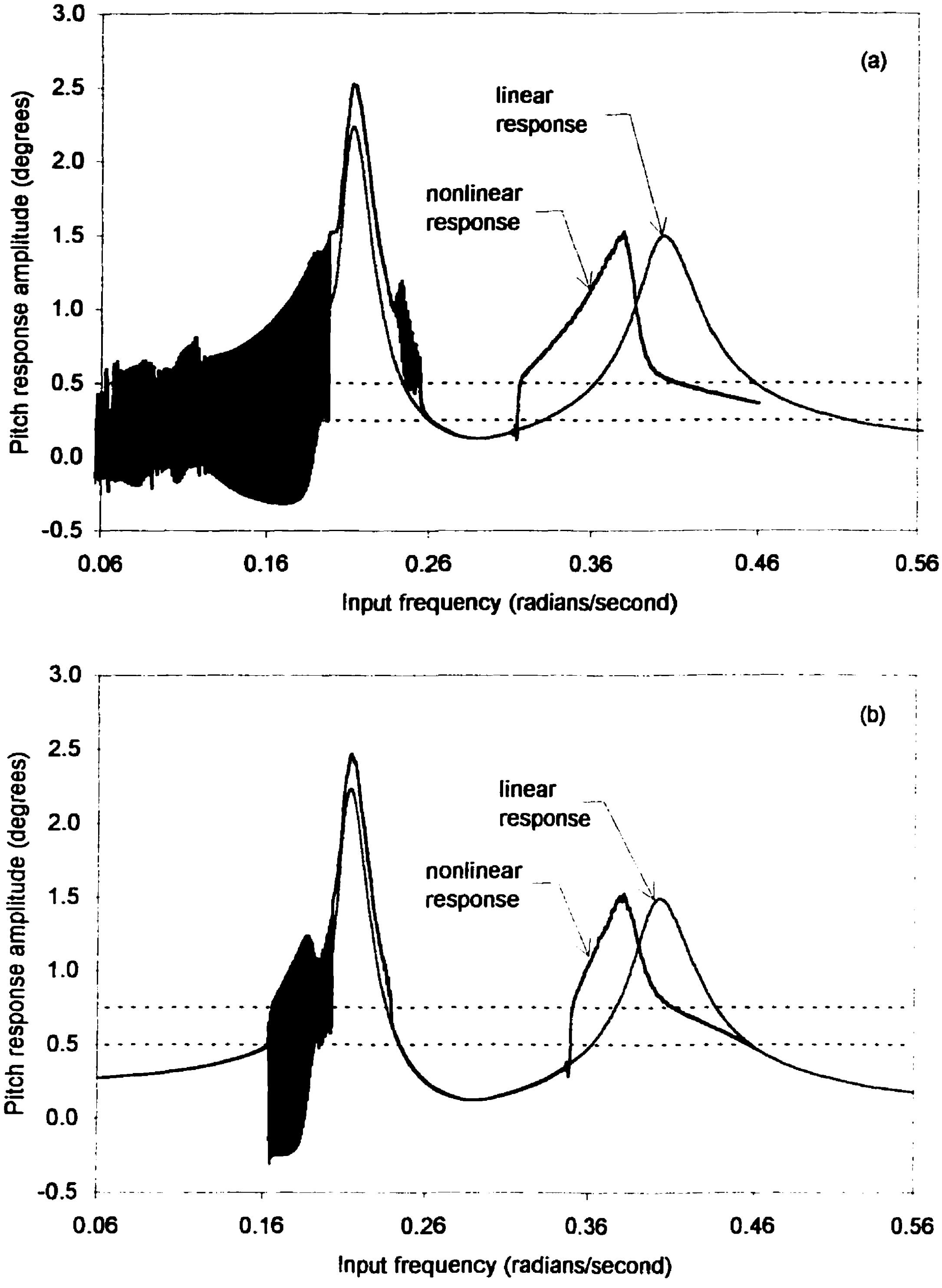

Figure 93. Linear and nonlinear frequency responses to a decreasing frequency sweep at a sweep-rate of .000012 radians/(non-dimensional second)^2, and a non-dimensional airspeed equivalent to U/U*=0.64. Nonlinear curves obtained for a nonlinear region length of 0.25 degrees and a preload of (a) 0.25 degrees, and (b) 0.50 degrees.

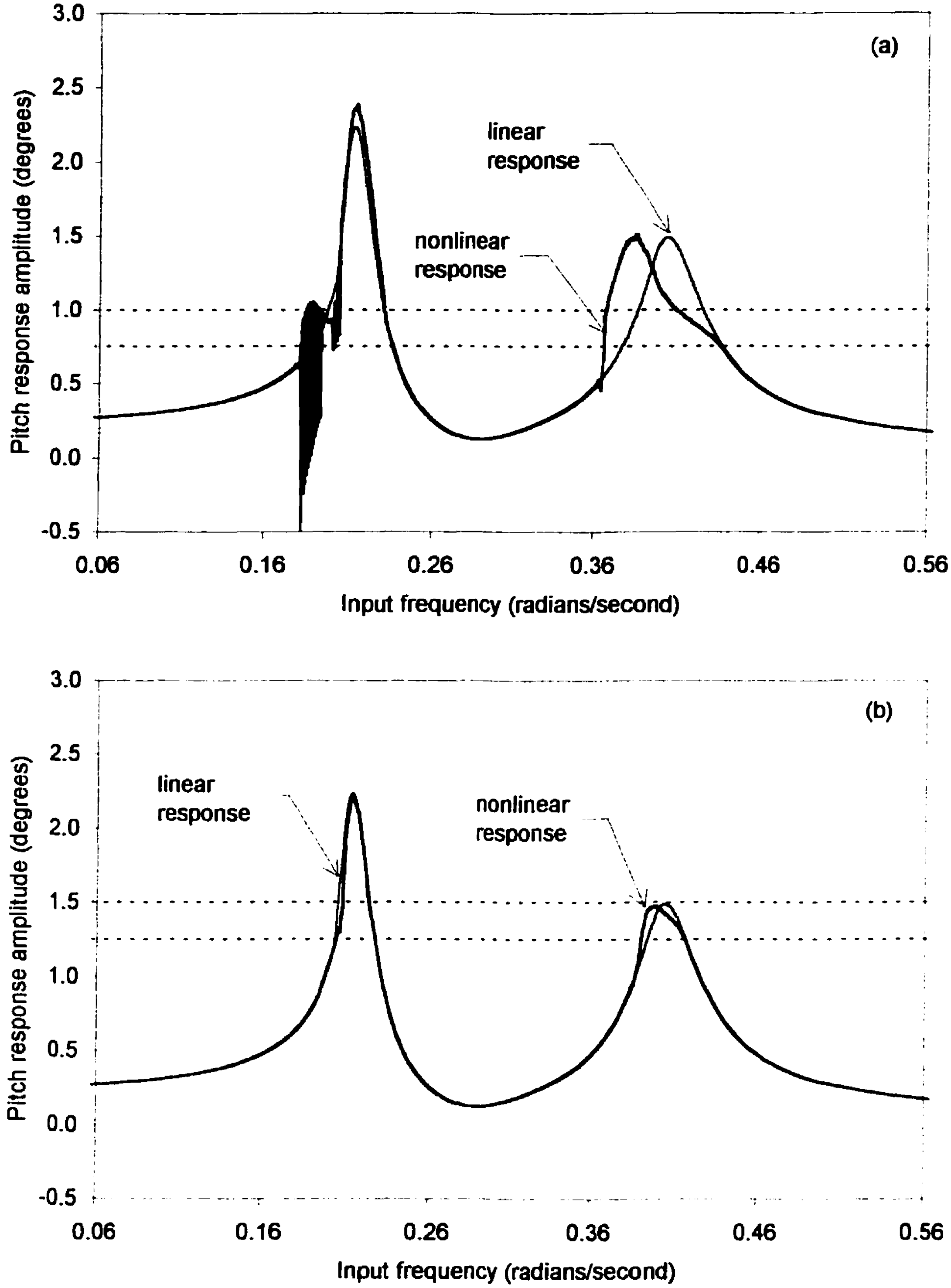

Figure 94. Linear and nonlinear frequency responses to a decreasing frequency sweep at a sweep-rate of .000012 radians/(non-dimensional second)^2, and a non-dimensional airspeed equivalent to U/U*=0.64. Nonlinear curves obtained for a nonlinear region length of 0.25 degrees and a preload of (a) 0.75 degrees, and (b) 1.25 degrees.

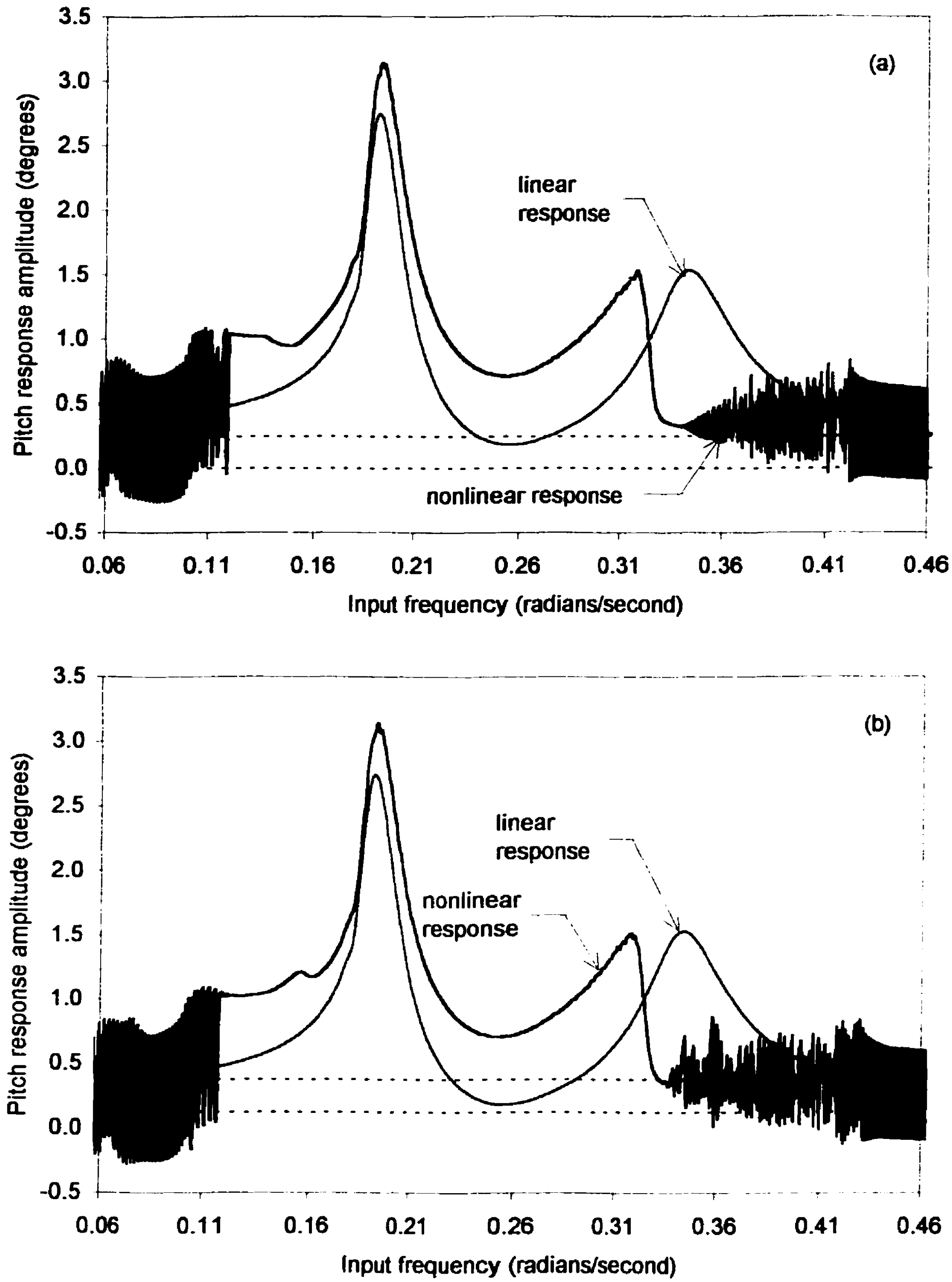

Figure 95. Linear and nonlinear frequency responses to a decreasing frequency sweep at a sweep-rate of .000012 radians/(non-dimensional second)^2, and a non-dimensional airspeed equivalent to U/U*=0.73. Nonlinear curves obtained for a nonlinear region length of 0.25 degrees and a preload of (a) 0.0 degrees, and (b) 0.125 degrees.

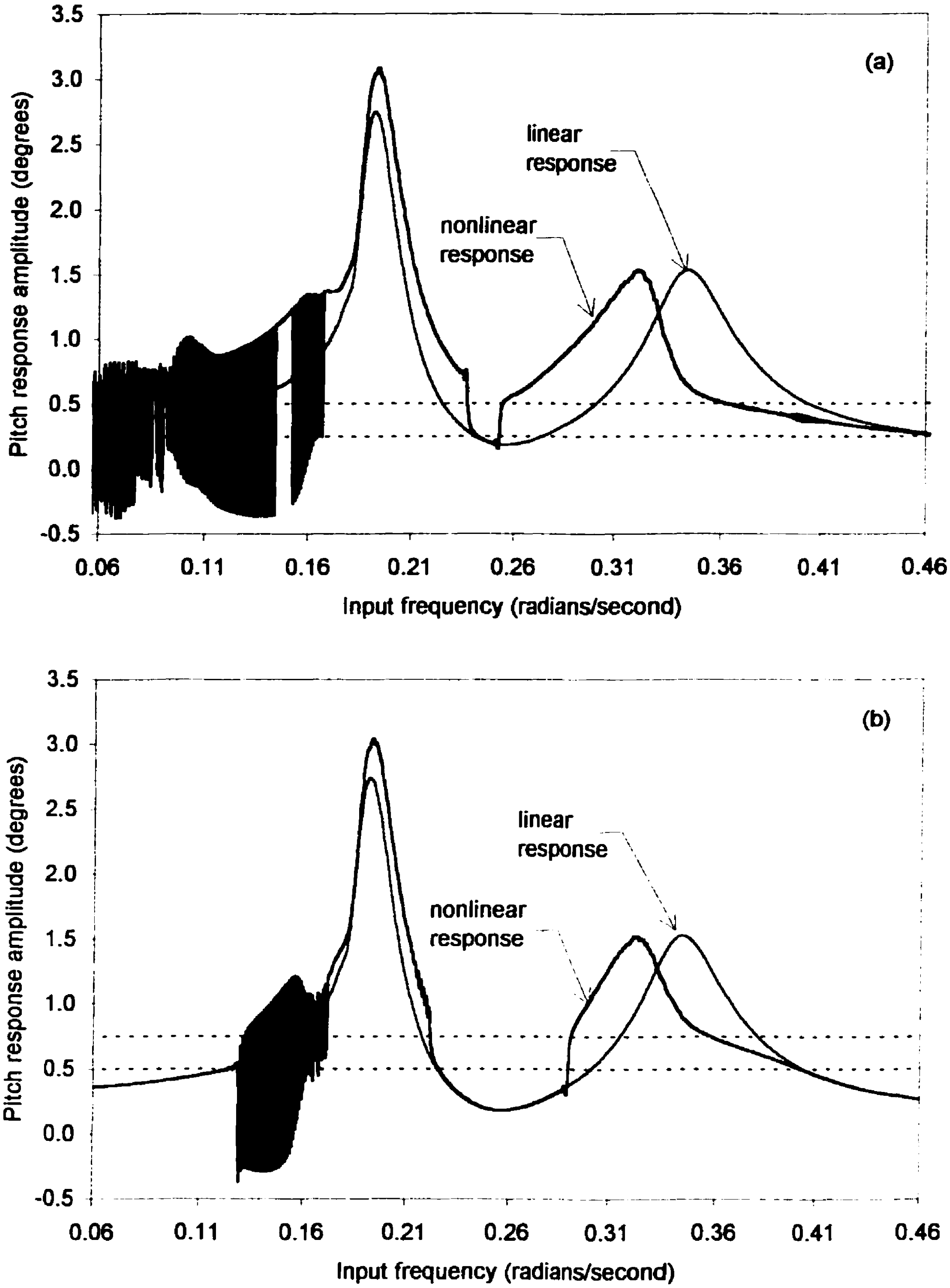

Figure 96. Linear and nonlinear frequency responses to a decreasing frequency sweep at a sweep-rate of .000012 radians/(non-dimensional second)^2, and a non-dimensional airspeed equivalent to U/U*=0.73. Nonlinear curves obtained for a nonlinear region length of 0.25 degrees and a preload of (a) 0.25 degrees, and (b) 0.50 degrees.

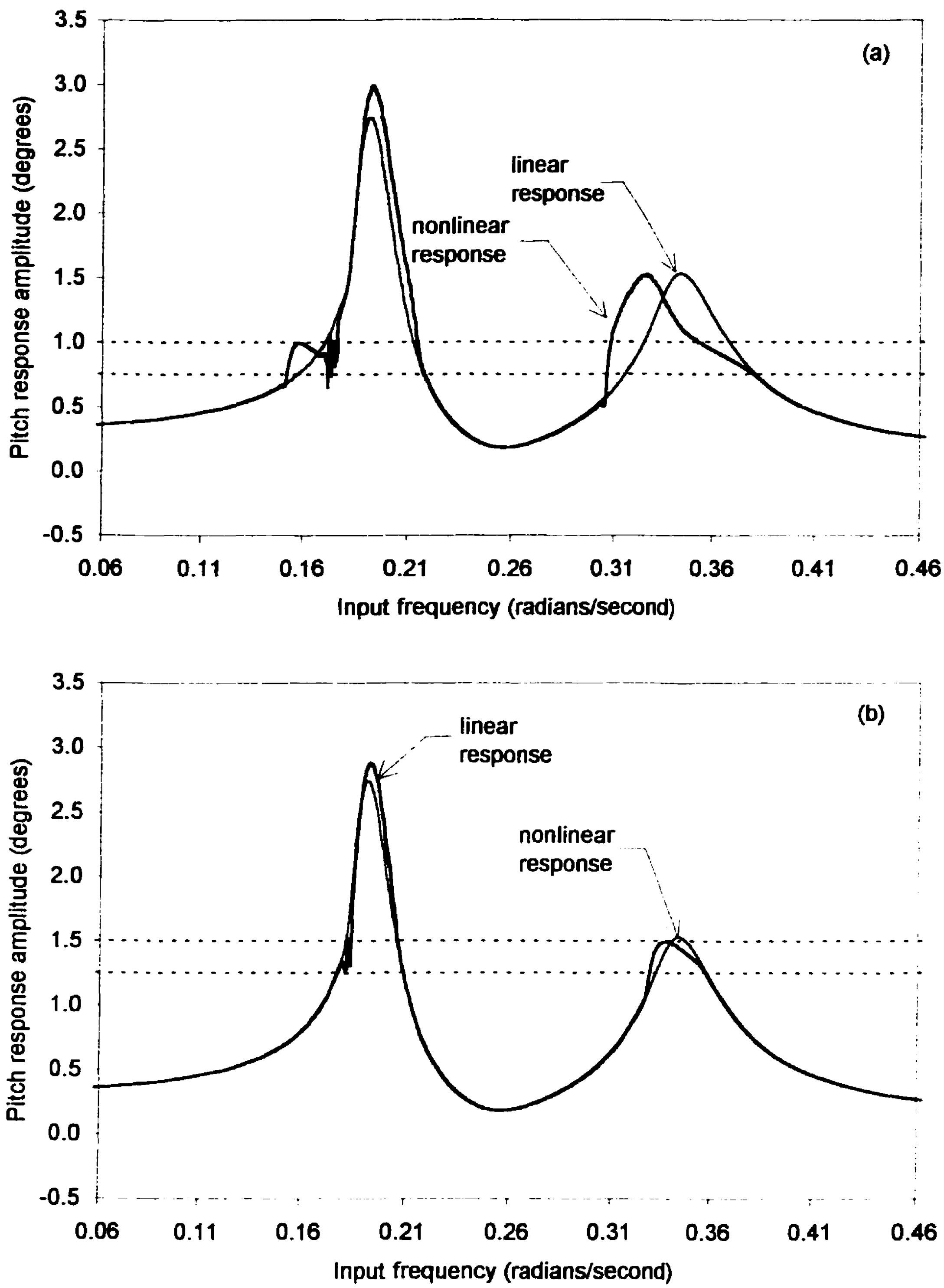

Figure 97. Linear and nonlinear frequency responses to a decreasing frequency sweep at a sweep-rate of .000012 radians/(non-dimensional second)^2, and a non-dimensional airspeed equivalent to U/U*=0.73. Nonlinear curves obtained for a nonlinear region length of 0.25 degrees and a preload of (a) 0.75 degrees, and (b) 1.25 degrees.

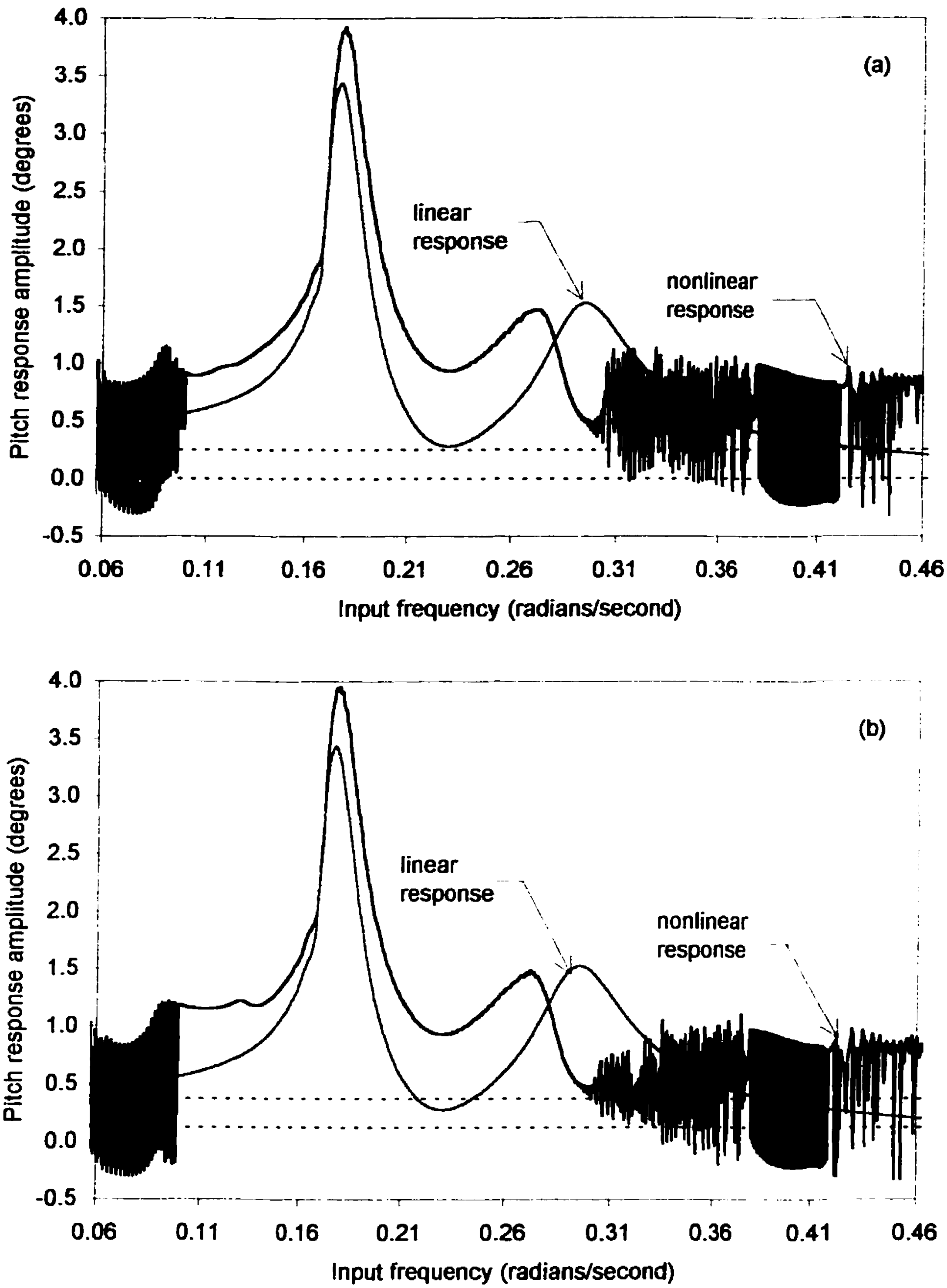

Figure 98. Linear and nonlinear frequency responses to a decreasing frequency sweep at a sweep-rate of .000012 radians/(non-dimensional second)^2, and a non-dimensional airspeed equivalent to U/U*=0.82. Nonlinear curves obtained for a nonlinear region length of 0.25 degrees and a preload of (a) 0.0 degrees, and (b) 0.125 degrees.

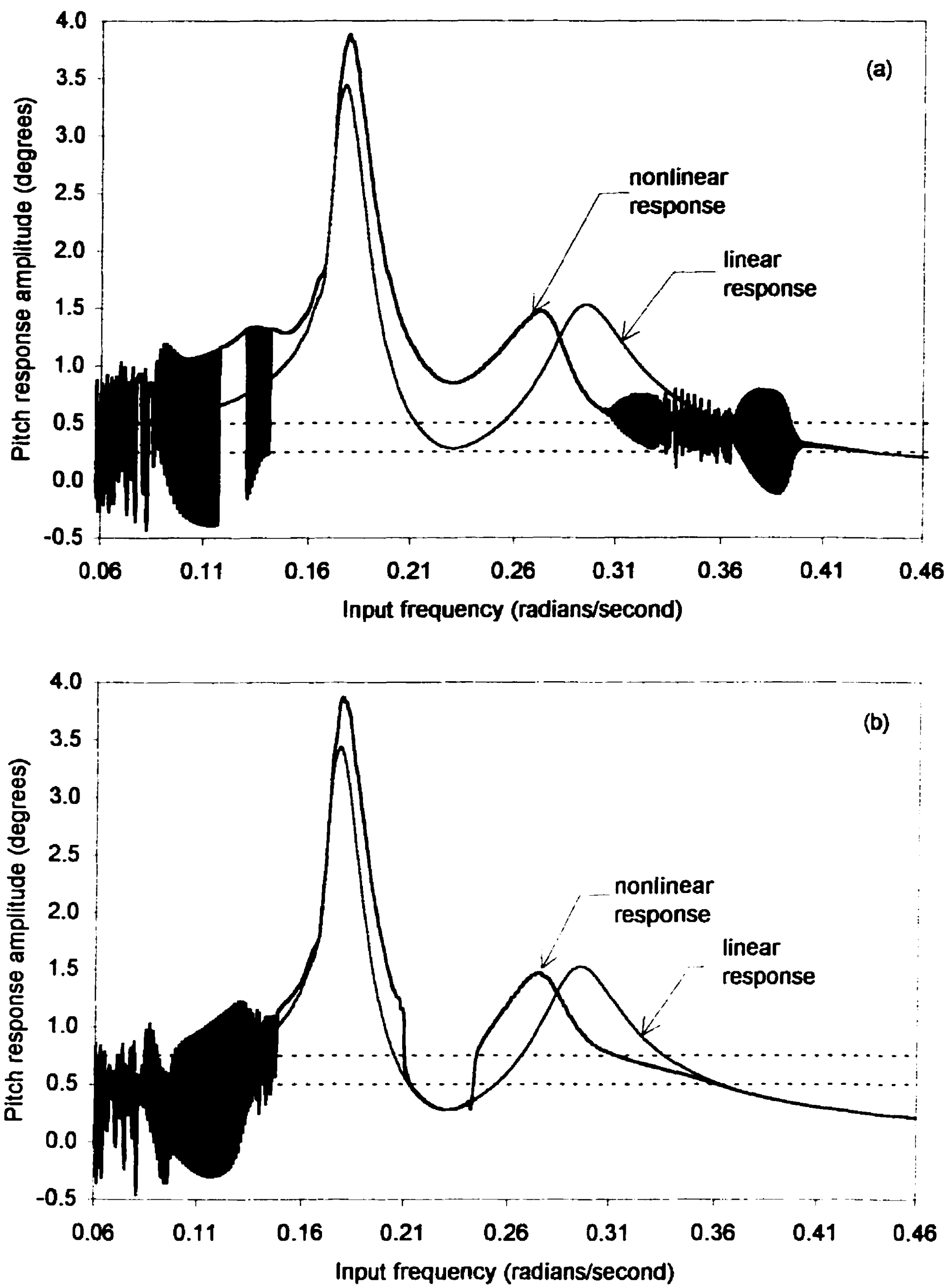

Figure 99. Linear and nonlinear frequency responses to a decreasing frequency sweep at a sweep-rate of .000012 radians/(non-dimensional second)^2, and a non-dimensional airspeed equivalent to U/U*=0.82. Nonlinear curves obtained for a nonlinear region length of 0.25 degrees and a preload of (a) 0.25 degrees, and (b) 0.50 degrees.

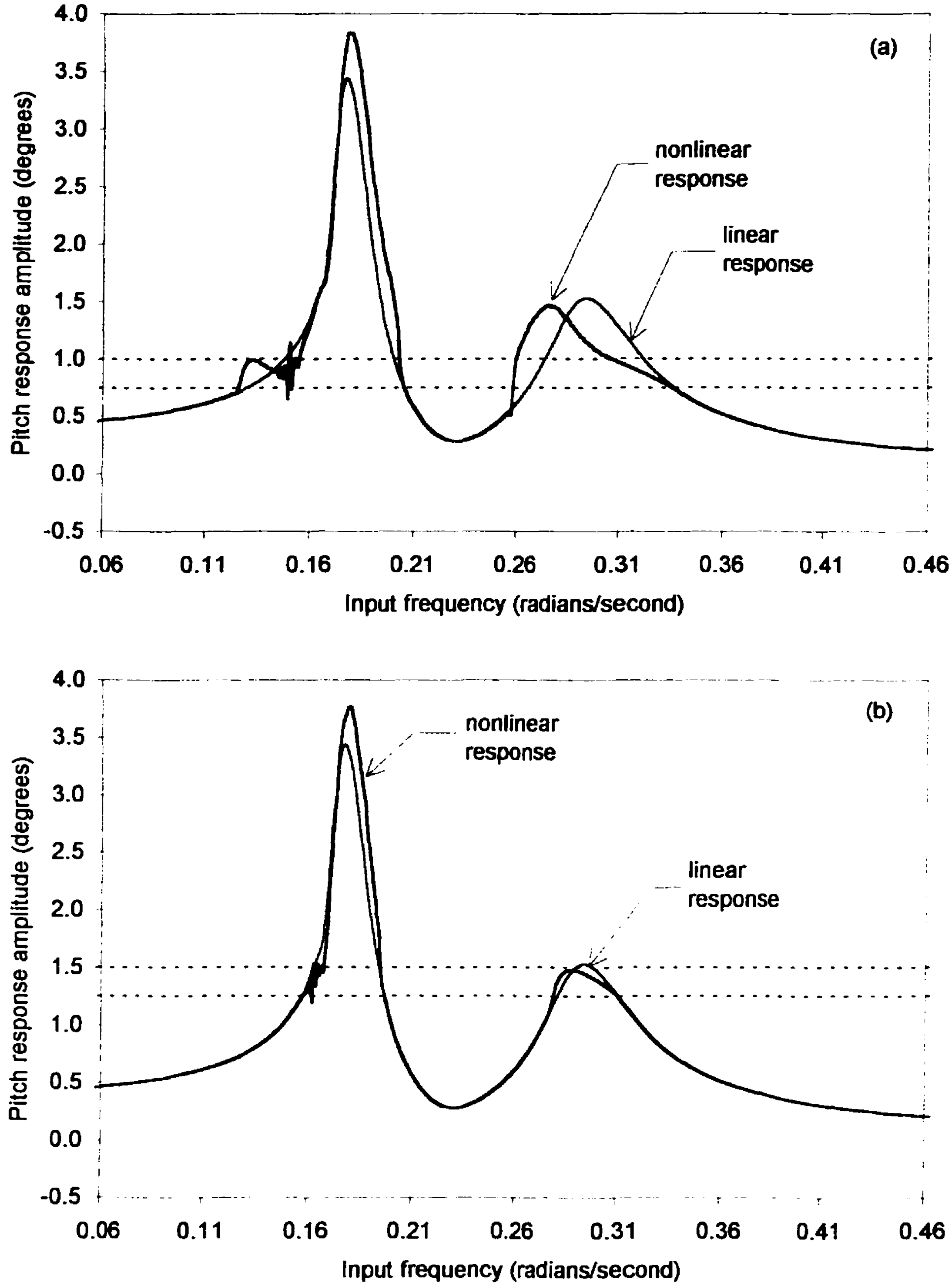

Figure 100. Linear and nonlinear frequency responses to a decreasing frequency sweep at a sweep-rate of .000012 radians/(non-dimensional second)^2, and a non-dimensional airspeed equivalent to U/U*=0.82. Nonlinear curves obtained for a nonlinear region length of 0.25 degrees and a preload of (a) 0.75 degrees, and (b) 1.25 degrees.

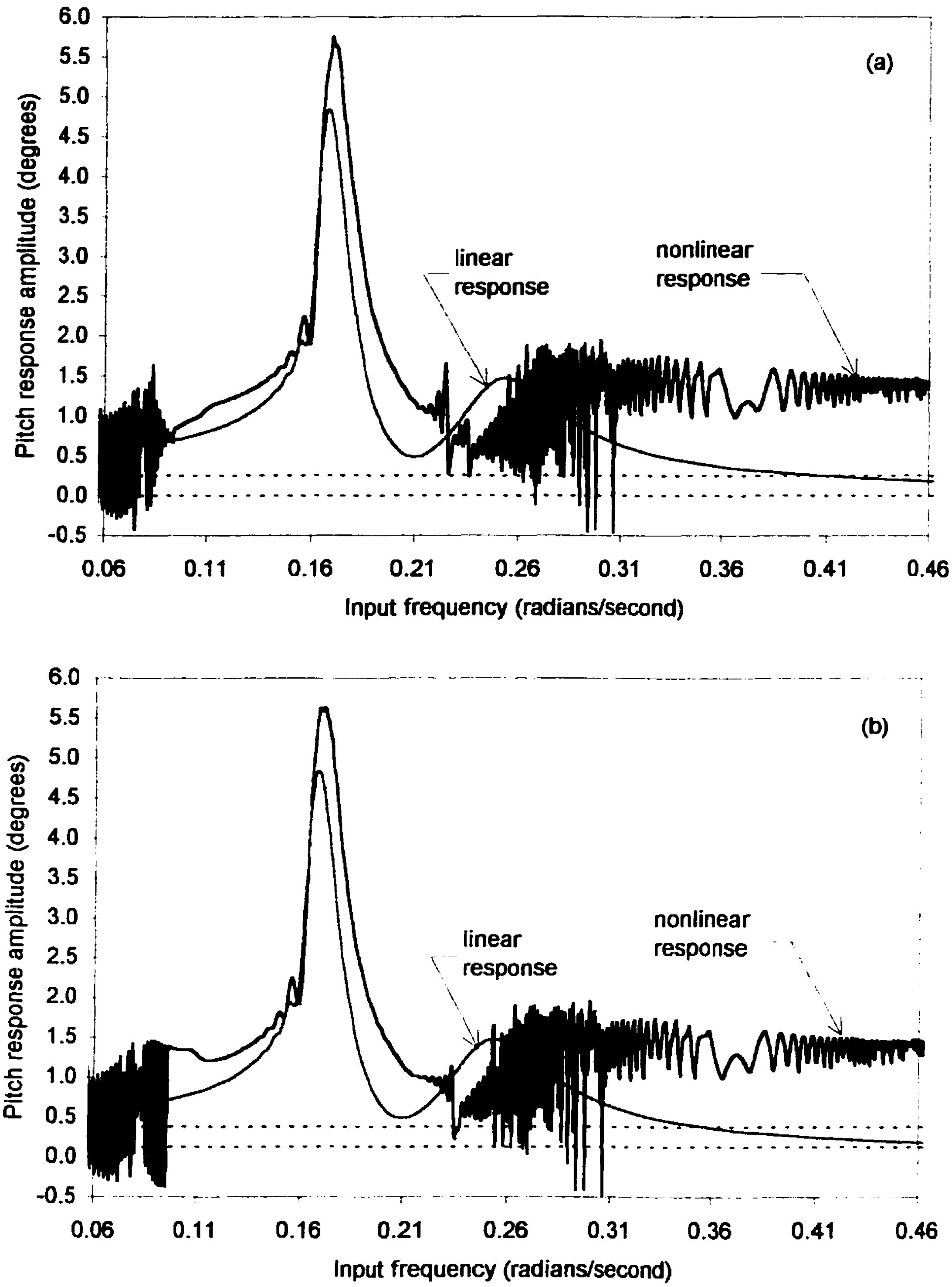

Figure 101. Linear and nonlinear frequency responses to a decreasing frequency sweep at a sweep-rate of .000012 radians/(non-dimensional second)^2, and a non-dimensional airspeed equivalent to U/U*=0.91. Nonlinear curves obtained for a nonlinear region length of 0.25 degrees and a preload of (a) 0.0 degrees, and (b) 0.125 degrees.

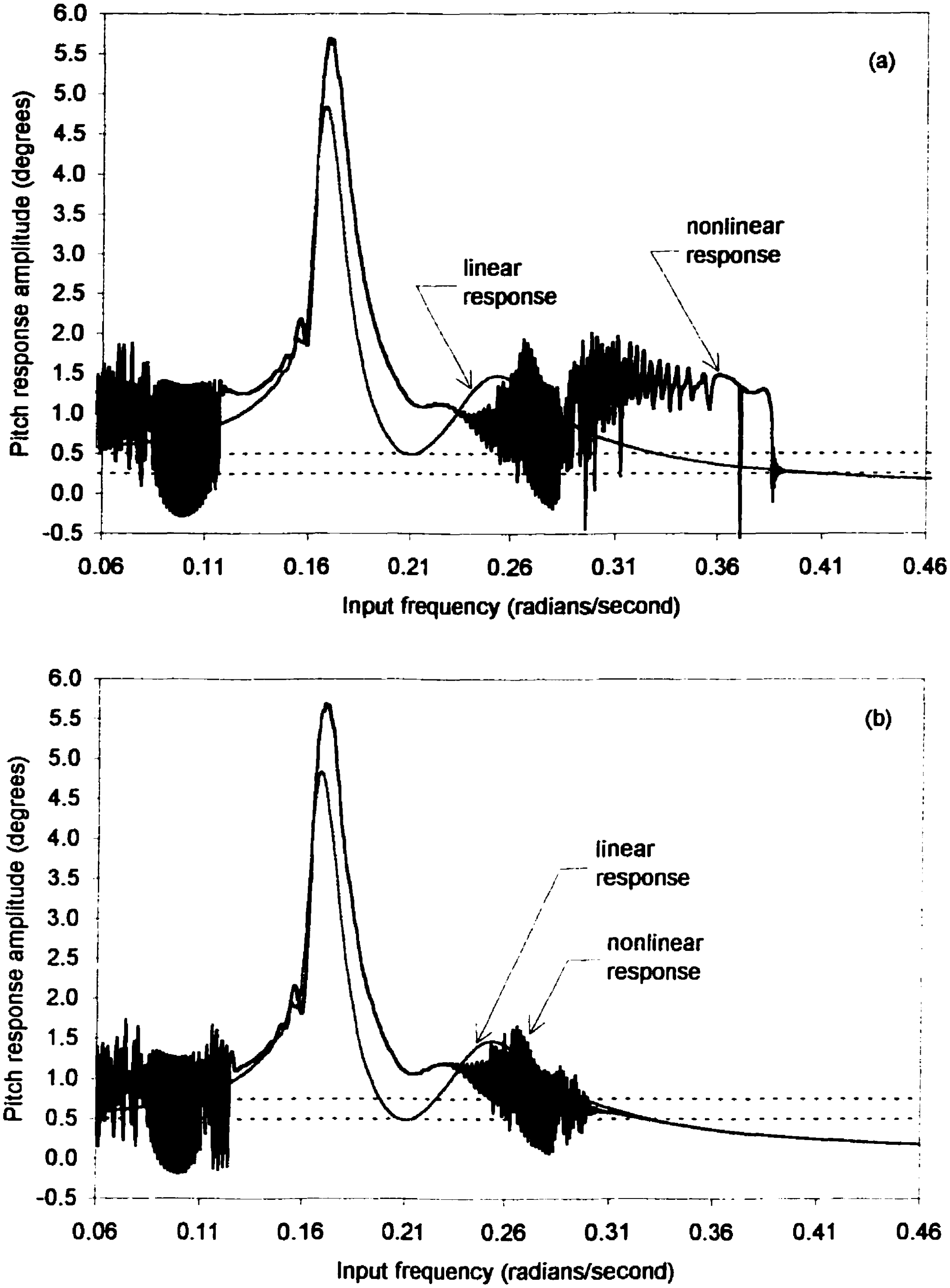

Figure 102. Linear and nonlinear frequency responses to a decreasing frequency sweep at a sweep-rate of .000012 radians/(non-dimensional second)^2, and a non-dimensional airspeed equivalent to U/U*=0.91. Nonlinear curves obtained for a nonlinear region length of 0.25 degrees and a preload of (a) 0.25 degrees, and (b) 0.50 degrees.

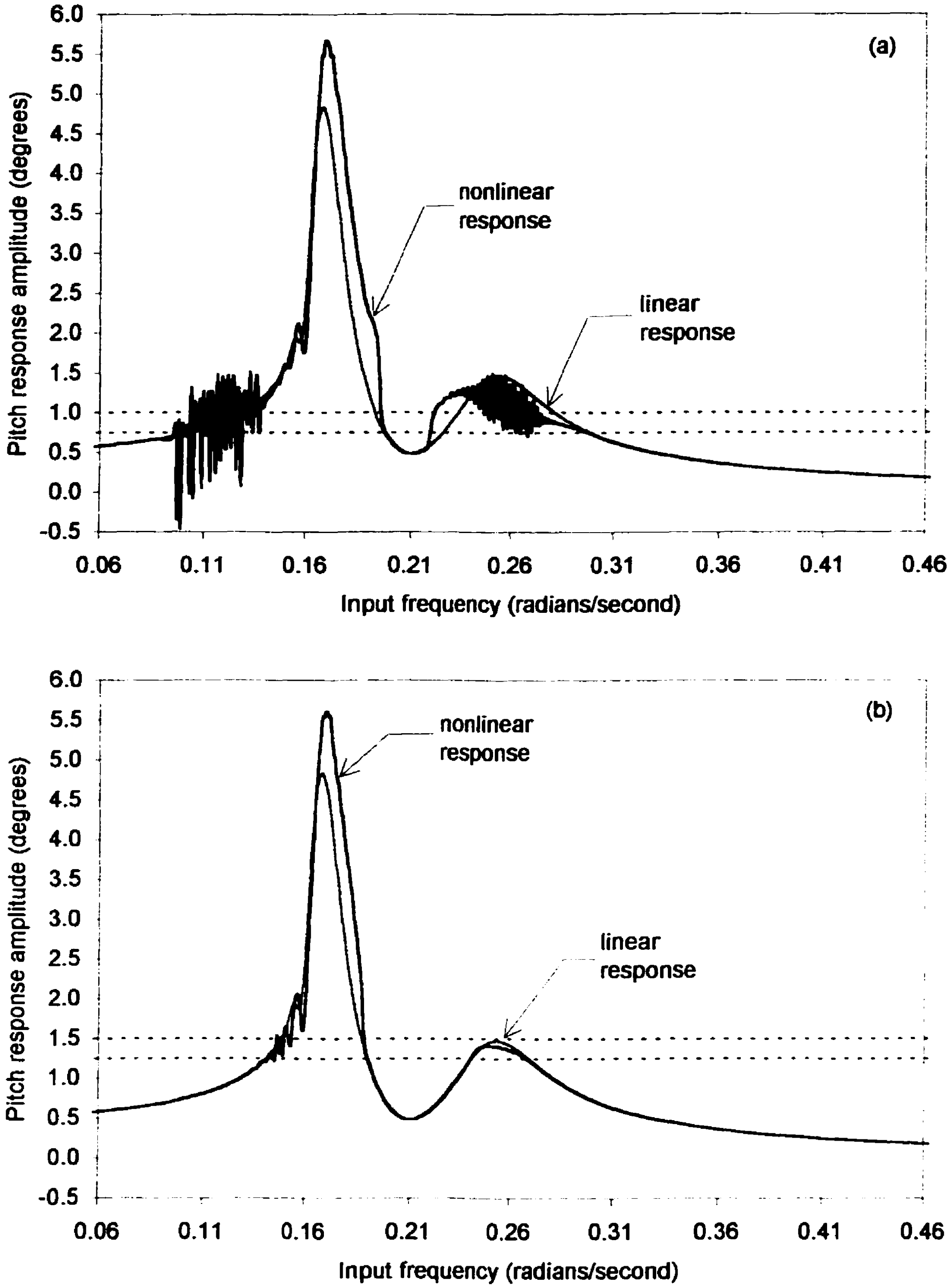

Figure 103. Linear and nonlinear frequency responses to a decreasing frequency sweep at a sweep-rate of .000012 radians/(non-dimensional second)^2, and a non-dimensional airspeed equivalent to U/U*=0.91. Nonlinear curves obtained for a nonlinear region length of 0.25 degrees and a preload of (a) 0.75 degrees, and (b) 1.25 degrees.

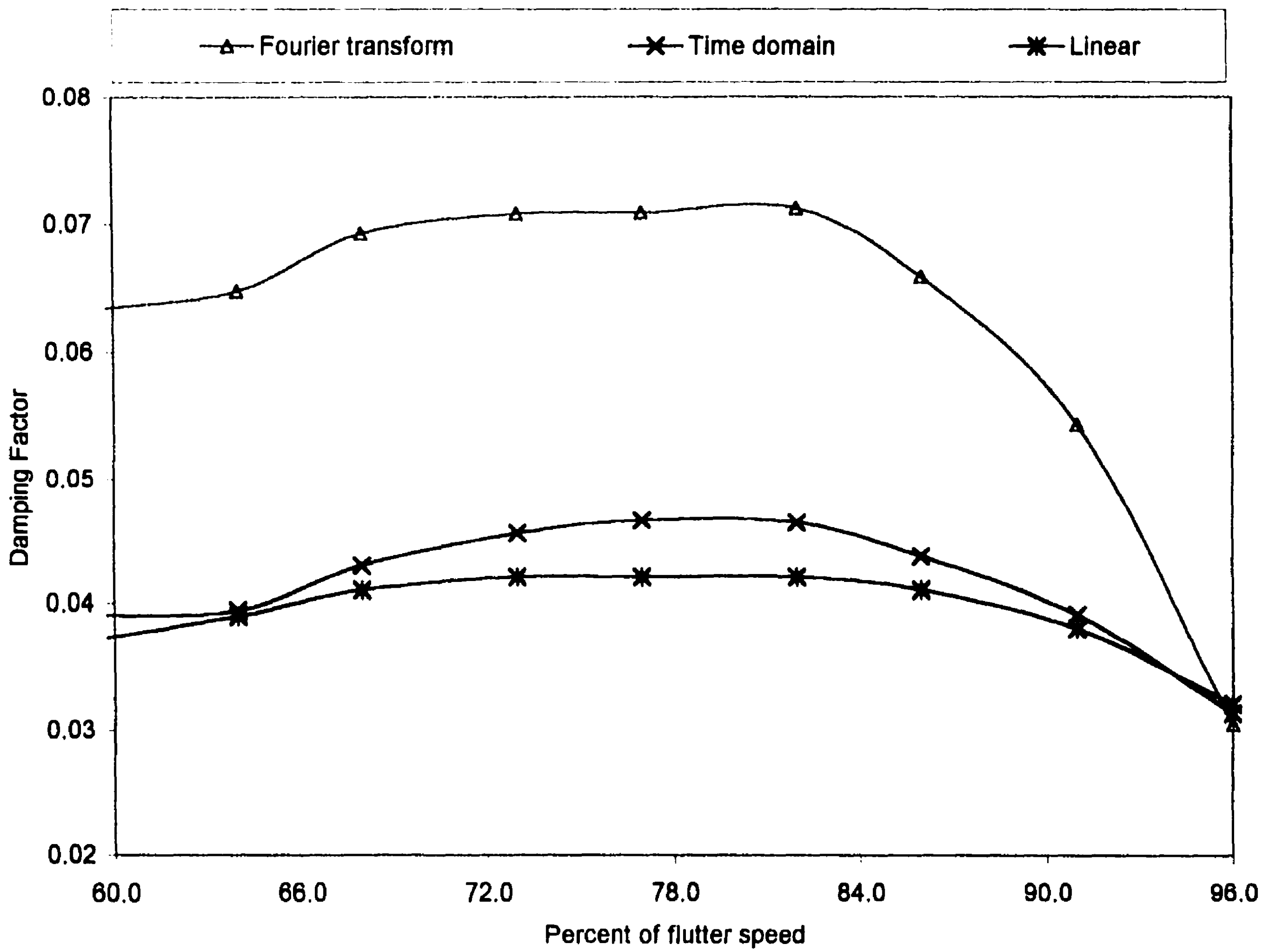

Figure 105. First mode damping estimates obtained using pitch response to a decreasing frequency sweep and flap velocity input. Sweep rate .000012 radians/(non-dimensoinal second)^2.

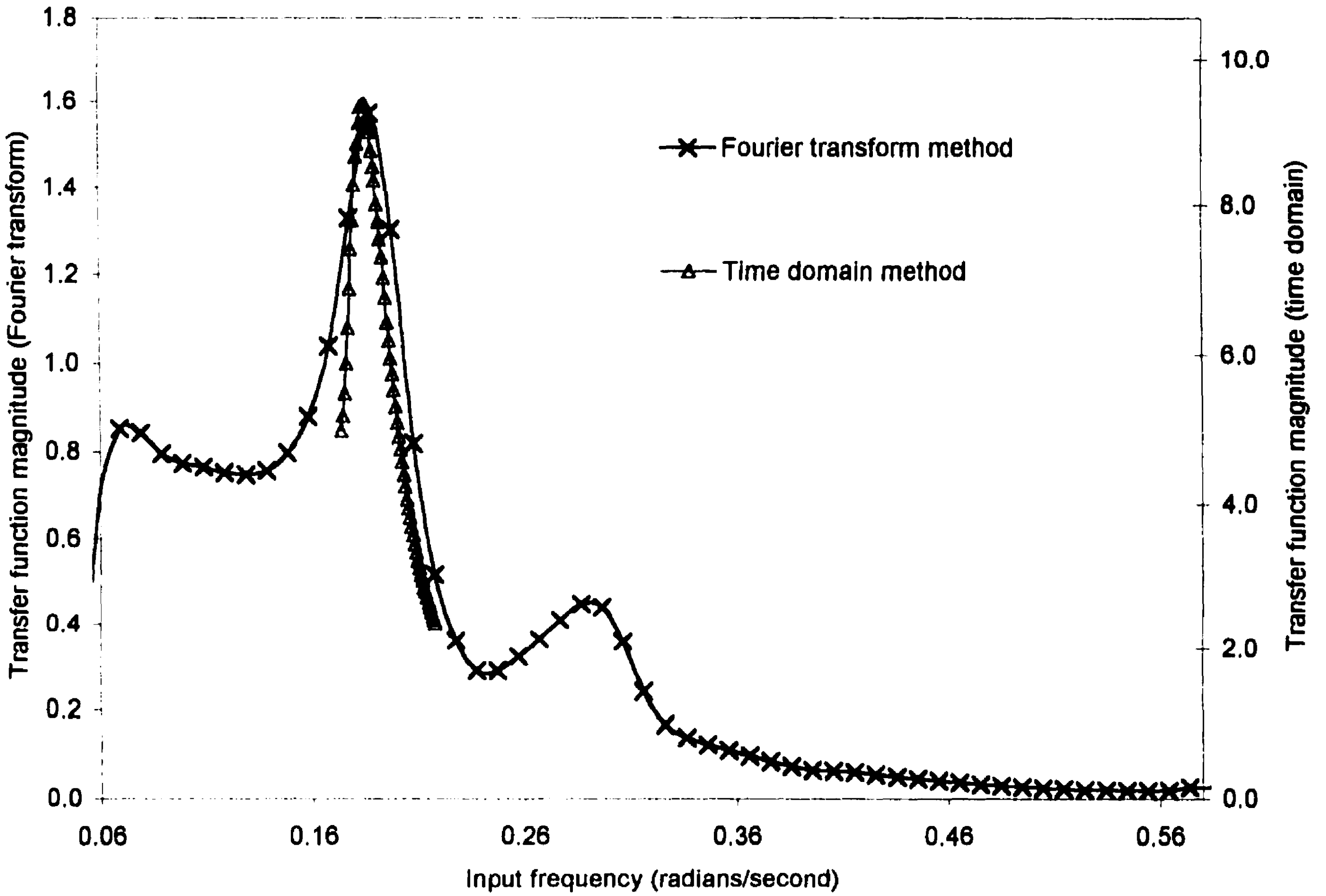

Figure 104. Transfer functions obtained using Fourier tranform and time domain methods. Results from the pitch response to a decreasing frequency sweep with flap velocity input at U/U*=0.77. Sweep-rate .000012 radians/(non-dimensoinal second)^2.